SEASONAL AND INTERANNUAL VARIABILITY OF SEA TEMPERATURE AND SURFACE HEAT FLUXES IN THE NORTHWEST ATLANTIC

By

Joseph U. Umoh

SUBMITTED IN PARTIAL FULFILLMENT OF THE
REQUIREMENTS FOR THE DEGREE OF
DOCTOR OF PHILOSOPHY
AT
DALHOUSIE UNIVERSITY
HALIFAX, NOVA SCOTIA
JULY 1992

ISBN 0-315-80208-1

To God's glory

Contents

List of Tables

List of Figures

ABSTRACT

The Northwest Atlantic is a region of extremely strong sea surface temperature (SST) variability. The seasonal cycle in SST of about 16°C, and the anomalies about this seasonal cycle that occasionally exceed 5°C, are the largest in the North Atlantic. The purpose of this study is to explain the seasonal and interannual variability of water temperature in this region. Analysis of hydrographic data from the Scotian Shelf and Slope shows that the *seasonal* temperature signal is confined to the top 75 m of the water column. As a first step in the development of a model to explain the seasonal temperature variability, the heat budget is examined. The most important term in the long-term mean heat budget is horizontal advection, with a contribution of about -40W m^{-2}, and is almost exactly balanced by the combined effect of the net surface heat flux (Q = 25W m^{-2}), horizontal mixing (11W m^{-2}) and vertical diffusion (6W m^{-2}). On the seasonal time scale, about 85% of the local rate of heat storage ($\partial H/\partial t$) can be accounted for by Q. Horizontal advection and Q together explain about 99% of $\partial H/\partial t$. Motivated by the results of the heat budget, the seasonal cycle is modelled by a modified 1-D heat diffusion equation: $\partial T/\partial t = \partial/\partial z(K_v \partial T/\partial z) + \Gamma(z,t)$, where $\Gamma(z,t)$ is dominated by horizontal advection. Considerable attention is paid to the estimation of K_v, an extremely important parameter in the model. Three methods of estimating $K_v(z,t)$, on a monthly time scale, are presented. In two of the methods, $K_v(z,t)$ is assumed to vary with density stratification, and hence with depth and time, as $K_v(z,t) = K_0(1+\alpha N^p)^{-1}$. An important contribution of this work is providing an effective way of determining the parameters p, α and K_0. The attraction of this approach is that it does not allow negative diffusivities. $T(z,t)$ predicted using the seasonal varying $K_v(z,t)$ compares much more favorably with observations than $T(z,t)$ calculated using the best *constant* K_v. This emphasizes the importance of allowing $K_v(z,t)$ to vary with depth and time. The modified 1-D heat diffusion model is also used to study the origin of the cold intermediate layer (CIL), and it is shown that both local heating *and* horizontal advection of cold water are needed to maintain the permanent CIL on the Scotian Shelf.

Focusing now on the monthly anomalies (i.e. variations about the seasonal cycle), over 90% of Q' may be accounted for by the latent and sensible heat flux. Overall, Q' has a smaller spatial scale and shorter time scale than SST anomalies (SSTAs). Previous studies have hypothesized that SSTAs are the result of stochastic forcing by Q'. For the first time, this study has quantified through numerical modelling, the contribution of Q' to the evolution of the SSTAs. The results show that Q' is *not* the primary cause of the interannual variability of SSTAs in the Northwest Atlantic, and suggest that the primary cause lies in the ocean. Empirical modelling indicates that, on the whole, the SSTAs originate from variations in the top 50 m of the water column. It is speculated that fluctuations in the transport of water from the Gulf of St. Lawrence and the inshore Labrador Current are the dominant cause of the interannual variability of SSTA in the Northwest Atlantic.

ACKNOWLEDGMENTS

A research work of this magnitude would not be possible without the support of many people. I would like to thank my supervisor Dr. Keith Thompson whose motivation and insistence on a thorough work contribute to the quality of this thesis. His encouragement, time and sharing of insight are very much appreciated.

I am grateful to the members of my thesis and examining committee: Drs. Dan Kelley, Owen Hertzman, Chris Garrett and Tony Bowen and to the external examiner Dr. Wendell Brown. Their comments and suggestions have greatly enriched the work. I acknowledge with thanks the support of many scientists at the Bedford Institute of Oceanography. Drs. Ken Drinkwater and Brian Petrie kindly provided some of the data used in the thesis, setting a good example on free exchange of scientific data and information. Dr. John Loder's expressed interest in the work provided much encouragement. Drs. Stu Smith and Fred Dobson provided some guidance on the estimation of the surface heat fluxes. Thanks are due to several other people at Dalhousie University: Jackie Hurst for her assistance in different forms during my student years in the Department of Oceanography and Kevin Marinelli for supplying the NCAR contouring programs and helping in the graphics. I would not forget the encouragement of Drs. Keith Louden and Bob Moore during the critical period in the program. Their help is deeply appreciated. I acknowledge with thanks the invaluable friendship and special support of Isaac, Chinyere, Mike, Ihedinma, Dele, Moji, Estella and Julian throughout the program. The financial support of the Canadian Commonwealth Scholarship is gratefully acknowledged.

I specially thank my parents Mr. and Mrs. Udo Umoh Antia, whose love and confidence in me gave me the first stepping stone to success. Foremost, I thank my wife Mercy, whose endless love, understanding, care, patience and encouragement piloted me through the graduate program. To my daughter Inem and son Ubong whose smiles were an inspiration to me, I say, thank you.

Finally, my gratitude goes to God for His special grace and blessings throughout my years of study.

Chapter 1

INTRODUCTION

1.1 Background

The Northwest Atlantic is the most energetic sea surface temperature region in the North Atlantic. The range of the seasonal cycle is about $16°C$. Anomalies about this seasonal cycle have, at times, exceeded $5°C$. The standard deviation of the anomalies ($\sim 1.6°C$) is greater than that found off the coast of Peru *[Weare et al., 1976; Weare, 1977; Cayan, 1986]*. Interest in the water temperature of this region has increased in recent years because of its possible influence on the atmospheric circulation and fisheries. For example, *Ratcliffe and Murray [1970]* have shown that sea surface temperature off the coast of Newfoundland may be used to predict the weather in Europe. They found a lagged correlation between sea surface temperature and air pressure anomalies, with the water temperature in this region leading the air pressure over Europe by about one month. *Palmer and Sun [1985]* examined this empirical result using a general circulation model. They found that a significant atmospheric response over Europe could indeed be associated with sea surface temperature anomalies in the Northwest Atlantic. Considering the possible climatic effects of the North Atlantic mid-latitude SSTAs, this region can not be overlooked *[Lau and Nath, 1989]*. The seasonal migration of fishes may be connected, in part, to the seasonal variability of the water temperature [e.g. *Rose, 1990]*. Hence, the possibility of predicting water temperature, one of the goals of this study, is of interest to oceanographers, atmospheric scientists and fisheries biologists.

The portion of the Northwest Atlantic treated in this study covers the Scotian Shelf and Slope region (Figure 1.1). It is bounded to the north by the Laurentian Channel, to the south by Georges Bank and extends seaward about 200 km from the shelf break. In physical oceanographic terms, this is a special region. The St. Lawrence, Ottawa and Saguenay rivers discharge about $10,000\ \mathrm{m^3\,s^{-1}}$ of fresh water which spills out of the Gulf of St. Lawrence and onto the Scotian Shelf. To fit this discharge into perspective, it is about 14% of that of the Amazon, the largest river by volume flux in the world *[Paxton, 1986]*). Alternatively, it is equivalent to adding about 6 m of freshwater to the Scotian Shelf each year. This region is also the meeting place of two important current systems: the warm Gulf Stream from the south and the cold Labrador current from the north (Figure 1.1b). In fact, I will show that much of the interannual variability in the water temperature of the Northwest Atlantic is controlled by these river and current systems.

1.2 Problems and Objectives

The outstanding problems addressed in this study concern (1) explaining the seasonal cycle of water temperature (2) estimating vertical eddy diffusivity in the upper water column, as a function of depth and time, (3) explaining the formation of the cold intermediate layer on the Scotian Shelf, and (4) finding the primary causes of sea surface temperature anomalies on the Scotian Shelf and Slope.

Explaining the seasonal cycle of water temperature.

There are several mixed layer models *[e.g., Price et. al., 1986, 1987; Gaspar, 1988]* that have had some success in simulating the evolution of the sea surface temperature (SST). These models require, as input, atmospheric forcing terms averaged over a short time (hours to days). The main problem of applying such models in

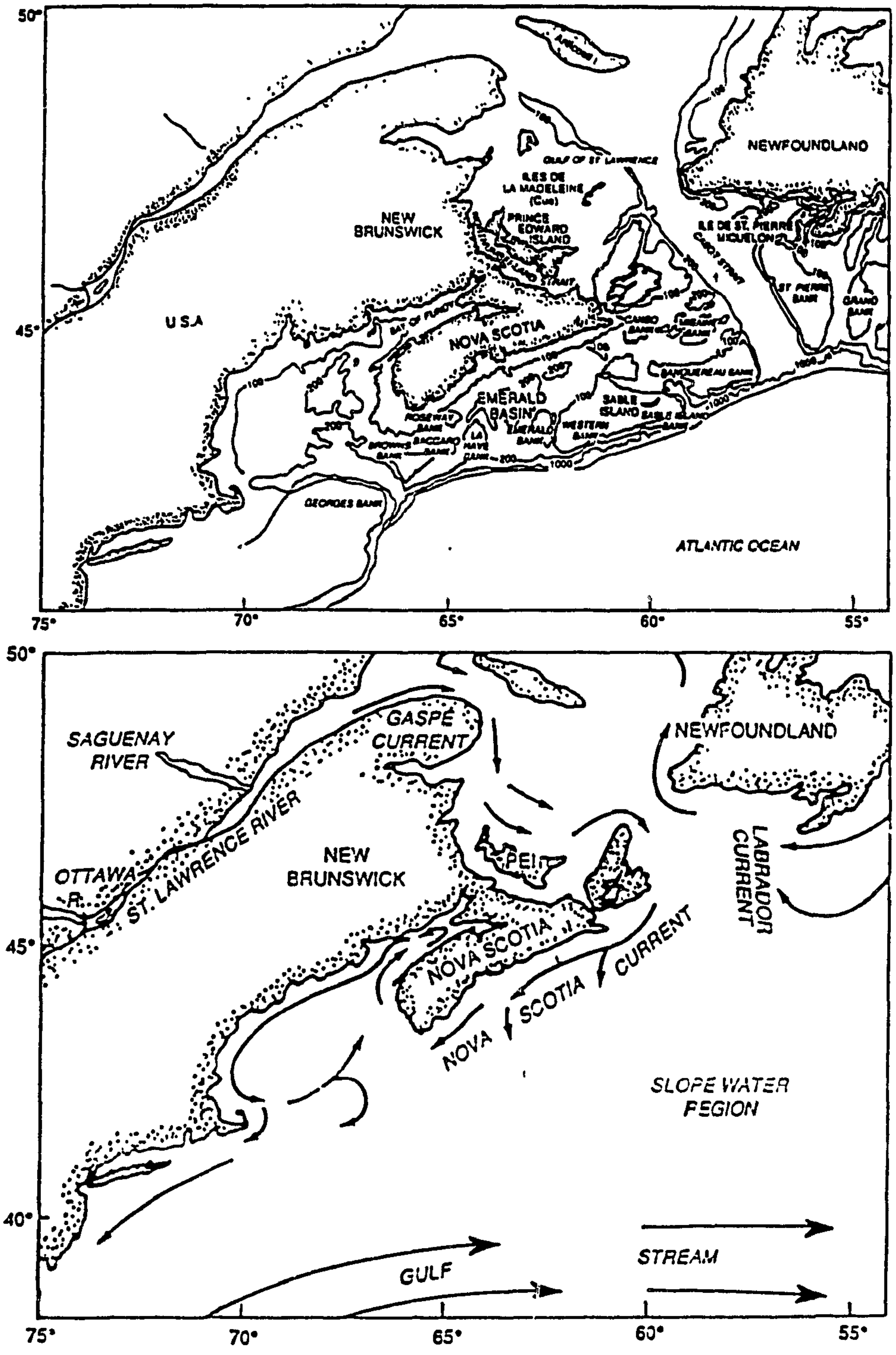

Figure 1.1: Map of Northwest Atlantic showing (a) some topographic features and (b) the mean circulation pattern (adapted from *Sutcliffe et al. [1976]*).

the study area is that one may not have spatially complete atmospheric or oceanographic data sampled on such short time scales. The model that I will develop uses monthly averaged quantities. The surface forcing is the monthly air-sea heat flux, computed from 43 years of data from COADS (Comprehensive Ocean Atmosphere Data Set), and that estimated by *Isemer and Hasse [1987]*. The model is a modified one-dimensional (vertical) heat diffusion equation. The specific problem addressed, with respect to modelling, is: can a simple modified one-dimensional model simulate the seasonal surface and subsurface temperature on the Scotian Shelf? It will be shown that the model successfully reproduces the seasonal cycle of the surface and the subsurface temperatures.

Estimating vertical eddy diffusivity in the upper water column

Methods have been developed for estimating the eddy diffusivity in stably stratified systems, such as lakes and fjords *[Jassby and Powell, 1975; Gargett, 1984; de Young and Pond, 1988]*. The success of these methods depends on a well defined vertical temperature gradient. Where the temperature gradient is weak the values of the diffusivities are unreasonable; in some cases negative values are obtained, which are unphysical. What is needed is a method of estimating the eddy diffusivity in the upper ocean (where there is a mixed layer and sometimes the vertical temperature gradient is weak) that will overcome the frustrating cases of negative values of diffusivities. A related question is how the estimated diffusivities vary with the buoyancy frequency.

The need for an accurate estimates of the diffusivities arises not only because the diffusivities are required in my model but also because their values have implications to other issues. In a one-dimensional diffusion model, *Hansen et al. [1985]* have shown that the climate response time is largely dependent on the values of the diffusivities. Thus, the value of the diffusivity influences the transient response of the ocean to greenhouse warming and the estimation of the ocean's ability to absorb fossil fuel carbon dioxide *[Yin and Fung, 1991]*. In this study, a considerable effort is made to determine the best method of estimating the diffusivities, as a function of depth and time, since the predicted temperatures largely depend on these diffusivities.

Explaining the formation of the cold intermediate layer on the Scotian Shelf

A characteristic feature of the temperature structure in the study region is the existence of a temperature minimum, between about 50 and 100 m depth. This is often referred to as the cold intermediate layer *[Hachey, 1938; Smith et al., 1978]*. The cold intermediate layer has also been observed in the Gulf of St. Lawrence *[Banks, 1966]* and on the Labrador and Northeast Newfoundland Shelves *[Petrie et al., 1988]*. The question is: how is the cold intermediate layer formed and maintained? Besides the influence of the cold intermediate layer on the diffusivities, an understanding of the origin of the cold intermediate layer has scientific merit on its own. *Banks [1966]* suggested that in situ winter cooling is the dominant mechanism that produces the cold intermediate layer on the Gulf of St. Lawrence. For the cold intermediate layer on the Scotian Shelf, *Hachey [1938]* suggested that it forms as a result of horizontal advection of cold water into the region. It will be shown in this study that both horizontal advection of cold water and local heating are needed to produce the cold intermediate layer on the Scotian Shelf.

Finding the primary causes of the sea surface temperature anomalies in the Northwest Atlantic

As noted above, the Northwest Atlantic is a highly active region in terms of sea surface temperature (SST). *Weare [1977]* performed an empirical orthogonal function analysis on the SST in the Atlantic ocean. His results show that the maximum variance of the SST in the Atlantic ocean occurs on the Scotian Shelf and slope region. *Cayan [1986]* presented contour maps of the North Atlantic seasonal sea surface temperature anomalies (SSTAs). The maps, again, show that the maximum variability of the SSTAs is found on the Northwest Atlantic. *Thompson et al. [1988]* showed that the SSTAs are large scale and that winter SSTAs persist longer than those in summer. They suggested that the dominant cause of the anomalies was air-sea fluxes. Their results suggest that summer SSTAs may also be influenced by winter conditions. Most of the studies on temperature anomalies have been limited to surface temperatures. In this study, I will examine both surface and subsurface temperature.

The specific problem addressed in this thesis is the cause of the SSTAs in the Northwest Atlantic. The general idea is that the SSTAs are caused by large scale atmospheric circulation through anomalous net air-sea heat fluxes *[Bunker, 1976; Thompson et al., 1988]*, horizontal advection, upwelling and entrainment of cold water into the mixed layer *[Bjerknes, 1964]*. Other processes include horizontal mixing and the variability of the mixed layer depth. In other areas, the effect of horizontal mixing has been found to be generally insignificant *[Clark, 1972; Daly 1978]*. In this study, I will examine the usefulness of the COADS heat flux to the development of the SSTAs in the study region. It will be shown in this thesis that the dominant cause of the SSTAs in the Northwest Atlantic comes from variability within the ocean and not from the atmosphere.

In summary, the specific objectives of this study are to:

1. Estimate and explain the seasonal heat storage rates of the upper layer of the Northwest Atlantic, and compare them with the net surface heat flux;

2. Explore new methods of estimating the coefficient of vertical eddy diffusivity in the upper water column, on a monthly time scale, as a function of water stratification;

3. Develop a simple model to explain and simulate the seasonal water temperature and its anomalies at different depths and time of the year;

4. Explain the formation of the cold intermediate layer;

5. Test the usefulness of the COADS heat flux to the creation of the SSTAs; and

6. Explain the cause of the interannual variability in the net surface heat flux and SSTAs in the Northwest Atlantic.

The thesis is arranged as follows: Chapter 2 presents a description of the observed seasonal variability in the surface and subsurface temperature and salinity, together with derived quantities such as local rates of heat storage, steric height and the buoyancy frequency. These quantities are used in Chapter 3, in combination with other data, to examine the seasonal heat and salt budget. An understanding of the dominant processes in the temperature equation is crucial to the development of the modified one-dimensional heat diffusive model. This is the essence of the seasonal heat budget. Different ways of estimating the coefficient of eddy diffusivity are presented in Chapter 4. The model is developed in this chapter using the estimated diffusivities. In Chapter 5, the model is used to study the formation of the cold intermediate layer. Chapter 6 describes the interannual variability of the net surface heat flux and the SSTAs. The causes of the SSTAs are also treated in Chapter 6. Finally, in Chapter 7, the main conclusions from this study are given together with suggestions for further work.

Chapter 2

SEASONAL VARIABILITY

2.1 Introduction

The purpose of this chapter is to describe the seasonal variability in temperature and salinity, together with the local rate of heat storage, steric height and buoyancy frequency. The estimates of the above quantities will be used in subsequent chapters. For example, the rate of heat storage will be used in Chapter 3 as part of the heat budget. The rate of heat storage is also important in that it provides information on the variation of the sea level and geostrophic current. The buoyancy frequency will be used in chapter 4 to estimate the vertical eddy diffusivity.

The monthly mean temperature and salinity data used in the analyses were compiled by *Drinkwater and Trites [1987]*. The data were collected between 1910 and 1982, with about 85% of the data collected after 1950. *Drinkwater and Trites* have grouped the data into 35 subareas, according to topography and availability of sufficient data to form a monthly mean. The subareas are shown in Figure 2.1 and their names listed in Table A.1, of Appendix A. Subarea 31 is not included in the analysis because data were not available. For the 34 subareas used in this study, there are some months where data are missing. In such cases (which occur mostly in the eastern part of the shelf), I linearly interpolated between two adjacent months, at a given depth.

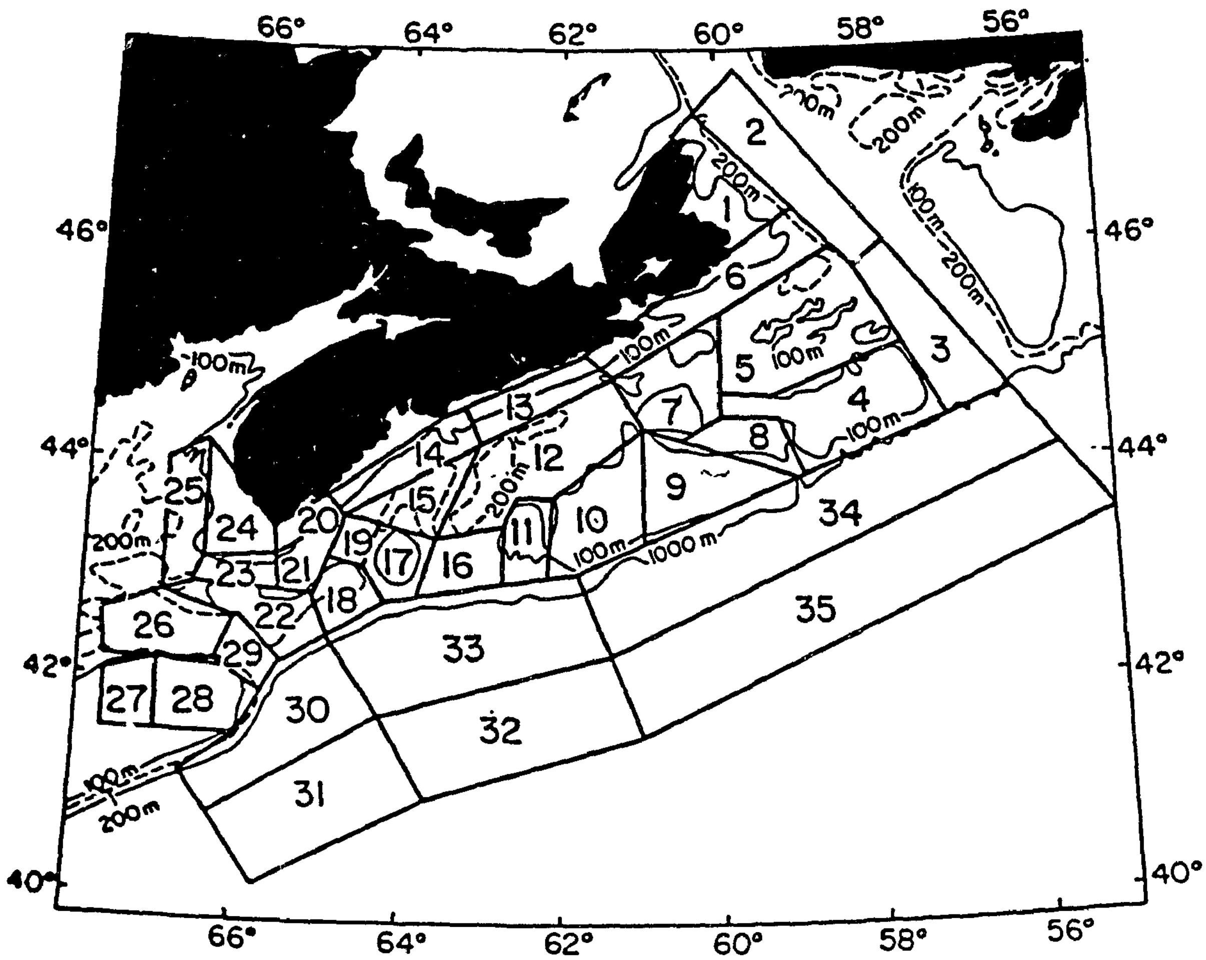

Figure 2.1: Map of the study region showing the subareas where the hydrographic data were collected *[Drinkwater and Trites, 1987]*.

To set the stage for the computations that will follow, and for the purpose of clarity, it is necessary to note that the word *seasonal* refers to the average variation of a quantity about the annual mean. An *annual harmonic* denotes a fitted sinusoid with a period of 1 *year*, from which amplitude and phase are obtained.

Before describing the seasonal variation in temperature and salinity, the analyses of their annual harmonics will be presented. It will be shown that the seasonal temperature signal is confined to the upper 75 m of the water column, and that both the long term mean temperature and the salinity annual amplitude have a subsurface minimum.

2.2 Mean and Annual Harmonics

The monthly mean temperature at a given position is expressed as the sum of the long term (annual) mean and harmonics:

$$T(z,t) = A_0(z) + A_1(z)\ \cos\{\omega[t - t_1(z)]\} + A_2(z)\ \cos\{2\omega[t - t_2(z)]\}, \tag{2.1}$$

where $A_0(z)$ is the long term mean, which varies with depth. A_1 and t_1 are the amplitude and phase (in days) of the annual harmonic while A_2 and t_2 are the amplitude and phase of the semi-annual harmonic. $\omega = 2\pi/365$ days is the annual frequency and t the time in days. Equation (2.1) is also used for salinity. The variations of the long term temperature and salinity and their harmonics are described below.

2.2.1 Spatial Variation of Temperature

(a) Long Term Mean

The distribution of the mean SST is shown in Figure 2.2a. The value increases from 5.5°C in the northern part of the region to 14.0°C in the south. Superimposed on this overall latitudinal dependence of the SST, there is a mechanism that tends to deflect the isotherms so that the mean temperature decreases towards the coast. Another striking feature of the long term mean temperature may be observed along

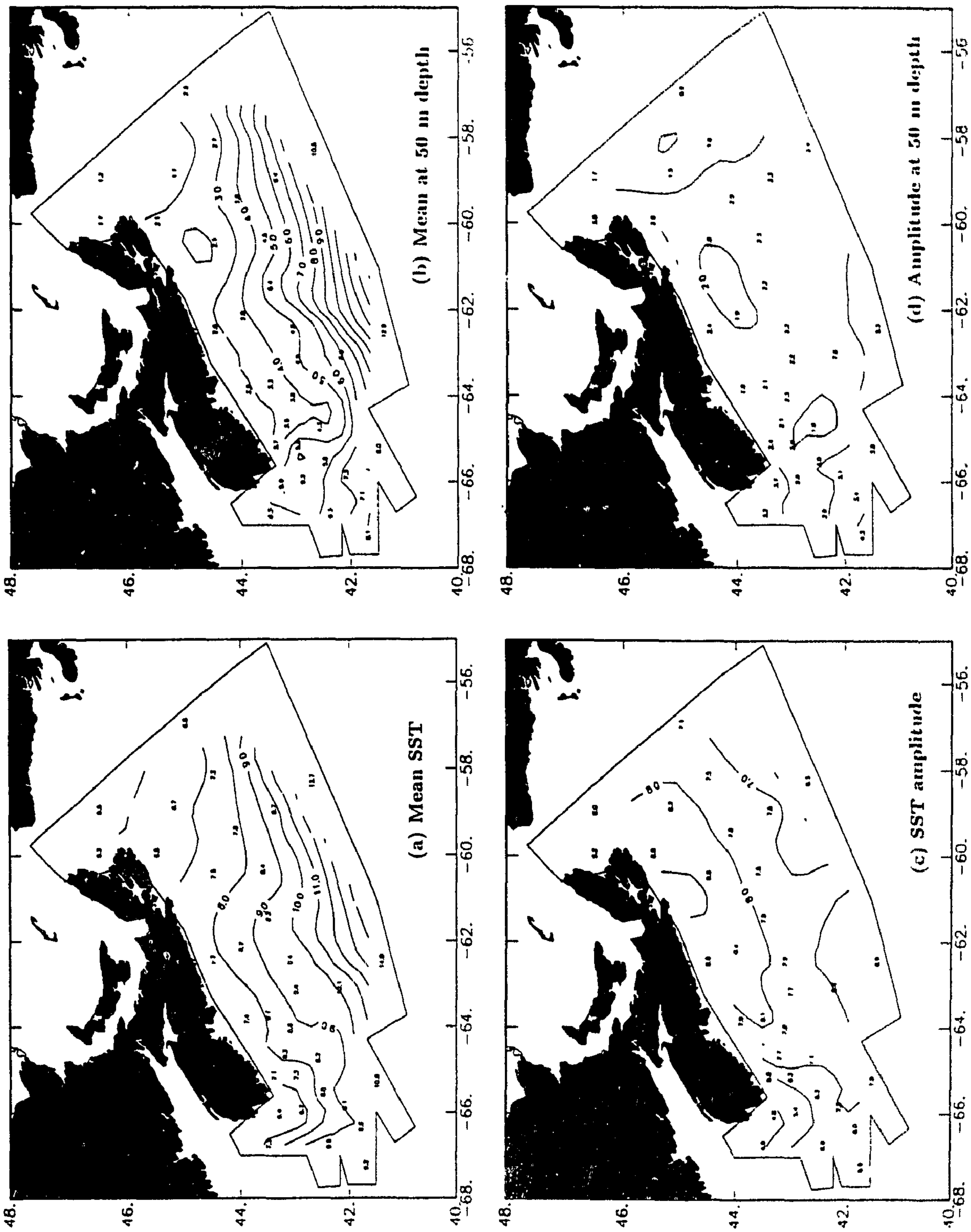

Figure 2.2: Maps showing the spatial distribution of the mean temperature and its annual amplitude. The contour interval is 1°C. The small numbers, in this and subsequent maps, indicate the averaged values for each of the subareas.

the slope region: the strong horizontal gradients are presumably associated with the Gulf Stream.

Figure 2.2b shows the spatial distribution of the long term mean temperature at $50\,m$ depth (at this depth, the seasonal temperature signal, though small, can still be detected. More on the depth of seasonal penetration later). The horizontal pattern of the mean temperature at the 50 m depth is similar to that of the mean SST, except that the subsurface values are lower. For instance, for subarea 12, the mean temperature decreases from $8.7°C$ at the surface to $7.1°C$ at 20 m depth and $3.8°C$ at 50 m depth. The values of the annual mean temperature (as well as salinity and density) at different depths for all the subareas are given in Table A.2 of Appendix A.

The vertical variation of the annual mean temperature with depth, for subarea 12, is shown in Figure 2.3a. In this chapter, subarea 12 is chosen to represent the variation on the Scotian Shelf. The important feature in the figure is the existence of a temperature minimum at about 50 m depth. This feature will be explained when the cold intermediate layer is treated in Chapter 5.

(b) Annual Amplitude

The map of the surface annual amplitude is shown in Figure 2.2c. In the study region, the surface amplitude ranges from $4.8°C$ to $9.2°C$. A noticeable feature is the low amplitude found in the eastern Gulf of Maine, probably due to the strong tidal mixing in that region. At subarea 24 ($43°N$), the amplitude is $4.8°C$, which is the lowest value for the whole region.

The annual amplitude decays with depth. For subarea 12, the amplitude decreases from $8.4°C$ at the surface to $1.9°C$ at 50 m depth (Figure 2.3b), with an e-folding depth of about 30-50 m. Figure 2.2d shows the horizontal distribution of the amplitude at 50 m depth. The amplitude varies between $1.5°C$ (subarea 5) and $4.7°C$ (subarea 27). The spatial average of the annual amplitude at 50 m is about 35% of the spatial average of the surface annual amplitude.

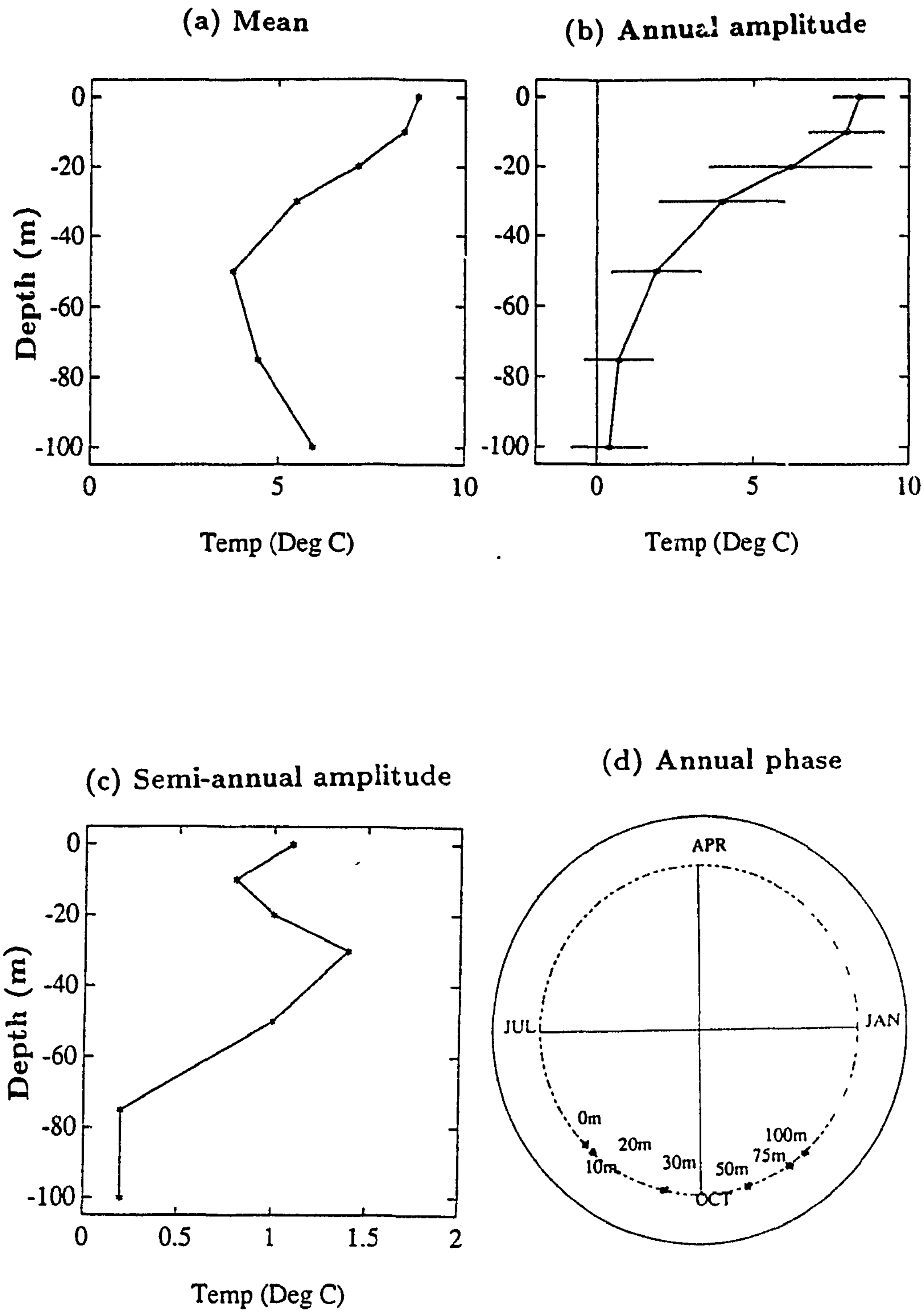

Figure 2.3: Variation of the mean temperature and its annual harmonics with depth for subarea 12, representative of other subareas on the shelf.

(c) Semi-annual Amplitude

The amplitude of the semi-annual signal (Figure 2.3c) is generally smaller than ($<$ 14%) that of the annual. An interesting feature of the vertical distribution of the semi-annual amplitude is the occurrence of a secondary maximum between 30 m and 50 m depth. This feature has also been observed on the Eastern Newfoundland shelf *[Petrie et al., 1991]*.

(d) Annual Phase

For subarea 12, the phase of the annual harmonic (Figure 2.3d) at the surface corresponds to the surface amplitude reaching its maximum value at day 229 (19 August). Figure 2.4 presents the spatial distribution of the phase of the temperature annual harmonic at the surface (upper panel) and at 50 m depth (lower panel). For the subareas on the Scotian Shelf, the surface annual harmonic reaches its maximum at about day 226 – 232 (16-22 August).

Generally, the phase of the annual harmonic increases with depth. At 50 m depth, the phase on the Shelf is between day 260 and 294 (20 September and 24 October). At 75 m depth, the phase for subarea 12 on the shelf lags the surface by about 80 days (see Figure 2.3d). On the other hand, in the slope region (subarea 32), the seasonal signal lags the surface by only 32 days.

2.2.2 Spatial Variation of Salinity

Salinity, throughout the thesis, is expressed in psu (practical salinity unit of 1978, *[Unesco, 1981]*).

(a) Long Term Mean

The distribution of the surface mean salinity is shown in Figure 2.5a. Low values occur near the coast and towards the Laurentian channel, presumably associated with fresh water discharge at the St. Lawrence River *[Sutcliffe et al., 1976]*. The isohalines are almost parallel to the coastline, with salinity increasing offshore. For example, the salinity increases across the shelf from 30.8 near the coast (subarea 13) to 33.7 on

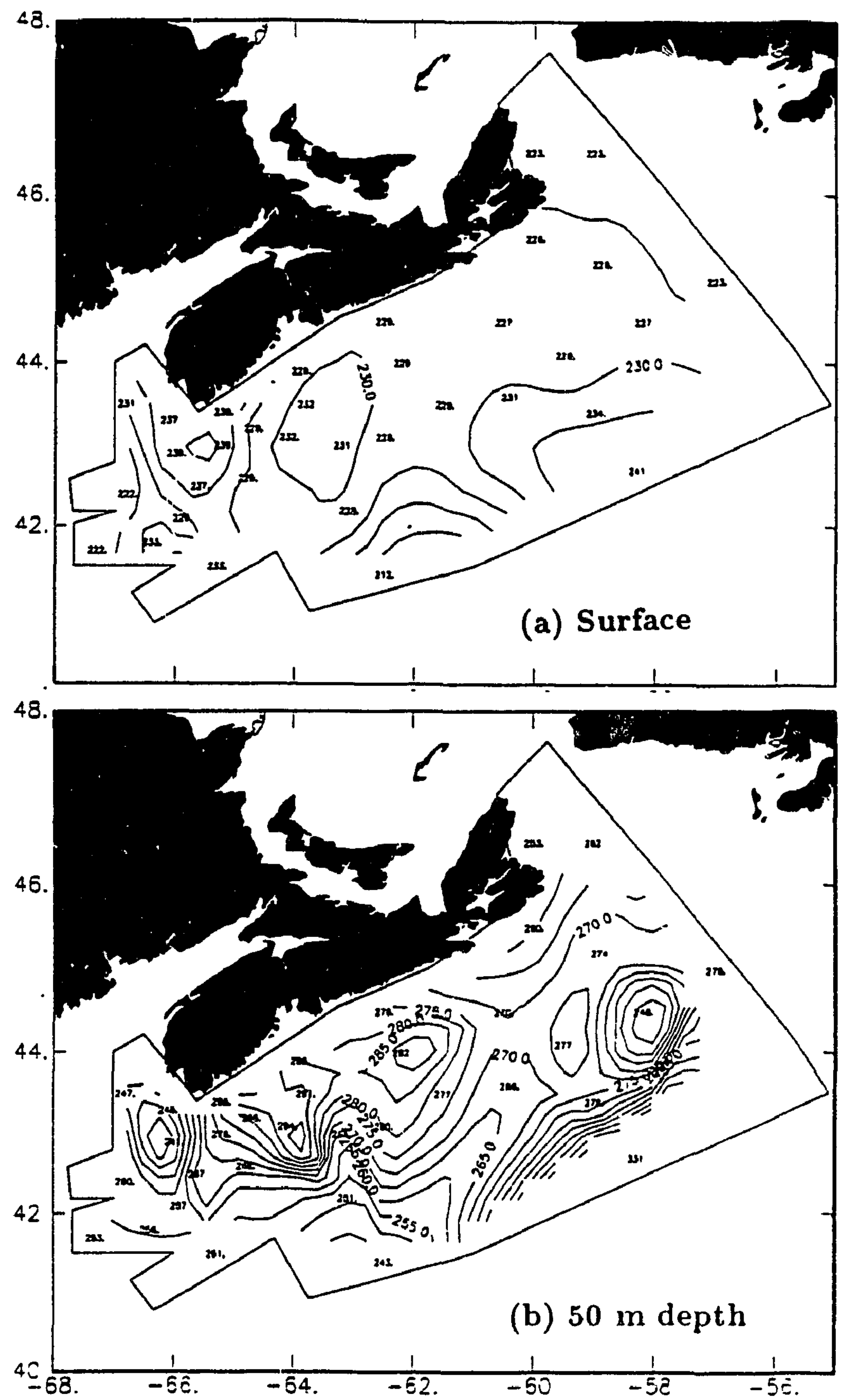

Figure 2.4: Maps showing the spatial variation of the phase of the annual temperature harmonic at the surface (upper panel) and at 50 m depth (lower panel). The contour interval is 5 days.

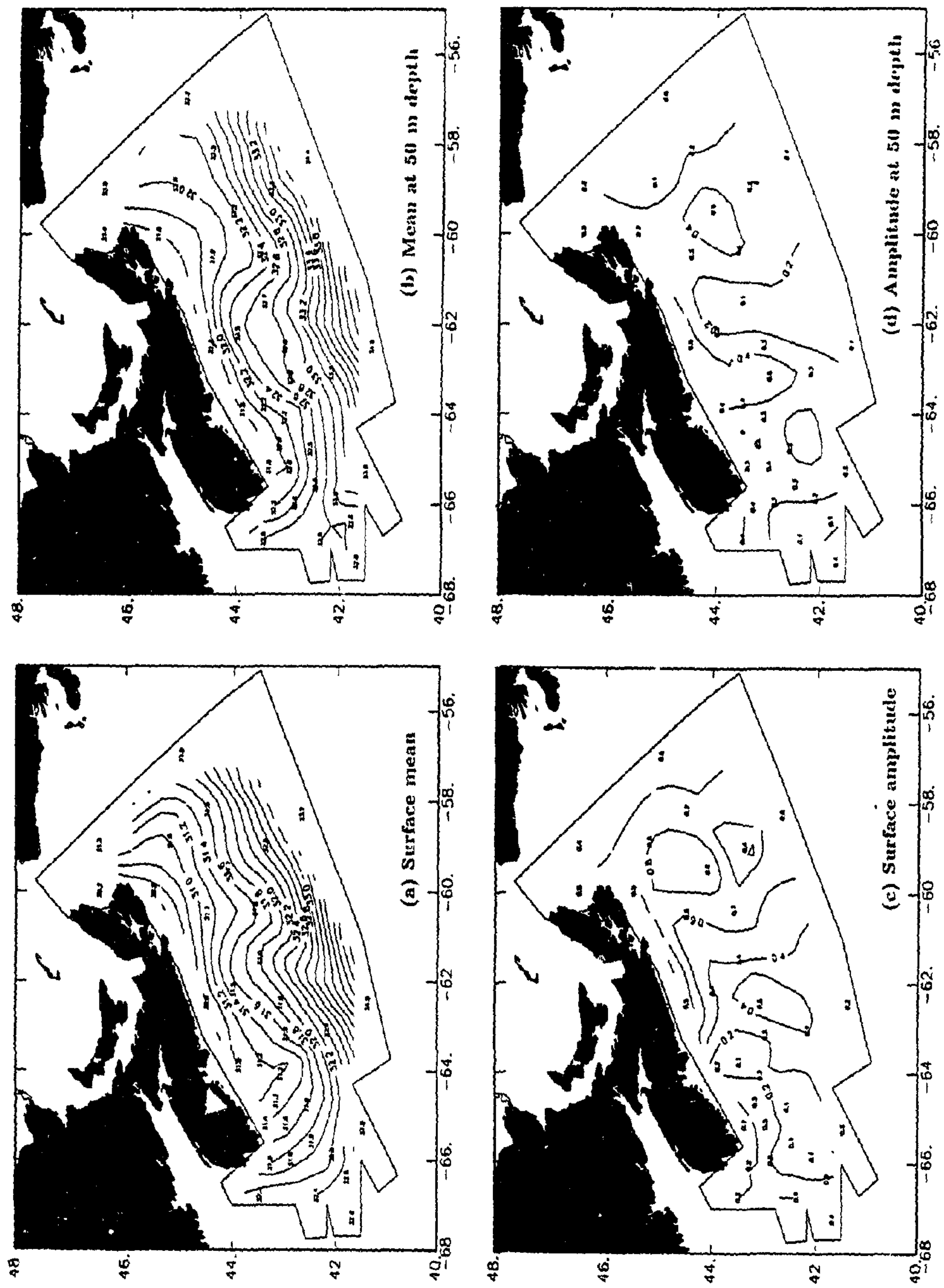

Figure 2.5: Maps showing the spatial distribution of the mean salinity and its annual amplitude.

the slope (subarea 35). High values also occur in the low latitudes. At about $42.7°N$ (subarea 35), a value of 34.0 is obtained. For the region considered, the surface mean salinity ranges from 30.2 (subarea 1) to 34.0 (subarea 32). The horizontal distribution of the mean salinity at 50 m depth, shown in Figure 2.5b, portrays the same pattern as that of the surface, except that the values are higher.

In the vertical direction, the long term mean salinity generally increases with depth (see Table A.2b of Appendix A). At subarea 12, it increases from 31.5 at the surface to 33.2 at 75 m depth (Figure 2.6a). Unlike the vertical structure of the mean temperature where there is a temperature minimum at about 50 m depth, the mean salinity increases downward without any intermediate minima or maxima.

(b) Annual Amplitude

The amplitudes of the annual harmonic at the surface and at 50 m depth are shown in Figures 2.5c and d respectively. Generally the amplitudes, both at the surface and at depths, are small compared with their annual mean. The surface values range from 0.1 to 0.9, while at 50 m depth, it varies between 0.1 and 0.6.

(c) Annual Phase

The spatial distribution of the phase of the salinity annual harmonic at the surface is at 50 m depth are presented in Figures 2.7a and b. For subarea 12 (for example) the surface salinity is maximum at day 41, that is, 11 February (see Figure 2.6c), unlike the surface temperature which reaches a maximum in August.

Important information about the surface horizontal advection may be obtained from the phase propagation. Along the shelf (between subareas 5 and 21), a distance of about 500 km, the phase changes by about 90 days (see Figure 2.7a). This gives a mean westward surface drift of about 5.6×10^{-2} m s^{-1}, which is comparable with the estimate from drifters *[Drinkwater et al., 1979]*.

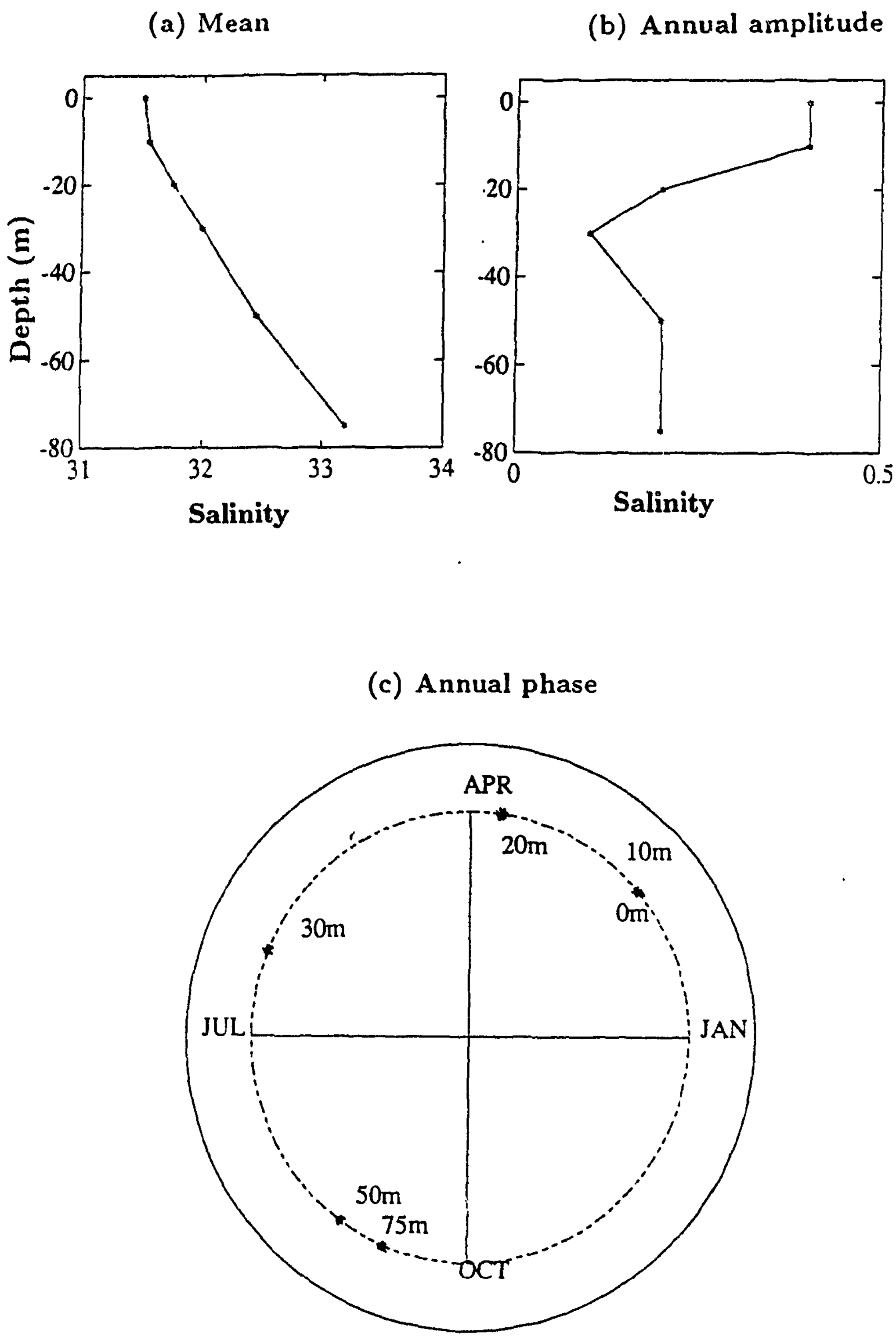

Figure 2.6: Variation of the salinity harmonic with depth for subarea 12.

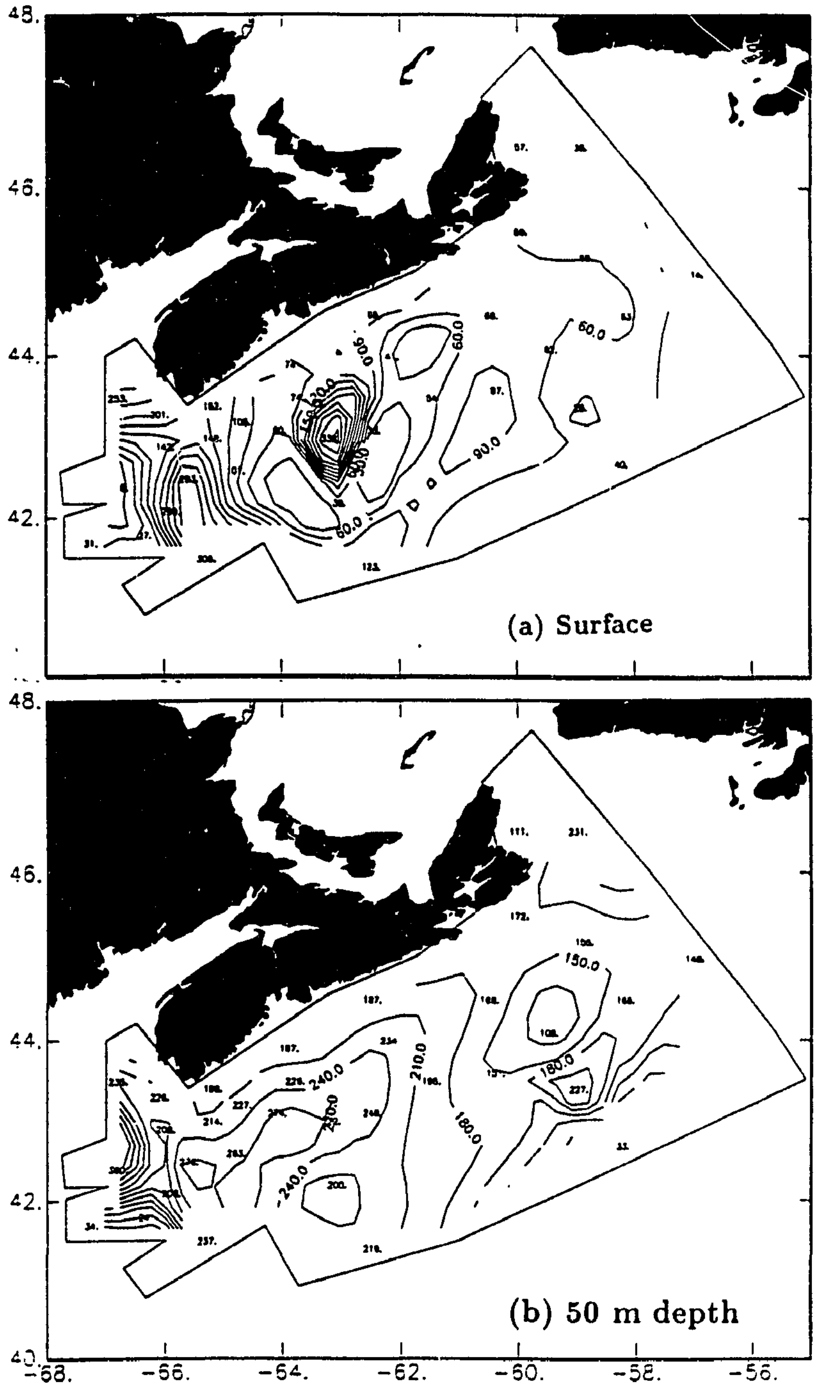

Figure 2.7: Maps showing the spatial variation of the phase of the annual salinity harmonic at the surface (upper panel) and at 50 m depth (lower panel). The contour interval is 30 days.

2.3 T-S Characteristics

The T-S relationship for a given area may be influenced by many factors, such as surface heat flux, horizontal advection, horizontal mixing and upwelling. In the study region, the strong wind in winter increases the latent heat flux from the ocean through evaporation. Evaporation reduces SST and increases the sea surface salinity (SSS). Generally, a negative T-S correlation may be caused by latent heat flux (via evaporation) and upwelling of cold-salty water. On the other hand, a positive T-S correlation may be brought about by horizontal exchange of cold-fresh water, warm-salty water, and an upwelling of warm-salty water at depth.

The goal of this subsection is to use T-S plots to show how the thermal and salt properties of the top 75 m of the water column vary seasonally. Since the source waters forming the water masses, in this region, fluctuate seasonally it is to be expected that the water characteristics will correspondingly change with the season. Referring to the T-S properties inferred from his November 1951 cruise, *McLellan [1954]* commented that " the water movements inferred do not necessarily hold for all seasons". I have chosen to describe the T-S characteristics for subarea 12 (representing the water properties on the Shelf) and for subarea 32 (representing the water characteristics on the Slope region). Figure 2.8 shows the T-S diagram for February, June and October. In each subarea, the data are plotted at 0, 10, 20, 30, 50, and 75 m depth.

The main points from the T-S plots are that the water properties undergo larger seasonal changes at the surface than at depth on the shelf, and that the water on the slope, at a given time, is warmer and saltier than that on the shelf.

On the shelf, the SST increases from $2.4°C$ in February to $10.2°C$ in June and $14.2°C$ in October while the SSS decreases correspondingly from 32.1 to 31.7 and to 31.3. The surface density decreases by about 2.3 kg m^{-3} between February and October, and is dominated by the large change in the temperature. This variation in the water properties is not surprising since it is known that the high surface temperature in summer and fall is due to local surface heating. It is worth also noting that at 75 m depth, the T-S properties do not change significantly.

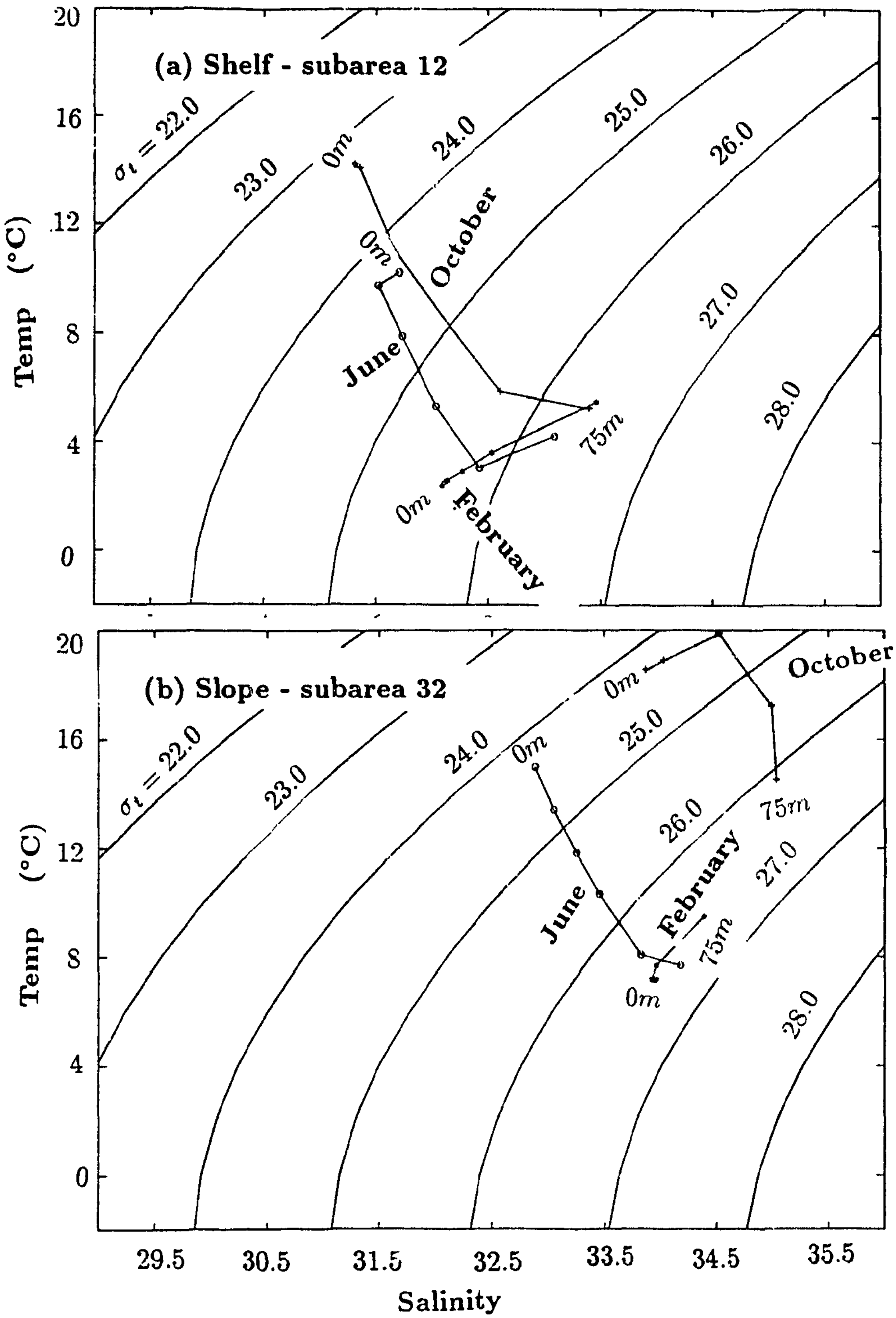

Figure 2.8: T-S diagrams for February, June and October, showing the seasonal changes in the water properties at various depths (0 – 75 m). The diagrams are shown for subareas 12 and 32.

2.4 Local Rate of Heat Storage

As mentioned above, the reason for the estimation of the local rate of heat storage is to set the stage for the heat budget in Chapter 3. In that chapter, I will compare the local changes in the heat storage with the net surface heat flux, in order to determine how much of the local heat storage rates can be explained by the surface heat fluxes. In this section, the purpose is simply to estimate and describe the seasonal and spatial variability of this term. Following *Bryan and Schroeder [1960]*, the monthly changes in the heat storage is defined by $\partial H/\partial t$, where

$$H = \int_{-h}^{0} \rho c_p T \, dz \tag{2.2}$$

is the depth integrated heat content between the surface ($z = 0$) and some depth $z = -h$. ρ and c_p are the water density and the specific heat at constant pressure.

Since the present analysis is focused on seasonal changes, it is necessary to determine the depth (h), sufficient to capture the seasonal signal penetration. In the description of the annual temperature harmonics above, I have shown that the amplitude of the annual signal is much larger than the semi-annual at all depths. The spatial average of the semi-annual amplitude is about 14% of the spatial averaged annual amplitude. To find the depth of the seasonal signal penetration, I computed the annual amplitude at various depths. The result that was presented in Figure 2.3b (Emerald basin), is typical of other subareas. Clearly, the result shows that the seasonal signal penetrates down to 50 m depth. Below this depth, the signal is buried in the noise (notice the error bar in Figure 2.3b). The e-folding depth of the amplitude is about 30 m. In the following analysis, I use 75 m as the average depth of seasonal penetration.

The seasonal estimates of the local rates of heat storage, for subareas 12 and 33 (representing the slope region) are shown in Figures 2.9 a and b respectively. Negative sign corresponds to heat loss from the ocean. The highest rate of heat gain by the ocean occurs in June with a typical value of 200 W m^{-2} while the greatest heat loss from the ocean is in December with a typical value of -300 W m^{-2}.

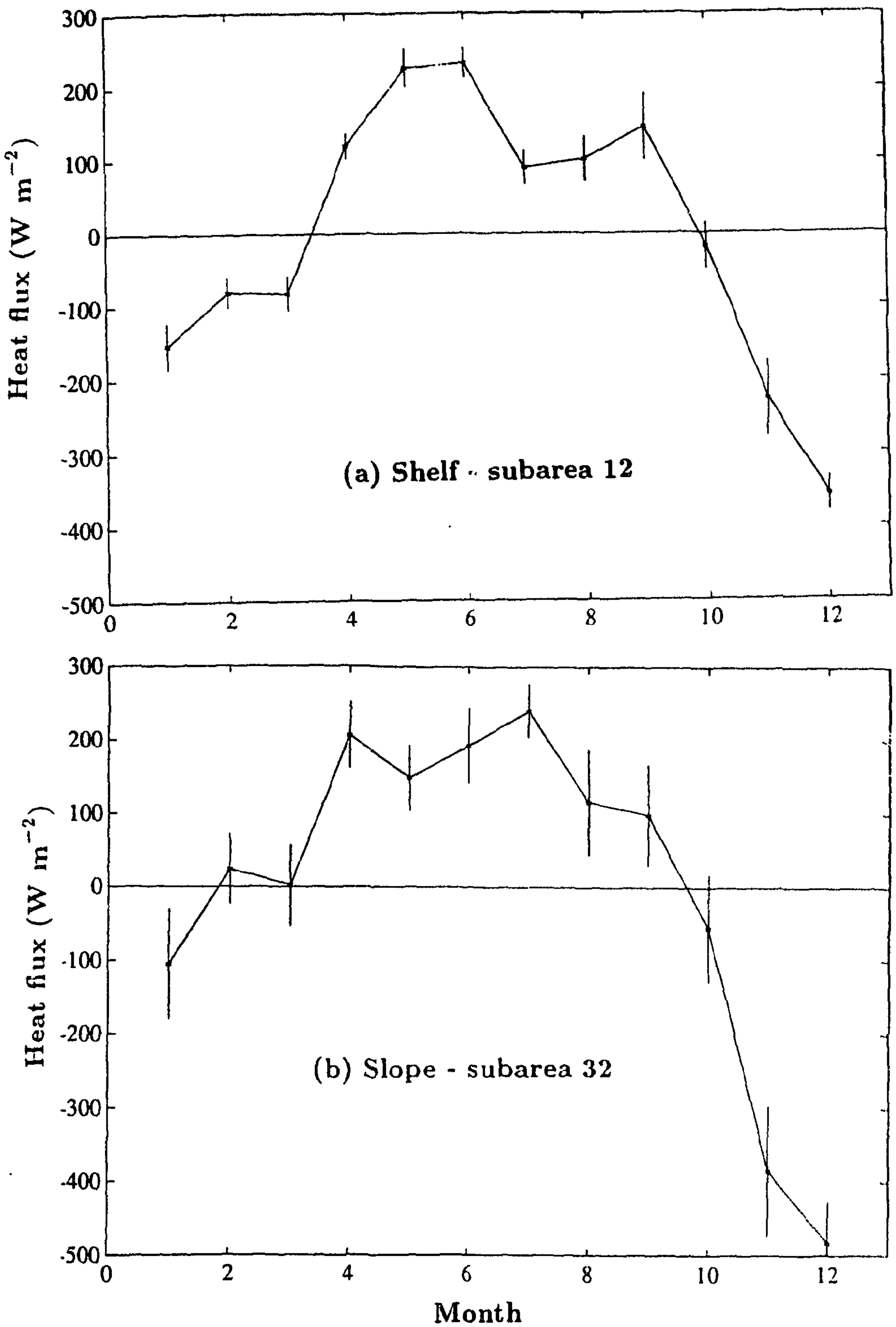

Figure 2.9: Seasonal variation of the local rate of heat storage for subareas 12 and 32. The vertical lines are the error bars for 95% confidence interval.

Figures 2.10, 2.11 and 2.12 present the monthly map of the local rates of heat storage in the study region. (The values for the whole subareas are listed in Table A.5 of Appendix A.) From about November to February, the ocean loses heat (see Figures 2.12 and 2.10). The average rate of heat loss, for the whole region, in December is about -345 W m^{-2}. On the other hand, the ocean gains heat from April to September (Figures 2.10 and 2.11). The maximum rate of heat gain (obtained in June), for the whole region averages about 215 W m^{-2}. There is a phase lag of about 90° between the time of occurrence of the maximum (and minimum) rate of heat storage and that of the depth integrated heat content as expected. The analysis (not shown) indicates that the maximum (minimum) depth integrated heat content occurs in September (March) whereas the rate of heat storage is in June (December). The spatial variability in the rate of heat storage reflects, largely, the data quality. Inadequate data sampling (in space) together with the very few observations, especially in the eastern part of the Shelf, used to form the monthly mean could cause the large variability in the local rate of heat storage. A map of the annual amplitude of $\partial H/\partial t$ shown in Figure 3.3a (Chapter 3), gives a smoothed version of the term. In addition to data quality, the spatial variation in $\partial H/\partial t$ gives some indications of other processes, such as horizontal advection, operating in the study region.

2.4.1 Estimation of Error

The error variance of the local rates of heat storage can be expressed as

$$\begin{aligned} \mathrm{var}\left[\rho\, c_p \frac{\partial}{\partial t}\sum_{-h}^{0} T\, dz\right] &\approx \mathrm{var}\left[\frac{\rho\, c_p}{2\Delta t}\sum_{i=1}^{6}\left(T_i^{n+1} - T_i^{n-1}\right)\Delta z_i\right] \\ &= \frac{\rho^2\, c_p^2}{4\Delta t^2}\left[\sum_{i=1}^{6}\Delta z_i^2\left(s^2_{T_i^{n+1}} + s^2_{T_i^{n-1}}\right)\right] \end{aligned} \tag{2.3}$$

and thus

$$E = \frac{\rho\, c_p}{2\Delta t}\sqrt{\sum_{i=1}^{6}\Delta z_i^2\left(s^2_{T_i^{n+1}} + s^2_{T_i^{n-1}}\right)} \tag{2.4}$$

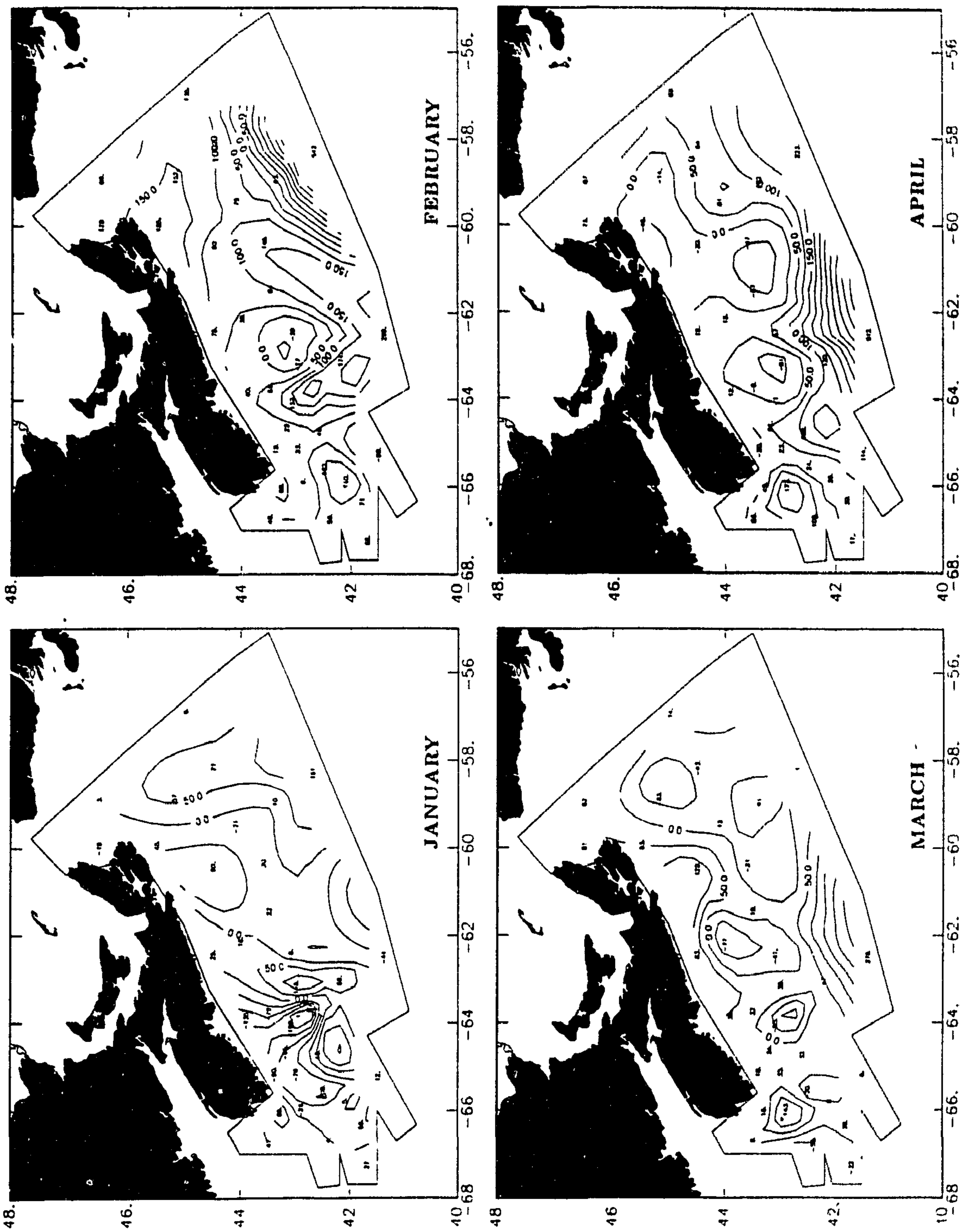

Figure 2.10: January-April Maps showing the monthly distribution of the local rate of heat storage. The contour interval is 50 W m^{-2}.

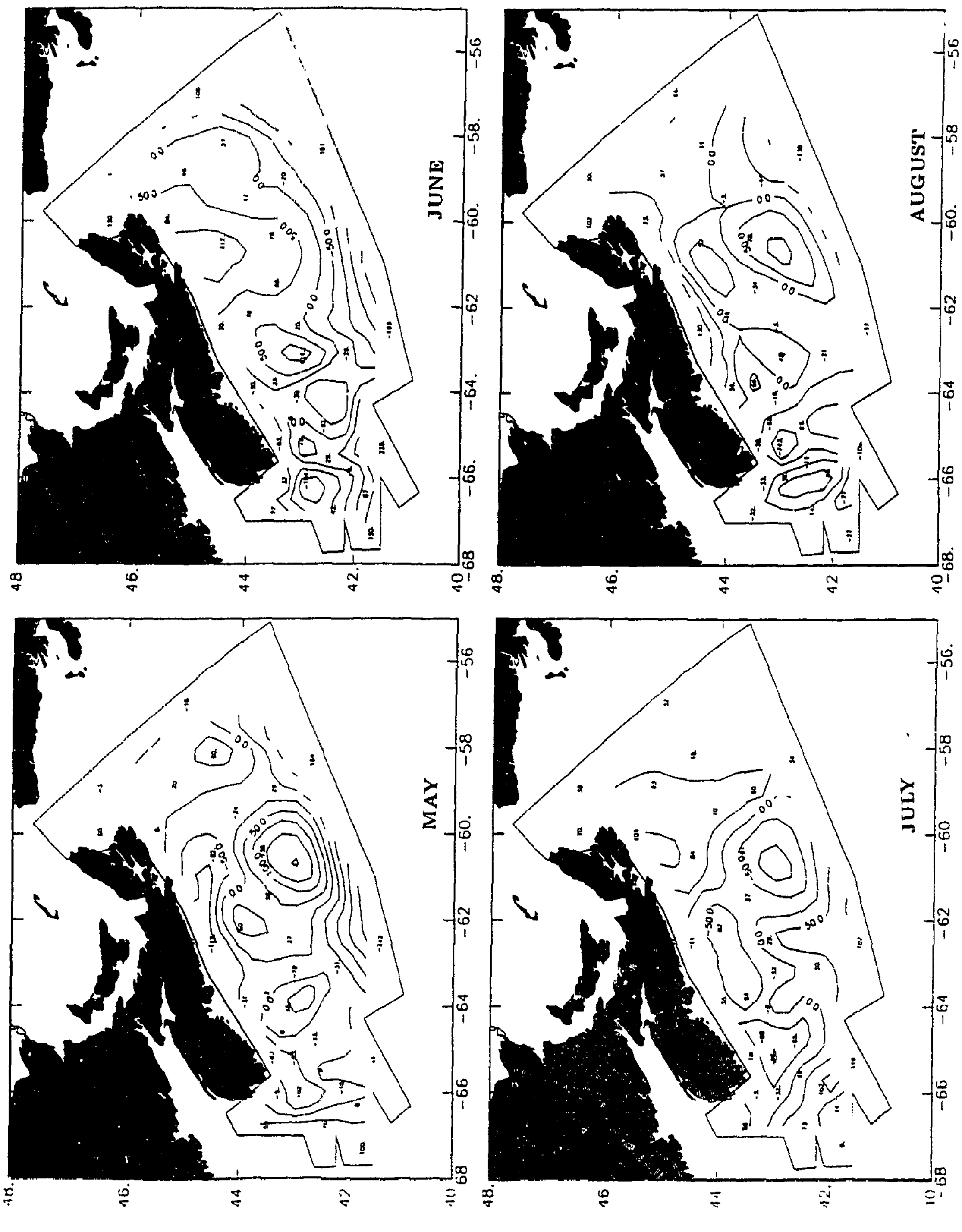

Figure 2.11: May-August maps showing the monthly distribution of the local rate of heat storage. The contour interval is 50 W m^{-2}.

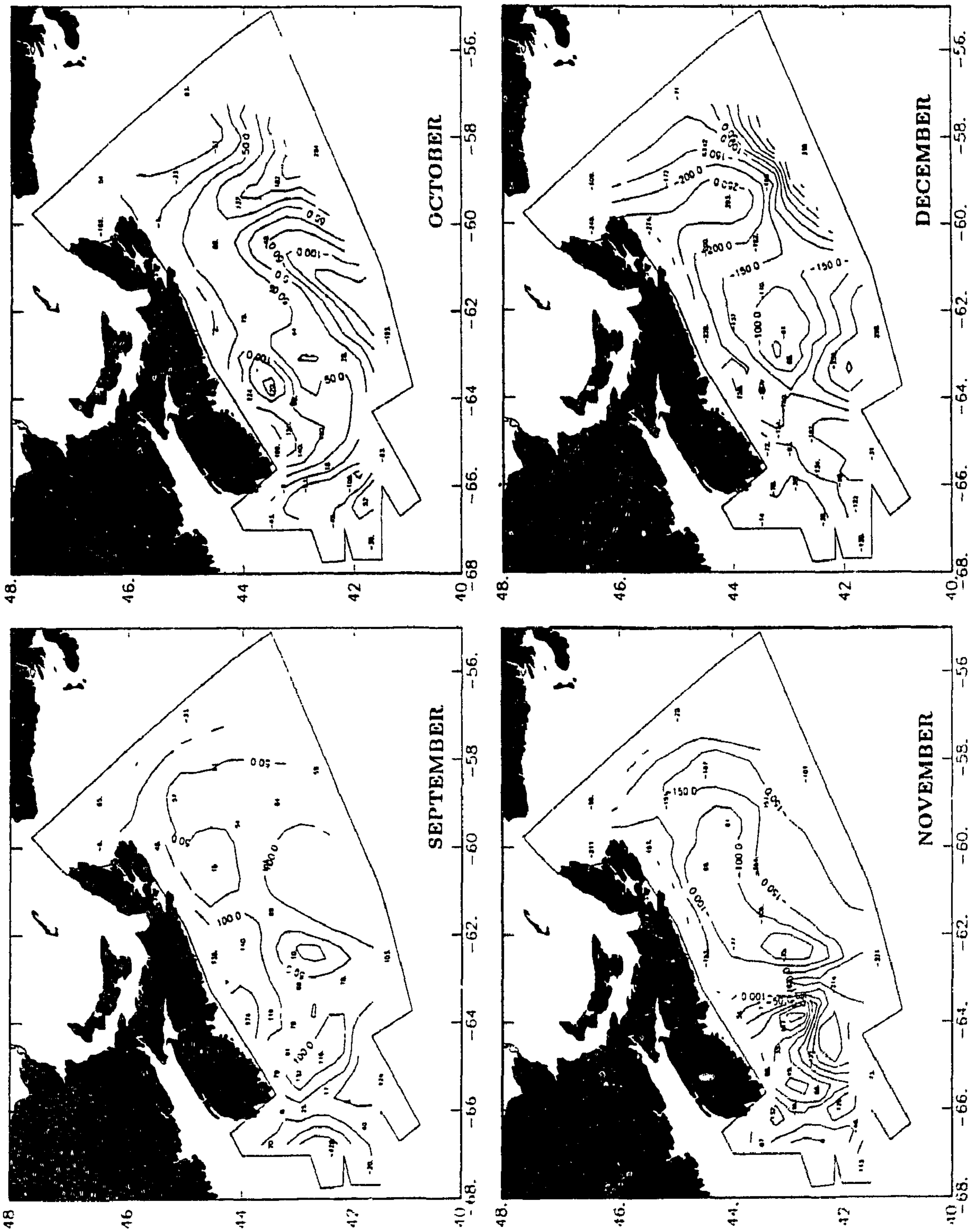

Figure 2.12: September-December maps showing the monthly distribution of the local rate of heat storage. The contour interval is 50 W m^{-2}.

where E is the error in W m^{-2} associated with the estimated local rates of heat storage, $\Delta t = 30 \times 24 \times 3600$ s is the monthly time interval and Δz is the depth interval. T is the temperature. The summation is taken over the 6 standard depths (0, 10, 20, 30, 50 and 75 m) whose temperature data are used to compute the rate in the heat storage. The superscript n denotes time index while the subscript i refers to the depth index. $s = std/\sqrt{M}$ is the estimated standard deviation of the monthly mean, where std is the standard error of the observations in the month. The error analysis thus takes into consideration the number of temperature observations M for a given month, used to form the monthly mean. In (2.3), I have assumed that the covariance between T_i^{n+1} and T_i^{n-1} is zero. Two standard errors (equivalent to a 95% confidence interval) are plotted in Figure 2.9.

2.5 Steric Height Variation

In this section, I will describe the seasonal changes in sea level caused by the density distribution. The purpose is to show how seasonal changes in the surface geostrophic current shear, associated with the density variation, are distributed in the region. Let the monthly mean density ρ be expressed as

$$\rho(z) = \rho_O + \Delta\rho(z) \tag{2.5}$$

where ρ_O is a reference density and $\Delta\rho$ the deviation of the monthly mean density about the reference. The steric height is then defined as

$$\eta_s = -\frac{1}{\rho_O}\int_h^0 \Delta\rho \, dz \tag{2.6}$$

$h = 75$ m is used, based on the depth of seasonal temperature signal penetration. Following *Csanady [1979]*, I choose ρ_O as the largest density value in the depth range ($h = 75$ m) considered. That ensures that $\Delta\rho$ is everywhere negative and $\eta_s > 0$. In the analysis, $\rho_O = 1028$ kg m^{-3} is used. The density is computed from temperature and salinity data, using the International equation of state of seawater *[Unesco, 1981]*.

The values of the computed steric height are listed in Table A.6 of Appendix A and the monthly maps presented in Figures 2.13, 2.14 and 2.15.

There is clearly a seasonality in the variation. The maximum values for most of the subareas occur in September and October while the minimum is in March and April. The annual range varies from about 16 *cm* at $46.5°N$ (subarea 1) to about 5 *cm* at $43.3°N$ (subarea 24).

This seasonal variation in the steric height reflects, in part, the seasonal changes in the depth-integrated heat content of the upper water column. A high (low) heat content causes the expansion (contraction) of the water column. A quick calculation shows that temperature dominates salinity in the steric level variation, which is in accordance with other investigations elsewhere in the same latitude range *[Pattullo et. al., 1955; Lisitzin and Pattullo, 1961; Gill and Niiler, 1973]*.

The main feature of the map is a high sea level near the coast, and a gradual drop offshore. The high coastal sea level may be due to the influx of freshwater from St. Lawrence River. In September, the surface slope is about -3.9×10^{-7} (i.e. 5.3 cm in 137 km) across the shelf (see Figure 2.15 i - the slope of the line is indicated). This is related to a westward geostrophic flow of about $3.9 \times 10^{-2}\,\mathrm{m\ s^{-1}}$ along the shelf. The westward flow, especially near the coast, is observed throughout the year. This flow pattern is consistent with the circulation observed on the shelf *[Smith et al., 1978; Drinkwater et al., 1979; Smith, 1983]*. The estimates of the seasonal variation of the geostrophic current with depth will be given in Chapter 3.

The estimated surface steric level compares favorably with the observed Halifax sea level. *Thompson [1986, 1990]* has described the sea level and circulation in the North Atlantic. He found the amplitude of the seasonal cycle on the Scotian Shelf to be about 8 cm, which is consistent with the annual range of about 16 cm, estimated in this study.

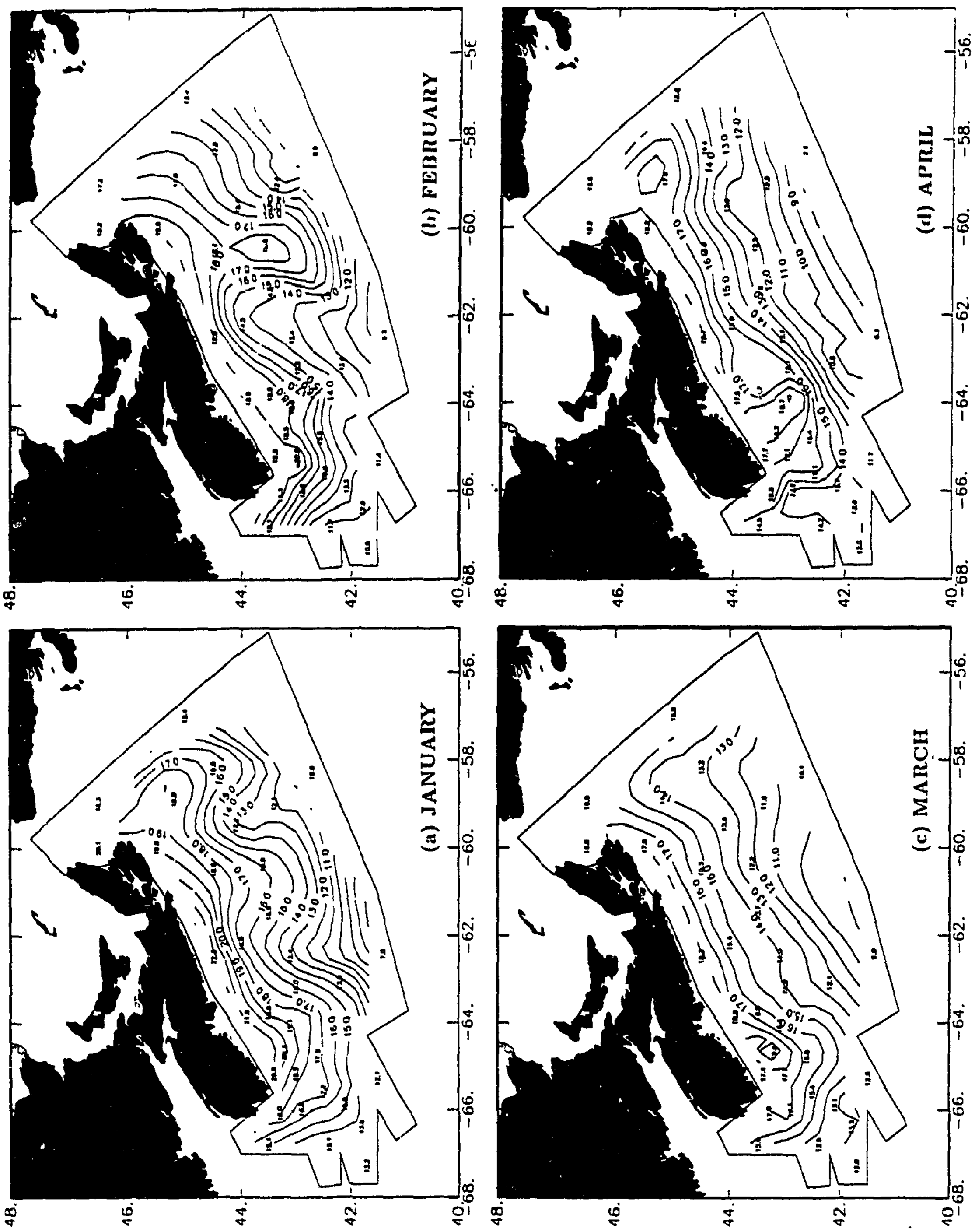

Figure 2.13: January-April maps showing the monthly changes in the surface steric height, in cm, relative to 75 m depth. The contour interval is 1 cm.

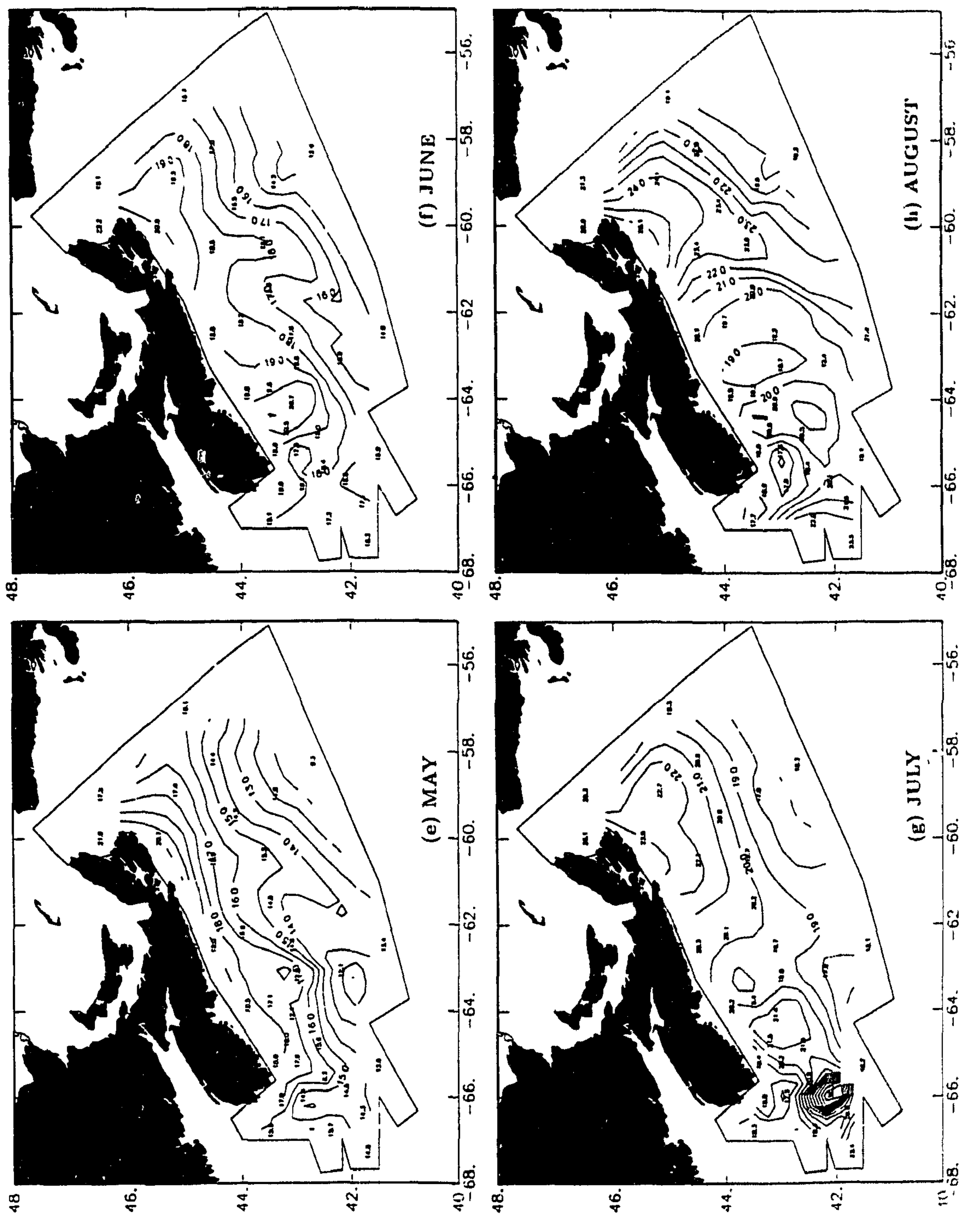

Figure 2.14: May-August maps showing the monthly changes in the surface steric height, in cm, relative to 75 m depth. The contour interval is 1 cm.

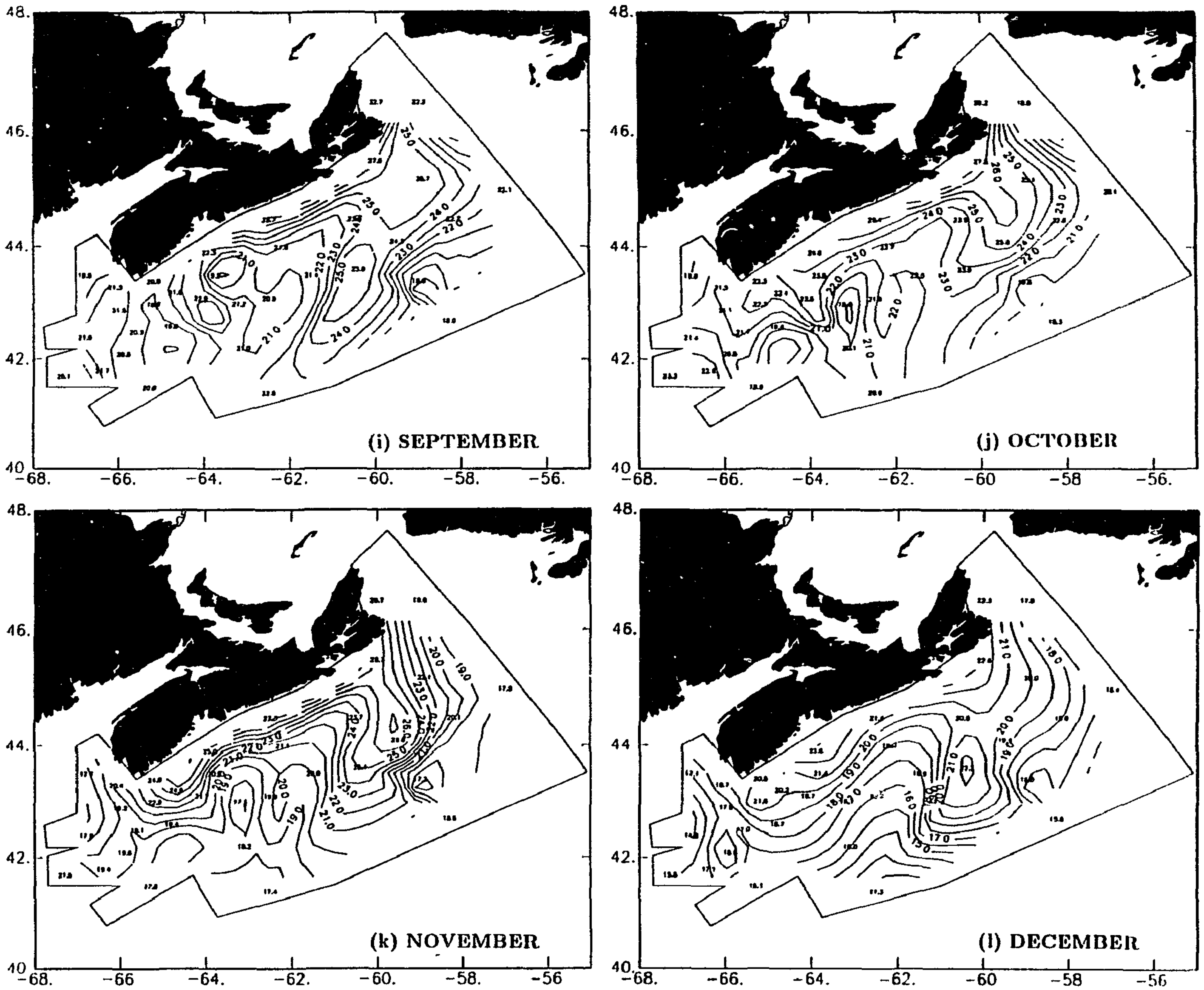

Figure 2.15: September-December maps showing the monthly changes in the surface steric height, in cm, relative to 75 m depth. The contour interval is 1 cm.

2.6 Buoyancy Frequency Variation

The focus of this section is the buoyancy or Brunt Vaisala frequency, which will be used to estimate the vertical eddy diffusivity in Chapter 4. The buoyancy frequency is defined by

$$N^2 = -\frac{g}{\rho_o}\frac{\partial \rho}{\partial z} \tag{2.7}$$

where g is the acceleration due to gravity, $\rho_o = 1025$ kg m^{-3} is a reference water density and ρ the *in situ* water density.

Figure 2.16 shows the seasonal variation of the buoyancy frequency at 15 m and 62.5 m with depth, for Emerald Basin (subarea 12) and the eastern Georges Bank (subarea 28). The N^2 is estimated over a vertical scale of about 10 m. The variation of N^2 in these two subareas is typical of the other subareas. The figure clearly shows a seasonality in N^2, with a maximum in August and a minimum in February. The values, as well as the amplitude of the seasonal cycle, decrease with depth.

2.7 Summary

The long term mean temperature increases offshore, both at the surface and subsurface. The mean temperature has a subsurface minimum at about 50 m. The amplitude of the annual harmonic is typically 8°C at the surface and decreases to about 1°C at 75 m depth. Below this depth the signal can not be distinguished from the noise. Thus, the average depth of seasonal signal penetration is about 75 m. The amplitude of the semi-annual harmonic has a secondary maximum at about 30 m depth. Generally, the amplitude of the semi-annual harmonic is small - less than 14% of the annual harmonic.

For the salinity, its long term mean ranges from 30.2 to 34.0 at the surface. Unlike the mean temperature, the mean salinity increases with depth with no subsurface minima. At 75 m depth, the mean salinity varies between 32.0 and 35.0, in the study area. The annual amplitude of the salinity is between 0.1 and 0.8, at the surface and

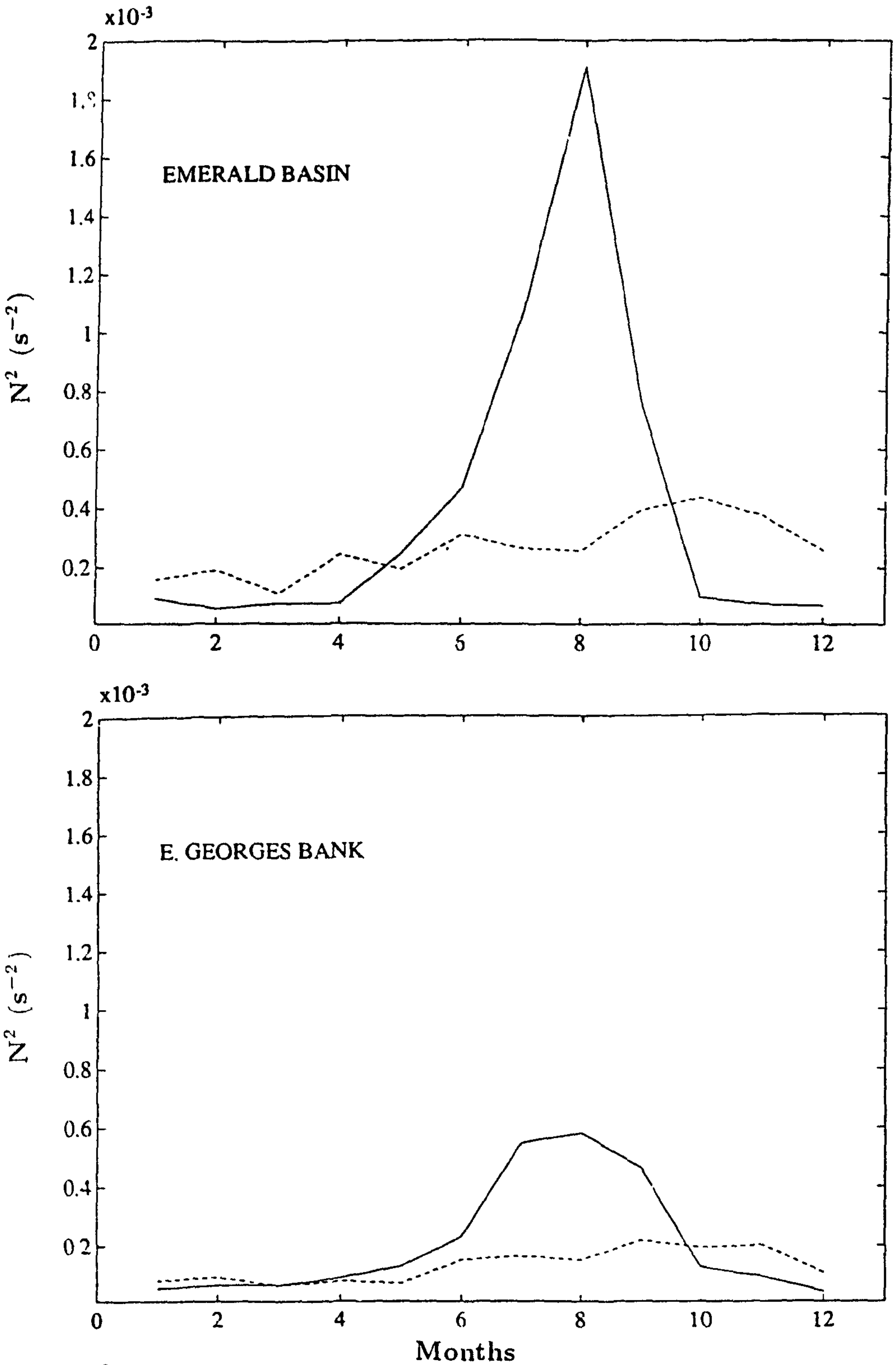

Figure 2.16: Seasonal variation of the buoyancy frequency at 15 m (solid line) and 62.5 m (dashed line) depth. The figure compares the variation at subareas 12 (Emerald Basin) and 28 (E. Georges Bank).

between 0.1 and 0.6 at 50 m depth. The amplitude of the salinity annual harmonic has a subsurface minima at about 30m. The southwestward drift, estimated from the phase of the salinity annual harmonic is consistent with measured surface current.

Like the temperature, the local rates of heat storage also show pronounced seasonality. But unlike the spatial variability in temperature, the local rate of heat storage does not present a clear consistent maximum variability near the coast and north of the mid-latitude. This is an important observation for it means that estimating local rate of heat storage using only the sea surface temperature (as is done in some mixed layer models) does not reflect the real variability.

The maps of the monthly surface steric level indicate geostrophic current moving in the southwestward direction on the shelf, which is consistent with observation. The estimated steric height compares well with the observed Halifax sea level. The buoyancy frequency also varies seasonally as expected, and its values decrease with depth.

The purpose of this chapter has been simply to describe the seasonal variability in temperature and salinity and their derived quantities. In the next chapter, the mechanisms causing these variabilities will be determined through a heat and salt budget. The seasonal surface and subsurface temperature variability will be modelled using the seasonal diffusivities estimated in Chapter 4. The formation of the subsurface mean temperature minima will be treated in Chapter 5 while the interannual variabilities in the temperature anomalies will be presented in Chapter 6.

Chapter 3

SEASONAL HEAT AND SALT BUDGET

3.1 Introduction

Seasonal changes in water temperature occur in response to fluctuations in surface heat flux, horizontal advection, upwelling and mixing. Similarly, seasonal changes in salinity occur as a result of variation in river runoff, precipitation, evaporation, horizontal advection and mixing. The relative contributions of the different processes to the seasonal heat and salt budget, at different locations, will be quantified and discussed in this chapter. Estimation of the various terms in the heat budget is a very important first step in the development of models to explain the variability in the temperature. The salt budget will serve as a check on the heat budget.

The chapter begins with the governing equations for heat and salt, followed by a presentation of the seasonal variation in the climatological net surface heat flux. The net surface heat flux is then compared with the local rates of heat storage (computed in chapter 2). In particular, it will be shown that on the Scotian Shelf, about 85% of the seasonal changes in the local rates of heat storage can be explained by the net surface heat flux and that the long term mean heat budget is primarily dominated by horizontal advection.

3.2 Governing Equations for Heat and Salt

The depth-integrated temperature conservation equation may be written [e.g. *Frankignoul and Reynolds, 1983*]

$$\begin{aligned}\frac{\partial H}{\partial t} &= Q - \rho c_p \int_{-h}^{0} \underline{u} \cdot \nabla T\, dz - \rho c_p \int_{-h}^{0} w \frac{\partial T}{\partial z}\, dz + \rho c_p \int_{-h}^{0} K_H \nabla^2 T\, dz \\ &- \rho c_p K_V \frac{\partial T}{\partial z}\bigg|_{-h} \qquad (3.1)\end{aligned}$$

where

$$H = \rho c_p \int_{-h}^{0} T\, dz$$

is the heat stored between the surface ($z = 0$) and some depth $z = -h$. Q is the net surface heat flux. $\underline{u} = (u, v)$ consists of the cross-shore (u) and along-shore (v) components of the water velocity. $\nabla T = (\partial T/\partial x, \partial T/\partial y)$ is the horizontal temperature gradient. The second and third terms on the right hand side of (3.1) are contributions from horizontal and vertical advection respectively. w is the upwelling velocity. The fourth term represents the contribution of the horizontal diffusion (mixing) to the depth-integrated heat budget while the last term is the vertical diffusive flux of heat at some depth $z = -h$. As shown in chapter 2, h=75 m is the average depth of the seasonal temperature signal penetration. K_H and K_V are the coefficients of the horizontal and vertical eddy diffusivity.

The depth-integrated salinity conservation equation, similar to the above temperature equation, may be expressed [e.g. *Miller, 1975]*

$$\begin{aligned}\int_{-h}^{0} \frac{\partial S}{\partial t}\, dz &= S_o(E - P) - \int_{-h}^{0} \underline{u} \cdot \nabla S\, dz - \int_{-h}^{0} w \frac{\partial S}{\partial z}\, dz + \int_{-h}^{0} K_H \nabla^2 S\, dz \\ &- K_V \frac{\partial S}{\partial z}\bigg|_{-h} \qquad (3.2)\end{aligned}$$

where S_o is the surface salinity, E the rate of evaporation (in m s^{-1}) and P the rate of precipitation (also in m s^{-1}). Here, K_H and K_V are taken to be the same for heat and salt, since the eddy distribution of heat and salt at any time are simultaneously accomplished by the same turbulent processes.

3.3 Net Surface Heat Flux, Q

The net surface heat flux presented here was estimated by *Isemer and Hasse [1987]* from meteorological and oceanographic data. The monthly heat flux represents the climatological mean of 32 years, taken over the period 1941 to 1972. The net surface heat flux

$$Q = Q_S - Q_I - Q_L - Q_H \tag{3.3}$$

comprises the short wave (solar) radiative flux, Q_S, minus the sum of the long wave radiative flux, Q_I, latent heat flux, Q_L, and sensible heat flux, Q_H. Positive Q means that the net heat flux is into the ocean. The complete formula for each component of the surface heat flux will be given in Chapter 6, when I examine the interannual variability. In this section, my goal is to show how the long-term monthly mean surface heat flux varies spatially and seasonally in the study region.

Isemer and Hasse [1987] evaluated Q on a 1° grid using data interpolated from *Bunker's [1976]* original irregular shaped areas (at times up to 10° square). They applied a two-dimensional, quadratic polynomial interpolation method. They also revised the exchange coefficients used by Bunker, since recent measurements *[Smith and Dobson, 1984]* have shown that Bunker's exchange coefficients underestimate Q_S and overestimate Q_L and Q_H. It is these revised estimates of Q that I have used.

Figure 3.1a shows the spatial variation of the annual mean Q. It is clear from the figure that north of about 43°N, the ocean gains heat. The rate of net warming increases with increasing latitude, with a typical value of about 20 W m^{-2} on the Scotian Shelf. The amplitude of the annual cycle (Figure 3.1b) on the Scotian Shelf is about 200 W m^{-2}. A natural question is how much of the annual variation in the local rates of heat storage, $\partial H/\partial t$, may be accounted for by Q?

3.4 Comparison of Q and $\partial H/\partial t$

In Figure 3.2, the seasonal time series of Q is compared with $\partial H/\partial t$ for two areas: subareas 12 (on the shelf) and 33 (on the slope). I have also plotted the estimated error

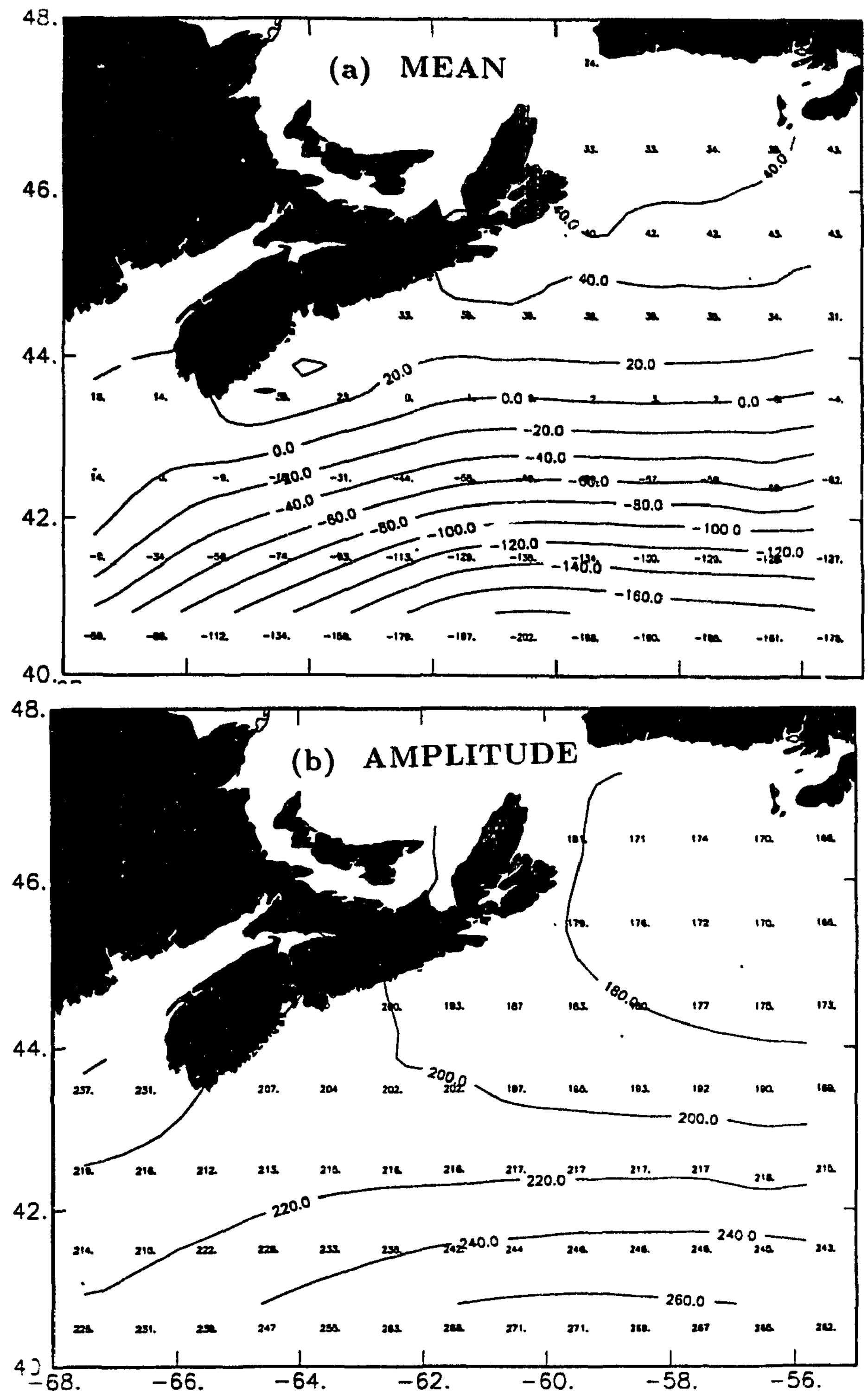

Figure 3.1: Map of Q *[Isemer and Hasse, 1987]* showing its annual mean and amplitude in W m^{-2}. Input data are plotted in small print. The contour interval is 20 W m^{-2}.

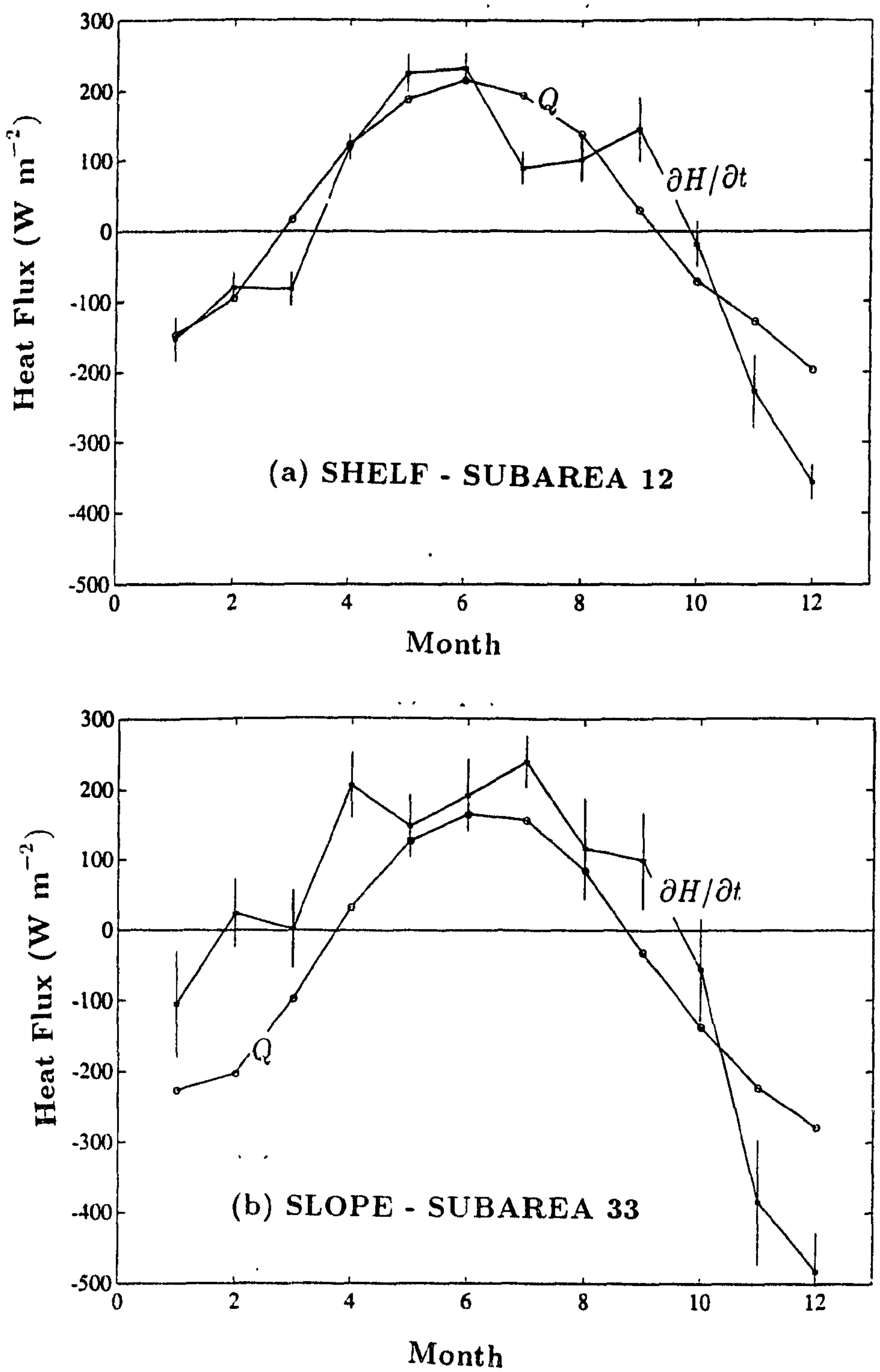

Figure 3.2: The comparison of the seasonal Q and $\partial H/\partial t$ for the shelf and slope regions. The vertical lines define a 95% confidence interval for $\partial H/\partial t$.

associated with $\partial H/\partial t$ - two standard deviations, approximating a 95% confidence interval, are also plotted in the figure. The error was estimated as described in section 2.4.1 of Chapter 2. Both terms have their maximum in June and minimum in December. On the Scotian Shelf, the spatial averaged Q accounts for about 85% of the seasonal variation of the $\partial H/\partial t$. For the slope region (Figure 3.2b), $\partial H/\partial t$ is higher than Q. About 87% of the spatial averaged $\partial H/\partial t$ may be explained by the seasonal Q. The mechanisms that may be responsible for the discrepancies between $\partial H/\partial t$ and Q for both shelf and slope regions will be discussed when the heat budget are balanced.

In order to give a spatial overview of how much of $\partial H/\partial t$ can be accounted for by Q, I have compared the annual amplitude of $\partial H/\partial t$ and Q in Figure 3.3a and b (The amplitudes and phases of the two terms are listed in Table B.1 of Appendix B). Again, on the shelf, the two amplitudes compare fairly well, with values ranging between 200 and 240 W m^{-2}. Over the slope region, $\partial H/\partial t$ has a larger amplitude than on the shelf, with values greater than 240 $W\ m^{-2}$.

To show the imbalance between $\partial H/\partial t$ and Q, I have computed the difference, $(\partial H/\partial t - Q)$, hereafter referred to as the residual, for the study region. The maps of the monthly residual are shown in Figures B.1, B.2 and B.3, and their values listed in Table B.2 of Appendix B. In December, a consistent pattern of the residual is observed throughout the study region. In this month, the residual is negative, that is, $\partial H/\partial t$ is less than Q. In other months, the residual at any subarea is variable and does not have any strong seasonal cycle.

Figure 3.3c shows the amplitude of $\partial H/\partial t - Q$. The main point from the figure is that the amplitude of the residual is less on the shelf than in the slope region and in the region around the Laurentian Channel. On the shelf, the amplitude is less than 40 W m^{-2} whereas on the slope and toward the Laurentian Channel regions the amplitude exceeds 100 W m^{-2}. These regions of large amplitude residual are regions of known strong horizontal advection. A large magnitude of the residual (allowing for error in Q) is attributed to the contribution of other terms like horizontal advection,

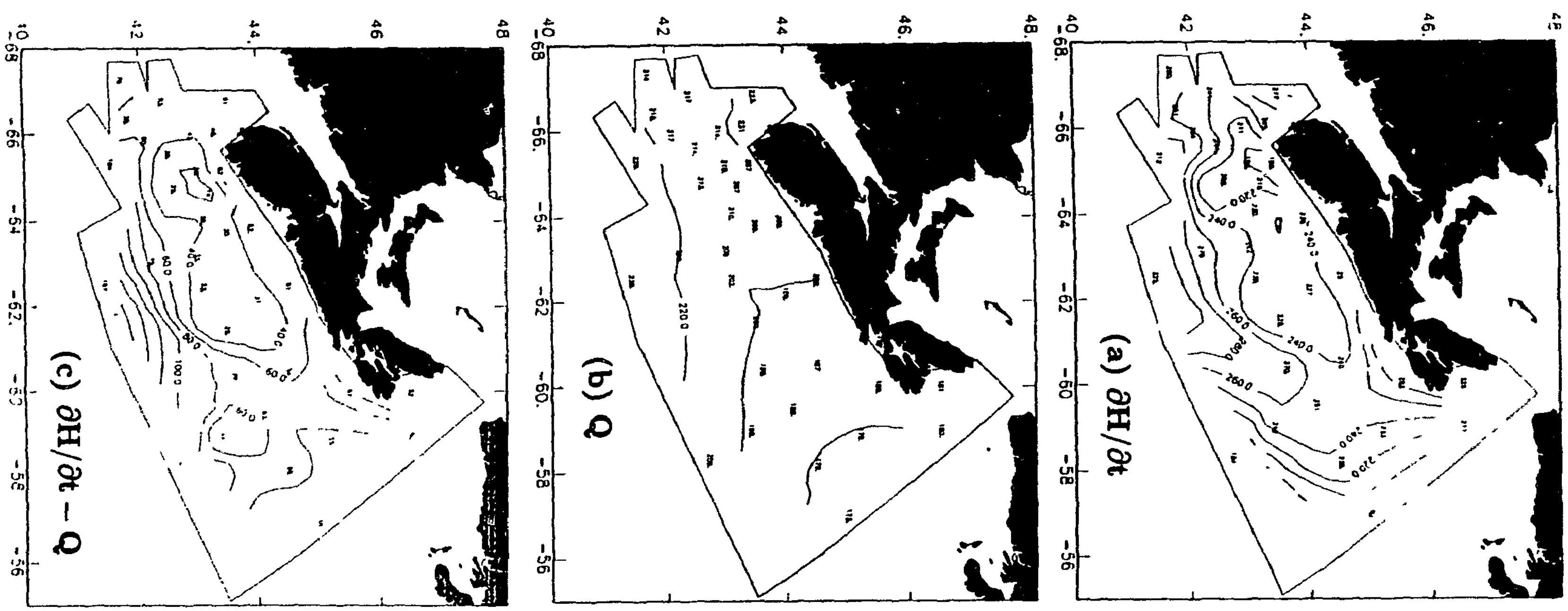

Figure 3.3: Maps showing the amplitudes of $\partial H/\partial t$, Q and $\partial H/\partial t - Q$ in W m^{-2} Input data are plotted in small print. The contour interval is 20 W m^{-2}. (Note that the values of Q are grouped according to the subareas where the $\partial H/\partial t$ is estimated.

mixing, upwelling, etc.) to the heat budget of this region. The magnitudes of these terms are estimated below.

3.5 Comparison of $\int_{-h}^{0}(\partial S/\partial t)\,dz$ and $S_o(E-P)$

The E-P data required to estimate the surface flux of salinity are obtained from *Schmitt et al. [1989]*. I have fitted a sinusoid to the seasonal mean values of E-P in order to interpolate to monthly values. For the shelf region (subarea 12), the values of E-P range from 3.4×10^{-2} m yr^{-1} in June to 54.0×10^{-2} m yr^{-1} in December.

In Figure 3.4, the seasonal variation of the surface flux of salinity $S_o(E-P)$ is compared with $\int_{-h}^{0}(\partial S/\partial t)\,dz$, on the shelf (subarea 12) and over the slope (subarea 33). h is taken as 75m - the same as in the heat budget. The 95% confidence intervals for the local change in the salt content are also plotted on the figure. The main feature in the figure is that the magnitude of $S_o(E-P)$ is much smaller than $\int_{-h}^{0}(\partial S/\partial t)\,dz$ in both regions. That means that the local changes in the salinity can not be explained by the surface flux of evaporation and precipitation. The imbalance between $\int_{-h}^{0}(\partial S/\partial t)\,dz$ and $S_o(E-P)$ will be discussed when other terms in the salt budget are estimated.

In the following subsections, I will show how the different terms in the heat and salt equations vary spatially and temporary in the different areas of the study region. My goal is to balance the heat and salt budget within the error bars of $\partial H/\partial t$ and Q and $\partial S/\partial t$, if possible. I have regrouped the 34 hydrographic subareas (Figure 2.1) into 18 subareas. The original subareas are regrouped because from the analyses of the temperature and salinity annual harmonics it is observed that the variability in some subareas is similar. It is on the basis of the seasonal variability and also topography that the regrouping is done. These regrouped subareas (whose number begins with A) are shown in Figure 3.5 and their names listed in Table B.3 of Appendix B. Where no change has been made to the original subarea, the original name is retained. The Q is also regrouped by taking the monthly average of all the $1° \times 1°$ data falling within

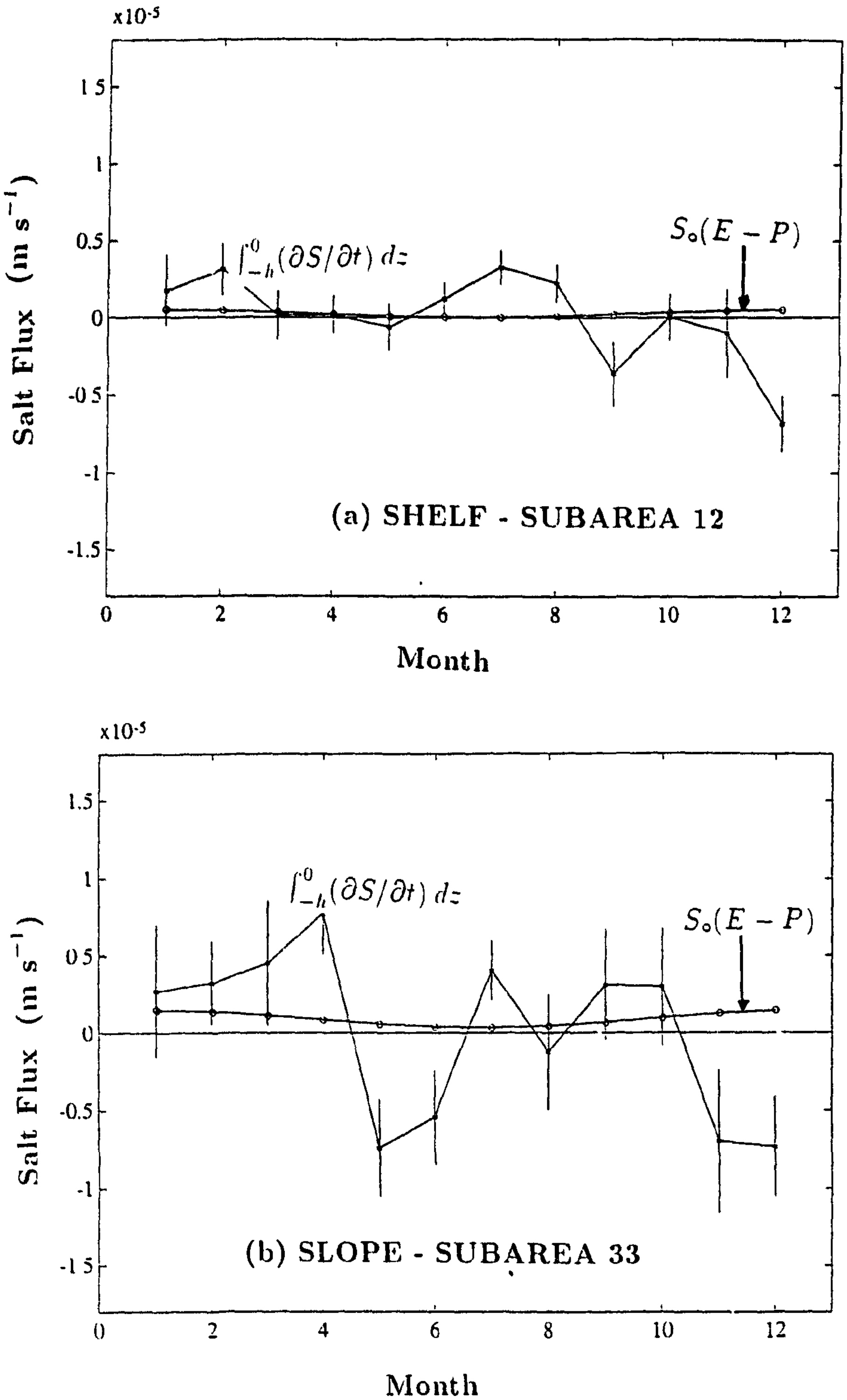

Figure 3.4: The comparison of the seasonal $S_o(E-P)$ and $\int_{-h}^{0}(\partial S/\partial t)\,dz$ for the shelf and slope regions. The vertical lines show the 95% confidence interval for $\int_{-h}^{0}(\partial S/\partial t)\,dz$.

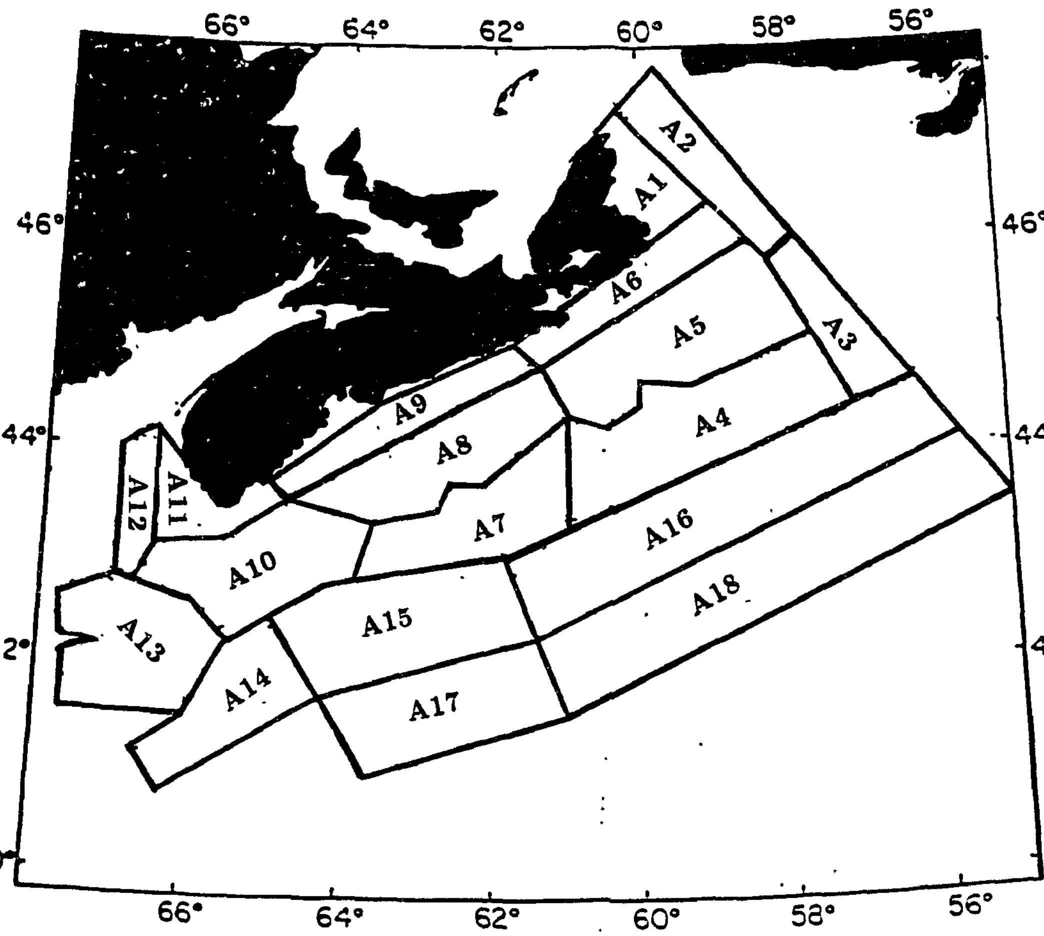

Figure 3.5: Map of the study region showing the regrouped subareas. Names of the subareas are listed in Table B.3 of Appendix B.

each subarea.

I have selected four subareas for the heat and salt budget: the central mid-shelf (subarea A8), central outer shelf (subarea A7), west outer shelf (subarea A10), and the central slope (subarea A15). The heat and salt budget of subarea A8 are chosen to represent the budget on the shelf while those of subarea A15 represent the slope region. These two subareas will be described in the main text while the budgets of subareas A7 and A10 are given in Figures B.4 and B.6 of Appendix B, for comparison.

3.6 Heat and Salt Flux due to Horizontal Advection

To estimate the heat and salt flux due to horizontal advection, the total current (which comprises the geostrophic and Ekman) are needed. The following subsections show how these currents are estimated.

3.6.1 Estimation of Geostrophic Velocities

Geostrophic velocity shears are computed using the thermal wind equations:

$$\frac{\partial v_g}{\partial z} = -\frac{g}{\rho_o f}\frac{\partial \rho}{\partial x} \tag{3.4}$$

$$\frac{\partial u_g}{\partial z} = \frac{g}{\rho_o f}\frac{\partial \rho}{\partial y} \tag{3.5}$$

where u_g and v_g are the cross-shore and along-shore geostrophic velocities. ρ is the water density and $\rho_o = 1025\,\mathrm{kg\ m^{-3}}$, the reference water density. g is the acceleration due to gravity and f the Coriolis parameter. The axis x is normal to the shore with x increasing seaward and the y is parallel to the coast with y increasing to the northeast. $\partial\rho/\partial x$ and $\partial\rho/\partial y$ for any subarea are computed from the density field of the neighbouring subareas. For example. for subarea A8

$$\left.\frac{\partial \rho}{\partial x}\right|_z \approx \left.\frac{\rho_7 - \rho_9}{\Delta x}\right|_z \tag{3.6}$$

$$\left.\frac{\partial\rho}{\partial y}\right|_z \approx \left.\frac{\rho_5 - \rho_{10}}{\Delta y}\right|_z \tag{3.7}$$

where ρ_7 (for instance) stands for the density for subarea A7. Δx is the cross-shore distance between the mid-point of subareas A7 and A9 and Δy the along-shore distance between the mid-point of subareas A5 and A10. Equations (3.6) and (3.7) are computed at $z = 0$, 10, 20, 30, 50 and 75 m. To compute the absolute velocities, I assume a depth of no motion at $100m$ (which is the average water depth on most part of the Shelf) and depth-integrate (3.4) and (3.5) to obtain the absolute geostrophic velocities.

Figure 3.6a shows the seasonal estimates of $-v_g$ at $z = 0$, 20, 50 and 75 m for subarea A8. The v_g exhibits strong seasonality. At the surface, the velocity has a maximum of 6.2×10^{-2} m s^{-1} in January and a minimum of 0.9×10^{-2} m s^{-1} in July. $|v_g|$ decreases with depth - the annual mean at 0, 20, 50 and 75m depths are 3.5×10^{-2}, 2.9×10^{-2}, 2.0×10^{-2} and 1.0×10^{-2} m s^{-1} respectively. The direction of the surface velocities is towards the southwest, consistent with the steric height distribution shown in chapter 2. The seasonal variation of u_g at 0, 20, 50 and 75 m depths is shown in Figure 3.6b. Note the change in the direction of u_g, unlike v_g. In March and June u_g flows offshore while in other months the flow direction is onshore. The annual mean $|u_g|$ decreases from 0.3×10^{-2} m s^{-1} at the surface to 0.1×10^{-2} m s^{-1} at 30 m depth. $|u_g|$ is typically a factor of 10 smaller than $|v_g|$. The seasonal and depth variation of the geostrophic velocities at subarea A8 is typical of other subareas.

3.6.2 Estimation of Ekman Velocities

Mean Ekman velocities in the surface Ekman layer were calculated from

$$v_E = -\frac{\tau^x}{\rho\, h_E f} \tag{3.8}$$

$$u_E = \frac{\tau^y}{\rho\, h_E f} \tag{3.9}$$

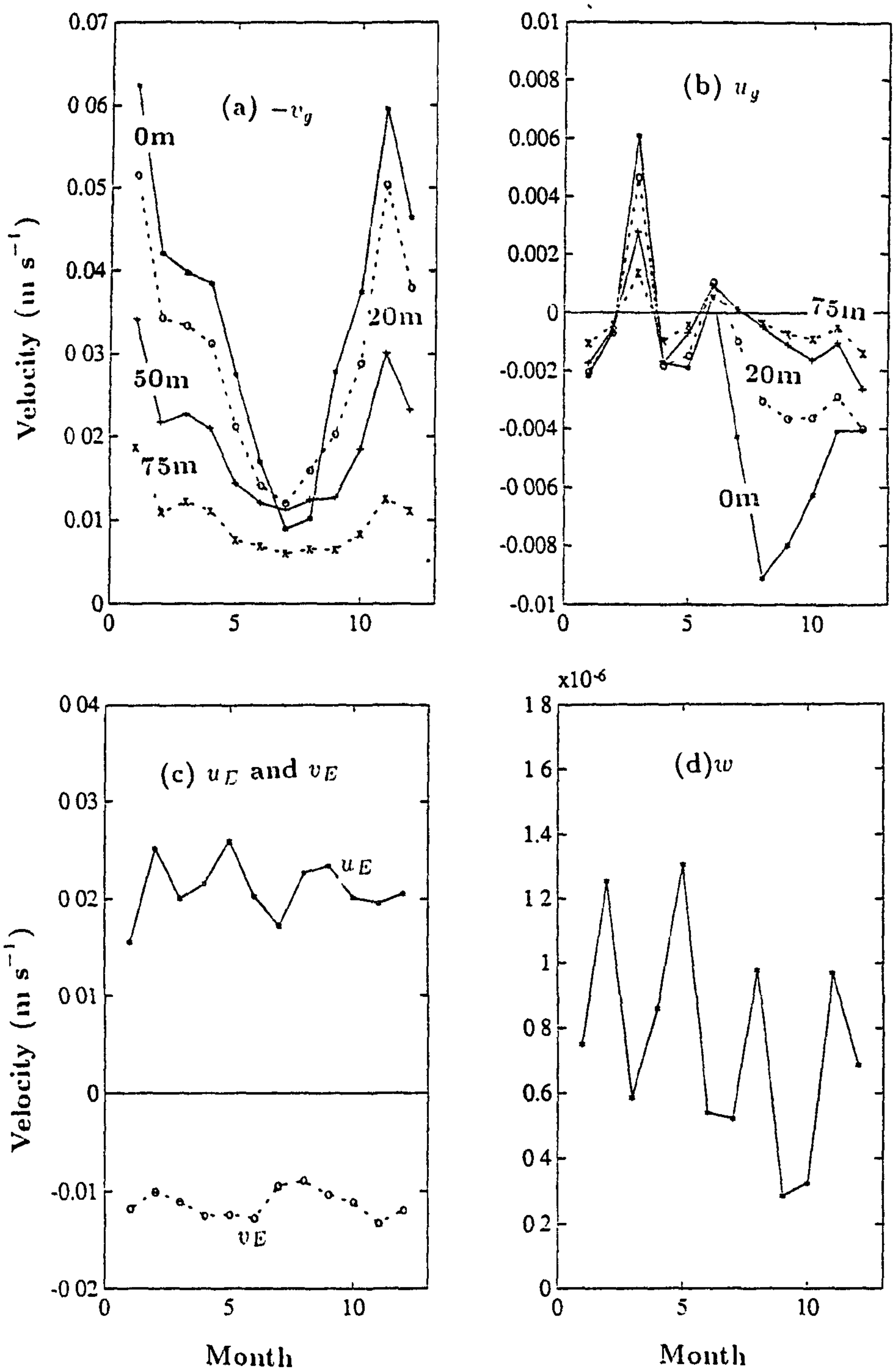

Figure 3.6: Seasonal estimates of geostrophic velocities $-v_g$ and u_g, Ekman velocities u_E and v_E, and upwelling velocities w for the shelf (subarea A8). Note that $-v_g > 0$ means that the current is moving in the southwestward direction along the Shelf.

where τ^x and τ^y are cross-shore and along-shore wind stresses and h_E the Ekman depth is assumed to be 15 m. The monthly wind stress is estimated from

$$\tau^x = \rho_a\, c_d(\overline{|\underline{u}_a|})\, \overline{|\underline{u}_a|\; u_a} \tag{3.10}$$

$$\tau^y = \rho_a\, c_d(\overline{|\underline{u}_a|})\, \overline{|\underline{u}_a|\; v_a} \tag{3.11}$$

where $\rho_a = 1.2\ kg\ m^{-3}$ is the air density. $\overline{|\underline{u}_a|}$ is the monthly mean wind speed. The overbar refers to a monthly mean. u_a and v_a are cross-shore and along-shore wind components. These wind statistics are obtained from COADS (Comprehensive Ocean-Atmosphere Data Set). In this formulation, the drag coefficient c_d varies with wind speed according to *Large and Pond [1981]*:

$$10^3\, c_d = \begin{cases} 1.14 & 4 < |\underline{u}_a| < 10 \text{ m s}^{-1} \\ 0.49 + 0.065\,|\underline{u}_a| & 10 \leq |\underline{u}_a| < 26 \text{ m s}^{-1} \end{cases} \tag{3.12}$$

The estimated τ^x at subarea A8 ranges from $1.4 \times 10^{-2}\,Pa$ in August to $2.0 \times 10^{-2}\,Pa$ in November, while τ^y varies between $2.7 \times 10^{-2}\,Pa$ in July and $4.0 \times 10^{-2}\,Pa$ in May. Substituting the values of τ^x and τ^y into (3.8) and (3.9) gives the Ekman velocities u_E and v_E shown in Figure 3.6c. The cross-shore Ekman velocities are larger in magnitude than the along-shore counterparts: u_E varies between 1.6×10^{-2} m s^{-1} and 2.5×10^{-2} m s^{-1} with no seasonal pattern, whereas $|v_E|$ ranges from 1.0×10^{-2} m s^{-1} and 1.3×10^{-2} m s^{-1}. The depth-integrated heat flux due to horizontal advection is computed from

$$-\rho c_p \int_{-h}^{0} \underline{u} \cdot \nabla T\, dz = -\rho c_p \int_{-h}^{0} \left[(u_g + u_E)\,\frac{\partial T}{\partial x} + (v_g + v_E)\,\frac{\partial T}{\partial y} \right] dz \tag{3.13}$$

In the analysis, u_E and v_E are assumed to be distributed uniformly over the top 15 m, the Ekman depth, and zero below. The seasonal estimates of the heat flux due to horizontal advection are shown in Figure 3.7a. For the shelf region, it ranges from -76 W m^{-2} in December to 7 W m^{-2} in September with an annual mean of -40 W m^{-2}. For the slope region, it varies from -257 W m^{-2} in May to -23 W m^{-2} in January with no obvious seasonality. The annual mean is -80 W m^{-2}. The large

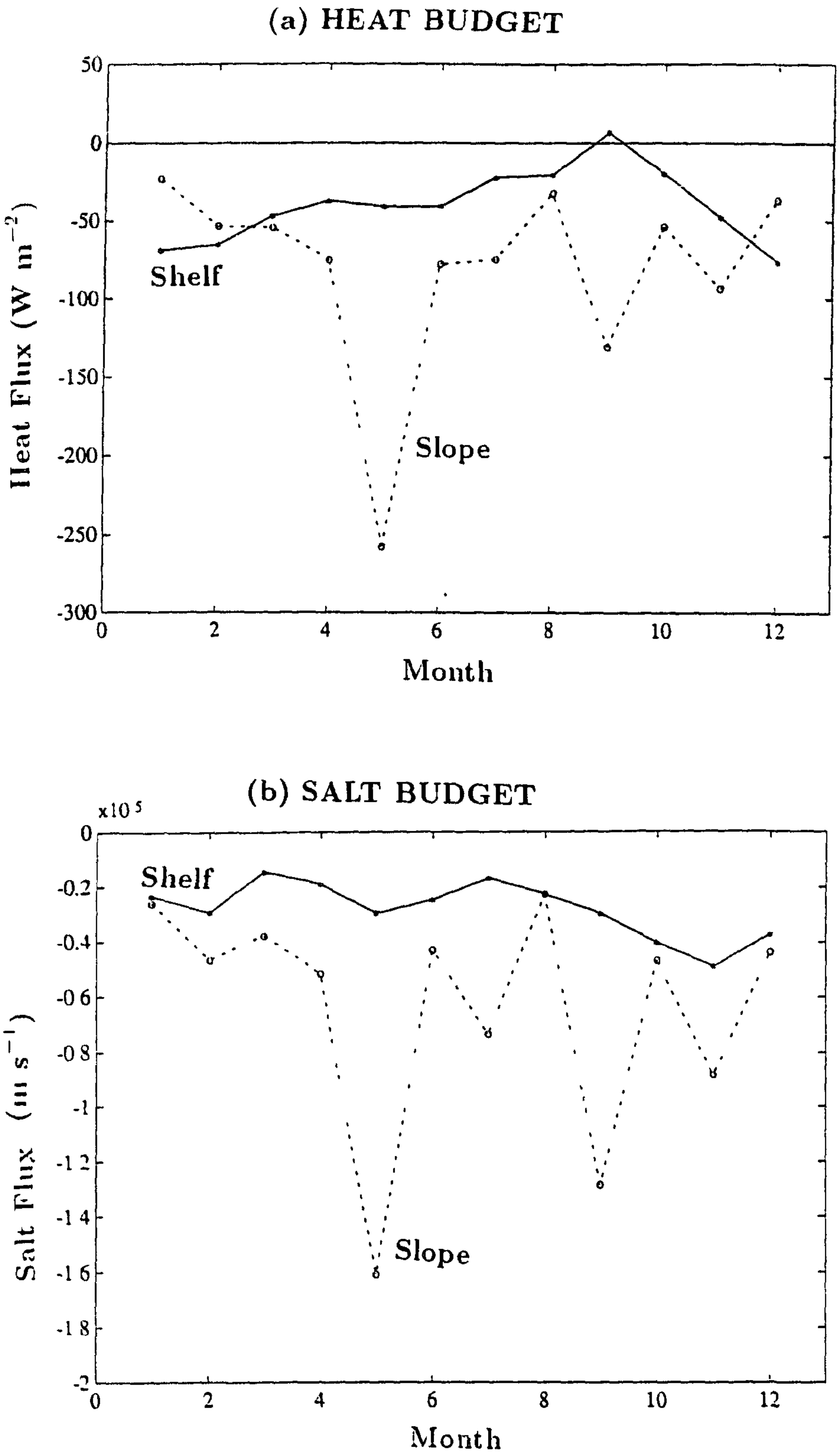

Figure 3.7. Seasonal estimates of the heat and salt flux due to horizontal advection, for the shelf and slope regions.

fluctuation in the horizontal heat flux on the slope region might be due, in part, to the back-and-forth movements of the water masses in this region.

For the salt budget, the contribution of the horizontal advection varies between -49×10^{-7} m s^{-1} in November and -14×10^{-7} m s^{-1} in March on the shelf. For the slope, it is between -161×10^{-7} m s^{-1} in May and -23×10^{-7} m s^{-1} in August. Like the heat budget, the contribution of horizontal advection to the salt budget is larger on the slope region than on the shelf. The comparisons of the heat flux due to horizontal advection with other terms in the heat and salt budget are shown in Figure B.5 of Appendix B.

3.7 Heat and Salt Flux due to Upwelling

3.7.1 Estimation of Vertical Velocity

The vertical water velocity, w, away from the coast has been computed from the Ekman upwelling relation:

$$w = \frac{\partial}{\partial x}\left(\frac{\tau^y}{\rho f}\right) - \frac{\partial}{\partial y}\left(\frac{\tau^x}{\rho f}\right) \tag{3.14}$$

where the wind stress components (τ^x, τ^y) are estimated as described earlier.

The seasonal variation of the estimated upwelling velocity for subarea A8 is shown in Figure 3.6d. The values range from 0.3×10^{-6}m s^{-1} in September to 1.3×10^{-6}m s^{-1} in May. These values compare favourably with previous estimates *[Thompson and Hazen, 1983; Isemer and Hasse, 1987]*. who found that the upwelling velocity is generally of the order of 10^{-6} m s^{-1} throughout the year.

In estimating the heat flux due to upwelling, $-\rho c_p \int_{-h}^{0} w(\partial T/\partial z)\,dz$, I assume that the vertical velocity linearly decreases from w at 75 m depth (the depth of seasonal signal penetration) to zero at the surface. The upwelling heat flux (Figure 3.8a) for the shelf ranges from -7 W m^{-2} in November to 9 W m^{-2} in February, with an annual mean of 1 W m^{-2}. For the slope, it varies between -5 W m^{-2} in November and 5 W m^{-2} in May with an annual mean of 1 W m^{-2}. The contribution of upwelling

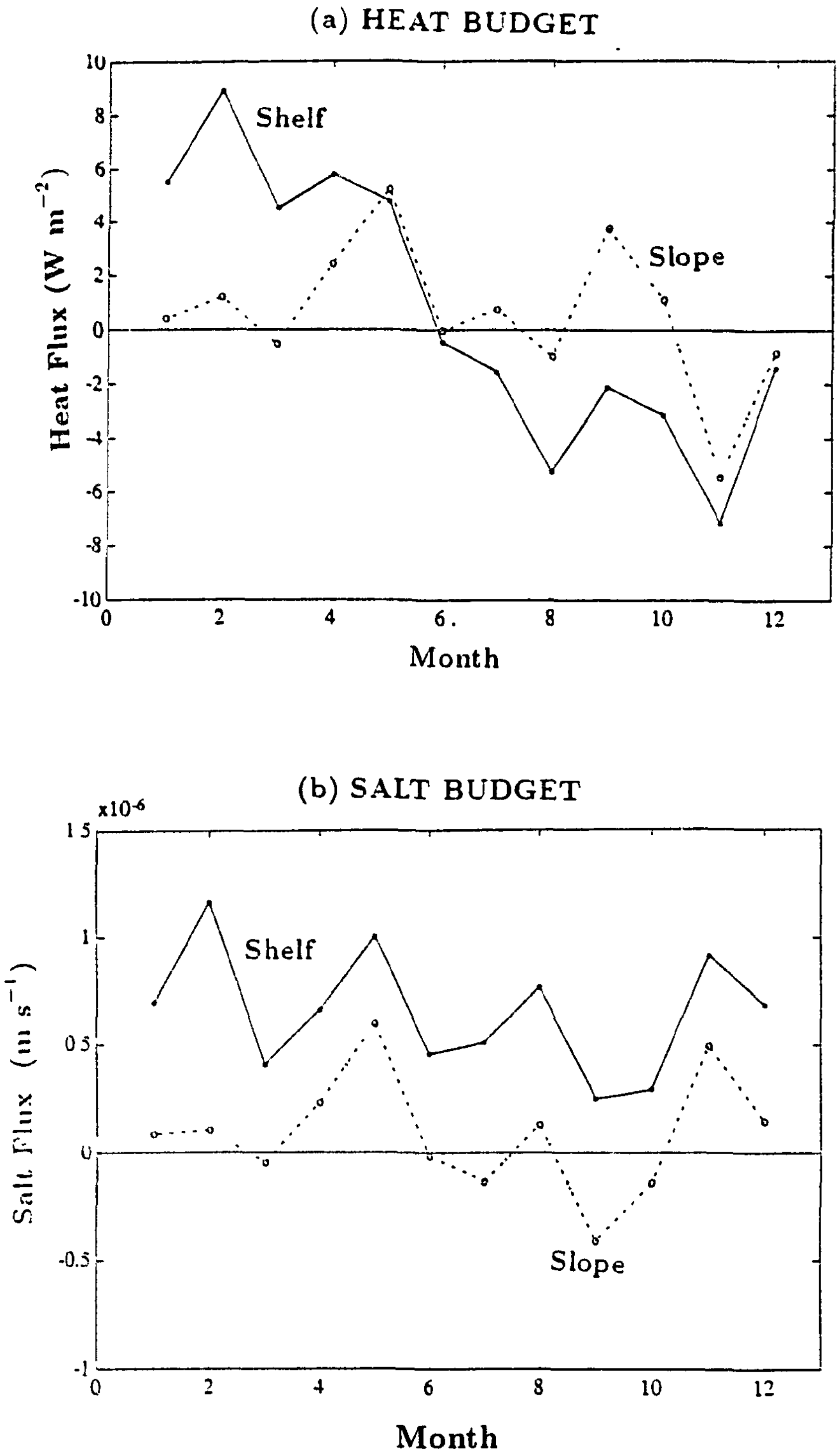

Figure 3.8: Seasonal estimates of the heat and salt flux due to upwelling, for the shelf and slope regions.

to the heat budget compared with other terms (Figure B.5) is generally small, < 1% of $\partial H/\partial t$ on the shelf.

This analysis indicates that open ocean upwelling may not offer any significant contribution to the seasonal temperature variability, in contrast with the ideas of *Bjerknes [1964]* and *Lacy [1988]* who suggested that upwelling could be an important mechanism in changing the sea surface temperature in summer. However, although (3.10) applies only to the open ocean, the fact that the open upwelling flux increases towards the coast (from the slope to the shelf, see Table B.5b of Appendix B) suggests that coastal upwelling could be important near the shore. For a baroclinic case, coastal upwelling may be estimated from $w = \tau/\rho f R_o$, where τ is the wind stress and R_o is the internal Rossby radius. *Petrie et al. [1987]* has, indeed, found that coastal upwelling is strong within one internal Rossby radius - about 15 km from the coast. The effect of the coastal upwelling is that it changes the heat flux of the shelf region (away from the coast) through horizontal advection, via the Ekman flux.

For the salt budget, the contribution of upwelling (Figure 3.8b) is also small. For the shelf and slope region, the upwelling salt flux is between -4×10^{-7} and $12 \times 10^{-7}\, m\, s^{-1}$.

3.8 Heat and Salt Flux due to Horizontal Mixing

3.8.1 Estimation of K_H from CASP Data

In order to estimate the heat and salt flux due to horizontal mixing one needs $K_H(K_x, K_y)$ which is defined by

$$K_x = -\overline{u'T'}/(\partial\overline{T}/\partial x) \qquad \text{and} \qquad K_y = -\overline{v'T'}/(\partial\overline{T}/\partial y) \tag{3.15}$$

The overbar denotes a monthly mean and the prime a deviation from the monthly mean. K_x and K_y are estimated using CASP (Canadian Atlantic Storms Program) data. The CASP experiment ran on the Scotian Shelf from November, 1985 to March, 1986. Figure 3.9a shows the locations where the hydrographic data were obtained

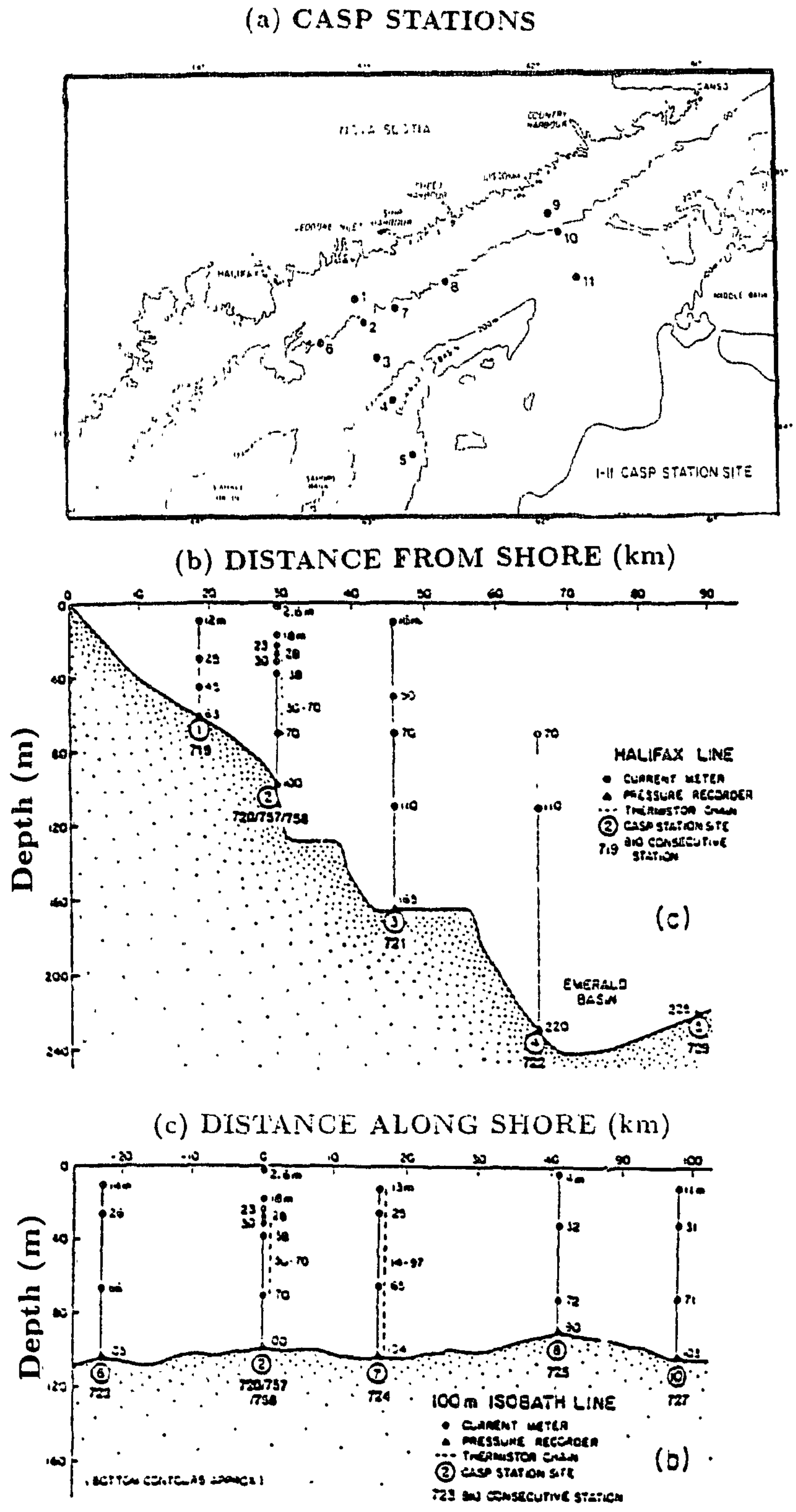

Figure 3.9: Map showing the region occupied during CASP experiment [from *Schwing, 1989*].

while Figure 3.9b presents the water depths where the measurements were taken. The CASP data set provides the temperature (T) and current (u,v) used to estimate K_x and K_y. In some months and depths, data are not available either due to instruments malfunctioning or other problems. The horizontal diffusivities are computed at those locations where there are enough data to compute the horizontal temperature gradients and $\overline{u'T'}$ and $\overline{v'T'}$. The estimated diffusivities are listed in Table 3.1.

As shown in the table, the individual estimates of K_x and K_y from (3.15) vary widely. In some cases negative or abnormally high values of the K's are obtained. To estimate a mean value for K_x and for K_y the following approach was adopted. The approach is based on the principal components analysis of $\overline{u'T'}$ and $\partial\overline{T}/\partial x$ (and also of $\overline{v'T'}$ and $\partial\overline{T}/\partial y$). This method is particularly useful when both types of observation are subject to error. In this method, the values of $\overline{u'T'}$ and $\partial\overline{T}/\partial x$ are first normalized by dividing by their standard deviations and then the principal components of the normalized values computed. The procedure is fully described by *Morrison [1976]*. Following *Morrison*, the first principal component of $\overline{u'T'}$ and $\partial\overline{T}/\partial x$ may be expressed as the linear compound

$$Y_1 = a_{11}\,\overline{u'T'} + a_{12}\,\partial\overline{T}/\partial x \tag{3.16}$$

where the coefficients a_{11} and a_{12} define the eigenvector corresponding to the largest eigenvalue (characteristic root). They are determined from the normalized covariance matrix. Figure 3.10 shows the scatter plot of the normalized $\overline{u'T'}$ and $-\partial\overline{T}/\partial x$. The solid line is the plot of $a_{11}\,\overline{u'T'}$ against $-a_{12}\,\partial\overline{T}/\partial x$. The slope of the line gives the mean value of K_x. (Although the fit is not very good, it is better than a simple regression analysis.) Notice that the line corresponds to the principal axis of $\overline{u'T'}$ and $\partial\overline{T}/\partial x$. The same procedure was used to determine K_y. From the principal components analyses, the following values were obtained: $K_x = 679\ \mathrm{m^2\,s^{-1}}$, and $K_y = 546\ \mathrm{m^2\,s^{-1}}$.

The heat flux due to horizontal mixing is then computed as

$$\rho c_p \int_{-h}^{0} K_H \nabla^2 T\, dz = \rho c_p \int_{-h}^{0} \left[K_x \frac{\partial^2 T}{\partial x^2} + K_y \frac{\partial^2 T}{\partial y^2} \right] dz \tag{3.17}$$

STN #	Depth (m)	Month	$\overline{u'T'} \times 10^{-4}$ ($^\circ$ C m s^{-1})	$\partial\overline{T}/\partial x \times 10^{-6}$ ($^\circ$ C m^{-1})	K_x (m^{2}s^{-1})
S2	18	Nov	25.58	-33.70	85
		Dec	97.63	-24.81	393
		Jan	65.28	-14.81	441
		Feb	97.01	2.22	-4366
		Mar	40.92	9.26	-442
		Apr	43.81	-2.22	1971
S2	38	Nov	31.69	43.33	-73
		Dec	118.20	-12.59	939
		Jan	-27.28	-10.74	-254
		Feb	30.79	30.74	-100
		Mar	7.73	23.33	-33
		Apr	-66.99	7.78	861
STN #	**Depth (m)**	**Month**	**$\overline{v'T'} \times 10^{-4}$ ($^\circ$ C m s^{-1})**	**$\partial\overline{T}/\partial y \times 10^{-6}$ ($^\circ$ C m^{-1})**	**K_y (m^{2}s^{-1})**
S2	28	Nov	-23.90	-8.46	-282
		Dec	-116.33	-3.59	-3241
		Jan	153.86	-7.69	2000
		Feb	164.12	0.26	-64007
		Mar	-9.13	1.79	509
		Apr	-39.59	-2.31	-1716
S7	25	Nov	39.15	-0.45	8026
		Dec	-143	-10.24	-1396
		Jan	412.02	-10.24	4022
		Feb	-85.18	-7.80	-1091
		Mar	31.44	0.24	-12890
		Apr	-70.97	-12.20	-582

Table 3.1: Estimates of the horizontal diffusivities K_x and K_y from CASP data.

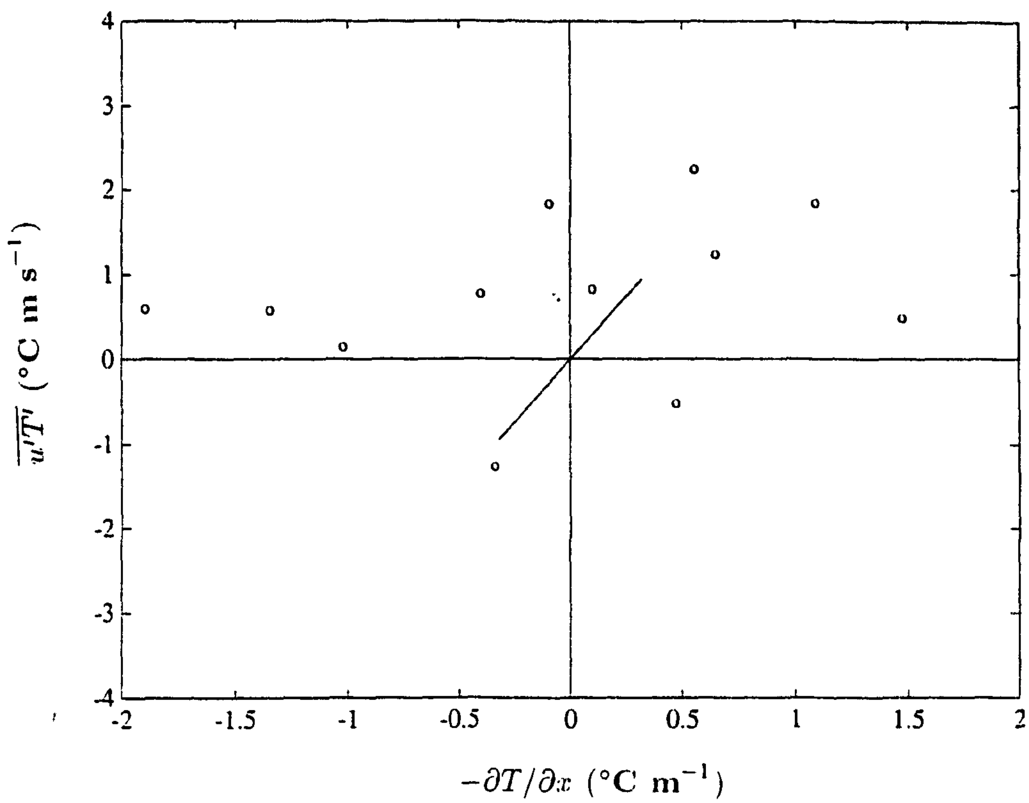

Figure 3.10: A scatter plot of the normalized $\overline{u'T'}$ and $-\partial\overline{T}/\partial x$ showing the principal axis. The slope of the line gives K_x. (See the main text for details).

On the shelf (Figure 3.11), the heat flux due to horizontal mixing varies from -38 W m^{-2} in December to 96 W m^{-2} in September. On the slope the magnitude of the horizontal mixing is larger - it ranges from 28 W m^{-2} in February to 258 W m^{-2} in September (see Table B.5 of Appendix B).

The contribution of the horizontal mixing to the salt budget for the shelf and slope regions (Figure 3.11b) shows the same pattern as in the heat budget. The salt flux is larger on the slope than on the shelf, ranging from -81×10^{-7} m s^{-1} in November to 22×10^{-7} m s^{-1} in August on the shelf, and 14×10^{-7} m s^{-1} in June to 165×10^{-7} m s^{-1} in January on the slope. The variation of the depth-integrated heat and salt flux due to horizontal mixing in both regions does not have any seasonality.

3.9 Vertical Heat and Salt Flux at $z = -h$

The vertical diffusive heat flux, $-\rho c_p K_v(\partial T/\partial z)|_{-h}$, at $h = 75\,m$ is computed using a constant $K_v = 10^{-4}\,\mathrm{m^2\,s^{-1}}$. This value of the constant vertical diffusivity is usually used for the ocean *[Yin and Fung, 1991]* and it will be shown in Chapter 4 that the value is about the best estimate for a constant K_V. The same value of the diffusivity is used for estimating the salt flux. Figure 3.12a shows the seasonal estimates of the vertical diffusive heat flux for the shelf and slope regions. From January to September, there is a flux of heat from the deep ocean into the top 75 m in both regions. For the shelf, the values are between 9 W m^{-2} in September and 26 W m^{-2} in March. For the slope, the values range from 2 W m^{-2} in September to 34 W m^{-2} in January. From November to December, the surface layer looses heat to the deep ocean in both regions. Furthermore, in both regions, the estimates show a seasonality in the diffusive heat flux. High values are obtained in winter and spring. Compared to other terms in the heat budget (Figure B.5, Appendix B), the contribution of the diffusive heat flux can not be neglected in the shelf region.

Figure 3.12b shows the seasonal estimates of the vertical diffusive salt flux at 75 m, for the shelf and slope regions. The values of the diffusive salt flux range

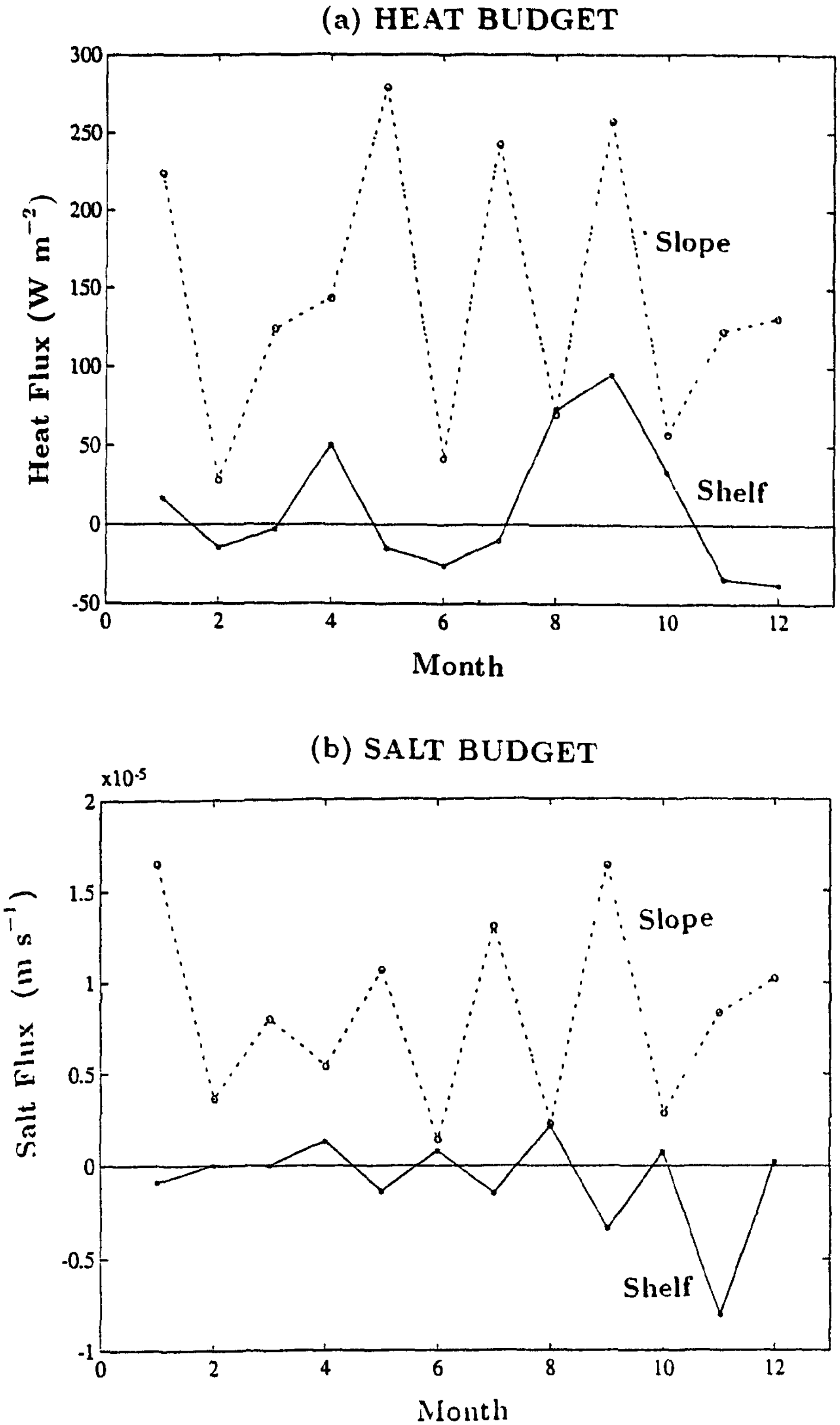

Figure 3.11: Seasonal estimates of the heat and salt flux due to horizontal mixing, for the shelf and slope regions.

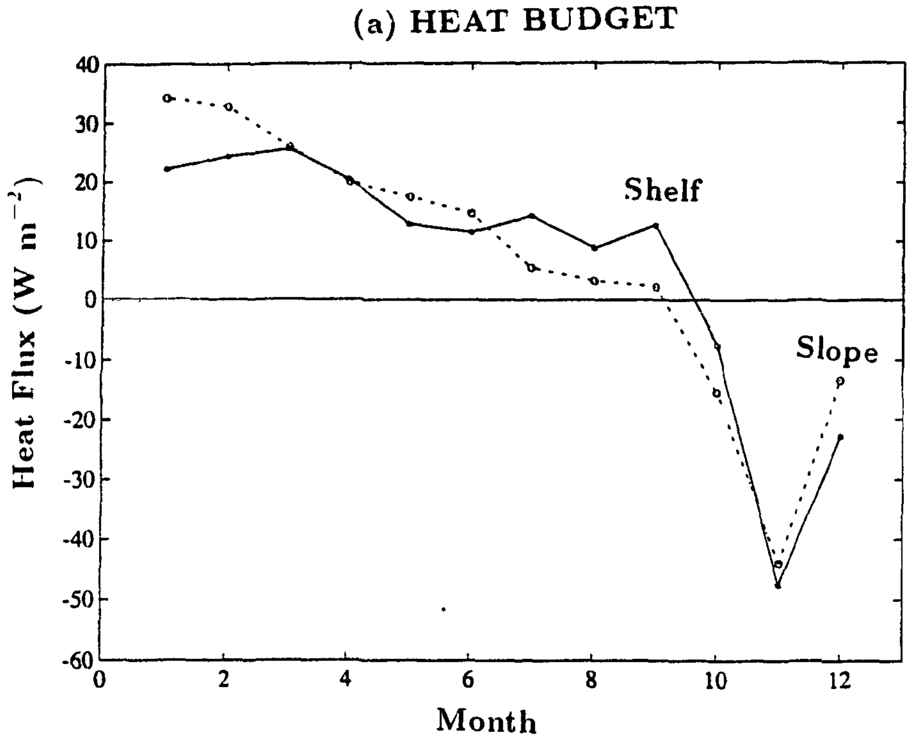

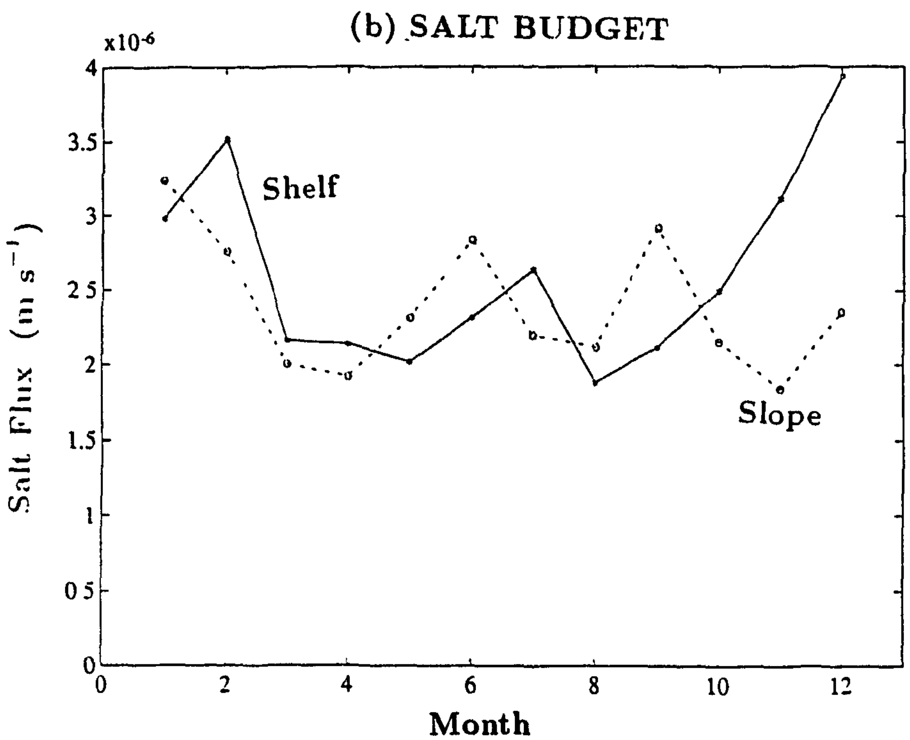

Figure 3.12: Seasonal estimates of the vertical diffusive heat and salt flux at $z = -h$, for the shelf and slope regions.

from 19 $\times$ 10^{-7} m s^{-1} to 39 $\times$ 10^{-7} m s^{-1} in the shelf region, and 18 $\times$ 10^{-7} m s^{-1} to 32 $\times$ 10^{-7} m s^{-1} in the slope region. Compared to other terms in the salt budget (Figure B.5b, Appendix B), it is clear that the vertical diffusive flux can not be neglected in the salt budget of both regions.

3.10 Balancing the Heat and Salt Budget and its Implications

To balance the heat [salt] budget, the estimate of the term on the left hand side of (3.1) [(3.2)] is compared with those terms on the right hand side.

3.10.1 Annual Mean Heat and Salt Budget

(a) Heat

The estimates of the long-term annual mean heat budget for the shelf and slope regions are shown in Figure 3.13a and their values listed in Table B.4 of Appendix B. The annual mean of $\partial H/\partial t$ is clearly zero. For the shelf region (represented by sub-area A8), the dominant term is horizontal advection. The contribution of horizontal advection (-40 W m^{-2}) alone balances the contributions of Q (25 W m^{-2}), horizontal mixing (11 W m^{-2}), vertical diffusion of heat from the deep ocean (6 W m^{-2}), and upwelling (1 W m^{-2}), to within 2 W m^{-2}. Given the errors in the data, such good agreement is probably fortuitous.

While the main focus of this chapter is to balance the heat budget for the Shelf, the heat budget for the Slope region is given for comparison. For the slope region, the balance of the mean heat budget is not as good as that on the shelf (Figure 3.13b). The imbalance is about 19 W m^{-2}. The reason for the imbalance will be discussed below. However, the analysis shows that horizontal mixing and advection, with the contribution of 144 and -80 W m^{-2} respectively, are stronger in the slope region than on the shelf. Again, in the slope region, there is a net annual surface heat loss from

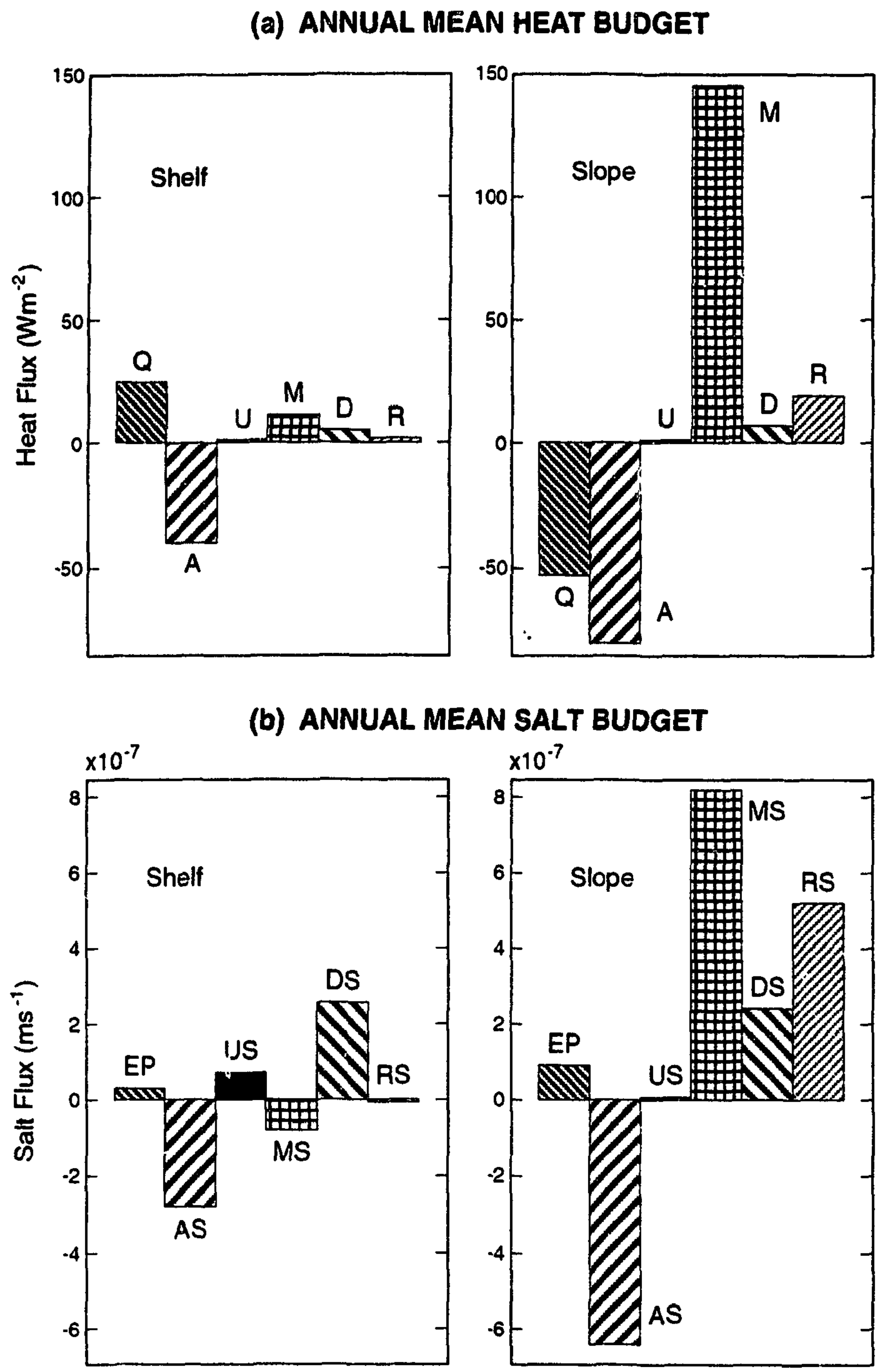

	Heat	Salt
	Q	EP
Advection	A	AS
Upwelling	U	US
Horizontal Mixing	M	MS
Vertical Diffusion	D	DS
Imbalance	R	RS

Figure 3.13: Estimates of the terms in the annual heat and salt budget for the shelf and slope regions. EP in the salt budget denotes the contribution of (E-P).

the ocean ($\sim -53\,\mathrm{W\ m^{-2}}$), in contrast to the shelf where there is a net annual surface heat gain by the ocean.

(b) Salt

The long-term annual mean salt budget for the shelf region (Figure 3.13b), like the mean heat budget for the shelf, is well balanced to within $\pm 1 \times 10^{-7}\,\mathrm{m\ s^{-1}}$. Again, the largest contribution ($-28 \times 10^{-7}\mathrm{m\ s^{-1}}$) to the mean salt budget on the shelf comes from horizontal advection (as in the mean heat budget). The next important term in the mean salt budget is the vertical diffusion of salt. The magnitudes of other terms are shown in Table B.6 of Appendix B. For the slope region (Figure 3.13b), the imbalance in the mean salt budget is again larger than that of the shelf, similar to the mean heat budget. The important information from the salt budget is that it confirms the dominant role of the horizontal advection in the annual mean heat budget on the Scotian Shelf.

3.10.2 Seasonal Heat and Salt Budget

The seasonal estimates of the heat and salt budget are summarized in Figures 3.14 and 3.15

This is a polar plot of the amplitude and phase of the terms in (3.1) and (3.2). Each term is represented by a segment, the length of which is proportional to the amplitude of the term. In the figures the amplitude of $\partial H/\partial t$ (and $\int_{-h}^{0}(\partial S/\partial t)\,dz$) is represented by line OL. The vector sum of the terms on the right hand side of (3.1) (and (3.2)) is represented by line OD. For a perfect balance in the seasonal heat (and salt) budget, the points L and D should converge. Where the two points do not meet, the distance between them gives the amplitude of the imbalance in the seasonal heat (and salt) budget.

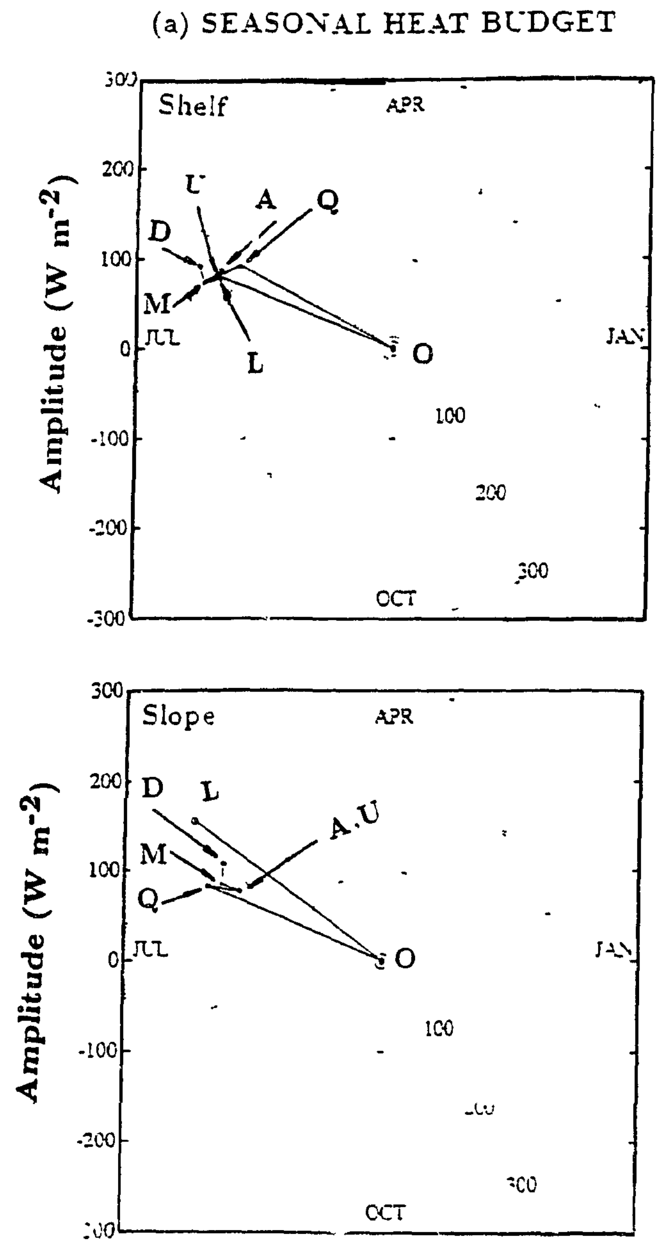

OL= ∂H/∂t
OQ=Q
QA=Horizontal advection

AU=Upwelling
UM=Horizontal mixing
MD=Vertical diffusion

Figure 3 14: Polar plots showing the amplitudes and phases of the terms in the heat budget, for the shelf and slope regions.

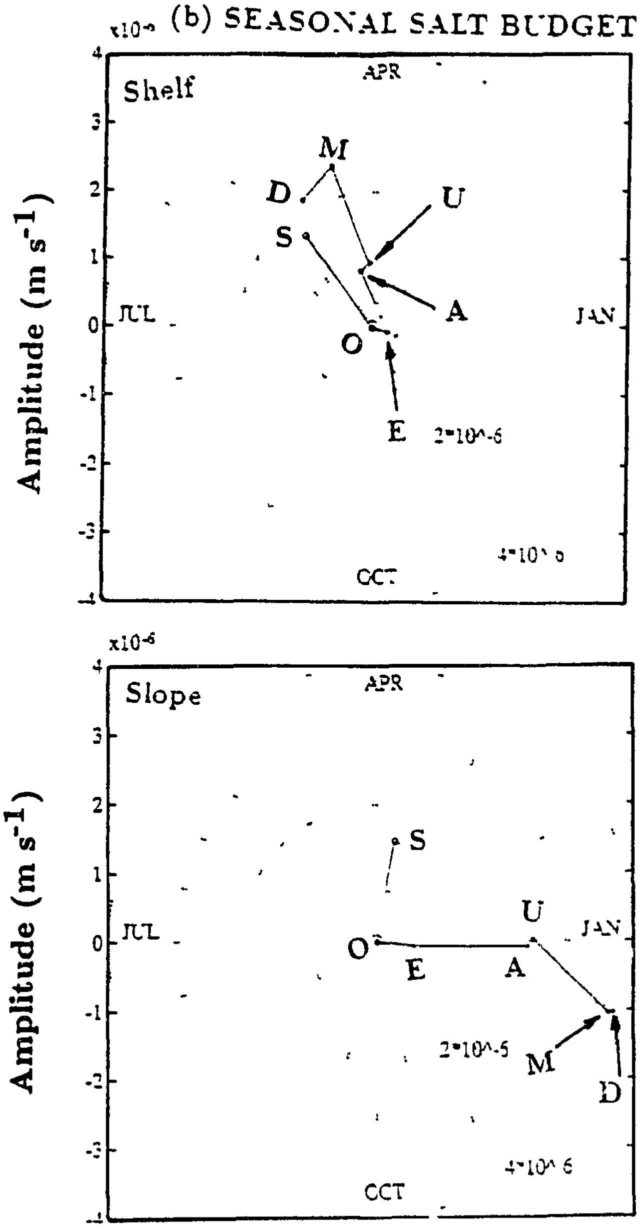

OS= $\int_{-h}^{0} \partial S/\partial t \, dz$
OE= S_0(E-P)
EA=Horizontal advection
AU=Upwelling
UM=Horizontal mixing
MD=Vertical diffusion

Figure 3.15: Polar plots showing the amplitudes and phases of the terms in the salt budget, for the shelf and slope regions.

(a) Seasonal Heat Budget

For the shelf region (Figure 3.14), the seasonal heat budget is dominated primarily by Q and secondarily by horizontal advection. The annual amplitudes of Q and the horizontal advection are 202 and 26 W m^{-2} respectively. The two terms explain best the seasonal heat budget on the shelf. Of the 202 W m^{-2} annual amplitude of $\partial H/\partial t$, the amplitude of the vector sum of the two terms accounts for 219 W m^{-2}. The inclusion of other terms (upwelling, horizontal mixing and vertical diffusion of heat from the deep ocean) does not improve the heat budget. The amplitudes and phases of the terms in the heat budget are listed in columns 4 and 5, Table B.4 of Appendix B. For the slope region (Figure 3.14), the seasonal heat budget is not as good as that on the shelf. The reasons for this will be discussed in section 3.10.3 below.

(b) Seasonal Salt Budget

The seasonal estimates of the terms in the salt budget for the shelf and slope regions are shown in Figure 3.15. The main feature of the budget is that on the shelf region (subarea A8), horizontal advection and vertical diffusive flux of salt from the deep ocean are important. Horizontal mixing is stronger on the slope than on the shelf (see Table B.6, columns 4 and 5, of for the amplitudes and phases of the terms). The contribution of evaporation minus precipitation (E-P) is negligible for both the shelf and slope. The plots of the seasonal estimates of the terms in the heat and salt budget for subareas A7, A8, A10 and A15 are shown in Figures B.4-B.7 of Appendix B. The analyses of the heat and salt budget show that the balance in the seasonal salt budget is not as good as that of the seasonal heat budget. The reasons for this will be discussed below.

3.10.3 Sources of Error

The imbalance (i.e., the left hand side of (3.1) minus its right hand side) for the shelf seasonal heat budget is about 15% of $\partial H/\partial t$. The imbalance may be caused by different factors, one of which is error in the data (temperature, salinity, Q, etc.)

used in the analysis. In many subareas there were very few observations used to form the monthly mean. For Emerald Basin, the error in the monthly mean temperature, (estimated by $s/\sqrt{n}$, where s and n are the sample standard deviation and the number of observation) creates an error in $\partial H/\partial t$ of about $18 - 50$ W m^{-2}. Again, in the monthly temperature data, no attempt was made to reduce all the data to the same reference time in the month. It is known that the temperature variability within a given month can be as high as $5°C$. Hence, a monthly mean temperature using the data collected in January 1 (for example) will be different from that sampled in January 30. Where it is feasible, a proper thing to do might be to use the data collected (or interpolated) in the middle of the month, say January 15, as a monthly mean. This will reduce the biases in the monthly mean temperatures. In the present analyses, it is not possible to do this because the number of observations in a month is very few.

Another important source of error arises from the estimate of Q. As mentioned before, *Isemer and Hasse [1987]* used a polynomial interpolation scheme to interpolate *Bunker's [1976]* original data onto a 1° grid. Although it is difficult to estimate the magnitude of this error, it is obvious that the interpolation scheme will introduce some error into the data used to estimate Q.

In addition to error in T, S and Q, the fact that constant K_x, K_y and K_v are used in the estimates could introduce another error in the budget. In reality the $K's$ vary seasonally. It appears that constant $K's$ could balance the annual mean heat budget on the shelf, but they are not good enough to balance the seasonal heat budget. For the slope region, it is not surprising that the mean and the seasonal heat budget do not balance as well as that of the shelf. In addition to the sources of error mentioned above, the values of the K_x and K_y (estimated from CASP) were meant for the shelf and not for the slope region. Since the values of the $K's$ vary spatially, it is to be expected that the estimates of the heat (and salt) budget on the slope using the $K's$ estimated for the shelf will not be as accurate as that of the shelf. It is worth mentioning here that it was not possible to estimate the $K's$ for the slope region because data for the slope region are not available.

For the salt budget, a large source of error is the (E-P) data. As described earlier, the monthly (E-P) data were obtained from *Schmitt et al.'s [1989]* three-monthly mean by fitting an annual cycle through it. These data were sufficient for my purpose, since the salt budget is taken as control to the heat budget.

3.10.4 Implications of the Heat Budget

The fact that the estimates of the terms in the heat budget for the shelf are different from those on the slope region clearly shows that the dominant physical processes operating on the shelf are different from those on the slope region. Very importantly, it is shown that on the Scotian Shelf (where there is a good balance in the heat budget), about 85% of the seasonal $\partial H/\partial t$ may be accounted for by Q. The close agreement between $\partial H/\partial t$ and Q encourages the use of a modified one-dimensional heat diffusion model on the shelf to study the seasonal variability of the water temperature on the Scotian Shelf. The vertical one-dimensional heat diffusion model is modified to include horizontal advection and mixing.

3.11 Summary

The long term annual mean heat budget on the Scotian Shelf has been balanced to within ± 2 W m^{-2}. (Such an excellent balance may be fortuitous, given the error in the data.) The main term is horizontal advection, with a contribution of about -40 W m^{-2} (of which alongshore horizontal advection accounts for about -27 W m^{-2}). The net surface heat flux contributes about 25 W m^{-2}. There is much scatter in the estimates of the seasonal heat budget in both the Scotian Shelf and slope region. However, for the shelf region, the analysis shows that the best explanation of the seasonal heat budget comes from a combination of Q and horizontal advection. About 85% of the spatial averaged $\partial H/\partial t$ may be explained by Q. Out of the 222 W m^{-2} amplitude of $\partial H/\partial t$, the amplitude of the vectorial sum of Q and horizontal advection accounts for 219 W m^{-2}. The inclusion of other processes (upwelling, horizontal mixing and vertical diffusion of heat from the deep water) does not improve the budget. The amplitude of the imbalance is about 25 W m^{-2}, which is much larger than the amplitude of the difference between $\partial H/\partial t$ and that of $Q - \rho c_p \int_{-h}^{0} \underset{\sim}{u} \cdot \nabla T \, dz$.

The annual mean salt budget on the Scotian Shelf, like the mean heat budget, is successfully balanced. The dominant role of horizontal advection that is seen in the mean heat budget is again seen in the mean salt budget.

On the contribution of the vertical one-dimensional processes, the analysis shows that about 80% of $\partial H/\partial t$ may be explained by $Q - \rho c_p \int_{-h}^{0} w(\partial T/\partial z) \, dz - K_V(\partial T/\partial z)|_{-h}$ on the Scotian Shelf. This means that to fully describe the seasonal temperature variability on the shelf, other processes must be added to the one-dimensional heat diffusion model. This leads to the use of a modified vertical one-dimensional heat diffusion model to study the evolution of the surface and subsurface seasonal temperature on the Scotian Shelf. The model is modified to include horizontal advection and mixing. Details are described in the next chapter.

Chapter 4

ESTIMATION OF VERTICAL EDDY DIFFUSIVITY

4.1 Justification for Using Seasonal $K_V(z,t)$

The primary purpose of this chapter is to estimate vertical eddy diffusivity $K_V(z,t)$ on time and space scales appropriate for a model to study the seasonal cycle and interannual variability of the surface and subsurface temperature structure of the top 75 m of the Northwest Atlantic. An efficient model for the seasonal cycle and interannual variability requires temporally averaged inputs. In this thesis, a model will be developed that is driven by monthly mean inputs and will be used specifically to hindcast the interannual variability in the surface and subsurface temperature. In addition to surface forcing, the model also needs monthly mean distributions of the eddy diffusivity with water depth and season.

The main reason for using seasonal eddy diffusivities concerns the unavailability of hourly (or even weekly) hydrographic and meteorological data in the study area, that could be used in the mixed layer models to simulate the sea surface temperature. Mixed layer models [e.g., *Price et. al.,1986, 1987; Gaspar, 1988*] have had some success in simulating the sea surface temperature. However, these models can not be used to simulate the subsurface temperature, which is a major goal of this study.

Furthermore, these models require atmospheric forcing terms averaged over a short time (hours to days). Therefore, the models can not be applied in the present study to investigate the interannual variability, as there are insufficient atmospheric data to define the surface forcing in such short time scales, over many years, in the study area.

In the following subsections, a review of some approaches that have been used to estimate the vertical eddy diffusivity will be given. This will be followed by a presentation of some new methods and discussion of their limitations and advantages. It will be shown that the parameterization $K_V(z,t) = K_O/(1 + \alpha N^p)$ provides an effective way of estimating eddy diffusivities in the upper ocean, where the source of energy for mixing includes wind stirring and buoyancy flux.

4.2 Past Parameterizations of K_V

Munk and Anderson [1948] pointed out that the eddy diffusivity depends on the stability of the water column and thus "may vary with time and position". The stability of the water column is usually measured in terms of the buoyancy frequency

$$N^2 = -\frac{g}{\rho_o}\frac{\partial \rho}{\partial z} \tag{4.1}$$

where g is the acceleration due to gravity, ρ is the water density and ρ_o a reference water density.

Munk and Anderson [1948] proposed the following formula for the upper ocean

$$K_V = \frac{K_O}{(1 + \beta Ri)^n} \tag{4.2}$$

where

$$Ri = \frac{N^2}{(\partial u/\partial z)^2} \tag{4.3}$$

is the gradient Richardson number. $\partial u/\partial z$ is the vertical current shear and K_O is the coefficient of eddy diffusivity when the vertical density gradient is zero. β and n are constants to be determined. Equation (4.2) requires that when R_i is very high, K_v varies as Ri^{-n}.

Henderson-Sellers [1982] modified (4.2) to the form

$$K_v = \frac{K_0}{\left(1 + 37Ri^2\right)} \tag{4.4}$$

He reported that (4.4) agreed well with observations, in the upper ocean.

Gargett [1984] suggested that in stably stratified regions where mixing is accomplished by only internal waves, one can parameterize the eddy diffusivity as

$$K_v = a_0 N^{-q} \tag{4.5}$$

where

$$a_0 = \frac{R_f \epsilon_0}{1 - R_f}.$$

Here R_f is the flux Richardson number and ϵ_0 is the rate of dissipation of kinetic energy. *Gargett [1984]* suggested that $0.5 \leq q \leq 1.0$, but for (4.5) to be dimensionally consistent q has to be 2. This functional dependence of K_v on N has been found to hold in stratified systems such as lakes and fjords [e.g., *Jassby and Powell, 1975*] and partially enclosed seas [e.g., *de Young and Pond, 1988*].

Parameterizations of K_v that are useful to the present study are those that apply to the upper ocean which is not always strongly stratified and the energy source for mixing is mostly from wind mixing and buoyancy flux. Equation (4.4), which is a version of (4.2), is a good choice. But to use (4.4), one needs vertical current shear. Although (4.2) and (4.4) have been useful in estimating the eddy diffusivity, it can not be applied in a study involving interannual variability (such as the present one), since it is very difficult to obtain a time series (for many years, as function of depth) of water velocity, that could be used to estimate $\partial u/\partial z$. To get over this difficulty, I simplify (4.4) to the form

$$K_v = K_0[1 + \alpha N^p]^{-1} \tag{4.6}$$

where $\alpha \equiv 37/\left(\partial u/\partial z\right)^p$ with $p = 4$ in *Henderson-Seller's* formulation. Thus $\partial u/\partial z$ is not explicitly represented in the model but it is embodied in α. My task then is to estimate the parameters p, K_0 and α that produce the "best" values of $K_V(z,t)$. The different approaches used to obtain the best estimate of the parameters are described below.

4.3 New Methods of Estimating $K_V(z,t)$

Based on the heat budget for the outer Scotian Shelf *[Umoh and Thompson, 1990]*, I assume

$$\frac{\partial T}{\partial t} = \frac{\partial}{\partial z}\left(K_V \frac{\partial T}{\partial z}\right) + \Gamma(z,t) \tag{4.7}$$

where $\Gamma(z,t)$ is a heat source/sink term that represents the small net contribution from horizontal advection, upwelling and mixing to the temperature equation. (Recall from Chapter 3 that $\int_{-h}^{0} \Gamma(z,t)\,dz$ is about 15% of the depth-integrated seasonal heat budget). Notice that (4.7) is a one-dimensional temperature diffusion equation that has been modified to include the imbalance between the $\partial H/\partial t$ and $Q - K_V \partial T/\partial z|_{-h}$.

Three methods of estimating $K_V(z,t)$ will be described. The methods depend on how $\Gamma(z,t)$ is represented in (4.7). In the first method, $K_V(z,t)$ is obtained by prescribing a functional form for $\Gamma(z,t)$. In the second method, $K_V(z,t)$ is computed by minimizing $\int_{z}^{0} \Gamma(z,t)\,dz$. In the third method, K_V is estimated by distributing $\int_{-h}^{0} \Gamma(z,t)\,dz$ obtained from the heat budget with depth, and minimizing the error between the observed and the predicted temperature. The third method is also modified to estimate the best constant K_V. It will be shown that the $K_V(z,t)$ from the last two methods produce the best $T(z,t)$, although all three methods give qualitatively similar results.

4.3.1 Method 1: Estimation of $K_V(z,t)$ with a Simple Heat Source/Sink

Assume that the heat source/sink, $\Gamma(z,t)$, can be written as

$$\Gamma(z,t) = \zeta(z)\gamma(t) \tag{4.8}$$

Then (4.7) becomes

$$\frac{\partial T}{\partial t} = \frac{\partial}{\partial z}\left(K_V \frac{\partial T}{\partial z}\right) + \zeta(z)\gamma(t) \tag{4.9}$$

Depth-integrating (4.9) from $z = -h$ to z:

$$\frac{\partial}{\partial t}\int_{-h}^{z} T\,dz = K_V \frac{\partial T}{\partial z}\bigg|_{z} + \gamma(t)\int_{-h}^{z} \zeta\,dz - K_V \frac{\partial T}{\partial z}\bigg|_{-h} \tag{4.10}$$

Taking $z = 0$ in (4.10) gives

$$\frac{\partial}{\partial t}\int_{-h}^{0} T\,dz = \frac{Q}{\rho c_p} + \gamma(t)\int_{-h}^{0} \zeta\,dz - K_V \frac{\partial T}{\partial z}\bigg|_{-h} \tag{4.11}$$

From (4.11) one obtains

$$\gamma(t) = \frac{1}{\int_{-h}^{0} \zeta\,dz}\left[\frac{\partial}{\partial t}\int_{-h}^{0} T\,dz - \frac{Q}{\rho c_p} + K_V \frac{\partial T}{\partial z}\bigg|_{-h}\right] \tag{4.12}$$

Substituting (4.12) into (4.10) one has

$$K_V \frac{\partial T}{\partial z}\bigg|_{z} = \left[\frac{Q}{\rho c_p} - \frac{\partial}{\partial t}\int_{-h}^{0} T\,dz\right]\zeta_s + \frac{\partial}{\partial t}\int_{-h}^{z} T\,dz + (1-\zeta_s)\,K_V \frac{\partial T}{\partial z}\bigg|_{-h} \tag{4.13}$$

where

$$\zeta_s = \frac{\int_{-h}^{z} \zeta\,dz}{\int_{-h}^{0} \zeta\,dz} \tag{4.14}$$

From the seasonal heat budget of Chapter 3, the last term on the RHS of (4.13) is about 24% of the second term on the RHS (see Figure 3.14 of Chapter 3), compared with the first term on the RHS, which is about 80% of the second term. Based on the heat budget, the last term on the RHS of (4.13) is therefore neglected. From (4.13) the diffusivity may then be expressed as

$$K_V(z,t) = \frac{\left[\frac{Q}{\rho c_p} - \frac{\partial}{\partial t}\int_{-h}^{0} T\,dz\right]\zeta_s + \frac{\partial}{\partial t}\int_{-h}^{z} T\,dz}{\left.\frac{\partial T}{\partial z}\right|_z} \tag{4.15}$$

In the computation, I assume $\zeta \propto e^{z/\delta}$, and hence

$$\zeta_s = \frac{e^{z/\delta} - e^{-h/\delta}}{1 - e^{-h/\delta}} \tag{4.16}$$

Notice in (4.13) that if the net surface flux equals the local rates of heat storage (i.e. $Q = \rho c_p \partial/\partial t \int_{-h}^{0} T\,dz$), the source term $\Gamma(z,t)$ is zero. The role of the term proportional to ζ_s in (4.15) is to distribute the imbalance with depth. In this method, it is worth stressing that $K_V(z,t)$ is computed directly from the data, with no assumptions made about its functional form. This method is similar to that of *de Young and Pond [1988]*, but has been modified to take account of the imbalance in the one-dimensional temperature equation that may be caused by horizontal advection, upwelling and mixing.

Throughout this chapter, the vertical diffusivities are computed at depths of 5, 15, 25, 40 and 62.5 m which are the mid-depths of 0, 10, 20, 30, 50, 75 m where the temperature and salinity data are collected.

The monthly estimates of the $K_V(z,t)$ for subareas A7 and A8 are shown in Table 4.1 for δ = 30 m. The results show both seasonal and depth variations in $K_V(z,t)$. Figure 4.1a shows the seasonal variation of K_V at 15 m and 62.5 m depths, for subarea A8. The diffusivity is greater in winter than in summer. At 15 m depth (subarea A8), a value of 16.4×10^{-4} m^2 s^{-1} is obtained in February whereas it is 0.2×10^{-4} m^2 s^{-1} in August. The diffusivities also vary with depth; in January K_V decreases from 21.8×10^{-4} m^2 s^{-1} at 15 m depth to 0.2×10^{-4} m^2 s^{-1} at 40 m depth. Figure 4.1b shows the plot of K_V versus N^2, for subarea A8. Large values of N^2 are associated with low K_V, and vice versa, but the large scatter in the plot makes it difficult to establish a precise relationship between the K_V and N^2.

(a) Subarea A7

Depth (m)	Jan	Feb	Mar	Apr	May	Jun	Jul	Aug	Sep	Oct	Nov	Dec
5	-9.9	80.3	-4.9	5.7	7.5	5.2	3.1	1.9	2.7	-1.9	-11.1	-4.5
15	68.0	10.1	-6.6	12.8	3.7	1.3	0.7	0.5	1.0	1.7	-11.0	8.0
25	13.7	7.6	-4.3	91.8	4.5	0.7	0.4	0.5	0.4	1.2	10.2	9.9
40	0.9	1.4	-1.7	-72.9	1.6	0.2	1.0	0.7	0.1	0.7	2.7	2.4
62.5	-0.6	-0.4	-1.1	-1.7	-3.1	1.4	-2.7	-0.6	-1.8	0.8	6.4	20.9

(b) Subarea A8

Depth (m)	Jan	Feb	Mar	Apr	May	Jun	Jul	Aug	Sep	Oct	Nov	Dec
5	76.1	15.2	2.8	6.7	18.3	13.0	1.6	1.5	1.6	-25.0	8.4	-8.5
15	21.8	15.5	-7.0	13.8	3.5	1.0	0.8	0.4	0.4	1.4	20.3	19.5
25	11.6	8.1	-2.2	69.8	2.0	0.7	0.8	0.5	0.0	0.1	27.8	3.3
40	0.2	4.4	-1.6	16.9	0.8	0.5	2.2	1.5	-0.7	-0.2	1.3	6.3
62.5	-2.4	1.4	-1.3	-1.0	0.1	-0.5	-7.7	-7.0	7.5	-14.7	1.4	8.1

Table 4.1: Estimates of $K_V(z,t)$ in $\times 10^{-4}\mathrm{m}^2\mathrm{s}^{-1}$ from Method 1.

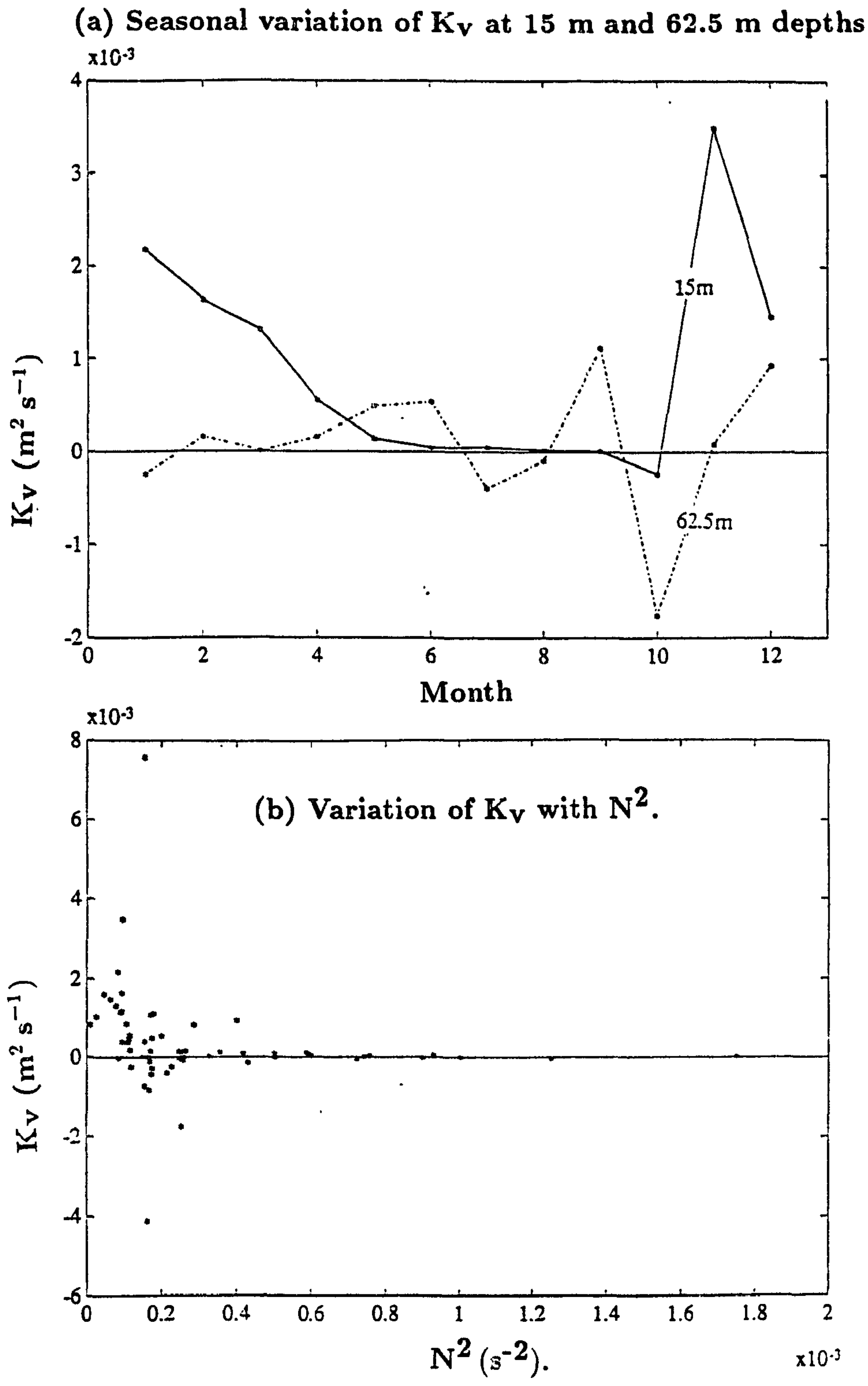

Figure 4.1: Variation of $K_V(z,t)$ in $\times 10^{-4}\, m^2 s^{-1}$ with (a) season and (b) depth from Method 1 for subarea A8.

This method works well (by producing positive $K_v's$) provided the vertical temperature gradient is strong, as expected from (4.15). Where the temperature gradient is weak, unphysical values of $K_V(z,t)$ (negative and abnormally high values) are obtained. To eliminate this problem, two new methods of estimating the eddy diffusivities are now presented.

4.3.2 Method 2: Estimation of $K_V(z,t) = K_O\left(1+\alpha N^p\right)^{-1}$ by Minimizing the Imbalance in the Heat Budget

Depth-integrating (4.7) from some depth z to the surface gives

$$\frac{Q}{\rho c_p} - \frac{\partial}{\partial t}\int_z^0 T\,dz = K_V \frac{\partial T}{\partial t}\bigg|_z - \int_z^0 \Gamma(z,t)\,dz \tag{4.17}$$

Equation (4.17) states that the difference between the net surface heat flux and local changes in the depth-integrated temperature between some depth z and the surface is equal to the difference between the vertical diffusive flux at z and the depth-integrated source-sink term.

The next step is to substitute (4.6), my assumed expression for $K_V(z,t)$ into (4.17) to obtain

$$\frac{Q}{\rho c_p} - \frac{\partial}{\partial t}\int_z^0 T\,dz = K_O\left(1+\alpha N^p\right)^{-1}\frac{\partial T}{\partial z}\bigg|_z - \int_z^0 \Gamma\,dz \tag{4.18}$$

For convenience, let

$$\begin{aligned} Y &= \frac{Q}{\rho c_p} - \frac{\partial}{\partial t}\textstyle\int_z^0 T\,dz, \\ X &= \left(1+\alpha N^p\right)^{-1}\frac{\partial T}{\partial z}\bigg|_z, \end{aligned}$$

and

$$\epsilon = -\int_z^0 \Gamma\,dz$$

Then (4.18) can simply be written as

$$Y = K_O\,X + \epsilon \tag{4.19}$$

(a) $p = 2$

Subarea	$K_O \times 10^{-4}\,(\mathrm{m^2\,s^{-1}})$	$\alpha_C \times 10^4\,\mathrm{s^2}$	R^2
A7	2.0	0.25	0.32
A8	21.0	5.50	0.32

(b) $p = 4$

Subarea	$K_O \times 10^{-4}\,(\mathrm{m^2\,s^{-1}})$	$\alpha_C \times 10^4\,\mathrm{s^2}$	R^2
A7	1.5	170.00	0.32
A8	1.7	330.00	0.25

Table 4.2: Variation of K_O and α_c for $p = 2$ and 4 from Method 2, at subareas A7 and A8

N is computed from the density field and thus X and Y are known from observations, at six depths for each month of the year, if we fix α and p. Thus one can treat (4.19) as a simple regression model. For a fixed p, K_O and α_c are determined by using a least squares method to minimize ϵ. Physically, minimum ϵ corresponds to the smallest value of $\int_z^0 \Gamma\, dz$ (i.e. advection, upwelling and mixing) that must be added to the vertical one-dimensional heat diffusive processes to account for the temperature variability. An estimate of the model fit is expressed by the square correlation coefficient

$$R^2 = \frac{\sum \hat{Y}_i^2}{\sum Y_i^2} \tag{4.20}$$

where

$$\hat{Y} = K_O X$$

The best estimates of K_O, α and p are those which give maximum R^2. The critical value of α, that results in maximum R^2, is referred to as α_c (Figure 4.2a).

Results for Method 2

(i) Variation of K_O with α_c

Table 4.2 shows the estimates of K_O and α_c, for $p = 2$ and 4, and their correspond-

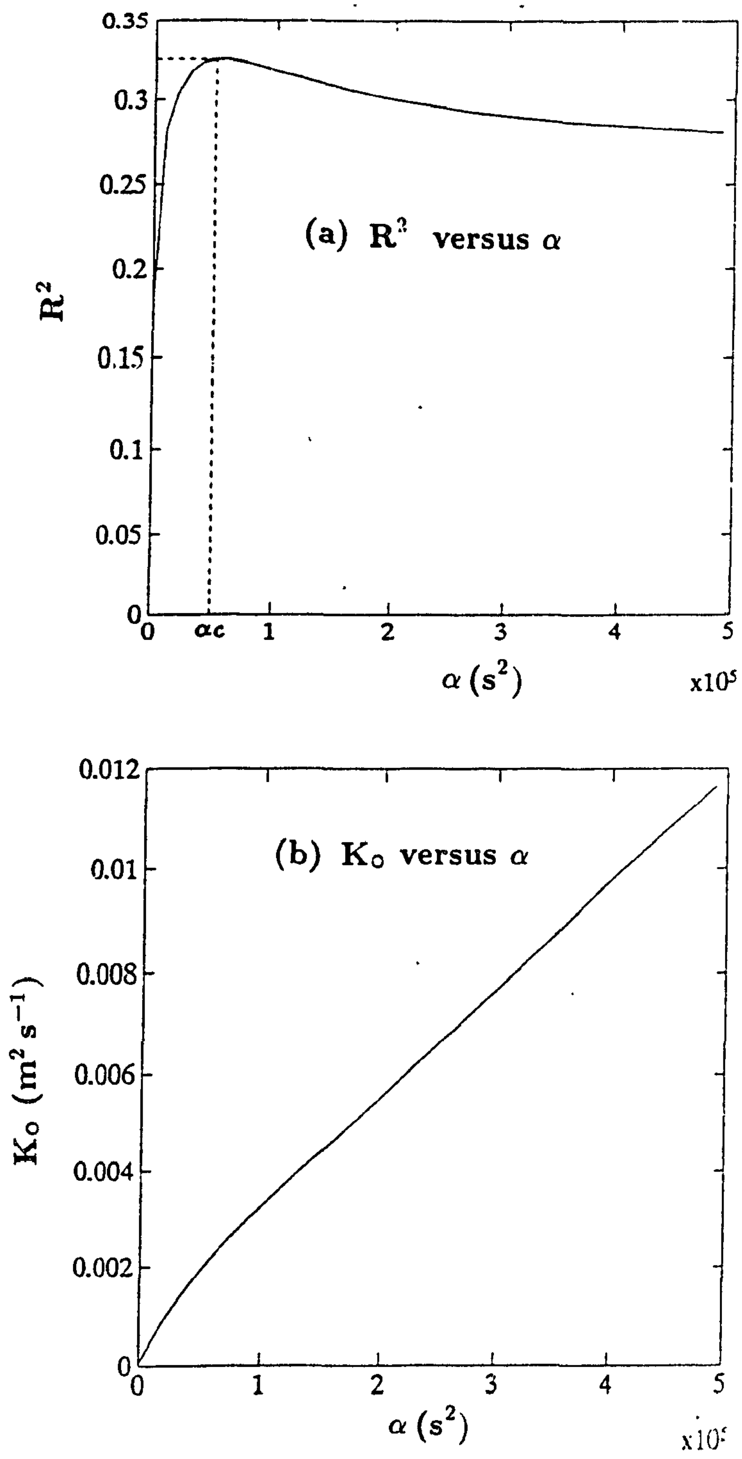

Figure 4.2: (a) A plot of R^2 versus α for $p = 2$ at subarea A8, showing how α_c is obtained. (b) A typical plot of K_O against α for $p = 2$, indicating that K_O and α covary.

Depth (m)	Jan	Feb	Mar	Apr	May	Jun	Jul	Aug	Sep	Oct	Nov	Dec
5	2.2	5.8	2.0	2.9	3.4	13.4	0.6	0.6	1.1	2.1	8.5	2.2
15	3.7	3.4	4.0	2.8	1.4	0.6	0.4	0.2	0.4	2.8	3.3	4.6
25	3.5	3.0	3.3	2.0	1.4	0.7	0.5	0.5	0.3	0.4	2.2	3.7
40	2.3	2.9	2.8	2.1	2.0	1.4	1.0	1.4	0.9	0.5	0.7	1.3
62.5	1.6	1.4	2.0	2.0	2.0	1.8	1.6	2.0	1.9	1.4	0.9	0.9

Table 4.3: Estimates of $K_V(z,t) = K_O\left(1+\alpha N^2\right)^{-1}$ in $10^{-4}\ m^2\ s^{-1}$ from Method 2 at subarea A8. $K_O = 21.0 \times 10^{-4}$ m^2 s^{-1} and $\alpha_c = 5.50 \times 10^4$ s^2.

ing R^2, for subareas A7 and A8. For subarea A8, the estimate of the parameters for $p = 2$ has a larger correlation coefficient R^2 than for $p = 4$. For subarea A7, R^2 for $p = 2$ and 4 are the same. Figure 4.2b shows a typical relationship between K_O and α_c, for $p = 2$ (subarea A8). The main point from the figure is that K_O and α_c covary; thus a large value of K_O can be compensated by a large value of α_c to produce the same diffusivity.

(ii) Dependence of K_V on N^2

Figure 4.3a shows the seasonal variation of N^2 with depths, for subarea A8. The values of the $K_V(z,t)$ estimated for $p = 2$ are presented in Table 4.3. Figure 4.3b shows the plot of K_V against N^2 for all depths (5, 15, 25, 40 and 62.5 m) and seasons, for subarea A8. The K_V ranges from 0.2×10^{-4}m^{2}s^{-1} to 13.4×10^{-4}m^{2}s^{-1}. The points corresponding to February and August, at 5 m depth, are marked for comparison. At 5m depth, for example, the buoyancy frequency is smaller in February than in August and hence the eddy diffusivity is larger in February than in August.

(iii) Predicted Temperature using the $K_V(z,t)$

To assess the performance of the model, I have shown in Figure 4.4b, the predicted surface and subsurface temperature structure using the K_V estimated for $p = 2$ from Method 2. I have also presented the observed temperature structure (Figure 4.4a) for comparison. Notice the weak temperature gradient in winter and the strong one in summer, in both the predicted and the observed temperature structure. Though

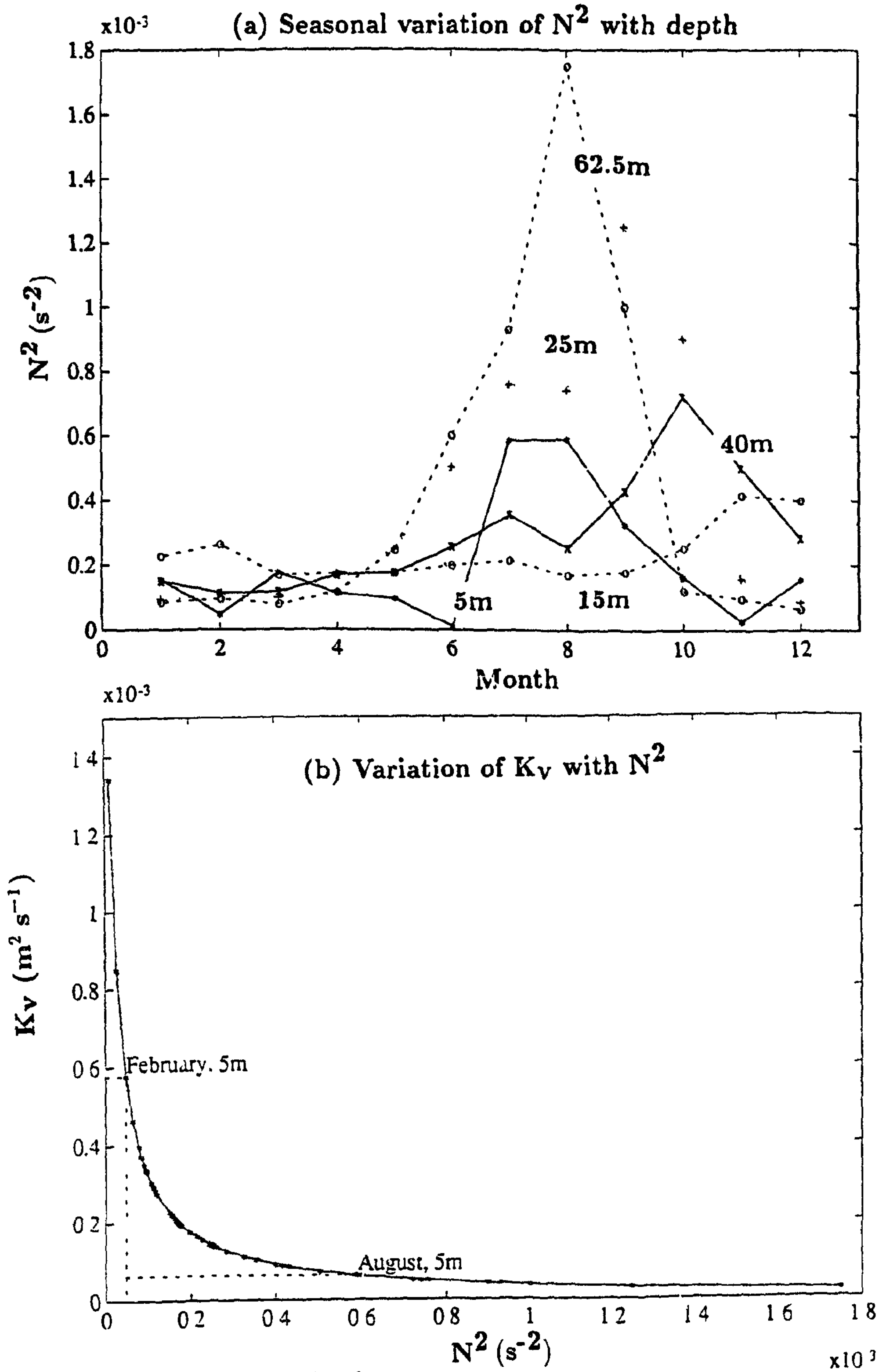

Figure 4.3: The variation of (a) N^2 with depth and (b) K_v with N^2 in Method 2, for subarea A8. The dotted lines show the K_v and the corresponding N^2 in February and August, at 5 m depth The stars are the predicted diffusivities.

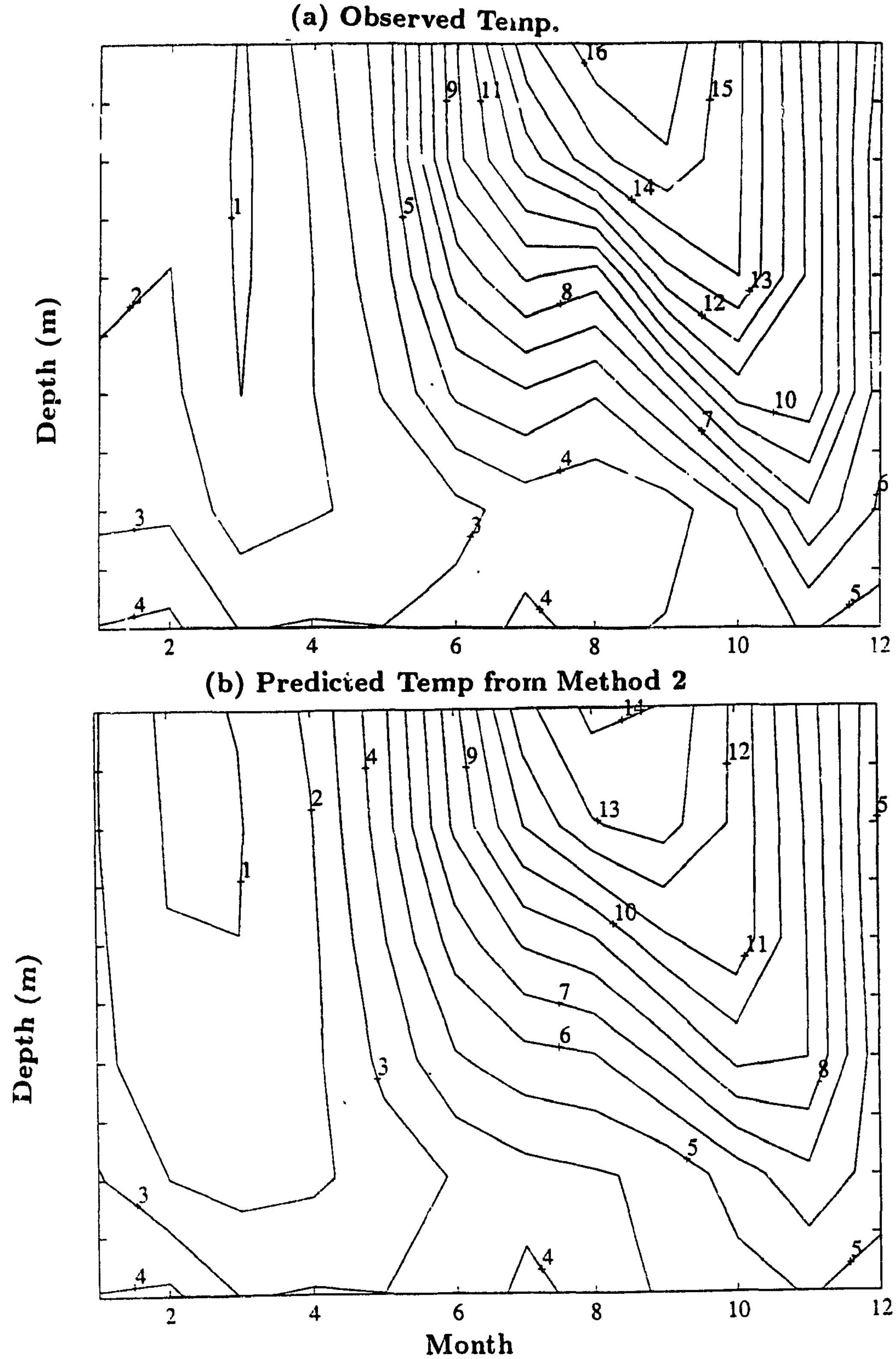

Figure 4.4: The comparison between (a) observed $T(z,t)$ and (b) predicted $T(z,t)$ from $K_V(z,t) = K_0/\left(1+\alpha N^2\right)$ in Method 2.

the model slightly underestimates the surface temperature in summer, on the whole the model temperature compares well with observations.

4.3.3 Method 3: Estimation of $K_V(z,t) = K_O(1+\alpha N^p)^{-1}$ by Minimizing Temperature Error

In this method, (4.7) is still used. It is similar to Method 2 in that 3 free parameters - K_O, α and p - are used. This method differs from the last method, essentially, in what is minimized. In Method 2, $\int_z^0 \Gamma(z,t)\, dz$ is minimized by least squares. In this method, the error between the observed and the predicted temperature is minimized. As in the first method, I prescribe a functional form which distributes $\Gamma(z,t)$ with depth as

$$\Gamma(z,t) = \zeta_s \left[\frac{\partial}{\partial t} \int_{-h}^{0} T\, dz - \frac{Q}{\rho c_p} + K_V \frac{\partial T}{\partial z}\bigg|_{-h} \right] \tag{4.21}$$

where

$$\zeta_s = \frac{\zeta(z)}{\int_{-h}^{0} \zeta\, dz} \tag{4.22}$$

and $\zeta = c_o e^{z/\delta}$, as in the first method. δ is estimated from the vertical correlation scale of the seasonal temperature profile. That is, I computed the correlation coefficient, R, between the seasonal temperature at depth z (from 0 to 75 m). From the plot of $R = r_o e^{z/\delta}$ against z, δ is estimated. In the following analysis, $\delta = 30$ m is used. Thus (4.21) provides a way of distributing the imbalance in the seasonal heat budget with depth.

As in the second method, I assume that $K_V(z,t)$ is related to the buoyancy frequency N according to (4.6). Substituting this expression of $K_V(z,t)$ and into the original equation (4.7), we have

$$\frac{\partial T}{\partial t} = \frac{\partial}{\partial z} \left[K_O \left(1+\alpha N^p\right)^{-1} \frac{\partial T}{\partial z} \right] + \Gamma(z,t) \tag{4.23}$$

(a) Determination of K_0, α and p

The details on the development of the modified one-dimensional heat diffusion model and how the parameters are determined are given in section C.1 of Appendix C. Briefly, the following steps are taken:

Step 1: Write (4.23) in finite difference form, using the Crank-Nicholson finite difference scheme. The Crank-Nicholson scheme is second-order accurate in both space and time, and stable for arbitrarily large time steps *[Press et al., 1986]*. The model is forced at the surface with the net surface heat flux and at $z = -h$ with the observed temperature. The finite differencing scheme reduces to a matrix equation of the form

$$\mathbf{A}^{n+1}\,\underline{\hat{T}}^{n+1} = \mathbf{B}^n\,\underline{\hat{T}}^n + \underline{F}^n \tag{4.24}$$

where n is a time index. In (4.24) bold face letters refer to matrices and the underlined letters to vectors. The matrix $\mathbf{B}^n$ contains the values of N^p and α at the depths 5, 15, 25, 40, and $62.5m$, at time step n, while the matrix $\mathbf{A}^{n+1}$ contains the values at time step $n+1$. The sixth depth is the boundary condition. The dimension of both matrices is 6×6. The vector $\underline{F}^n$ contains information on the boundary condition at the surface (Q) and at $z = -h$ together with Γ, at time step n, and has dimension 6×1.

Step 2: Choose a value of p, say 2. For that value of p, I then select α and K_0 and compute K_v according to (4.6).

Step 3: Use the computed K_v and solve the matrix equation (4.24) for $\underline{\hat{T}}$. This involves running the model for a long enough time to ensure that the predicted temperatures $\underline{\hat{T}}$ reach a periodic steady state.

Step 4: Compute the root mean square error, $E(p, \alpha, K_0)$, between the observed temperature T and the predicted temperature $\hat{T}$ over all depths and time, using the formula

$$E(p, \alpha, K_0) = \sqrt{\frac{1}{M}\sum_t \sum_z \left(T - \hat{T}\right)^2} \tag{4.25}$$

where $M = 5 \times 12$ is the total number of temperature points through depth and over one year. The above steps are repeated for different α and K_0 until a minimum E

(a) Subarea A7

p	$K_O\,(m^2\,s^{-1})$	$\alpha_C \times 10^6$	$E\,(^\circ C)$
1	0.2400	0.12	1.33
2	0.9000	20.00	0.81
4	0.0006	20.00	1.00

(b) Subarea A8

p	$K_O\,(m^2\,s^{-1})$	$\alpha_C \times 10^6$	$E\,(^\circ C)$
1	0.2000	0.12	1.79
2	0.5500	14.00	1.08
4	0.0006	20.00	1.17

(c) Subarea A15

p	$K_O\,(m^2\,s^{-1})$	$\alpha_C \times 10^6$	$E\,(^\circ C)$
2	0.9000	20.00	1.22
4	0.0009	30.00	1.30

Table 4.4: Estimates of $E(\alpha, K_O)$ for p = 1, 2, and 4, at subareas A7, A8 and A15. The units of α_c for p = 1, 2 and 4 are s^p.

is found. The value of α, referred to as α_c (as before), and the corresponding value of K_O for a chosen p, that give the minimum $E(\alpha, K_O)$ are then taken to be the best estimates used to compute $K_V(z,t)$.

(b) Results for Method 3

(i) Estimates of $E(p,\alpha,K_O)$ for p = 1, 2 and 4

I have determined the minimum $E(p,\alpha,K_O)$ for p = 1, 2 and 4 for subareas A7, A8 and A15. The results are summarized in Table 4.4. For subarea A7, when $p = 2$, the value of $E(p,\alpha,K_O) = 0.81°C$ is obtained, compared with $E(p,\alpha,K_O) = 1.00°C$ and 1.33°C when p = 4 and 1 respectively. A careful look at Table 4.4 reveals that the optimum p is in the range $2 \leq p \leq 4$. A typical contour of $E(p,\alpha,K_O)$ for p = 2, (subarea A7), is displayed in Figure 4.5. The lines show constant E. The minimum error is indicated as E in the figure. The figure clearly shows that K_O and

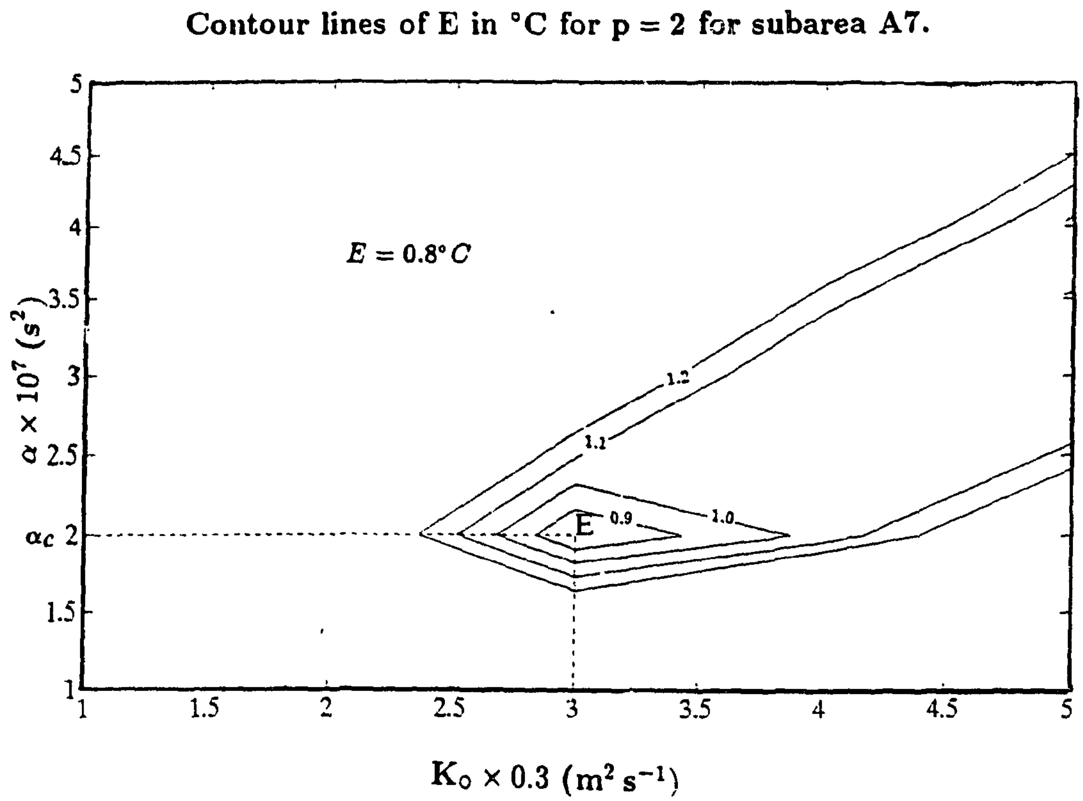

Figure 4.5: A plot showing lines of constant $E(\alpha, K_O)$ for fixed p. Note that K_O and α covary, and that there are combinations of K_O and α that can give the similar $E(p, \alpha, K_O)$.

Depth (m)	Jan	Feb	Mar	Apr	May	Jun	Jul	Aug	Sep	Oct	Nov	Dec
5	2.6	8.0	2.3	3.6	4.2	38.0	0.7	0.7	1.2	2.5	14.7	2.6
15	4.7	4.2	5.1	3.4	1.6	0.7	0.4	0.2	0.4	3.3	4.1	6.1
25	4.4	3.7	4.1	2.3	1.6	0.8	0.5	0.6	0.3	0.5	2.6	4.6
40	2.7	3.5	3.4	2.4	2.3	1.6	1.1	1.6	0.9	0.6	0.8	1.4
62.5	1.8	1.5	2.4	2.3	2.3	2.0	1.9	2.4	2.3	1.6	1.0	1.0

Table 4.5: Estimates of $K_V(z,t) = K_O\left(1+\alpha N^2\right)^{-1}$ in $10^{-4}\,m^2\,s^{-1}$ from Method 3 at subarea A8. $K_O = 0.55\,m^2\,s^{-1}$ and $\alpha_c = 1.4 \times 10^7\,s^2$.

α covary, and that there are combinations of α and K_O that can give almost the same $E(p,\alpha,K_O)$. For $\alpha N^p >> 1$, $K_V \approx (K_O/\alpha)N^{-p}$. Thus, although there are 3 free parameters, practically the model depends on the two parameters: p and K_O/α. A comparison of K_O/α for Methods 2 and 3 is given in section 4.4.

(ii) Dependence of K_V on N^2

The estimated $K_V(z,t)$ for $p = 2$ is shown in Table 4.5. The diffusivities vary both seasonally and with depth. At 15 m depth, the eddy diffusivity increases from a minimum of 0.2×10^{-4} m^2 s^{-1} in August to a maximum of 6.1×10^{-4} m^2 s^{-1} in December. In February, the diffusivity decreases with depth, from 8.2×10^{-4} m^2 s^{-1} at 5 m to 1.5×10^{-4} m^2 s^{-1} at 62.5 m depth.

The variation of K_V with N^2 for subarea A8 is presented in Figure 4.6a. Figure 4.6b shows the plot of K_V versus N^2 for subareas A7, A8 and A15. The estimates of the diffusivities in the three areas are similar.

(iii) Predicted Surface and Subsurface Temperature from the Model

The predicted temperature structure using the seasonal varying diffusivities $K_V(z,t) = K_O\,(1+\alpha N^2)^{-1}$ for subarea A8 is shown in Figure 4.7c. In September, the predicted surface temperature is 16.8°C compared with the observed temperature of 16.7°C. In January, the predicted temperature at 10 m depth is 1.5°C whereas the observed is 1.8°C. The model, however, slightly overestimates the sea surface temperature in August. On the whole, the standard deviation of the error (E) is

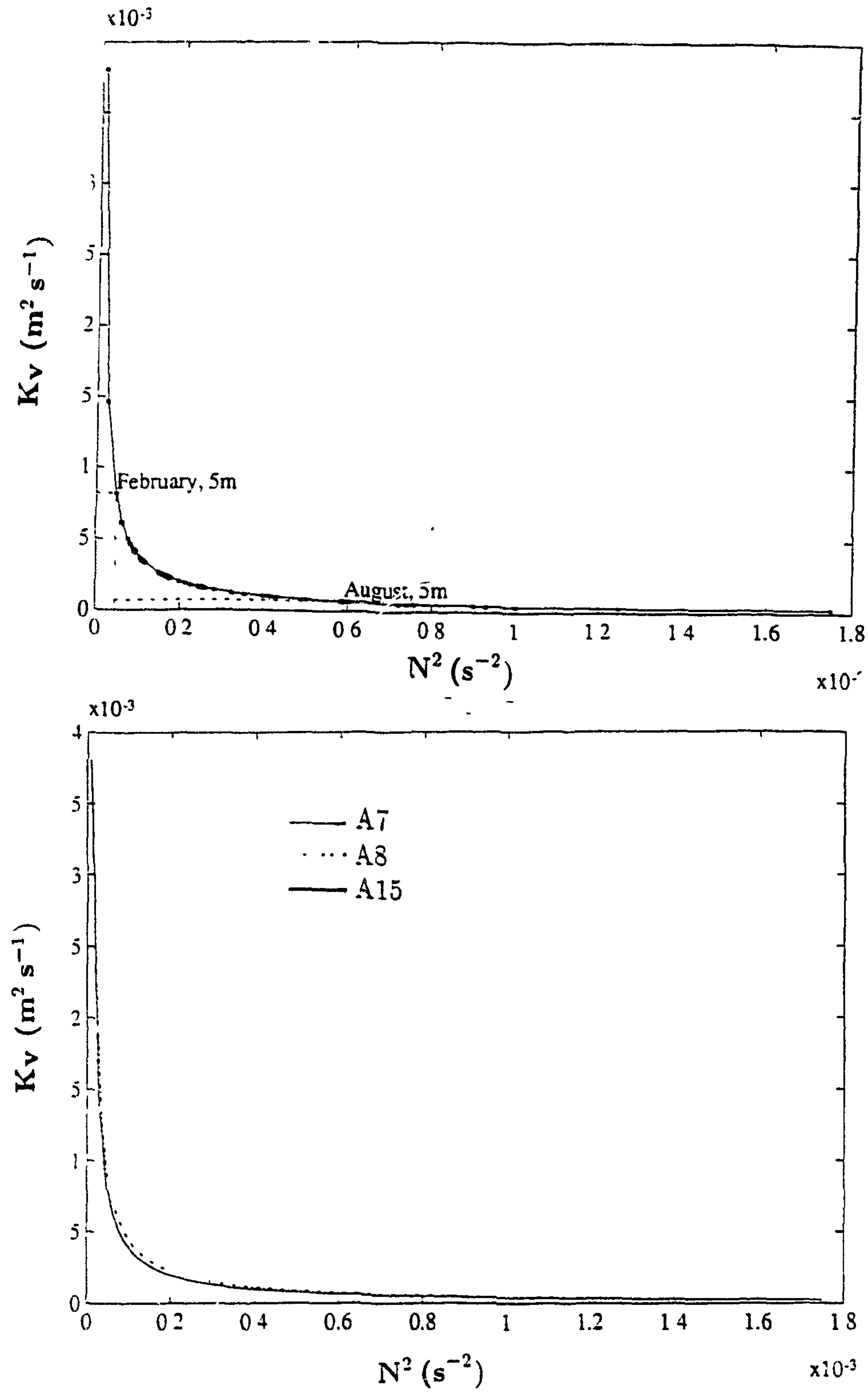

Figure 4.6: Dependence of K_v on N^2 at (a) subarea A8 and (b) subareas A7, A8 and A15, from Method 3.

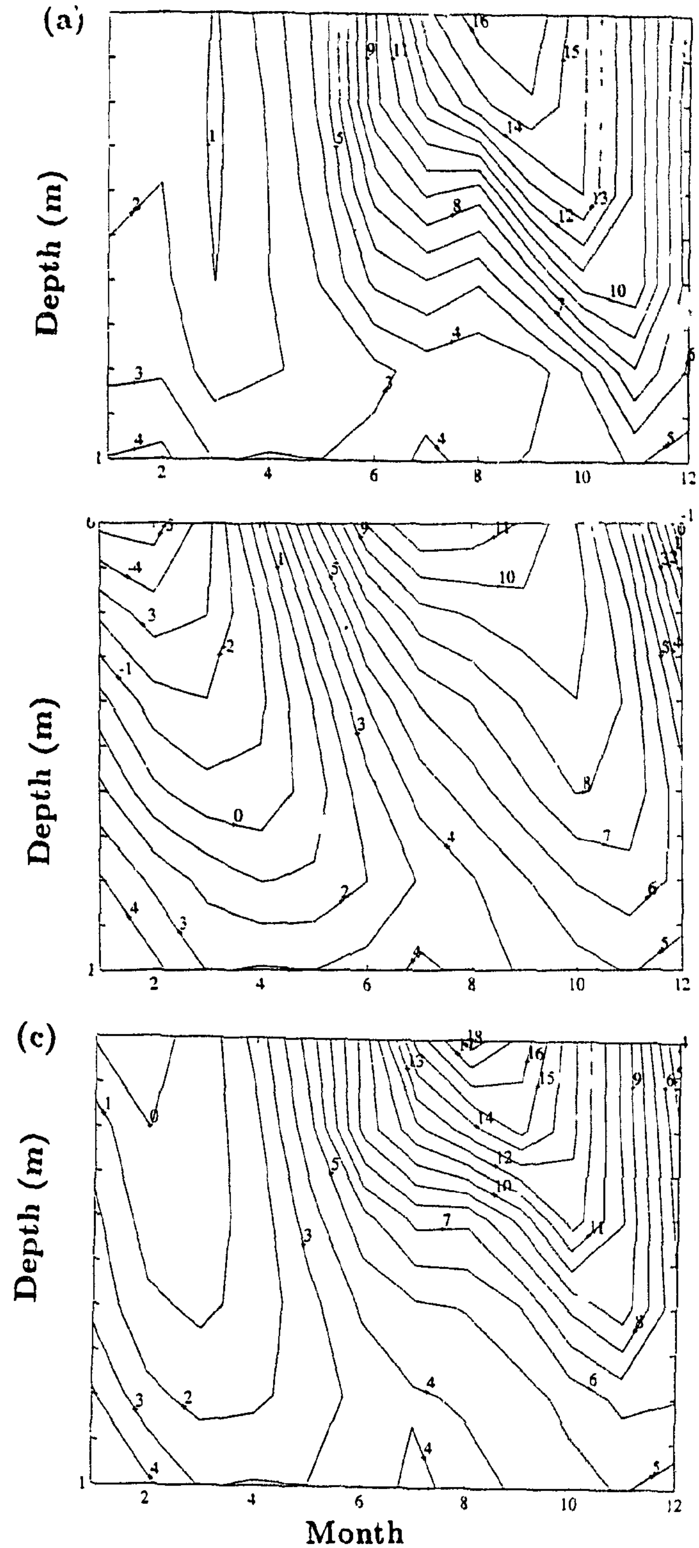

Figure 4.7: The comparison between (a) observed $T(z,t)$, (b) predicted $T(z,t)$ from a constant $K_v = 1.2 \times 10^{-4}\ m^2\ s^{-1}$, and (c) predicted $T(z,t)$ from $K_0/\left(1+\alpha N^2\right)$ from Method 3.

$1.08°C$. One advantage of this method of estimating the diffusivity is that it provides a direct measure of, and indeed the minimum, error associated with the predicted temperature.

The $E(p, \alpha, K_O)$ is comparable to the error in the temperature data. The error in the observed monthly temperature is estimated as $s/\sqrt{n}$, where s and n are the standard deviation and the number of observations in a month. In some months, $s = 2.6°C$, $n = 7$, giving an error in the temperature data of about $1\,°C$. Comparing the error in the temperature data used and the estimated $E(p, \alpha, K_O)$, we see that overall the model does as well as can be expected.

(c) Estimation of a Constant K_V

An objective method of estimating the best *constant* K_V is to determine that value of K_V that gives the minimum root mean square error, E, between the observed and the predicted temperature, for all depths and time. By setting $\alpha = 0$, the best constant K_V is obtained by simply prescribing a value for K_O and determining the corresponding error E. The best estimate of constant K_V is the K_O with the least E. Figure 4.8 shows the plot of E against K_O. The minimum $E = 3.11°C$ corresponds to a constant $K_V = 1.2 \times 10^{-4}\,\mathrm{m^2\,s^{-1}}$. For comparison, recall that for a seasonal varying $K_V(z,t)$, a much lower value of $E(p, \alpha, K_O) = 1.08°C$ was obtained.

The water temperature profile predicted by substituting a constant $K_V = 1.2 \times 10^{-4}\,m^2\,s^{-1}$ into (4.7) is shown in Figure 4.7b. The constant diffusivity reproduces the overall shape of the temperature structure, with a minimum in winter and a maximum in summer. The comparison between the predicted temperature and observation (Figure 4.7a) shows that the constant diffusivity grossly underestimates the temperature. For example, in February, the observed surface temperature is $1.8°C$ while the predicted is $-5.2°C$. In August, the observed surface temperature is $16.7°C$ whereas the constant diffusivity gives $12.2°C$.

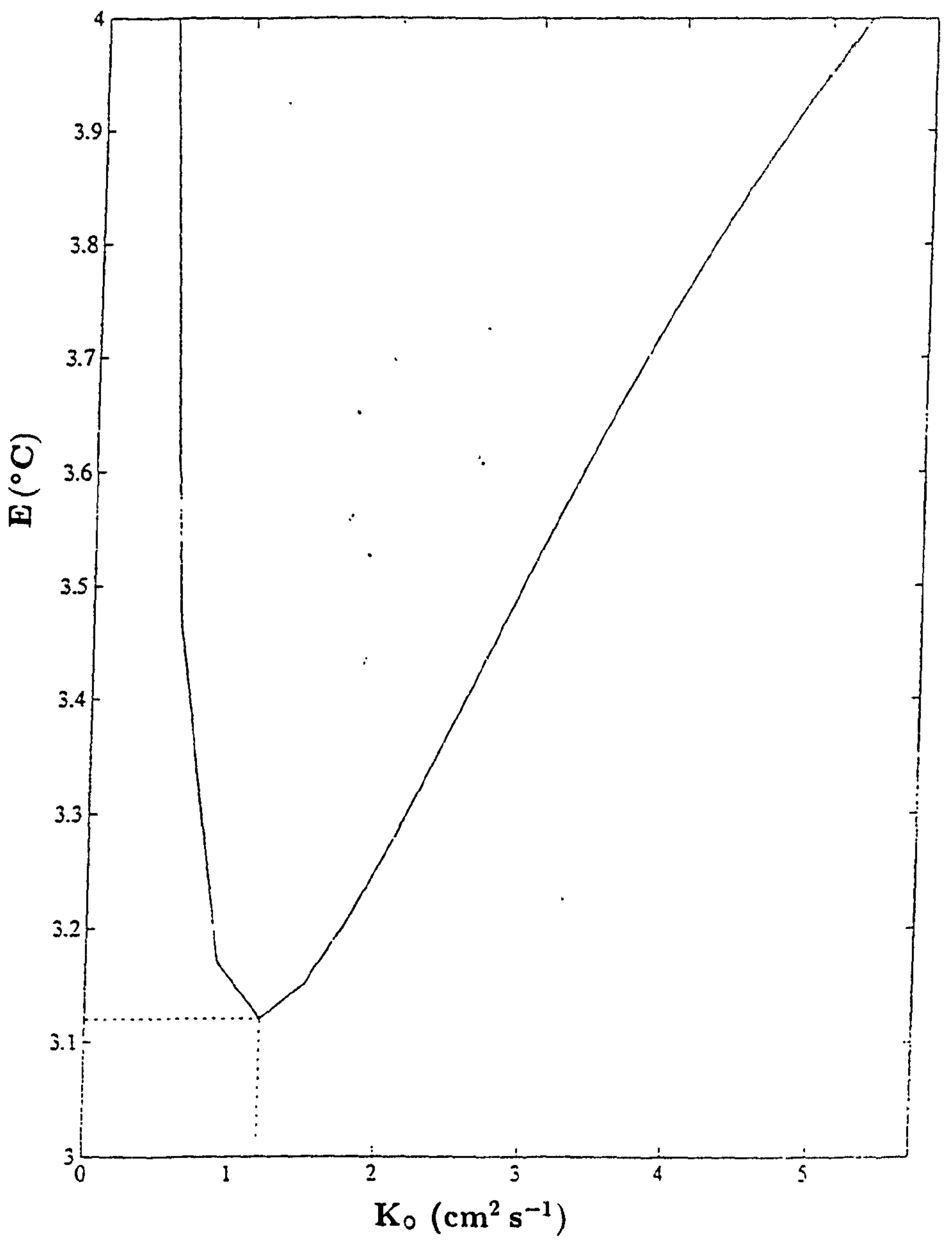

Figure 4.8: A plot of the error E against K_O, showing how the best estimate of the constant diffusivity is obtained. In the figure, the minimum $E = 3.11°C$ corresponds to the best estimate of $K_O = 1.2 \times 10^{-4}\, m^2\, s^{-1}$.

4.4 Comparison of the Three Methods and Conclusions

Method 1 depends strongly on the vertical temperature gradient in the water column and works well when the temperature gradient is strong. When the temperature gradient is weak, the method breaks down, resulting in unrealistic and negative diffusivities. Negative diffusivity has the effect of accentuating the vertical temperature gradient, instead of smoothing the gradient as it is supposed to do. This has serious consequences [*Hansen et al., 1985; Yin and Fung, 1991*], one of which is that the negative diffusivity produces high temperature and model instabilities when there should be none.

Methods 2 and 3, fortunately, overcome the problems of negative diffusivities. In the two methods, the diffusivities have been estimated for different values of the exponent (p) of the buoyancy frequency (N). The comparison between the functional dependence of $K_V(z,t)$ on N^2 estimated from Methods 2 and 3 (Figure 4.9) for subarea A8, shows that the two methods are very similar: they only differ in the quantity being minimized. In fact, in the two methods, the ratio K_O/α is essentially the same - about 3.8×10^{-8} - showing that the results from the two methods are quite robust. Again the comparison of the predicted temperature from the two methods (Figure 4.10) indicates that the $K_V(z,t)$ estimated from Method 2 underestimates the sea surface temperature in summer. The $K_V(z,t)$ from Method 3 slightly overestimates the sea surface temperature in August. Generally, the temperature structure produced by $K_V(z,t)$ in Method 3 agrees best with observation as expected.

The predicted temperature structure from the best estimated constant K_V is generally lower than observations, with the difference between the observed and the predicted temperature as high as 6 $°C$, at the surface, in August. The poor performance of the constant diffusivity in the model points to the importance of allowing the diffusivity to vary with depths and season.

On the numerical diffusivity in the model, it is shown in section C.2 of Appendix C

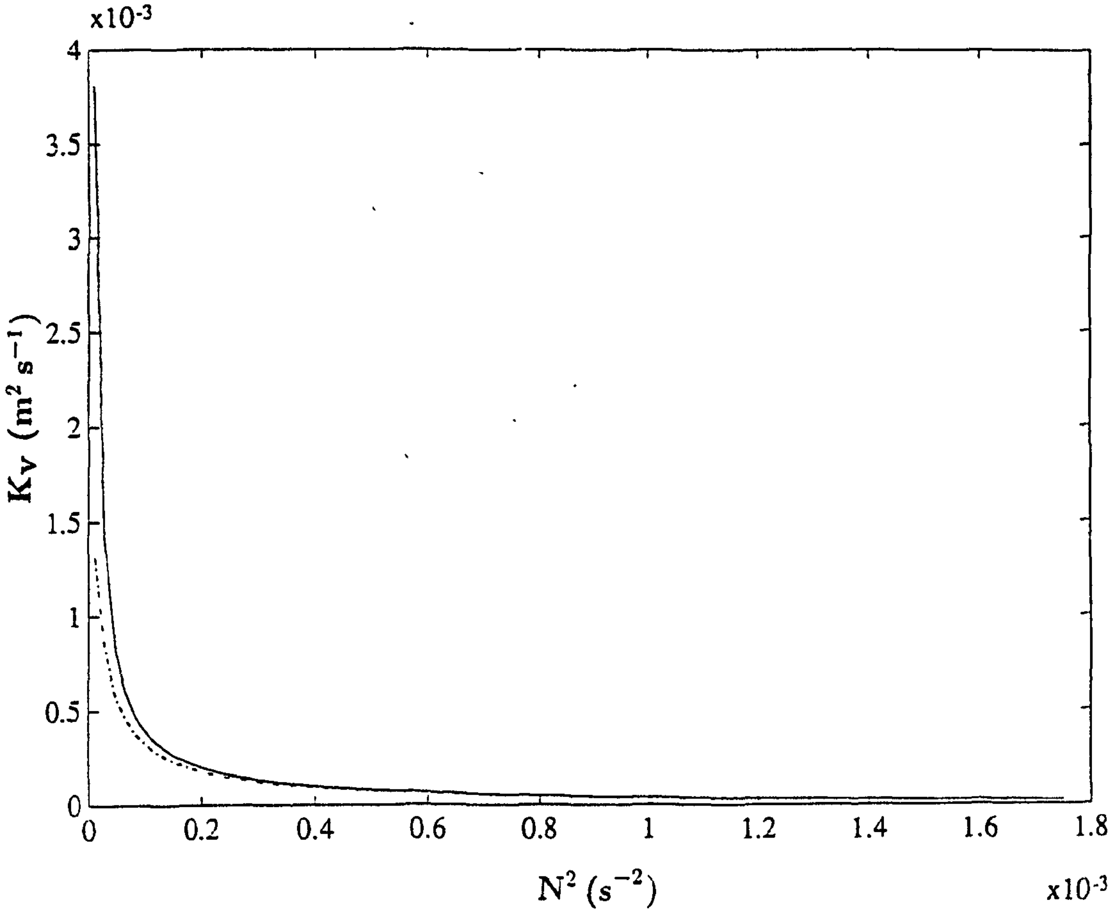

Figure 4.9: The comparison between the variation of K_v with N^2 in Method 2 (broken line) and Method 3 (solid line) for subarea A8.

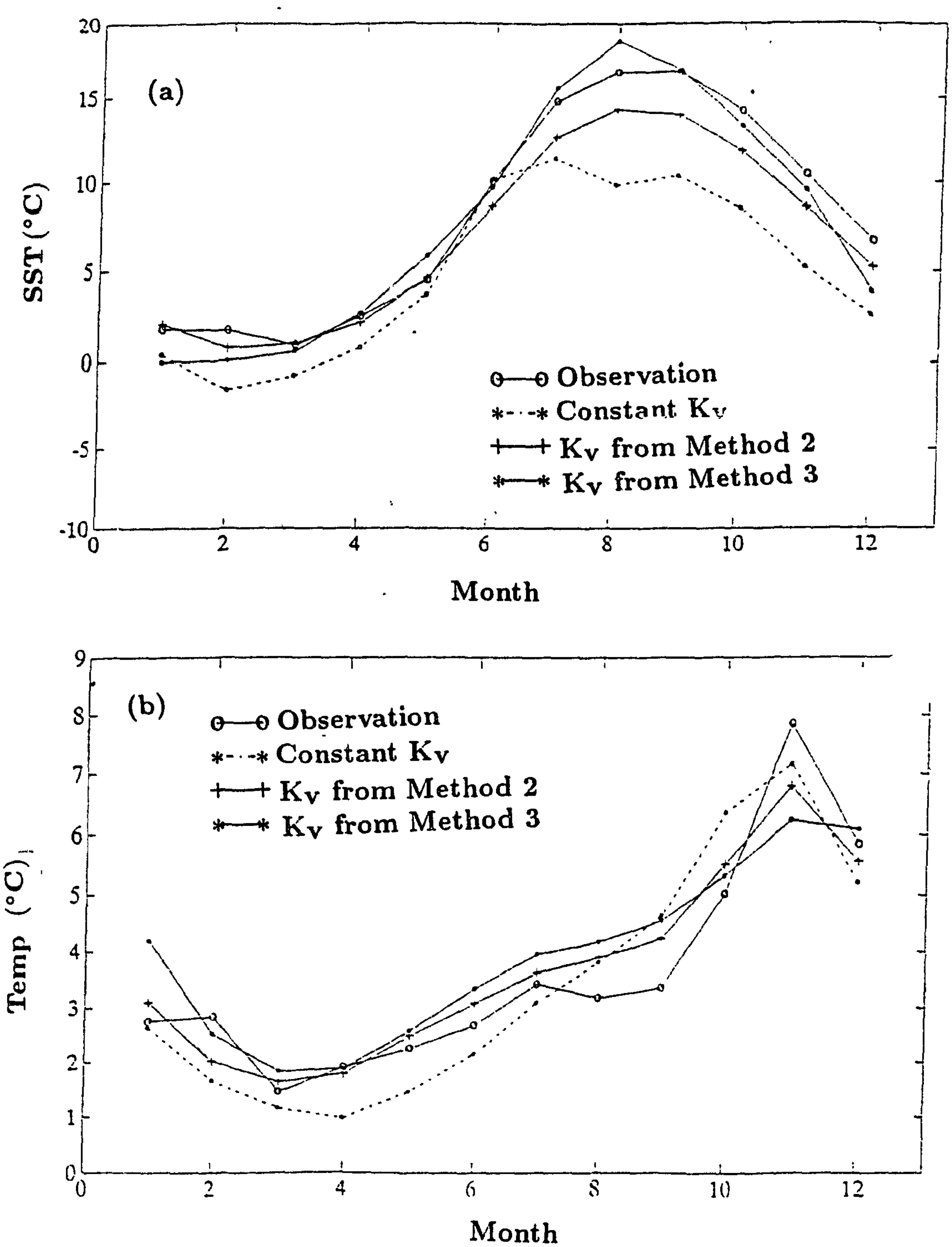

Figure 4.10: The comparison between the observed temperature and that predicted from the different models at (a) the surface and (b) 50 m depth.

that the maximum numerical diffusivity, for a time scale of 1 month and a space scale of about 10 m, is about 10% of the expected K_V. Thus the effect of the numerical diffusivity is small and is not expected to alter significantly the results from the model.

Based on how well the estimated diffusivity reproduces the observed temperature, Methods 2 and 3 are chosen. The important point from the above analyses is that the best methods of estimating $K_V(z,t)$ are those (Methods 2 and 3) in which the $K_V(z,t)$ depends on N^p. Again, because Method 3 has the added advantage of providing the minimum uncertainty, $E(p, \alpha, K_O)$, in the model temperature structure, I conclude that the parameterization

$$K_V(z,t) = \frac{K_O}{(1+\alpha N^p)} \tag{4.26}$$

from Method 3, provides the best estimates of the diffusivities, on seasonal time scales, for the top 75 m of the water column for subarea A8, where $2 \leq p \leq 4$. This method of estimating the eddy diffusivities has a further advantage in that it does not explicitly depend on velocity data, which is often difficult and expensive to obtain. These diffusivities will be used to study the origin of the cold intermediate layer, in the next chapter.

Chapter 5

THE ORIGIN OF THE COLD INTERMEDIATE LAYER

5.1 Overview of the Water Temperature Structure

One prominent feature of the temperature structure on the Scotian Shelf is a cold intermediate layer (CIL). Figure 5.1 shows a CIL for subarea 12 (mid-shelf). Between 50 and 100 m depth, the temperature of the CIL for subarea 12 varies from 2.6°C in May to 3.9°C in July. The temperature difference between the CIL at 50 m depth and the water at the 30 m level (above the CIL) is about 5.4°C in September.

The distribution of the CIL in space and time is listed in Tables D.1 and D.2 of Appendix D. For ease of expression, let me define the temperature difference between the CIL and the adjacent level above or below the CIL as the CIL index (CILI). The upper CILI, therefore, refers to the temperature difference between the CIL and that of the adjacent upper level while the lower CILI denotes the temperature difference between the CIL and the adjacent lower level. (The levels in which the temperature data are recorded are 0, 10, 20, 30, 50, 75, 100, 125, 150, 200 m, etc.) Generally, the larger the CILI, the more well defined the CIL becomes. The tables show the

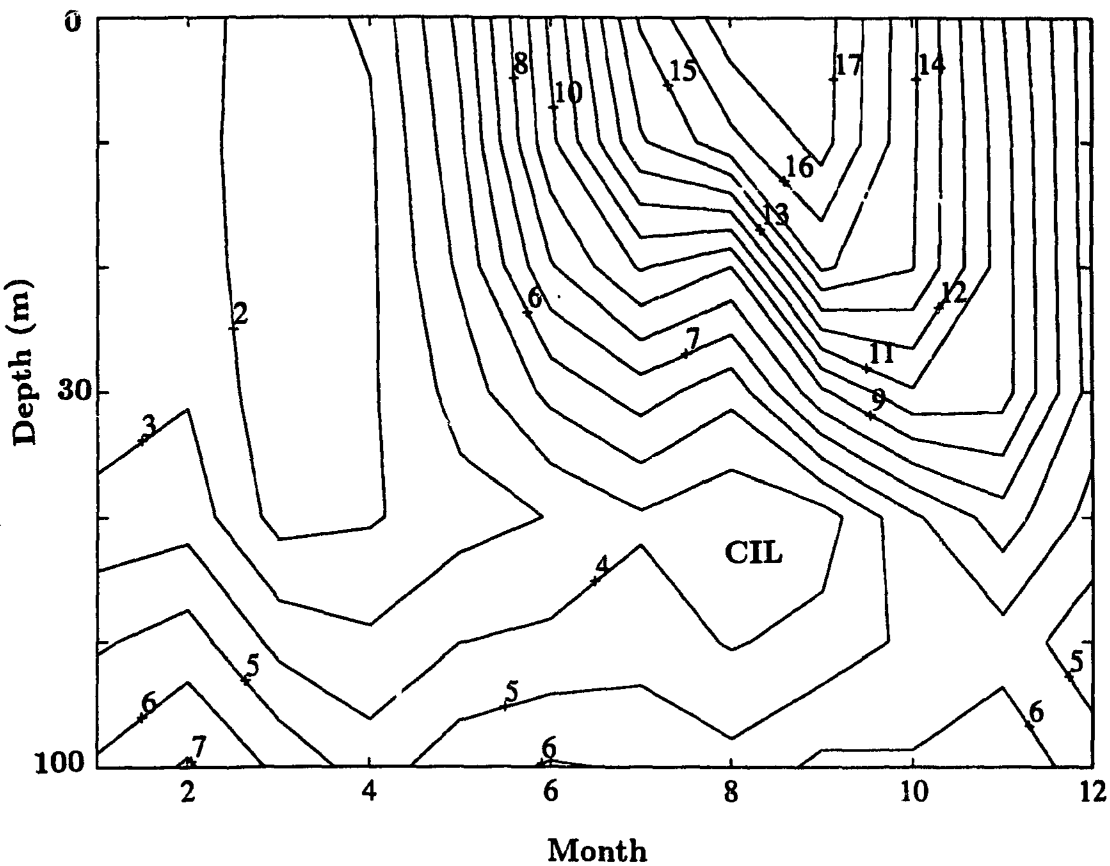

Figure 5.1: Location of the cold intermediate layer (CIL) for subarea 12. Shown are the contour lines in °C of the monthly temperature variation with depth.

depth and month where the CIL is observed for the 34 subareas (see Figure 2.1) of the study region. Also included in the tables are the upper and lower CILI. The important point from the table is that on the Scotian Shelf, well defined CILs (with CILI of about 2°C) are observed from April to September (Figure 5.2a), between 50 and 100 m water depth (Figure 5.2b).

The discussion on the origin of the CIL was initially put forward by *Hachey [1938]*. He observed the CIL in a temperature distribution obtained in a cruise carried out in February and June of 1938, on the Scotian Shelf. In an effort to explain the origin of the CIL, Hachey plotted the T-S characteristics of the water in February and in June. From the February T-S diagrams, he inferred that the water on the Scotian Shelf is a mixture of two water masses: cold water from the Gulf of St. Lawrence/Labrador current and warm slope water *[Gatien, 1976]*. He also estimated the alongshore volume transport in February and in June. His estimates showed that the alongshore volume transport in February was about twice that in June. He concluded that the CIL "is therefore the result of the volume transport of water". The recent estimates of the alongshore volume transport by *Drinkwater et al. [1979]* confirm Hachey's finding that the largest volume transport through the Scotian Shelf occurs in winter. *Drinkwater et al.'s* estimate of the mean geostrophic transport (about 0.35×10^6 m^{3}s^{-1}) for the mid-shelf is comparable to that of *Brown and Irish [1992]* for the Gulf of Maine. The CIL is not limited to the Scotian Shelf; it has been observed on the Labrador and Northeast Newfoundland Shelves *[Petrie et al., 1988]* and also in the Gulf of Maine *[Brown and Beardsley, 1978]*.

The goal of this chapter is to determine how the CIL is formed. Two possible mechanisms that can form the CIL are local heating, from above and below, and horizontal advection. To study the formation of the CIL, I have used my simple model that incorporates the seasonal distribution of the vertical eddy diffusivity with depth, estimated in Chapter 4. The model is used to assess the role of horizontal advection and local heating in the formation of the CIL. It will be shown that the CIL forms from a combination of horizontal advection of cold water into the region

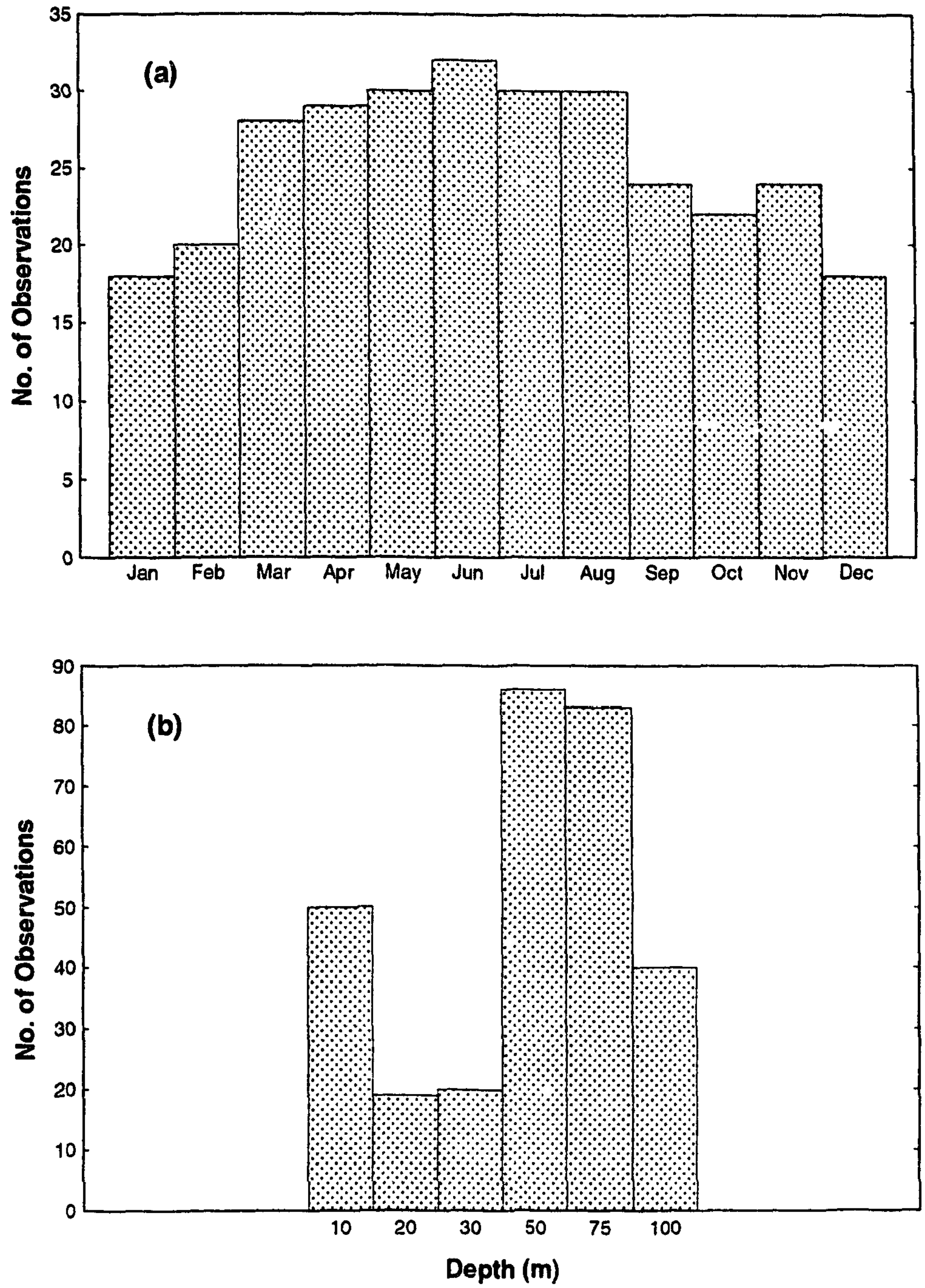

Figure 5.2: Monthly and depth distribution of the CIL on the Scotian Shelf. (a) shows the number of CILs observed for a given month, in the 34 subareas while (b) shows the number of CILs observed at a given depth, in the 34 subareas.

(as was suggested by *Hachey [1938]*), and local heating from the surface and from below the CIL.

5.2 Conditions Necessary to Form a CIL

As shown in Figure 2.3a of Chapter 2, an important feature of the long term mean temperature profile on the Scotian Shelf is a CIL at about 50 m depth, between April and September. This layer is referred to, in this study, as the permanent CIL. It is important to distinguish the formation of the permanent CIL from that of a transient CIL. A combination of factors can produce a transient CIL, some of which include the passage of a cold parcel of water at intermediate depth, and the combined effect of summertime surface warming and deep advection of warm water. In the following discussion, attention is focussed on a permanent CIL with a constant K_V. From a simple physical reasoning, a permanent CIL requires

$$\frac{\partial \overline{T}}{\partial z} > 0 \qquad z = 0 \tag{5.1}$$

$$K_V \frac{\partial \overline{T}}{\partial z} < 0 \qquad z = -h \tag{5.2}$$

where the overbar denotes long term mean. However, for the CIL to be maintained there must be an additional cold water. This is readily seen by taking the time average of

$$\frac{\partial}{\partial t} \int_{-h}^{0} T \, dz = \frac{Q}{\rho c_p} - K_V \frac{\partial T}{\partial z}\bigg|_{-h} + \int_{-h}^{0} \Gamma(z,t) \, dz \tag{5.3}$$

which gives

$$\overline{K_V \frac{\partial T}{\partial z}\bigg|_{-h}} = \frac{\overline{Q}}{\rho c_p} + \int_{-h}^{0} \overline{\Gamma}(z,t) \, dz \tag{5.4}$$

Assuming that $K_V \partial T / \partial z|_{-h}$ is constant through time, consistent with observations, it is clear that the conditions for the formation and maintenance of a permanent CIL are

$$\overline{Q} > 0 \tag{5.5}$$

and

$$\int_{-h}^{0} \overline{\Gamma}\, dz < -\frac{\overline{Q}}{\rho c_p} \tag{5.6}$$

Physically, (5.6) means that for the Scotian Shelf, there must be cold water (Γ) advected or mixed into the area, otherwise, local heating from the surface and from the deep ocean will just warm up the whole upper layer. These conditions are illustrated in Figure 5.3a. The arrow shows the direction of the heat flux. The broken line in the figure shows a situation in which $Q < 0$, that is, the heat flux is out of the ocean - a situation often found in winter. Even though there is heat flux from the deep ocean, it is clear that such a case cannot develop a CIL. Figure 5.3b illustrates a situation in which the heat flux at $-h$ is directed into the deep ocean: even when the net surface heat flux is directed into the ocean, it is clear that a CIL can not form. Therefore, it is clear from this simple discussion that one needs local heating from the surface and from the deep ocean, as well as cold horizontal advection. In other words, if there is heating from above and below, then horizontal advection of cold water is required to form the CIL.

5.3 Predicted Surface and Subsurface Temperature From the Model

The model is the one-dimensional diffusion equation

$$\frac{\partial T}{\partial t} = \frac{\partial}{\partial z}\left(K_v \frac{\partial T}{\partial z}\right) + \Gamma(z,t) \tag{5.7}$$

Γ is the net contribution of horizontal advection, upwelling and horizontal mixing, distributed with depth as described in section 5.5 below The other symbols are as defined earlier. The time and depth resolution of the model are the same as those

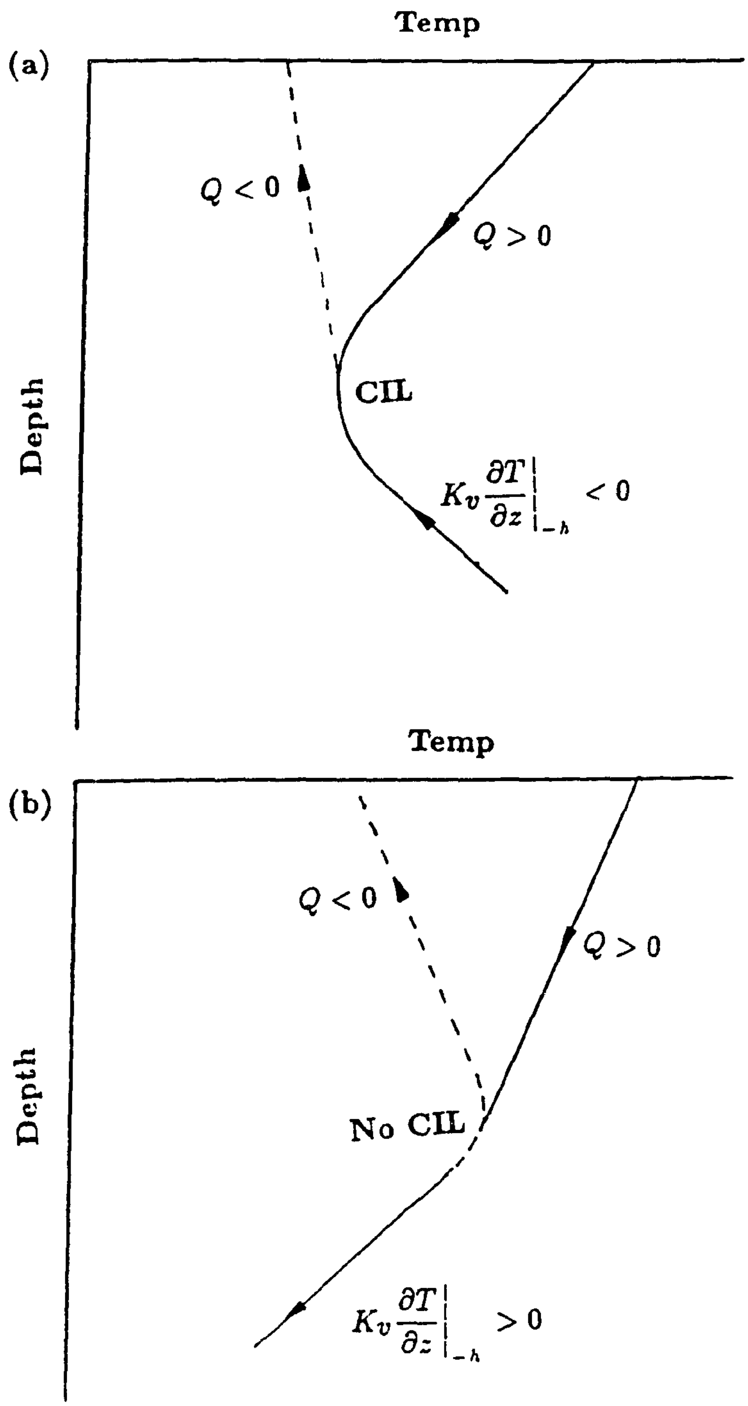

Figure 5.3: Diagrams illustrating the conditions that can form a CIL (a) and those which cannot form a CIL (b). The arrow shows the direction of the heat flux.

(a) Observed

z(m)	Jan	Feb	Mar	Apr	May	Jun	Jul	Aug	Sep	Oct	Nov	Dec
0	1.80	1.76	0.93	2.54	4.53	10.08	14.79	16.69	16.70	14.18	10.46	6.69
10	1.84	1.89	0.82	2.15	4.33	9.77	12.49	14.72	15.91	14.15	10.74	6.20
20	1.94	2.01	0.86	2.01	3.68	7.36	9.14	8.44	12.63	14.02	10.78	6.32
30	2.06	2.22	0.99	1.99	3.06	5.22	5.91	5.09	7.12	10.51	10.75	6.49
50	2.75	2.83	1.46	1.90	2.26	2.69	3.42	3.17	3.36	5.03	7.85	5.85
75	4.04	4.25	2.95	3.09	3.01	3.36	4.25	3.69	4.10	4.59	5.09	4.53

(b) Predicted from the model

z(m)	Jan	Feb	Mar	Apr	May	Jun	Jul	Aug	Sep	Oct	Nov	Dec
0	0.00	0.09	0.60	2.71	5.88	9.71	15.62	18.78	16.80	13.27	9.55	3.88
10	1.54	0.34	0.68	2.03	5.00	9.59	11.89	13.70	15.45	13.32	9.73	5.31
20	2.33	0.78	0.89	1.59	3.78	5.84	7.45	7.39	9.46	12.65	10.08	5.73
30	2.78	1.53	1.03	1.58	2.82	4.29	4.92	5.19	5.98	8.20	9.58	6.31
50	4.19	2.52	1.82	1.87	2.58	3.35	3.95	4.18	4.55	5.33	6.24	6.08
75	4.04	4.25	2.95	3.09	3.01	3.36	4.25	3.69	4.10	4.59	5.09	4.53

Table 5.1: The water temperature structure in $°C$ for subarea A8, showing the cold intermediate layer.

used in Chapter 4 (section 4.3.3) to estimate the eddy diffusivities. In this chapter, the diffusivity $K_V(z,t) = K_O\left(1+\alpha N^2\right)^{-1}$ is used to predict the surface and the subsurface temperature profile. As determined earlier, the best fit parameters are $K_O = 0.55\ \mathrm{m}^2\,\mathrm{s}^{-1}$ and $\alpha = 1.4 \times 10^7\ s^2$. N is the buoyancy frequency, determined from the observed density field. The details of the model are described in Appendix C (section C.1). Briefly, the model is forced at the surface with Q and at $z = -h$ with the observed temperature. In the model, $h = 75\,m$ is used as that represents the depth of seasonal temperature signal penetration (determined in Chapter 2). Note that the bottom boundary condition allows a heat flux between the upper layer and the deep ocean. The predicted temperature structure, for subarea A8, is listed in Table 5.1. Subarea A8 is representative of other subareas on the shelf for which the heat budget analysis was carried out. An important feature in the predicted temperature distribution is the existence of a CIL. The depth (50 m) at which the model predicts the fully developed CIL, and the formation of the CIL from May to July, agree well with observations. Note that the conditions for the formation of a CIL are satisfied by the model. The agreement between the model and observations is encouraging because it increases my confidence in the estimated $K_V(z,t)$ and $\Gamma(z,t)$. The next problem I want to address is the relative contribution of the net surface heat flux and $\Gamma(z,t)$ to the formation of the CIL.

5.4 Contribution From Q

To determine the role of local surface heat flux, the model equation (5.7) is forced with Q at the surface and with the observed temperature at 75 m. $\Gamma(z,t)$ is set to zero in (5.7). The model is run until it reaches a periodic steady state. The predicted temperature due to the surface heating is shown in Figure 5.4b. It is clear from the figure that most of the temperature structure is caused by surface heating. This result is in accord with the analysis of the seasonal heat budget on the shelf (section 3.3), where it was shown that about 85% of the local rate of heat storage can be explained by the net surface heat flux. Figure 5.4b also confirms that the high temperature stratification of the top 50 m of the water column in summer is caused by the surface heating.

In terms of the formation of the CIL, this calculation shows that the surface forcing alone does not produce a CIL, because (5.6) is not satisfied. In a steady state, $\partial T/\partial z|_{-h} > 0$ since $\overline{Q} > 0$. Hence there is net heat flux from the upper layer to the deep ocean.

5.5 Contribution From $\Gamma(z,t)$

5.5.1 Distribution of $\Gamma(z,t)$ with Depth

As mentioned in chapter 4, the imbalance is given by

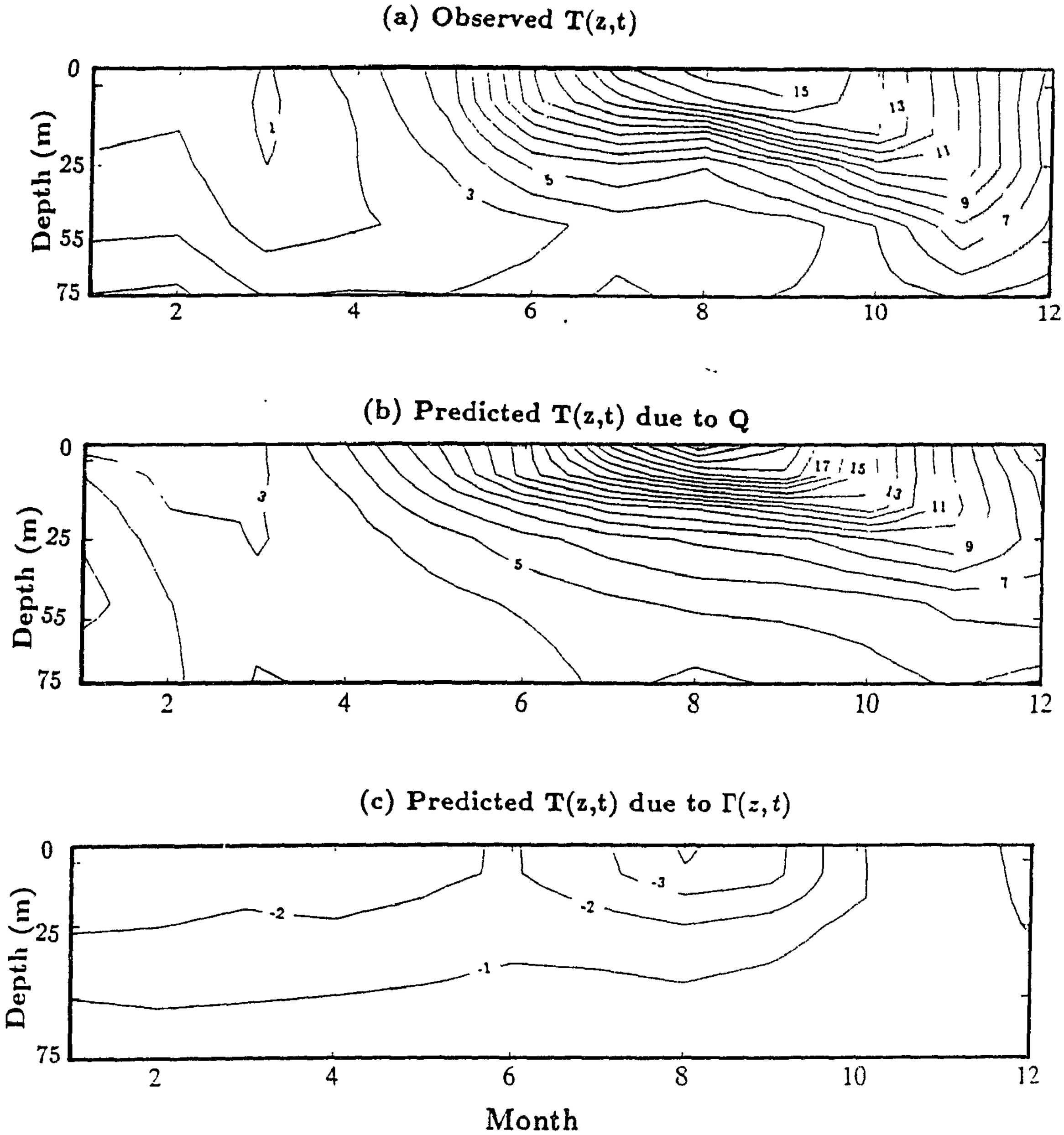

Figure 5.4: The comparison between (a) the observed $T(z,t)$, (b) the predicted $T(z,t)$ due to the net surface heat flux Q, and (c) the predicted $T(z,t)$ due to the residual heat flux $\Gamma(z,t)$.

$$\int_{-h}^{0} \Gamma(z,t)\,dz = \frac{\partial}{\partial t}\int_{-h}^{0} T\,dz - \frac{Q}{\rho c_p} + Kv\frac{\partial T}{\partial z}\bigg|_{-h} \tag{5.8}$$

(Note that RHS of (5.8) is observed). $\Gamma(z,t)$ is assumed to be distributed with depth as

$$\Gamma(z,t) = \zeta_s\left[\frac{\partial}{\partial t}\int_{-h}^{0} T\,dz - \frac{Q}{\rho c_p} + Kv\frac{\partial T}{\partial z}\bigg|_{-h}\right] \tag{5.9}$$

where

$$\zeta_s = \frac{\zeta(z)}{\int_{-h}^{0}\zeta\,dz} \tag{5.10}$$

and

$$\zeta = e^{z/\delta} \tag{5.11}$$

δ is determined as described earlier.

To determine the contribution of $\Gamma(z,t)$ alone to the generation of the temperature structure at subarea A8, both the surface boundary condition (Q) and the observed temperature at $z = -h$ were set to zero in (5.7). The model is only forced with $\Gamma(z,t)$. As before, starting with a zero temperature initial condition, the model is run to a periodic steady state.

The results are shown in Figure 5.4c. $\Gamma(z,t)$ produces negative temperatures everywhere. The effect of $\Gamma(z,t)$ is to cool the water column. The temperature increases with depth, for all months. With respect to the formation of the CIL, it is clear that $\Gamma(z,t)$ alone does not produce a CIL. Both Γ and local heating are needed to form the CIL.

5.6 Relative Importance of Advection and Local Heat Flux

We are now in a position to discuss the origin of the CIL. The model with seasonal varying diffusivities does, in fact, reproduce the CIL. The model forced with only $\Gamma(z,t)$ shows that horizontal advection generally cools the water on the shelf throughout the year.

It is most probable that the cooling is a result of the advection of cold water from the Gulf of St. Lawrence and/or the Labrador current onto the Shelf. A water parcel from the Gulf of St. Lawrence in November, moving with a speed of 5 $cm\ s^{-1}$, will be on the Scotian Shelf (about 450 km away) in February. The maximum transport of this cold water to the shelf occurs in winter. But as the cold water moves on to the Scotian Shelf it mixes with the shelf water and becomes warmer than the original advected water.

The heat budget and the model results (in this Chapter) confirm that horizontal advection does supply cold water to the shelf. The cold water alone does not produce a CIL, but it is necessary to the formation of a CIL on the Scotian Shelf.

The local heating is also needed to produce a CIL. In summer, for example, the strong local surface heat flux warms the surface layer of the ocean. The influence of the surface heating decreases with depth so that, although the temperature of the cold water below (that was brought in by horizontal advection) has been modified by the surface heating, a warmed version of the cold water still remains. The influence of surface heating also explains why the CIL is deeper in summer and fall (when the surface heating is strong and $Q > 0$) than in winter (when $Q < 0$). In fact (as mentioned before), in some subareas like A8, the CIL is not found at all in winter, when the maximum flux of the cold water is present. Again, in addition to the surface heating, there is another source of heating from the deep (> 75 m) ocean. The warm deep water has been shown *[Gatien, 1976]* to originate from the warm Gulf Stream water. Therefore, the CIL forms as a result of the warming of the cold water (which was originally advected from outside the region) by the surface heating and heat flux from the deep ocean.

There is no evidence to suggest that local surface winter cooling takes part in the formation of the cold intermediate layer. If it does, its effect is negligible. Rather, the analyses suggest that water cooled elsewhere in winter is necessary to the development of the CIL on the Scotian Shelf.

5.7 Summary

Q is generally responsible for the creation of the observed seasonal cycle in both the surface and subsurface temperature structure on the Scotian Shelf. This finding confirms the result of the seasonal heat budget, which showed that about 85% of the local rate of heat storage can be explained by the net surface heat flux on the Scotian Shelf. $\Gamma(z,t)$ produces cooling on the Scotian Shelf. This cooling is probably the result of the horizontal advection of cold water from the Gulf of St. Lawrence/Labrador current to the Shelf region. In winter, heat loss from the surface also produces water cooling.

On the formation of the CIL at subarea A8 (mid-shelf), it is shown that both Q and Γ are needed to explain the observed CIL. The CIL forms as a result of the cold water (produced elsewhere) being trapped between the local surface heating and heating from below. The fact that the estimated $K_V(z,t)$ and $\Gamma(z,t)$ reproduce the CIL gives us more confidence in the estimates of the diffusivities. In the next chapter, this model will be used to hindcast the surface and the subsurface water temperature, using the COADS heat flux.

Chapter 6

INTERANNUAL VARIABILITY

6.1 Introduction

The Northwest Atlantic is a region with strong interannual changes in sea surface temperature (SST). *Cayan's [1986]* time series plots of the seasonal sea surface temperature anomalies (compiled in Figure 6.1) and the seasonal cycle of the SST (Figure 6.2) show that this region has the most energetic sea surface temperature variations in North Atlantic. For example, a quasi-linear drop of about $4°C$ is observed from 1950 to 1965 in the Northwest Atlantic. The contour plots of the seasonal SSTAs (Figure 6.3, redrawn from *Cayan [1986]*) indicate that the anomalies have large spatial scale.

This chapter focuses on the interannual variability of SST in the Northwest Atlantic and its relationship with the interannual variability of the net surface heat flux, Q. Specifically, I want to determine how much of the interannual variability in SST may be explained by Q. The interannual variability in Q is estimated from the Comprehensive Ocean Atmosphere Data Set (COADS) while the interannual changes in both the surface and subsurface water temperatuie are estimated for the Emerald Basin using data kindly provided by Dr. B. Petrie of Bedford Institute of Oceanography *[personal communication]*. The SST for the Emerald Basin has about the same trend as other areas of the Northwest Atlantic. The problem is addressed by forcing

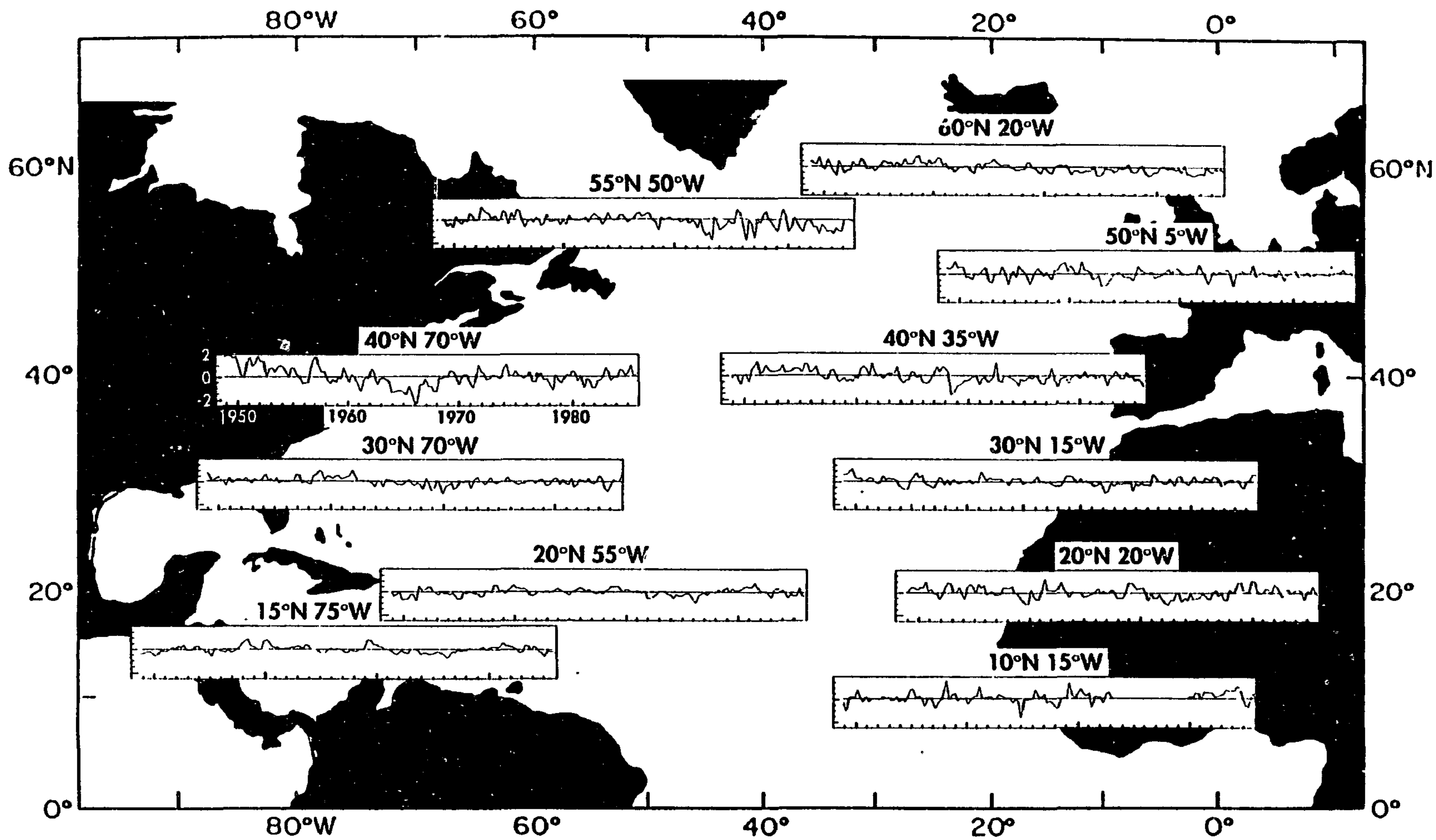

Figure 6.1: Time series of the seasonal SSTAs, in $°C$, for different regions of North Atlantic, showing the Northwest Atlantic to be the most energetic region. Redrawn from *Cayan [1986]*.

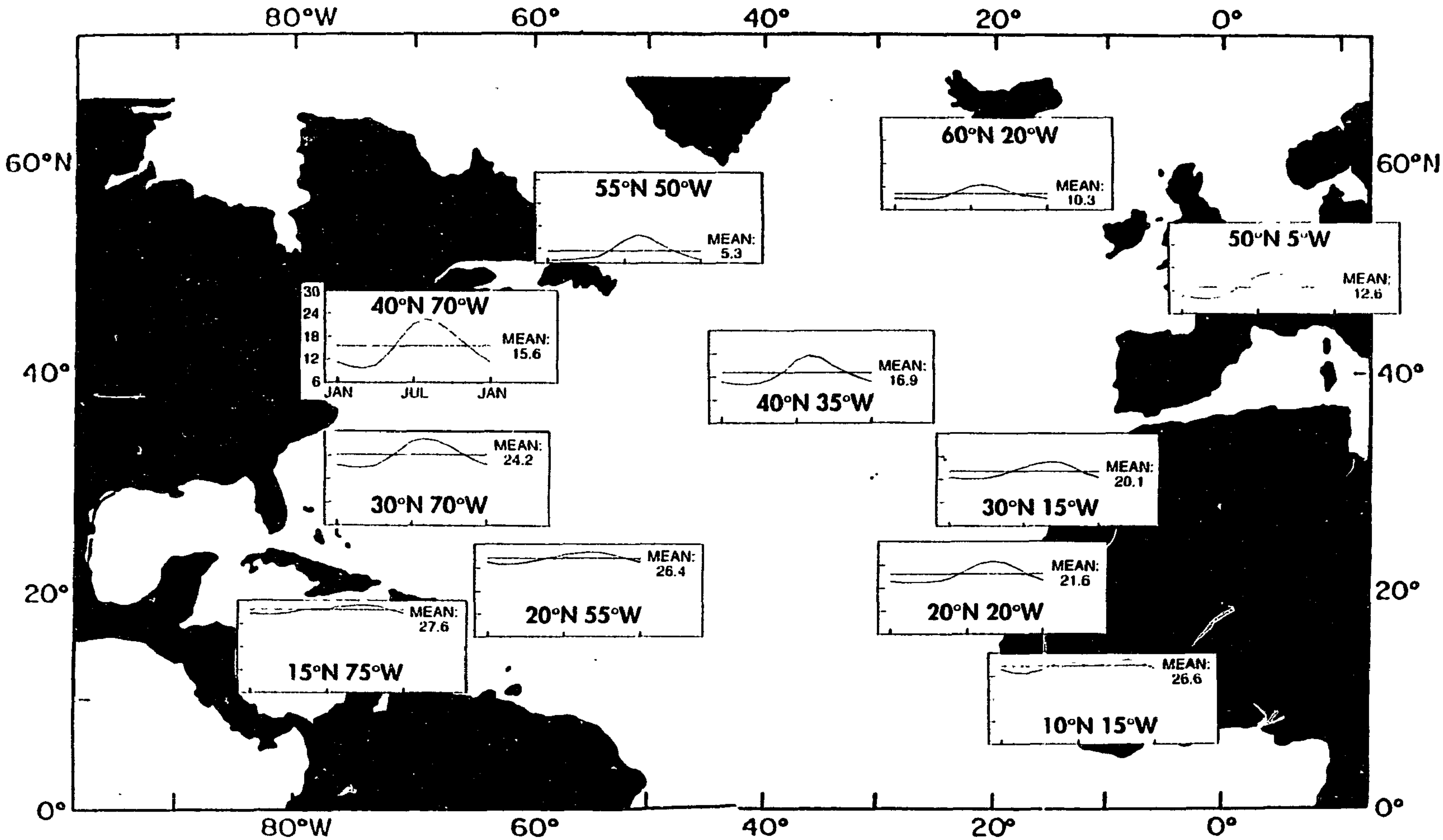

Figure 6.2: The seasonal cycle of the SST, in °C, for different regions of North Atlantic, showing that the largest range occurs in the Northwest Atlantic. Redrawn from *Cayan [1986]*.

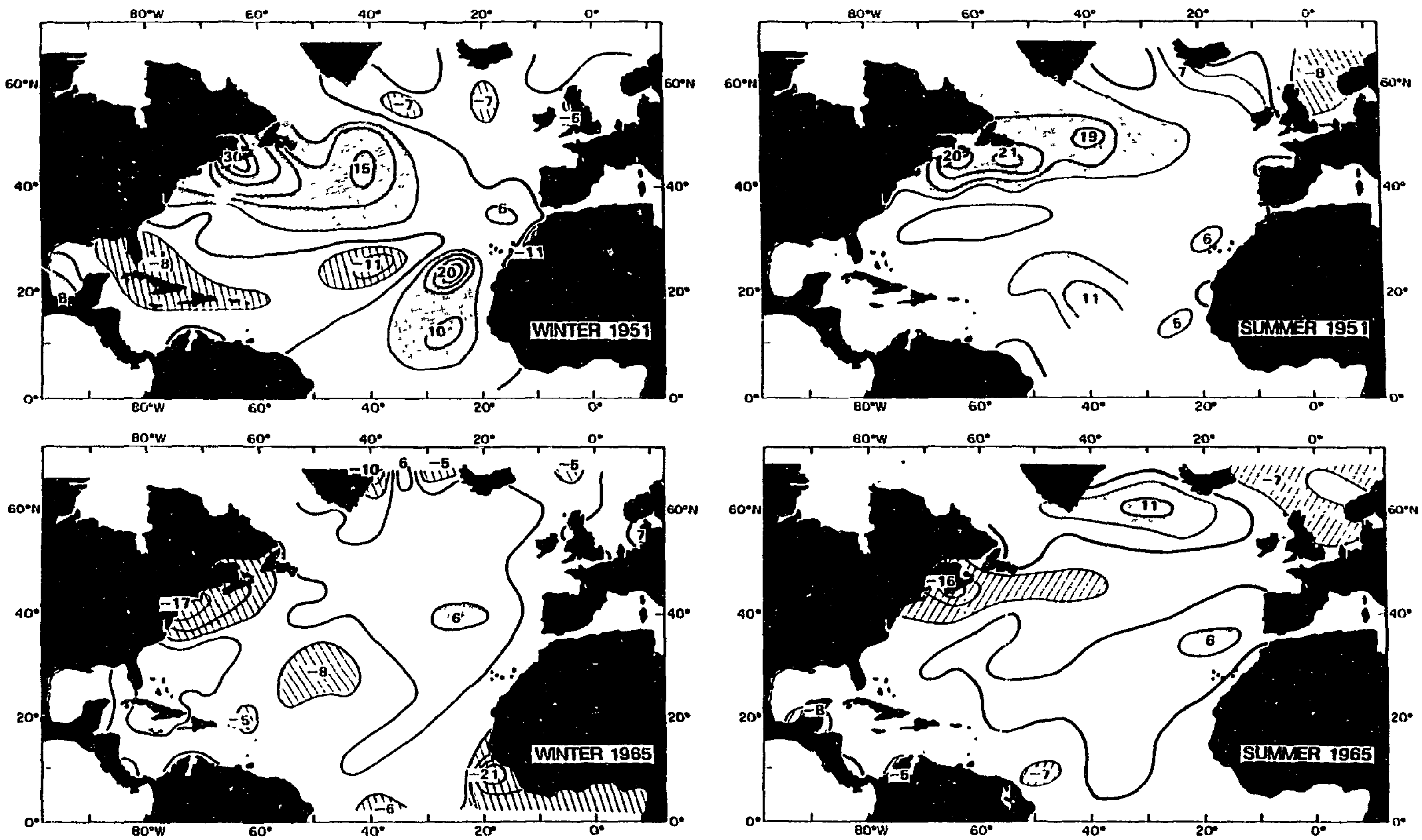

Figure 6.3: Contour plots of the seasonal SSTAs, in units of $0.1°C$, for 1951 and 1965, showing that the SSTAs are large scale. Redrawn from *Cayan [1986]*.

the model with the seasonal diffusivities (developed earlier) with the observed Q. The model SST is then compared with observations. It will be shown that much of the SST variability appears to be driven, not by Q, but by the ocean. Some discussion is given of the possible oceanic mechanisms.

6.2 Computation of the Net Surface Heat Flux

Following *Isemer et al. [1989]*, the net surface heat flux into the ocean is

$$Q = Q_S - Q_I - Q_L - Q_H \tag{6.1}$$

where Q_S is the net shortwave radiation, Q_I the net longwave radiation, Q_L the latent heat flux, and Q_H the sensible heat flux. The short wave radiative flux is computed from *[Reed, 1977]*

$$Q_S = Q_O(1-\alpha)(1-0.636n+0.0019h) \tag{6.2}$$

where Q_O is the solar radiation at the top of the atmosphere, for an atmospheric transmission of 0.7, which is kept constant for all months. The albedo of the sea surface, α varies with latitude and time. The monthly average values of α taken from the tables of *Payne [1972]*. For latitude $40°N$, the monthly mean albedos from January to December are: 0.10, 0.09, 0.07, 0.07, 0.06, 0.06, 0.06, 0.06, 0.07, 0.08, 0.10, 0.11. n is the fractional cloud cover; the monthly averages are obtained from COADS. h is the noon solar altitude in degrees. The details of the computation of Q_O and h are given in section E.1 of Appendix E. The values of h and Q_O are first computed for each day of the month, and monthly means are then formed.

The net longwave radiation is given by

$$Q_I = \epsilon\sigma T_a^4(0.254-0.00495e_a)(1-cn^d) + 4\epsilon\sigma T_a^3\overline{(T_s-T_a)} \tag{6.3}$$

where $\epsilon = 0.96$ is the emissivity of the ocean surface. $\sigma = 5.67 \times 10^{-8}$ W m^{-2}K^{-4} is the Stefan-Boltzmann constant. In the computations that follow, the subscripts a and s refer to air and sea respectively. T is temperature in degrees Kelvin. c is the cloud cover coefficient which depends on latitude *[Budyko, 1974]*. For latitude 45°, $c = 0.70$. For the cloud cover exponent d, the revised value $d = 1.1$ of *Isemer et al. [1989]* is used. e_a is the water vapour pressure in hPa (1 hPa = 10^2 Pa = 1 mb) - its estimation is discussed in Appendix E.

The latent and sensible heat fluxes are computed from the following bulk formulae:

$$Q_L = \rho_a L C_E \overline{(q_s - q_a)U} \tag{6.4}$$

$$Q_H = \rho_a c_p C_H \overline{(T_s - T_a)U} \tag{6.5}$$

where

$$\rho_a = \frac{p}{RT_a} \tag{6.6}$$

is the air density in kg m^{-3}. p is the sea level pressure in millibars and R = 287 J kg^{-1}K^{-1} is the gas constant for dry air. The latent heat of vaporization L, which is a function of T_s, is given as *[Pruppacher and Klett, 1980]*

$$L = 597.3 \left(\frac{273.15}{T_s}\right)^{\beta} \tag{6.7}$$

where

$$\beta = 0.167 + 3.67 \times 10^{-4}\, T_s$$

T_s, is in degrees Kelvin and L, in J kg^{-1}. C_E and C_H are the bulk exchange coefficients. The values of the exchange coefficients used are the revised and adjusted estimates of *Isemer et al. [1989]*, in which C_E varies with wind speed U and stability, and $C_H = 0.94 C_E$. The stability dependence of C_E is expressed by the virtual temperature difference $(\overline{T}_{sv} - \overline{T}_{av})$, where the overbar denotes a monthly mean. The virtual temperatures are estimated as shown also in Appendix E. c_p = 1005 J kg^{-1}K^{-1} is the specific heat of air at constant pressure. The monthly average product $\overline{(q_s - q_a)U}$ and $\overline{(T_s - T_a)U}$ are obtained from COADS. (Please note that all quantities obtained from COADS data set are trimmed, that is, checked to remove outliers.) The errors in the COADS will be discussed later.

6.3 Interannual Variability in the Surface Heat Fluxes

The components of the surface heat flux have been estimated for seven 2° squares, covering latitudes $42 - 44°N$ and longitudes $58 - 66°W$ in the North Atlantic. The 2° squares are shown in Figure 6.4. The results for two representative squares will be presented in this section. S1 is chosen to represent the variability on the Scotian Shelf while S7 represents the variability on the Slope region. The results for the other five squares are given in Appendix E. Throughout this chapter, the net surface heat flux and its components are presented as Q, Q_S, $-Q_I$, $-Q_L$ and $-Q_H$. With this convention, a positive value denotes a heat gain by the ocean.

6.3.1 Short Wave Radiative Flux, Q_S

The solar radiative flux is the major contributor to Q. The interannual variability of Q_S for the Shelf and Slope regions is shown in Figures 6.5a. The low frequency components of the Q_S (obtained by passing the fluxes through a 25-month running mean filter) for S1 and S7 are shown in Figures 6.6a and 6.8a respectively. On the Shelf, it ranges from 29 W m^{-2} in December, 1955 to 316 W m^{-2} in July, 1951. On the Slope region, it varies from 36 W m^{-2} in December, 1958 to 291 W m^{-2} in June, 1946.

The seasonal variation in Q_S is set by the position of the sun in the sky (solar altitude) and albedo. Hence the short wave radiation is maximum in June, when the solar altitude is highest and minimum in December, when the solar altitude is lowest.

The interannual variability in Q_S, at a given location, is dictated mainly by the cloud cover. Clouds reflect, scatter and absorb a fraction of the solar radiation reaching the sea surface. The higher the cloud fraction, the smaller the short wave radiative flux into the ocean. Much of the variability in Q_S occurs in summer, presumably due to the variability in the cloud cover.

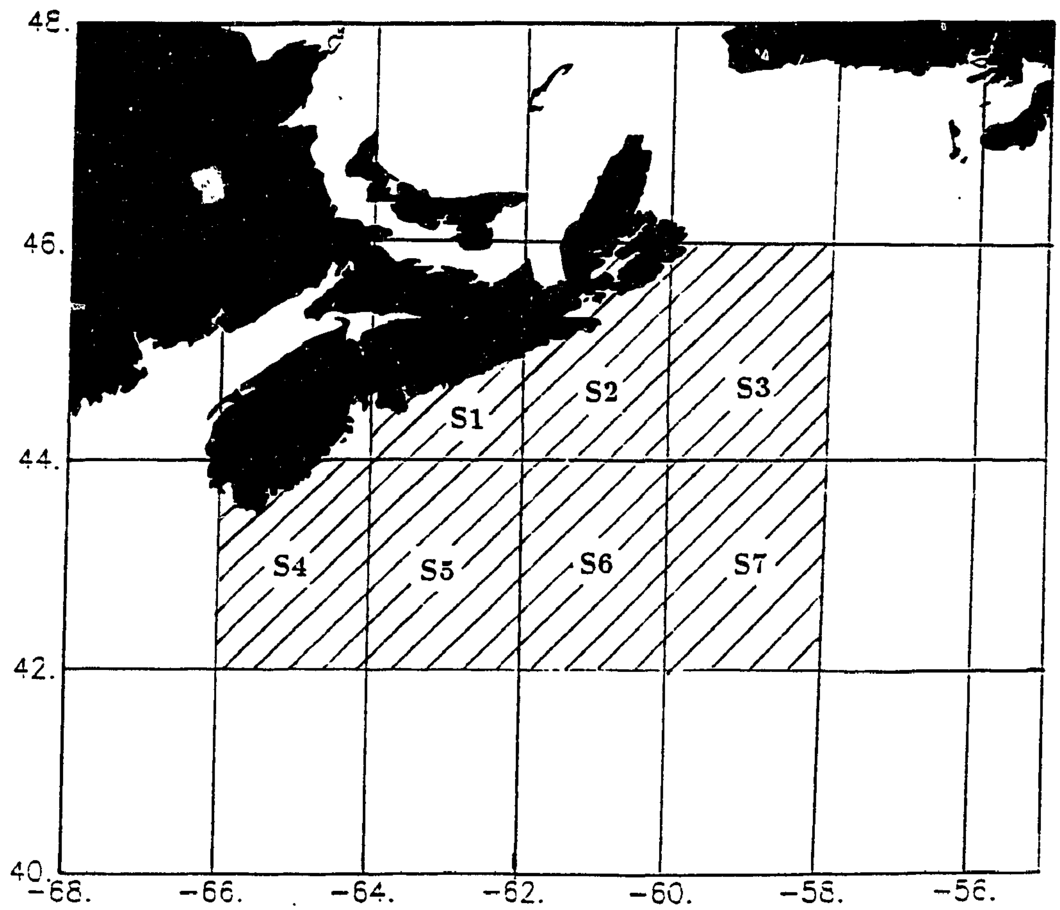

Figure 6.4: Map showing the COADS 2° squares where the Q's are estimated.

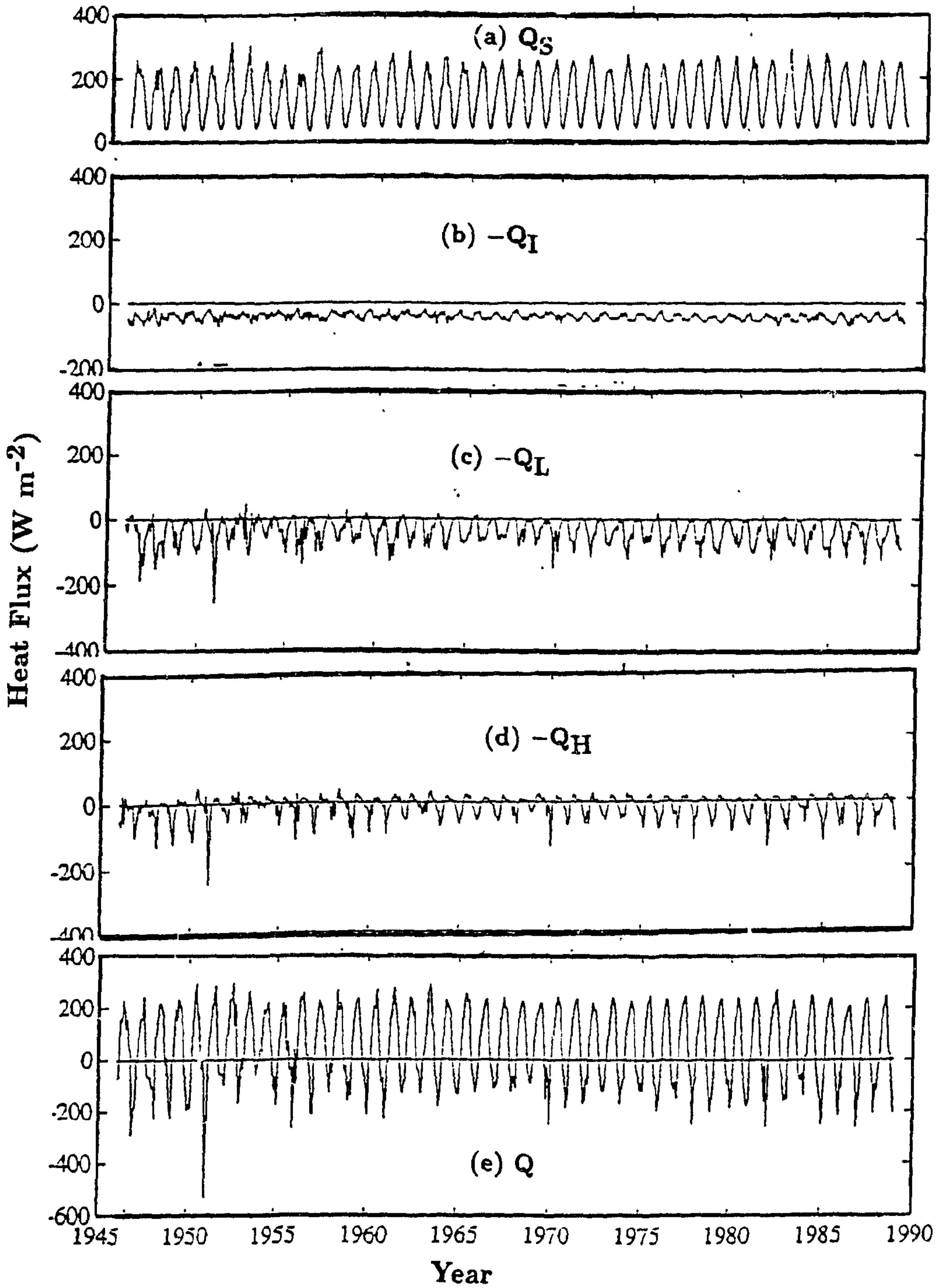

Figure 6.5: Time series of the monthly estimates of the different components of the surface heat flux for S1, representative of the variability on the Scotian Shelf.

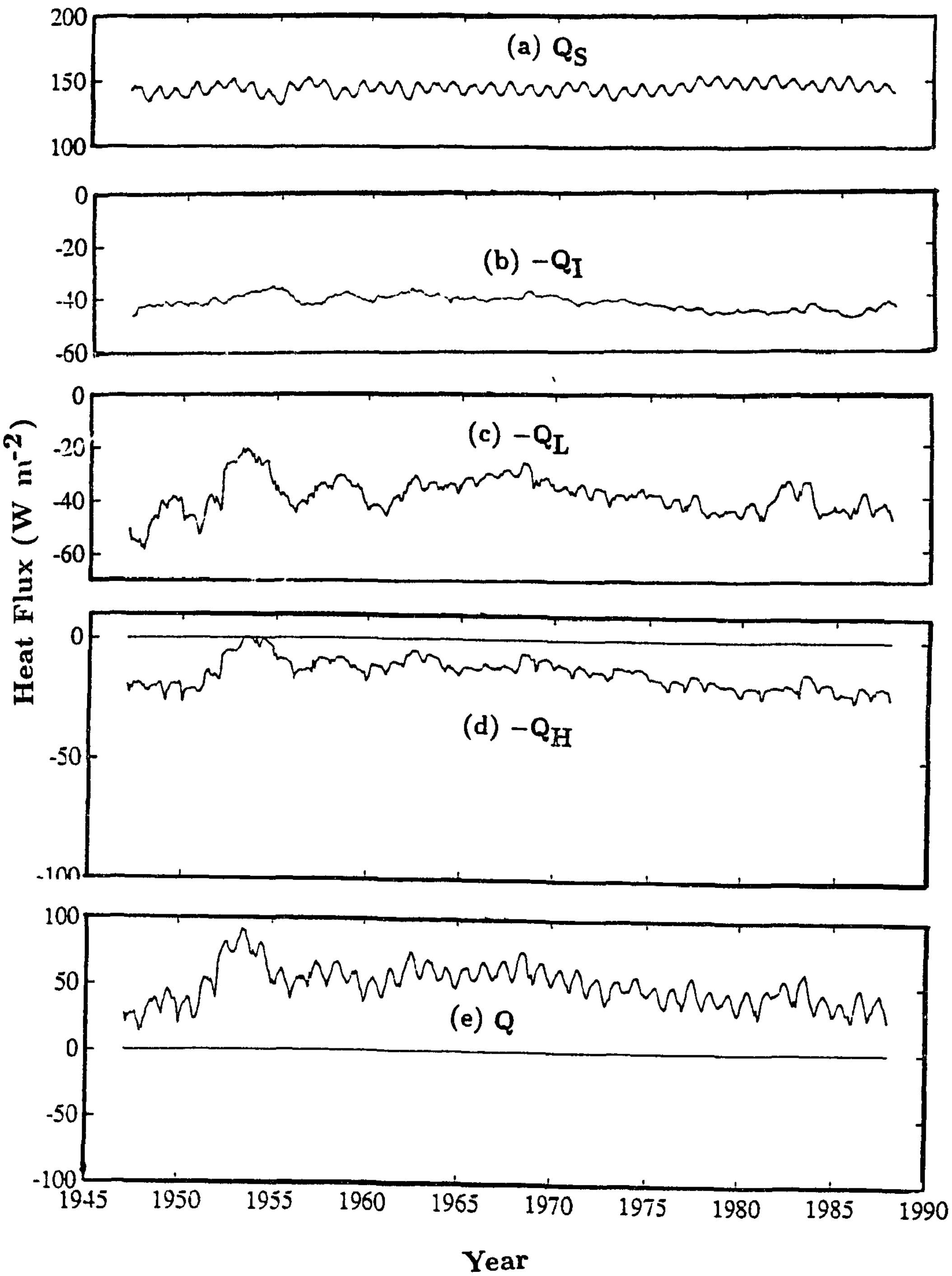

Figure 6.6: Time series of the monthly low frequency (25-month running mean filtered) components of the surface heat flux for S1, representative of the variability on the Scotian Shelf.

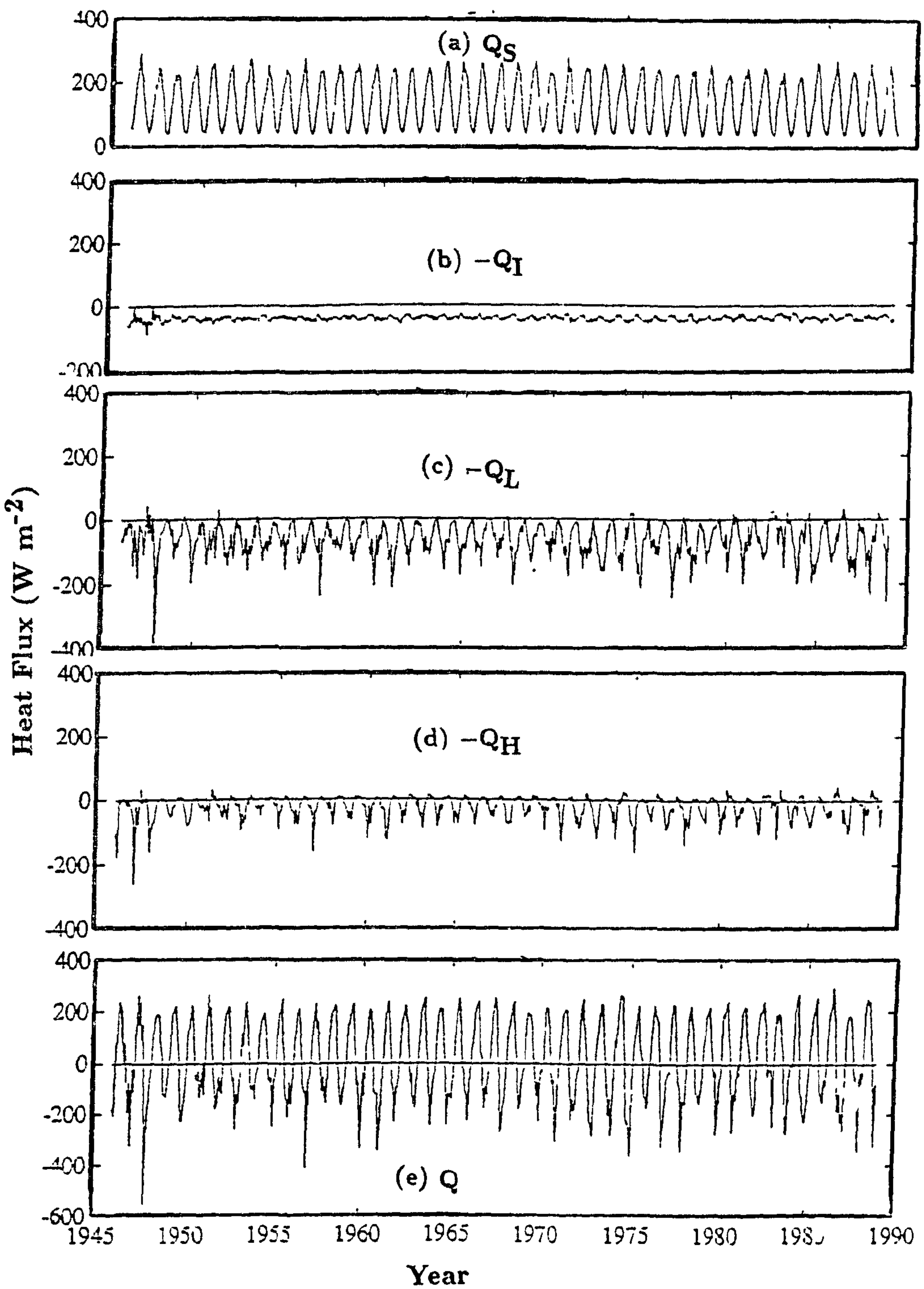

Figure 6.7: Time series of the monthly estimates of the different components of the surface heat flux at S7, representative on the Scotian Slope.

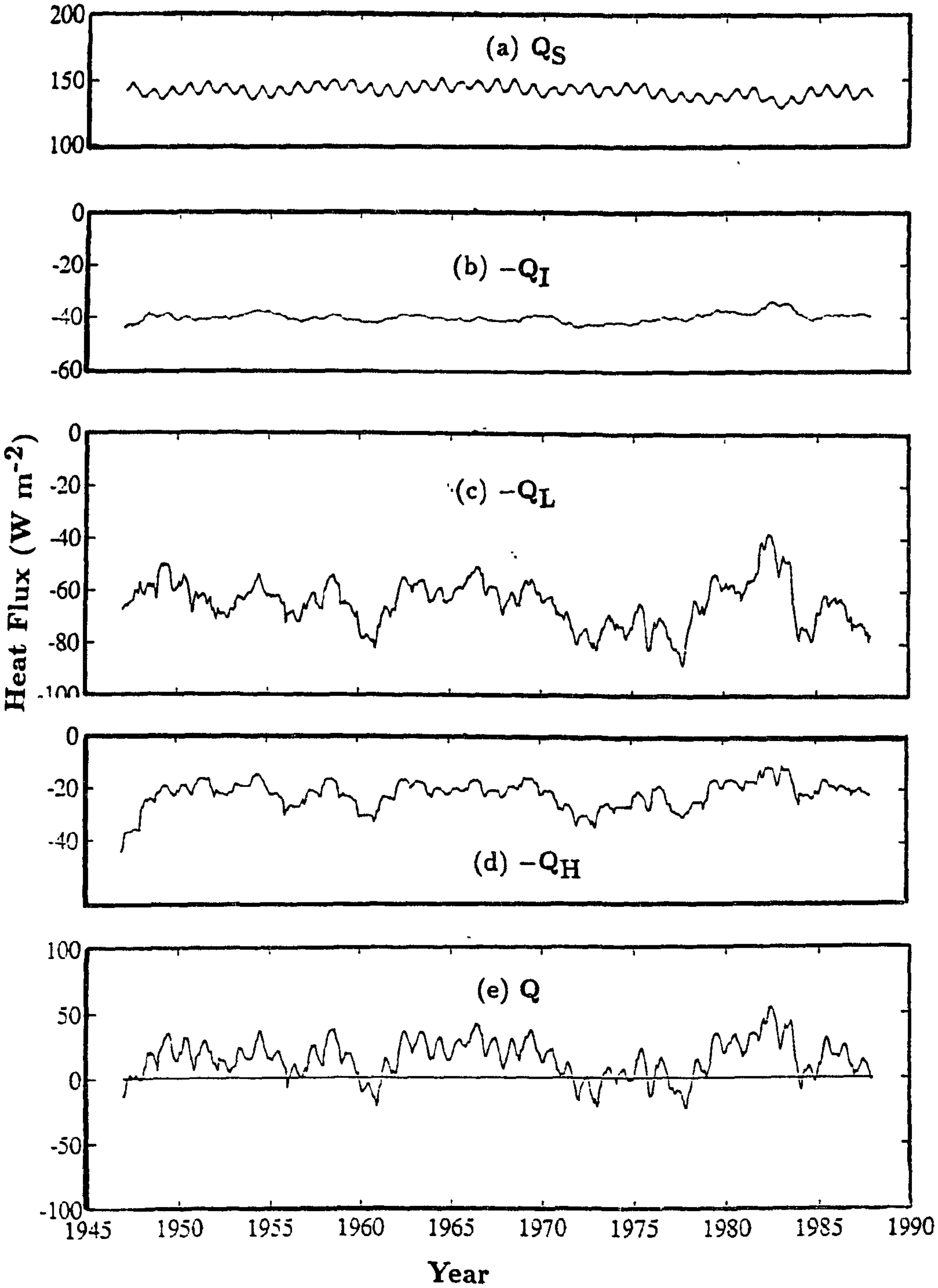

Figure 6.8: Time series of the low frequency components of the surface heat flux at S7, representative of the variability on the Scotian Slope.

6.3.2 Long Wave Radiation, $-Q_I$

Of the four components of Q, the long wave radiation is the least variable (Figures 6.5b and 6.7b), ranging typically between -30 and -50W m^{-2}. The interannual variability in the Q_I depends on the interacting effects of cloud cover, air temperature and the air-sea temperature difference.

6.3.3 Latent Heat Flux, $-Q_L$

The greatest heat loss from the ocean is through the latent heat flux. A heat flux of -255 W m^{-2} occurred in January, 1951 on the Shelf (Figure 6.5c) and -381 W m^{-2} in November, 1947 on the Slope region (Figure 6.7c). Occasionally, the ocean can gain heat through the latent heat flux. This happens when condensation dominates evaporation. Such was the case in May, 1952 when there was a heat input of 20W m^{-2} on the Shelf.

In addition to being the major source of heat loss by the ocean, the latent heat flux is also the most variable (see Figure 6.7c). It is worth noting that for the Slope region, more latent heat is lost and the latent heat flux is more variable than for the Shelf region. This might be caused by the interaction of the warm Gulf Stream water with the cold Labrador current. The meeting of these two current systems modifies greatly the sea temperature in the Slope region. The fluctuation of the sea temperature, coupled with wind effect, leads to a high rate of evaporation, hence a high latent heat flux. Generally, the latent heat flux is stronger in winter than in summer. The interannual variability in the latent heat flux is caused by the combined effect of wind speed and the difference in the air-sea specific humidity.

6.3.4 Sensible Heat Flux, $-Q_H$

The interannual variability in the sensible heat flux is controlled by the air-sea temperature difference and the wind speed. Ocean heat loss through sensible heat flux usually occurs in winter when the sea temperature is higher than the air temperature, while in summer there is sensible heat input into the ocean. Figures 6.5d and 6.7d show that more heat is lost in winter than is gained in summer. On the Shelf, a maximum heat loss of -246 W m^{-2} occurred in January, 1951 compared with a maximum heat gain of only 48 W m^{-2} in May, 1950. Similarly, the Slope region, lost up to -261 W m^{-2} in January, 1947 and gained a maximum of only 43 W m^{-2} in June, 1986. The sensible heat flux is the next most variable component in the net air-sea flux, after the latent heat flux. The low frequency components of the surface heat fluxes for S1 and S7 are shown in Figures 6.6 and 6.8 respectively. The near zero values of Q_H (Figure 6.6) in 1953-54 is probably due to filtering.

6.3.5 Net Surface Heat Flux Q

The net surface heat flux on the Shelf and Slope regions are shown in Figures 6.5e and 6.7e respectively. Note that the interannual variability in Q occurs mainly in winter. For example, on the Shelf, Q varies from -529 W m^{-2} in January, 1951 to -99 W m^{-2} in January, 1952. The winter variability in Q is caused, to a large extent, by winter variability in the latent heat and sensible heat fluxes.

6.4 Comparison of the Estimated Q with that of *Isemer and Hasse [1987]*

Isemer and Hasse [1987] independently estimated the different components of Q over the period 1941-1972, while the COADS data used to estimate the heat fluxes in this study (as mentioned before) cover the period 1946-1988. The parameterisations used in this study are the same as those of *Isemer and Hasse [1987]*. The comparison of the mean seasonal cycle of the two estimates for S7 is shown in Figure 6.9a. The figure shows that the two estimates of the Q_I, Q_L and Q_H agree well. The difference between *Isemer and Hasse*'s estimate of Q_S and mine is shown in Figure 6.9b to be due to the difference in the cloud cover used in the two estimates. *Isemer and Hasse*'s

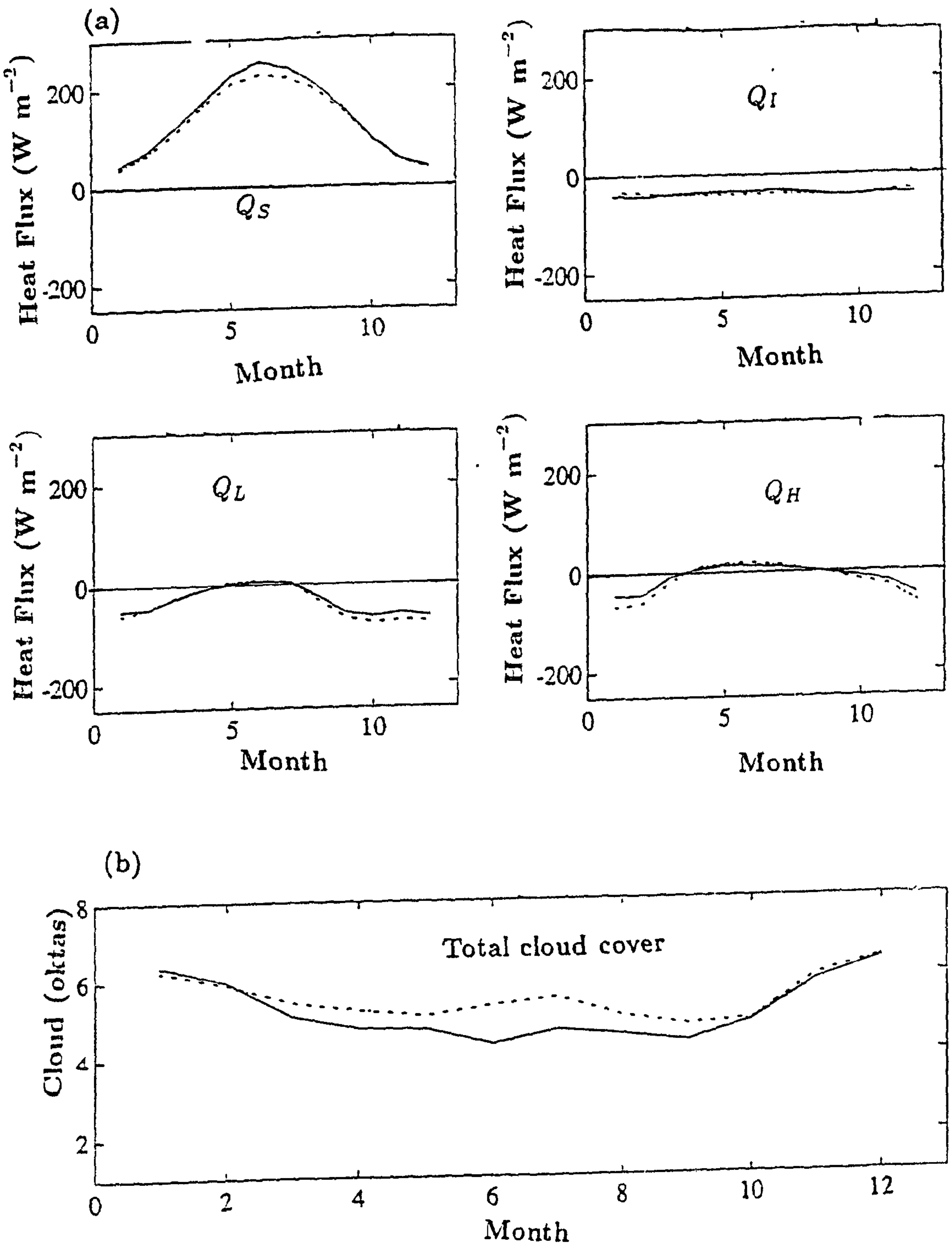

Figure 6.9: (a) The comparison between the mean seasonal surface heat fluxes at S7 estimated by *Isemer and Hasse [1987]* (dotted line) and this study (solid line). (b) The mean seasonal cloud cover, indicating that the difference between the above two estimates of Q_S is due to the difference in the cloud cover. The comparison is typical of other squares.

mean cloud cover in summer was larger than that of COADS, resulting in smaller Q_S. The overall agreement between the two estimates encourages me to use the COADS to study the interannual variability in Q.

6.5 Interannual Variability in the Surface Heat Flux Anomalies

The net surface heat flux anomaly $Q'(n,m)$ for a given year n and month m may be expressed as

$$Q'(n,m) = Q(n,m) - \overline{Q}(m), \qquad (6.8)$$

where

$$\overline{Q}(m) = \frac{1}{N}\sum_{n} Q(n,m), \qquad m = 1,12 \qquad (6.9)$$

is the long term monthly mean net surface heat flux taken over $N = 43$ years. Q is the monthly net surface heat flux. (Please note that the anomalies of all quantities referred to in this chapter are defined in a manner similar to (6.8), including SSTA.) For brevity, let prime ($'$) denote an anomaly. (For example, the net surface heat flux anomalies will be denoted by Q'). The sum of the latent and sensible heat flux anomalies is denoted by Q'_{LH}.

To determine the degree of variability in the surface flux anomalies, their standard deviations have been estimated. The estimates shown in Table 6.1a indicate that Q' is more energetic on the Slope region (S7, 60 W m^{-2}) than on the Shelf (S1, 47 W m^{-2}). The main contribution to the interannual variability in Q' comes from Q'_{LH} (see columns 2 and 3 in Table 6.1 and Figure 6.10) with the larger contribution resulting from Q'_L (column 4, Table 6.1). Q' is also more variable in winter than in summer, reflecting the stronger fluctuations of Q'_{LH} in winter. The fluctuations of Q'_S are stronger in summer. Throughout the year, Q'_I is the least variable, with a standard deviation of only about 6 W m^{-2}.

Square* #	Q' (W m^{-2})	Q'_{LH} (W m^{-2})	Q'_L (W m^{-2})	Q'_H (W m^{-2})	Q'_S (W m^{-2})	Q'_I (W m^{-2})	SSTA ($°C$)
(a) Year-round							
S1	47	42	24	21	15	8	1.2
S2	44	39	22	20	14	7	1.0
S3	40	36	21	18	14	6	1.0
S4	41	37	21	18	14	6	1.1
S5	45	40	25	17	14	6	1.2
S6	49	44	28	18	12	5	1.4
S7	60	55	36	23	12	7	1.5
(b) Winter (December, January and February)							
S1	73	66	33	37	6	9	1.2
S2	60	55	24	33	5	8	1.0
S3	59	55	26	31	5	7	0.9
S4	62	57	28	31	5	6	1.1
S5	65	60	32	30	4	6	1.2
S6	64	60	33	29	5	6	1.3
S7	81	76	46	36	4	7	1.6
(c) Summer (June, July and August)							
S1	29	19	15	6	22	6	1.3
S2	27	20	14	8	20	5	1.1
S3	30	24	17	9	20	6	1.2
S4	19	11	9	4	20	6	1.2
S5	25	16	13	5	21	6	1.3
S6	33	24	19	8	17	5	1.5
S7	32	25	20	7	16	5	1.6

* The 2° squares are shown in Figure 6.1.

Table 6.1: Standard deviation of the monthly anomalies (defined in the text).

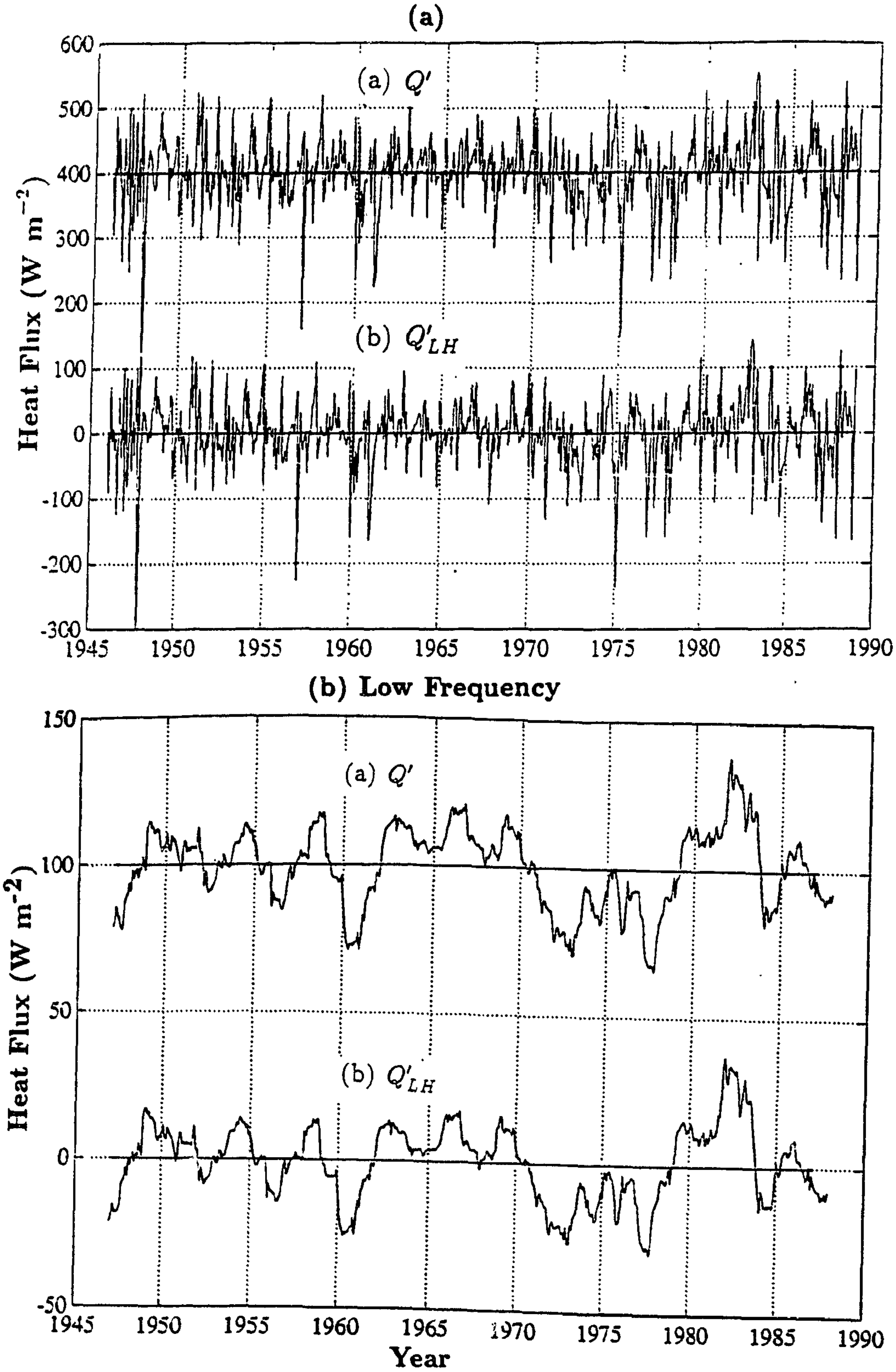

Figure 6.10: The interannual variability for S7 of (a) Q' and Q'_{LH} and (b) their low frequency version, in W m^{-2}, showing that Q' is mainly due to Q'_{LH}

	Q'	Q'_L	Q'_H	Q'_S	Q'_I	SSTA
Year-round	361	324	375	388	350	632
Winter	348	237	396	303	410	721
Summer	467	417	325	352	258	616

Table 6.2: Spatial scale, in kilometres, of the anomalies. (See text for the definitions of the anomalies)

6.5.1 Space and Time Scales

The spatial scales of the anomalies are found by computing the cross correlation coefficient, R, of the anomalies as a function of horizontal distance, X. The e-folding distance x_o is obtained by fitting the function

$$R = ce^{-X/x_o} \tag{6.10}$$

to the data. The plot of R versus X, for Q', is shown in Figure 6.11a. The stars show the data points while the solid line shows the line fitted according to (6.10). The intercept on the R axis, c, gives an estimate of the signal/noise ratio. In particular, $c = 1/[1 + (\sigma_n^2/\sigma_s^2)]$, where σ_n^2 and σ_s^2 are the variance of the noise and signal respectively. If $\sigma_n^2 = 0.2$ and $\sigma_s^2 = 0.8$, then $c = 0.8$. Table 6.2 shows the e-folding distances of the anomalies. The spatial scale of Q' ranges between 348 km in winter and 467 km in summer. Like Q', the spatial scale of Q'_L is larger in summer (417 km) than in winter (237 km). In contrast, the horizontal scales of Q'_I and Q'_H are larger in winter than in summer.

Similarly, the time scale is estimated by computing the autocorrelation function of the anomalies. In Figure 6.11, the Q' is the average of the 7 squares. Generally, the decay time scale for all the surface heat flux anomalies is less than one month.

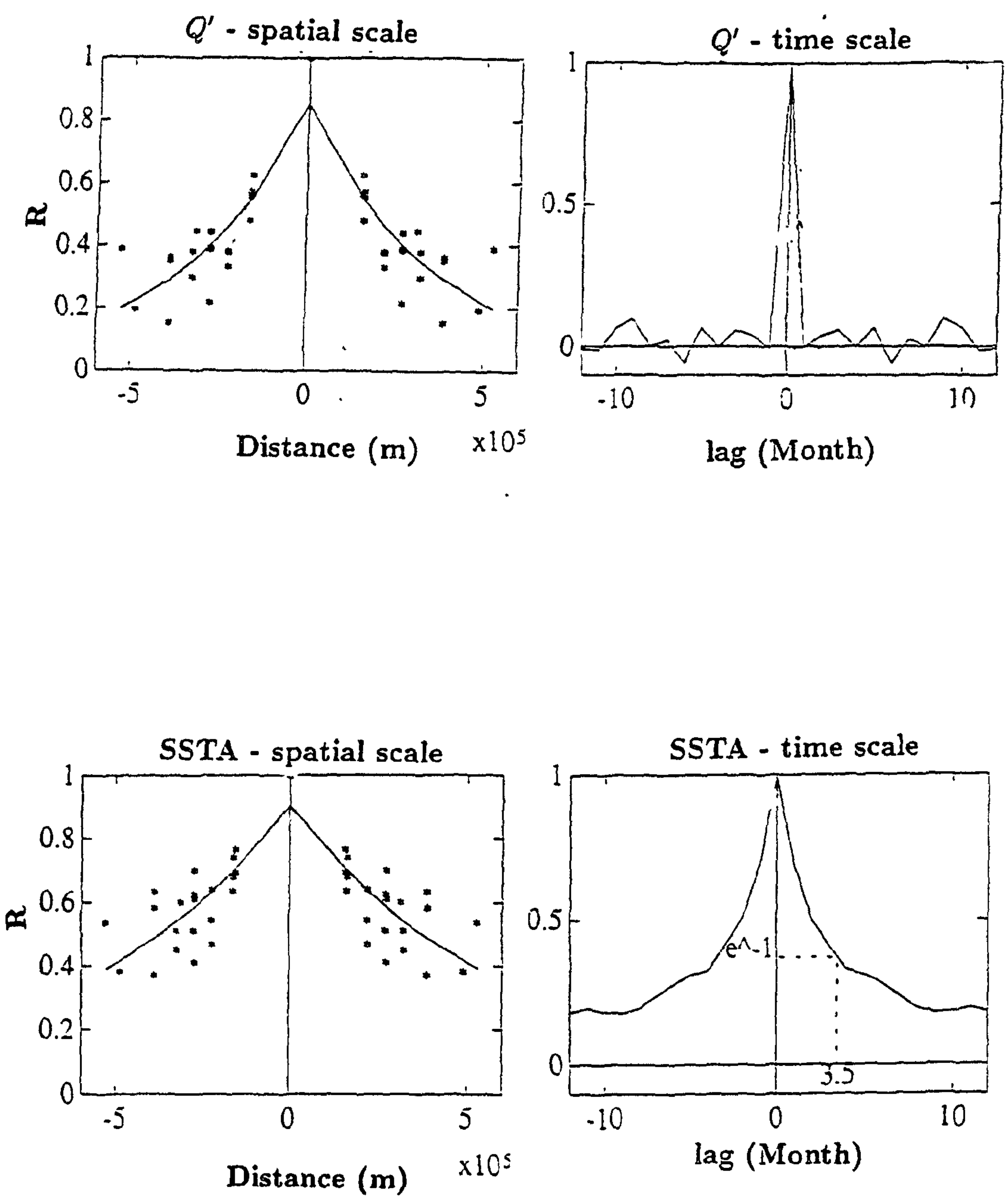

Figure 6.11: A plot showing how the spatial and time scales of (a) Q' and (b) $SSTAs$ are determined. R is the correlation coefficient. The e-folding time scale is shown by the dotted line.

6.5.2 Persistence of Q'

Persistence of Q' may also be quantified seasonally, following *Thompson et al. [1988]* using the estimator

$$\hat{R}(m_1, m_2) = \frac{\sum_n Q'(n, m_1) Q'(n, m_2)}{\left[\sum_n Q'^2(n, m_1) \sum_n Q'^2(n, m_2)\right]^{1/2}} \tag{6.11}$$

where $\hat{R}(m_1, m_2)$ is the sample correlation between Q' in month m_1 and Q' in month m_2. Where m is more than 12, then the year n increases accordingly. The persistence of Q' starting with June as the base month is shown in Figure 6.12a. The main point from the figure is that generally Q' is not persistent beyond 1 month, irrespective of the base month used.

6.6 Interannual Variability in the SSTAs

6.6.1 Observations

The interannual variability in the COADS SSTAs at S1, representative of the variability on the Shelf, and S7, representative of the Slope region, is shown in Figures 6.13a and b respectively. (The variability in the other five squares are shown in Appendix 5.) A typical value of the monthly SSTAs in both the Shelf and Slope region is $2°C$. Anomalies with magnitude up to $5°C$ have also been observed. Such high variability, as shown in Figures 6.1, 6.2 and 6.3, makes this region the most energetic sea surface temperature region in the whole of North Atlantic. The standard deviation of the SSTAs, shown in column 8 of Table 6.1 varies between 0.9 and $1.6°C$, with the most energetic area located offshore.

An important feature of the SSTA time series (Figure 6.13a) is the downward trend between 1951 and 1966. The SSTA cooled from about $3°C$ in 1951 to about $-4°C$ (about the mean) in 1966, and increased again to about $2°C$ in 1969. Thereafter,

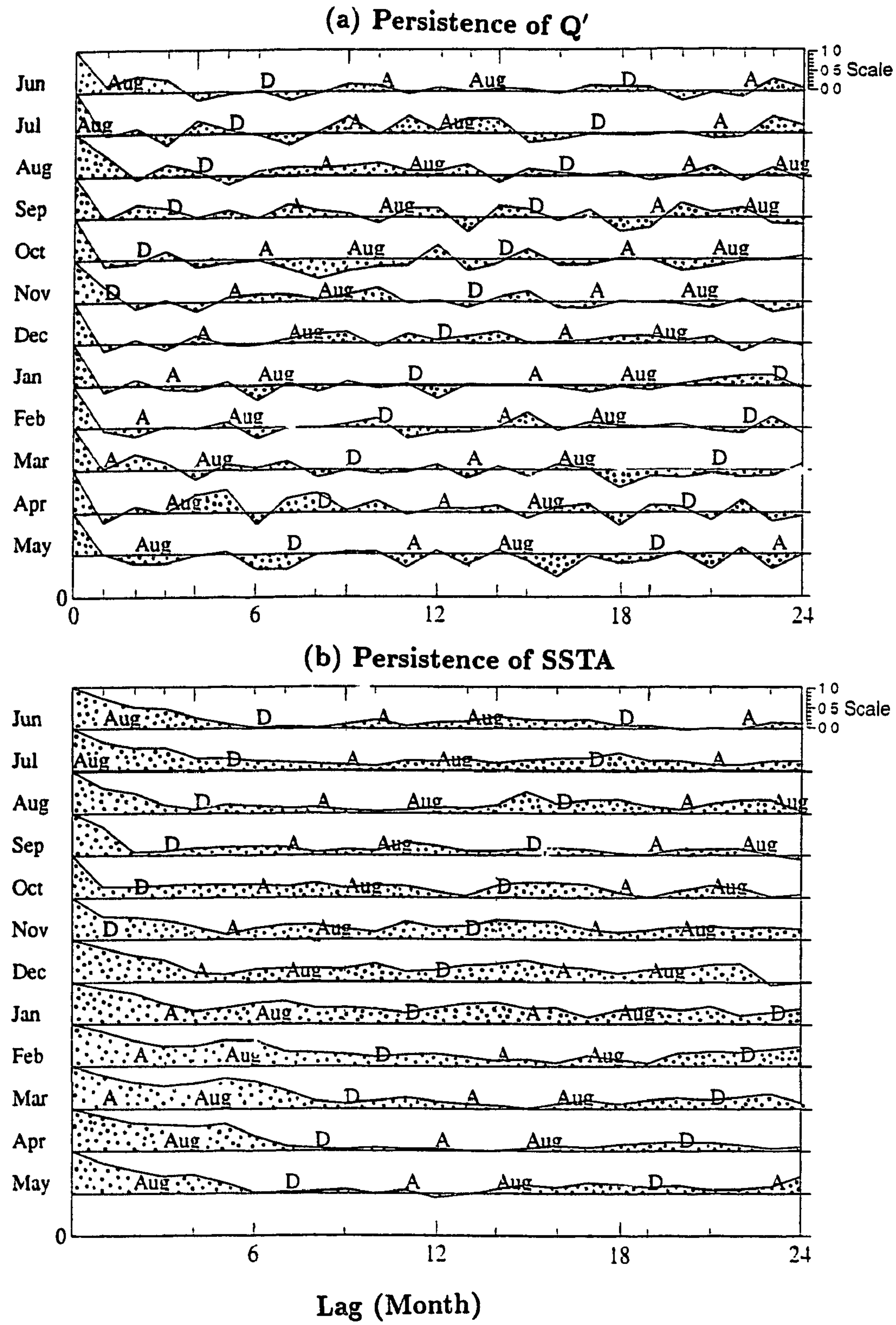

Figure 6.12: A plot of the autocorrelation function, showing the persistence of (a) Q' and (b) SSTA, according to base month beginning with June.

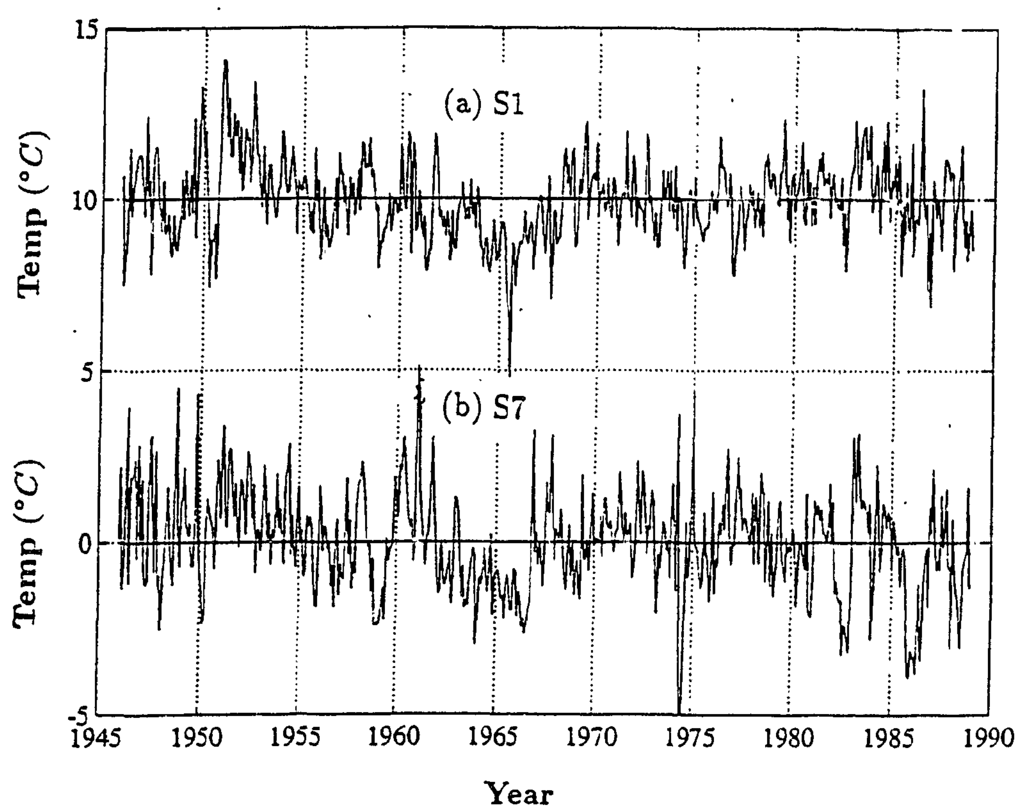

Figure 6.13: A time series of the observed SSTAs in $^{\circ}C$ at (a) S1 and (b) S7.

there is no obvious trend in the SSTAs. A natural question that arises: what is the cause of the observed trend? This question will be tackled below.

6.6.2 Space and Time Scales

The spatial scales of the SSTAs, estimated in the manner described in Section 6.5.1, are shown in column 7 of Table 6.2. The horizontal scale of the SSTA is large, more than 600 km (Figure 6.11c). The spatial scale is larger in winter (>700 km) than in summer (about 600 km). The e-folding time scale is about 4 months (Figure 6.11d). *Overall, the SSTAs have a larger spatial scale and a longer time scale than Q'.* At first thought, this result might be surprising since Q' (which is dominated by Q'_L and Q'_H) depends, to some extent, on SSTAs. But it is not surprising when one realizes that Q_H and Q_L depend on the air-sea temperature difference $T_a - T_s$ and not just on T_s. The e-folding time scale for T_s is about 4 months whereas for T_a, it is less than 1 month. Thus, T_a changes and adjusts faster than T_s. Hence, much of the variability in Q' could be due to fluctuation in T_a and q_a via Q'_L and Q'_H.

6.6.3 Persistence of the SSTA

The monthly persistence of the SSTAs, computed from (6.11) by replacing Q' with SSTA, is shown in Figure 6.12b. Notice that winter SSTAs persist longer ($>$ 5 months) than summer SSTAs. The strongest persistence occurs with February as the base month. In summer (August, for example), the SSTAs decorrelate after about 2-3 months. Another interesting feature is the re-occurrence of the winter anomalies in summer (August). Notice also that the correlation coefficient does not go to zero after 12 months lag. This indicates that the SSTAs persist from one year to the next and is related to the long term trend in the SST time series. These features were also found by *Thompson et al. [1988].*

One explanation for the increased SSTA persistence may be in the heat storage capacity of the upper ocean. The basic reason for the longer persistence of the winter SSTAs than those in summer may be related to the depth of the mixed layer in winter.

Winter, especially in the high latitudes, is characterized by low solar insolation and strong wind, in contrast with the high solar radiative flux into the ocean and reduced wind in summer. The low solar radiation combined with the wind stirring effect deepens the mixed layer and weakens the stratification of the upper water column. The high diffusivities, accompanying the weak stratification of the upper ocean, mix the surface temperature signal down to a great depth in winter. The signal is thus contained in a large volume of water, and it takes a long time to decay away. In summer the SSTAs reside in a shallow mixed layer, and quickly decays away with time. This argument was invoked by *Thompson et al. [1988]*.

The comparison between the scales of Q' and SSTA reveals that SSTA generally persist much longer than Q', and have a longer horizontal scale than Q'. The implication of this finding is that the small-scale Q' may not be the dominant cause of the SSTA on the monthly time scale considered in this study. Another possibility, of course, is that the Q' may be noise dominated. But the fact that there is some correlation in Q' between neighboring squares indicates that the Q' is not entirely noise.

6.7 Relationship between SSTA and Q'

The key objective in this subsection is to identify the causes of the interannual variability in SST. At the moment, the causes and effects of the SSTAs on the Scotian Shelf are not clearly understood. Generally, it is accepted that SSTAs may be generated by two factors: (i) atmospheric and (ii) oceanic. My purpose, here, is to determine the relative contributions of the two factors to the creation and decay of the SSTAs.

My approach is based, in part, on modelling. However, before any successful modelling of the SSTAs can be achieved, it is useful to establish empirical relationships between the SSTAs and the atmospheric and oceanic factors. *Gill [1983]* rightly observed that "much more work should be done in trying to relate the oceanic and atmospheric patterns by statistical techniques". To facilitate the interpretation of the empirical relationships that will be described, some background physics and a highly idealized coupled atmosphere-ocean model will now be outlined.

A simple coupled atmosphere-ocean temperature equation may be written

$$\frac{\partial T_a}{\partial t} = -\lambda_a(T_a - T_s) + F_a \tag{6.12}$$

$$\frac{\partial T_s}{\partial t} = \lambda_s(T_a - T_s) + F_s \tag{6.13}$$

where the subscripts a and s refer to air and sea respectively. λ is a feedback coefficient. $1/\lambda_s$ is typically 4 months while $1/\lambda_a$ is less than 1 month. Thus T_a responds faster to a given forcing than T_s. The first terms on the RHS of (6.12) and (6.13) represent forcing by the latent and sensible heat flux, Q_{LH}. F is the forcing terms from other processes that are not included in Q_{LH}. For example, the atmospheric forcing, F_a, includes processes such as advection of cold/warm air, cloud cover, solar radiative, etc. that could change T_a. Similarly, the oceanic forcing, F_s, includes horizontal advection, cross-shelf mixing and river discharge that affect T_s. The goal here is to show how T_s and the heat flux are related when the system is forced by (i) F_a the atmosphere and (ii) F_s, the ocean. To solve for T_a and T_s in (6.12) and (6.13), let us assume that

$$T_{a,s} = T_{a,s}e^{i\omega t} \quad \text{and} \quad F_{a,s} = F_{a,s}e^{i\omega t}.$$

Equations (6.12) and (6.13) reduce to the matrix equation

$$\begin{bmatrix} \lambda_a + i\omega & -\lambda_a \\ -\lambda_s & \lambda_s + i\omega \end{bmatrix} \begin{bmatrix} T_a \\ T_s \end{bmatrix} = \begin{bmatrix} F_a \\ F_s \end{bmatrix} \tag{6.14}$$

Hence

$$\begin{bmatrix} T_a \\ T_s \end{bmatrix} = \frac{1}{\text{Det}} \begin{bmatrix} \lambda_s + i\omega & \lambda_a \\ \lambda_s & \lambda_a + i\omega \end{bmatrix} \begin{bmatrix} F_a \\ F_s \end{bmatrix} \tag{6.15}$$

where

$$\text{Det} = (\lambda_a + i\omega)(\lambda_s + i\omega) - \lambda_a \lambda_s \tag{6.16}$$

From (6.15), one obtains

$$T_a = \frac{1}{\text{Det}} \left[(\lambda_s + i\omega) F_a + \lambda_a F_s \right], \tag{6.17}$$

$$T_s = \frac{1}{\text{Det}} \left[\lambda_s F_a + (\lambda_a + i\omega) F_s \right], \tag{6.18}$$

and hence

$$T_a - T_s = \frac{i\omega}{\text{Det}} (F_a - F_s) \tag{6.19}$$

Note that (6.19) is an expression of the latent and sensible heat parameter, and the long wave radiative flux. Other forcing that could affect both T_a and T_s include the solar radiative flux and the atmospheric humidity.

Atmospheric Forcing (by $\mathbf{F_a}$): Setting $F_s = 0$ in (6.18) and (6.19), it is clear that T_s and $T_a - T_s$ are in quadrature and hence the correlation between T_s' and Q_{LH}' is zero. Thus when SSTAs are generated directly by atmospheric factors (F_a), the SSTAs and Q' have zero correlation at zero lag.

Oceanic Forcing (by $\mathbf{F_s}$): Setting $F_a = 0$ in (6.18) and (6.19),

$$T_s = \frac{1}{\text{Det}} (\lambda_a + i\omega) F_s \tag{6.20}$$

$$T_a - T_s = \frac{-i\omega F_s}{\text{Det}} \tag{6.21}$$

Equations (6.20) and (6.21) are represented schematically in Figure 6.14. For $\lambda_a >> \omega$, T_s and the flux will be approximately in quadrature, implying a zero correlation. This means that if the atmospheric adjustment time scale (i.e., $1/\lambda_a$) is short compared to the oceanic forcing time scale (ω^{-1}), then T_s' and the Q_{LH}' will have a zero correlation. On the other hand, if $\lambda_a << \omega$, it is clear from (6.20) and (6.21) that T_s and the flux will be negatively correlated. This latter case corresponds

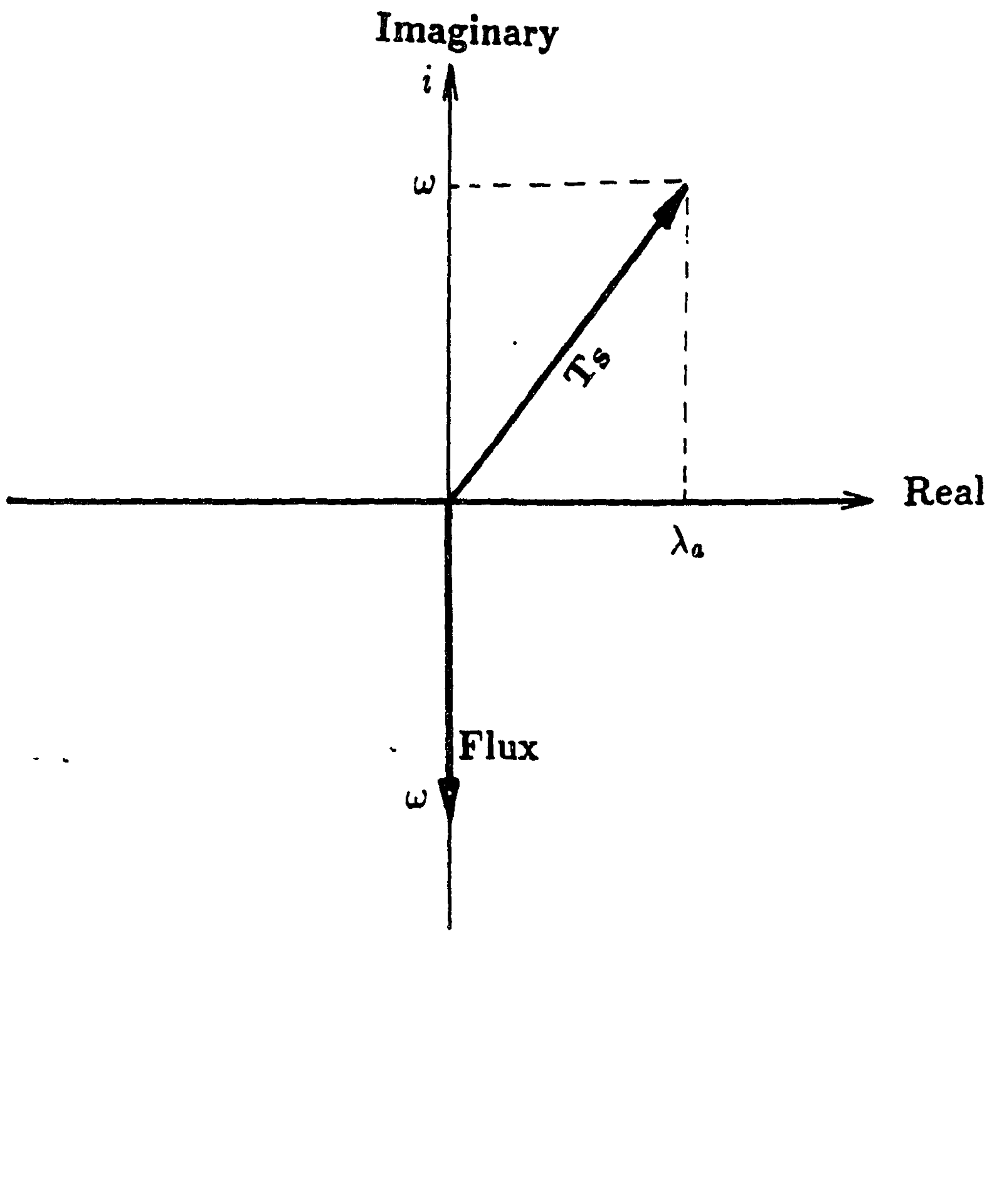

Figure 6.14: Schematic representation of the relationship between T_s and the heat flux $(T_a - T_s)$, for an oceanic forcing, F_s. See text for details.

to the situation in which it takes the atmosphere a very long time to respond to the oceanic forcing.

To illustrate forcing by the ocean, consider the effect of advection of cold water on the Scotian Shelf ($F_s < 0$). There are indications that the advection of cold water from the St. Lawrence Estuary affects the water temperature on the Scotian Shelf [*Sutcliffe et al., 1976]*. Advection of cold water will tend to reduce the T_s along with $q_s(T_s)$, the saturation specific humidity at the sea surface. If T_s is less than T_a, then clearly $Q > 0$. The situation will result in a heat gain by the ocean through Q_H. It is clear that the negative SSTA (created by the advection) will cause the positive Q'_{LH}. In this case, the SSTA and the Q' will be negatively correlated. This is also true if there is advection of warm water into a given region. Another example is the effect of river discharge. This increases the stability of the surface water, with the effect that the rate of mixing between the surface and the deeper layer is reduced.

The important points here are: (i) when SSTAs are directly caused by atmospheric forcing the correlation between the SSTA and Q' is zero at zero lag, and (ii) when SSTA are forced by oceanic factors, the correlation between the SSTA and Q' depends on the period of the forcing term and on the response time of the atmosphere. For an atmospheric response time that is short compared to the period of the oceanic forcing, the SSTA and Q' will have zero correlation, but for an atmospheric response time that is long, the SSTA and Q' will be negatively correlated, at zero lag.

6.8 Empirical Results

6.8.1 Correlation Analysis

The correlations between SSTAs and various atmospheric quantities are summarized in Table 6.3a. In addition to computing the correlation coefficient (R) for the whole year, I have computed it for different seasons. The data used in the analyses cover 1948-85. The winter months are December, January and February while summer is made up of June, July and August. *Overall, the correlation between the SSTAs and* *all atmospheric quantities (except T_a) is low and generally insignificant, even when the data are stratified into seasons.*

The correlation between the SSTAs and Q'_L is -0.27 with the SSTAs leading by about 1 month. The low correlation between the SSTAs and the Q' has several interpretations including (i) the SSTAs are forced by the atmosphere or SSTAs are forced by the ocean and the atmosphere responds quickly to the oceanic forcing, as explained above, (ii) the atmospheric and oceanic forcings are correlated, and (iii) the data are dominated by noise. There are at least two approaches to resolve this. One is to perform a cross spectral analysis between the SSTAs and the Q'. This would provide the amplitude and phase relationship between the two quantities. The other approach (the direct one), is to derive the SST using the model forced by Q. The phase relationship between Q' and the SSTAs are then taken care of by the model. The results from the two approaches are given below.

Note the significant negative correlation between the offshore wind anomalies and Q' (Table 6.3b). This is consistent with the simple coupled atmosphere-ocean model discussed earlier. Specifically in (6.19), let $F_a \propto -u_a$, where u_a is the offshore wind. Physically, F_a corresponds to horizontal advection of air temperature, as mentioned before. With this, (6.19) gives

$$T_a - T_s \propto \frac{-i\omega u_a}{i\omega(\lambda_a + \lambda_s) - \omega^2} \tag{6.22}$$

For $\lambda_a + \lambda_s >> \omega$, $T_a - T_s \propto -u_a$, i.e., the flux and the offshore wind will be negatively correlated.

The zero correlation between the fluctuations in SSTAs and the alongshore sea level pressure (P_y) is not consistent with the results of *Thompson et al. [1988]*. In their analysis *Thompson et al. [1988]* used P_y as an index of the offshore geostrophic wind. They correlated the winter wind (which was the average of November-February) with the February SSTAs, and found a correlation of -0.65. The basic difference between the present work and that of *Thompson et al.'s [1988]* is that the present work uses monthly mean anomalies - no averaging has been done.

The correlation between the SSTAs and some oceanic variables is shown in Table

(a) Correlation between monthly SSTAs and atmospheric anomalies on the Scotian Shelf.

Variable	Variable symbol	R Year-round	R Winter	R Summer
Net surface heat flux	Q'	-0.02	0.09	-0.09
Offshore wind	u'_a	-0.15	-0.15	-0.05
Alongshore sea level pressure	$-P'_y$	-0.05	-0.10	0.02
Air temperature	T'_a	0.48*	0.45*	0.50*
Sea minus air temperature	$(T_s - T_a)'$	-0.03	-0.07	0.09

(b) Correlation between some atmospheric anomalies.

Variables	R Year-round	R Winter	R Summer
Q' and u'_a	-0.58*	-0.65*	-0.41*
T'_a and u'_a	-0.44	-0.50*	-0.11

* Significant at 5% level.

(c) Correlation between SSTAs and oceanic variables: subsurface temperature in Emerald Basin and river discharge (Rivsum) anomalies.

Variable	R	Comments
T'_{20m}	0.70	In phase with SSTAs
T'_{50m}	0.46	In phase with SSTAs
T'_{75m}	0.36	SSTAs lead by about 1 month
T'_{100m}	0.32	SSTAs lead by about 2 months
Rivsum anomalies	0.25	SSTAs lead by about 10 months

Table 6.3: Empirical relationships.

6.3c. The monthly mean surface and subsurface temperatures are those of Emerald Basin (on the Scotian Shelf) covering 1948-85. Rivsum is the sum of the discharge from St. Lawrence, Ottawa and Saguenay rivers. The results show positive correlation between the SSTAs and the oceanic variables. In particular, the correlation analysis shows that the SSTAs are in phase with the water temperature anomalies of the top 50 m (Figure 6.15), and also that the SSTAs lead the deep water (> 100 m) anomalies. The cross spectral analysis will provide more information on the phase relationships of the water temperature anomalies.

6.8.2 Cross spectral Analysis

Figure 6.16 gives the results of the cross spectral analysis of the observed SSTAs for Emerald Basin and the COADS Q'. The analysis shows that most energy of the observed SSTAs is in the low frequency band, at periods greater than 1 year. In contrast Q' has a white spectrum. Overall, the coherence between the SSTAs and Q' is low, although there is a suggestion of significant coherence at periods of 15-22 months, with a phase of about 90°. This quadrature relationship at low frequency suggests that the SSTAs are driven, in part, by Q' (according to the simple argument presented earlier) but only 22% of the SSTAs may be explained by Q' in this frequency range.

The cross spectral analyses between the observed SSTAs and the subsurface temperature anomalies are presented in Figure 6.17. Shown are the spectral estimates between the SSTAs and the water temperature anomalies at 50 m depth (Figure 6.17a) and that between the SSTAs and the water temperature anomalies at 100 m depth (Figure 6.17b). Most of the energy of the SSTAs and the subsurface temperature anomalies occurs at low frequencies and increases with increasing water depth. The phase spectra show that the SSTAs are in phase with the temperature anomalies down to 50 m depth. The SSTAs lead the 100 m temperature anomalies by about 2 months, which is consistent with the results of the correlation analysis shown in Table 6.3c.

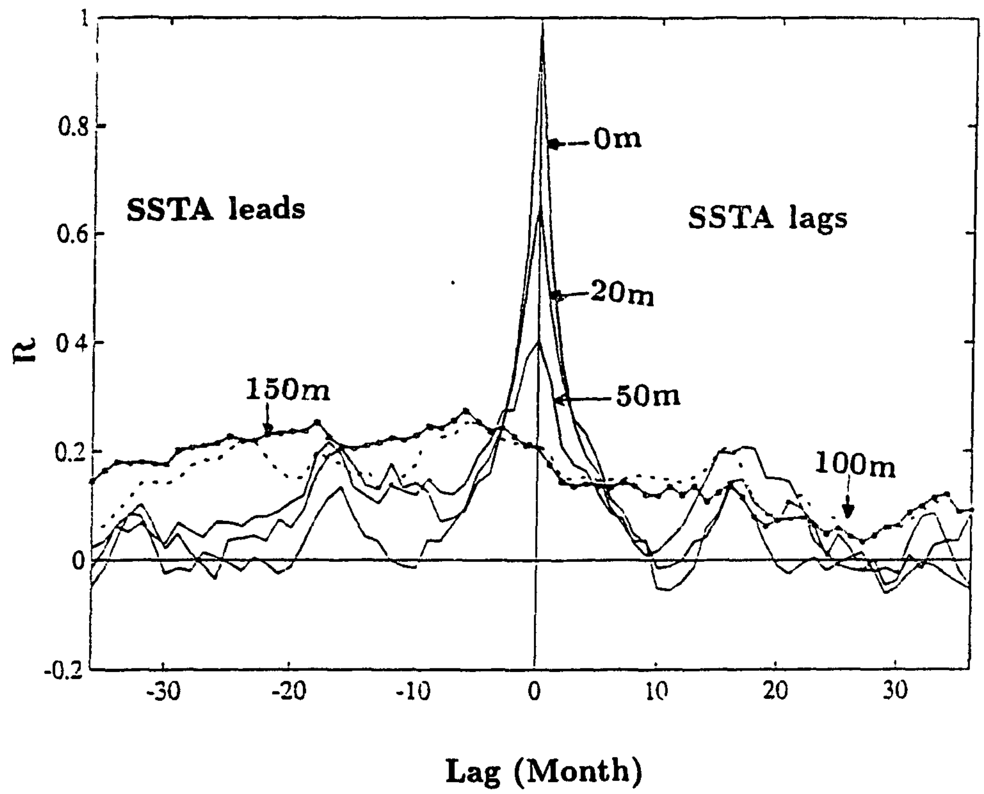

Figure 6.15: The cross correlation function, R, between the SSTAs and the subsurface temperature anomalies for Emerald Basin, with the SSTAs as the reference.

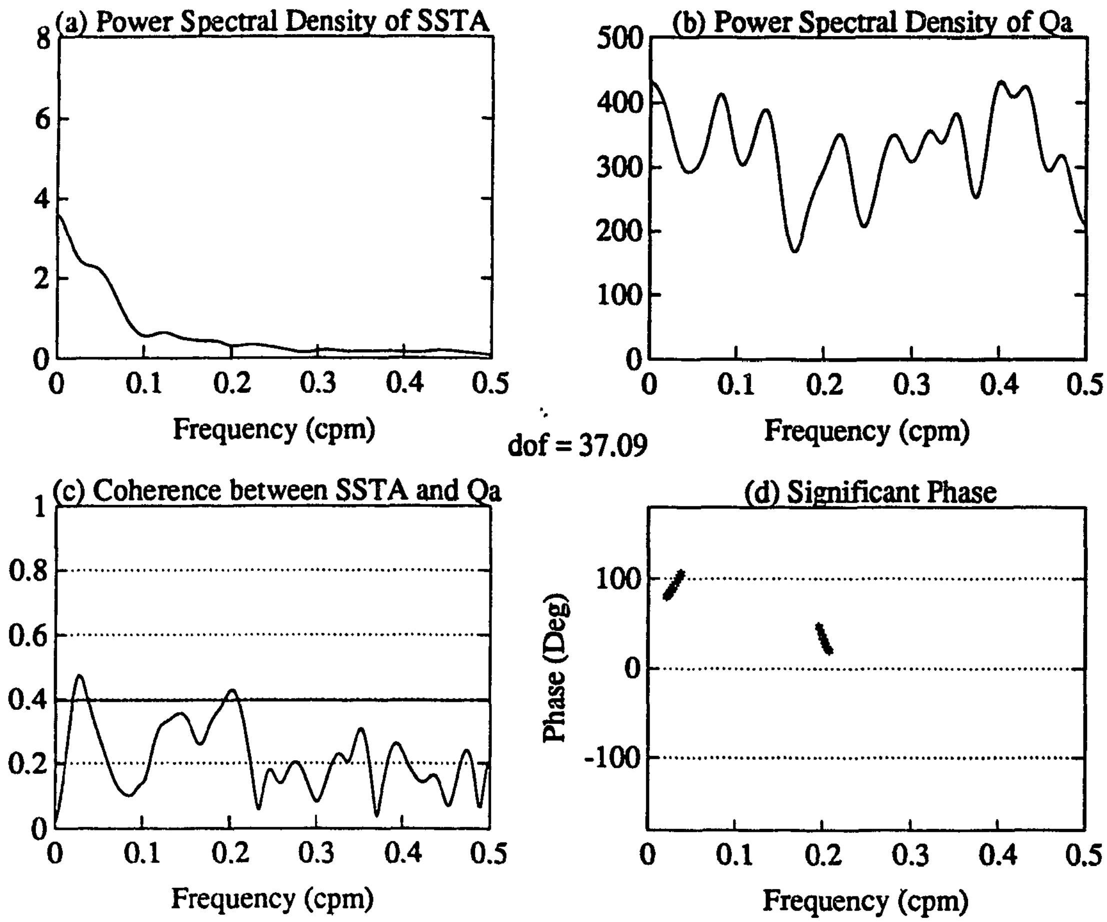

Figure 6.16: Power spectra of observed SSTAs and Q' including the coherence and phase between them. The horizontal line in the coherence spectrum (in this and subsequent plots) is the 5% significance level, and only the phases with significant coherences are plotted. dof denotes degrees of freedom.

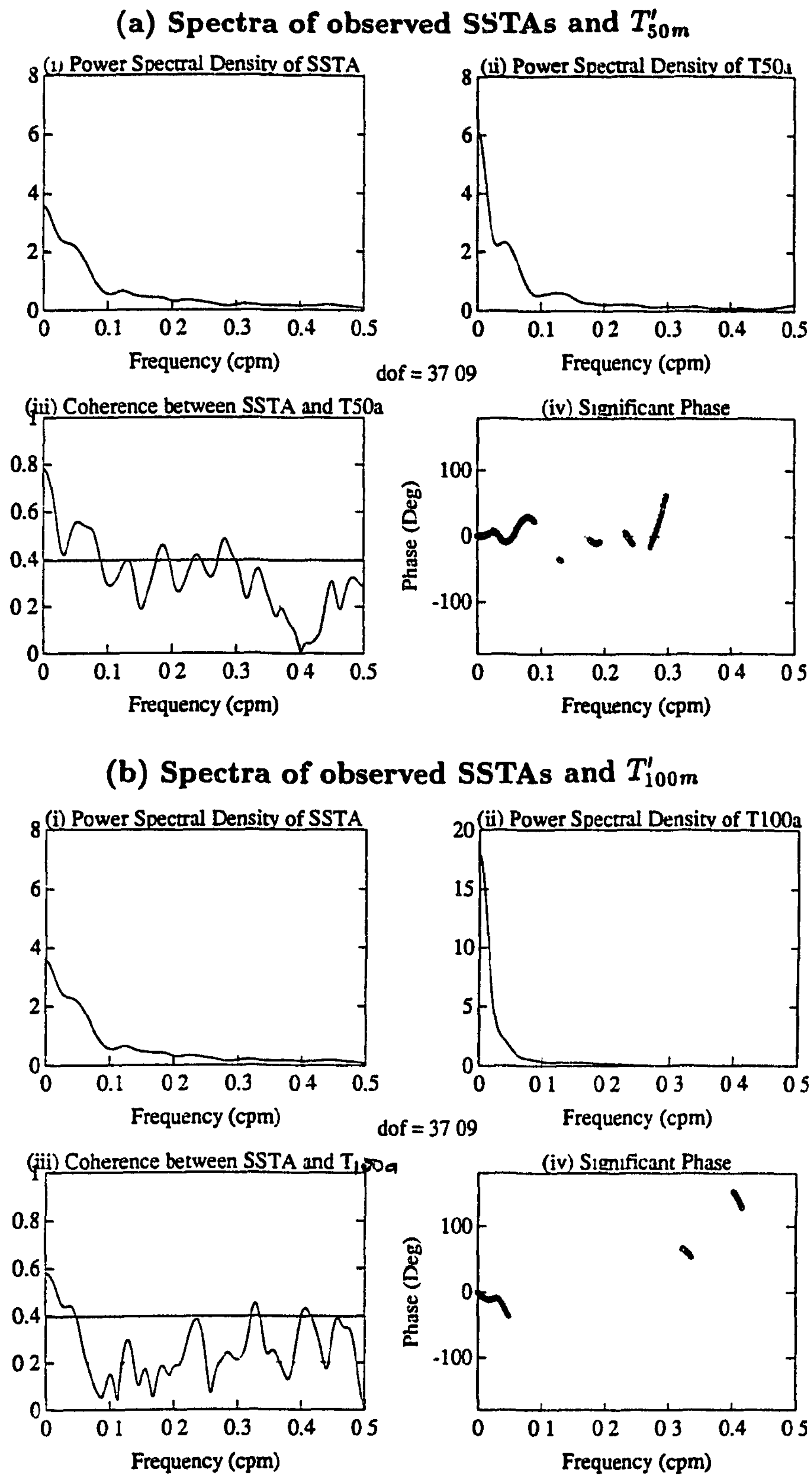

Figure 6.17. Power spectra of observed SSTAs, $T'_{50\mathrm{m}}$ (observed water temperature anomalies at 50 m depth), $T'_{100\mathrm{m}}$ and the coherence and phase between the SSTAs and the subsurface anomalies.

In summary, the empirical analysis gives no clear answer to the question of what causes the SSTA. The low correlation between the SSTA and Q', as mentioned earlier, might imply atmospheric forcing and might also mean oceanic forcing with short atmospheric response time. The important information from the cross spectral analyses is that at low frequencies, only a small fraction of the SSTA variance (about 22%), may be accounted for by the Q'.

6.9 Modelling of the SSTAs

6.9.1 Model

The equation for the water temperature anomaly may be expressed as

$$\frac{\partial T'}{\partial t} = \frac{\partial}{\partial z}\left(\widetilde{K_V}\frac{\partial T'}{\partial z}\right) + \Gamma' \tag{6.23}$$

where

$$\begin{aligned}\Gamma' = \quad & -\tilde{\underline{u}} \cdot \nabla T' - \tilde{w}\tfrac{\partial T'}{\partial z} + \widetilde{K}_H \nabla^2 T' \\ & +\tfrac{\partial}{\partial z}\left(K'_V \tfrac{\partial \tilde{T}}{\partial z}\right) - \underline{u}' \cdot \nabla \tilde{T} - w' \tfrac{\partial \tilde{T}}{\partial z} + K'_H \nabla^2 \tilde{T} \\ & -\tfrac{\partial}{\partial z}\left(\widetilde{K'_V \tfrac{\partial T'}{\partial z}}\right) + \widetilde{\underline{u}' \cdot \nabla T'} + \widetilde{w' \tfrac{\partial T'}{\partial z}} - \widetilde{K'_H \nabla^2 T'} \\ & +\tfrac{\partial}{\partial z}\left(K'_V \tfrac{\partial T'}{\partial z}\right) - \underline{u}' \cdot \nabla T' - w' \tfrac{\partial T'}{\partial z} + K'_H \nabla^2 T'\end{aligned} \tag{6.24}$$

The tilde ($\tilde{}$) denotes long term monthly mean while the prime ($'$) stands for the anomaly. (See section E.2 of Appendix E for the derivation of the anomaly equation.) Γ' includes the effects of mean horizontal and vertical currents $(\tilde{\underline{u}}, \tilde{w})$ and their anomalies $(\underline{u}', w')$ on the SSTAs. Also embodied in Γ' are the contributions of the mean horizontal mixing and its anomalies, together with the contribution of the anomalous vertical diffusivity (K'_v) to the development of the SSTAs. If we depth-integrate (6.23), we have

$$\int_{-h}^{0} \Gamma' \, dz = \frac{\partial}{\partial t} \int_{-h}^{0} T' \, dz - \frac{Q'}{\rho \, cp} + \widetilde{K_v} \frac{\partial T'}{\partial z}\bigg|_{-h} \tag{6.25}$$

As before, the right hand side of (6.25) is estimated from observations and Γ' is distributed with depth as

$$\Gamma'(z,t) = \zeta_s \left[\frac{\partial}{\partial t} \int_{-h}^{0} T' \, dz - \frac{Q'}{\rho \, cp} + \widetilde{K_v} \frac{\partial T'}{\partial z}\bigg|_{-h} \right] \tag{6.26}$$

where ζ_s is given by

$$\zeta_s = \frac{e^{z/\delta}}{\int_{-h}^{0} e^{z/\delta} dz} \tag{6.27}$$

To determine δ, I computed the correlation coefficient, R, between the temperature anomalies at various depth z (between 0 and 75 m). From the plot of $R = r_o e^{z/\delta}$ against z (not shown), $\delta \approx 50$ m was determined. (Note that for the seasonal case, $\delta = 30$ m)

The boundary condition at the surface is taken to be

$$\widetilde{K_v} \frac{\partial T'}{\partial z} = \frac{Q'}{\rho c_p} \tag{6.28}$$

At the bottom, the model is forced with the observed T', herein referred to as T'_b. The model uses seasonal values of $\widetilde{K_v}(z,t)$, estimated in Chapter 4.

6.9.2 Model Results

The predicted SSTAs when forced with Q', Γ' and T'_b are presented in Figure 6.18a. The correlation coefficient between the observed and the predicted SSTAs is $R = 0.62$. At 50 m depth the correlation between the observed and the predicted temperature anomalies increases to $R = 0.83$ (Figure 6.18b). Figure 6.20a shows the results of a cross spectral analysis of the observed SSTAs and predictions based on $Q' + \Gamma' + T'_b$

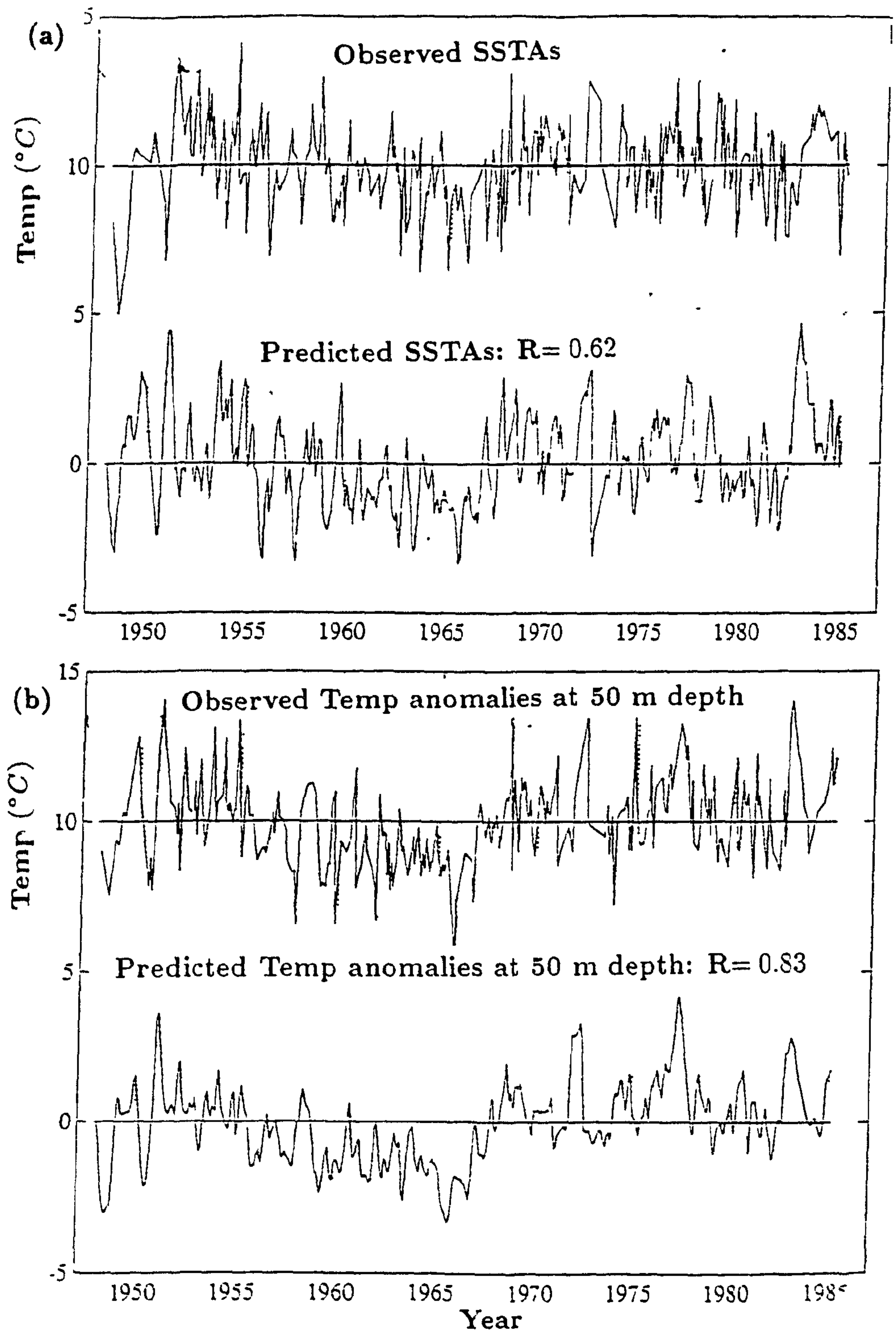

Figure 6.18: The comparison of the observed and predicted (a) SSTAs and (b) subsurface temperature anomalies at 50 m depth. R is the correlation coefficient between the observed and the predicted anomalies. (Please note the offset in the temperature axis)

(denoted by $T'_Q + T'_\Gamma + T'_b$). The squared coherence shows that the model can explain about 71% of the observed SSTAs for periods of about 12 to 24 months and the phase between them is zero.

(a) Contribution From Q'

By setting $\Gamma' = 0$ and $T'_b = 0$ in the model, the SSTAs produced by Q' alone are obtained (Figure 6.19b). These have a correlation of only 0.1 with the observed SSTAs. The diffusivities in the model act as a low pass filter on Q'. The power spectral densities of the observed SSTAs and those predicted from Q' (Figure 6.20) show that both quantities have most of their energy in the low frequencies. Estimates of the coherence and phase between the two quantities (Figure 6.20a) indicate that coherence, significant at 5% level, only occurs at a period of about 20 months with a phase of about 70°. The coherency of 0.48 means that at that frequency, about 23% of the observed SSTA power may be accounted for by Q'.

(b) Contribution From Γ' and T'_b

The SSTAs due to Γ' alone (Figure 6.19c) have a correlation of 0.33 with the observed while the correlation between the SSTAs from T'_b alone (Figure 6.19d) and the observed is 0.26. The predicted SSTAs from a combination of Γ' and T'_b gives a correlation of 0.57 with the observed. The power spectral density of T'_Γ and T'_b and the coherence and phase between them and the observed SSTAs are shown in Figure 6.21. Notice that the predicted SSTAs due to T'_b still appear to lag the observed SSTAs (as seen in the correlation analysis). This suggests that T'_b is not the only forcing term, and presumably may be part of the response from forcing by Γ'.

The spectral estimates of the predicted SSTAs from Q', Γ', T'_b and a combination of them are summarized in Table 6.4.

The important point is that the SSTAs from the different forcings appear to be significant at different frequencies. For periods between 12 and 24 months, the SSTAs from Q' account for about 23% of the observed SSTAs whereas at a period of about 13 months, Γ' alone explains about 66% of the observed SSTAs. The major cause of

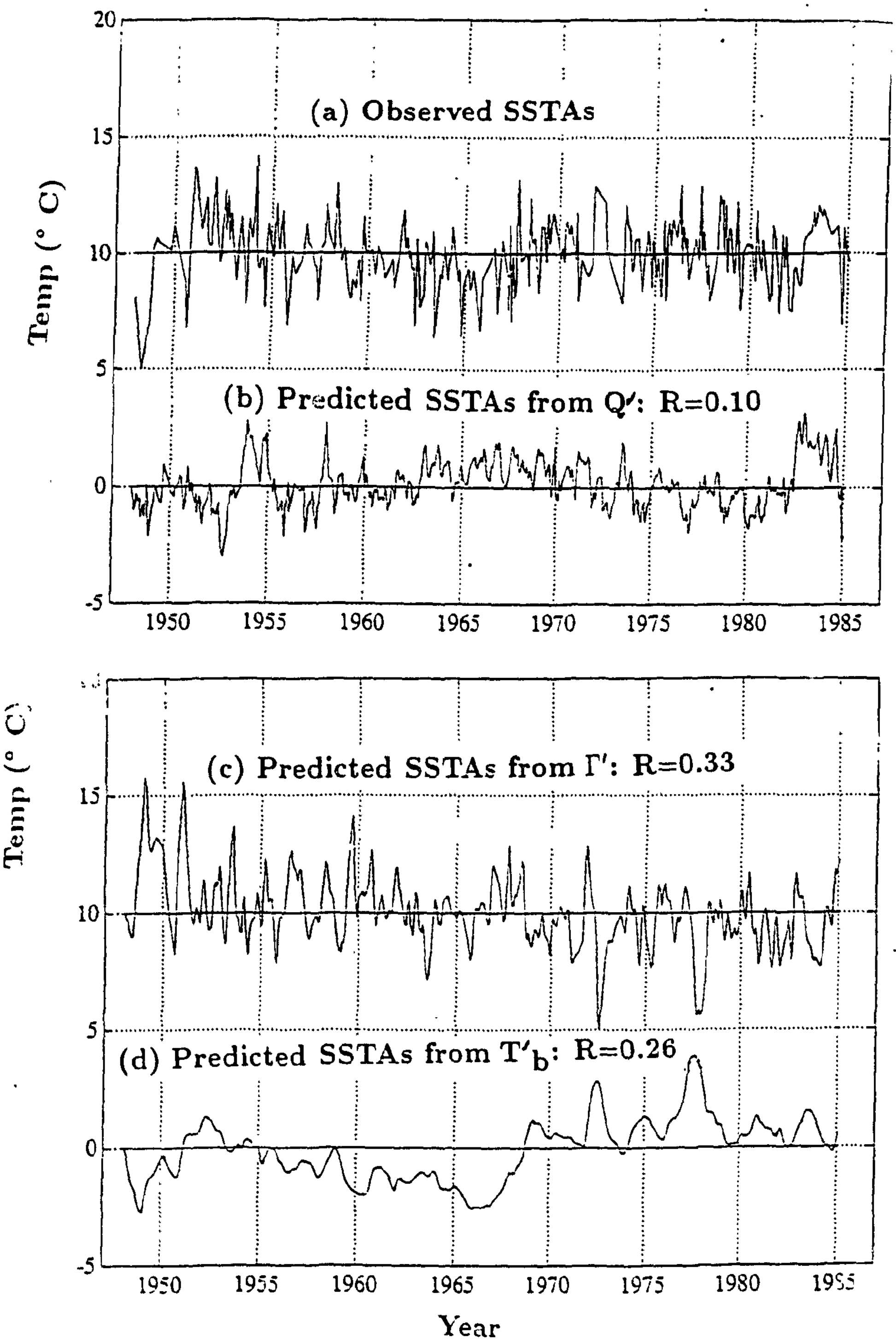

Figure 6.19: The contributions of Q', Γ' and T_b' to the generation of the SSTAs on the Scotian Shelf (Emerald Basin). R is the zero-lag correlation between the predicted and the observed SSTAs. (Please note the offset in the temperature axis)

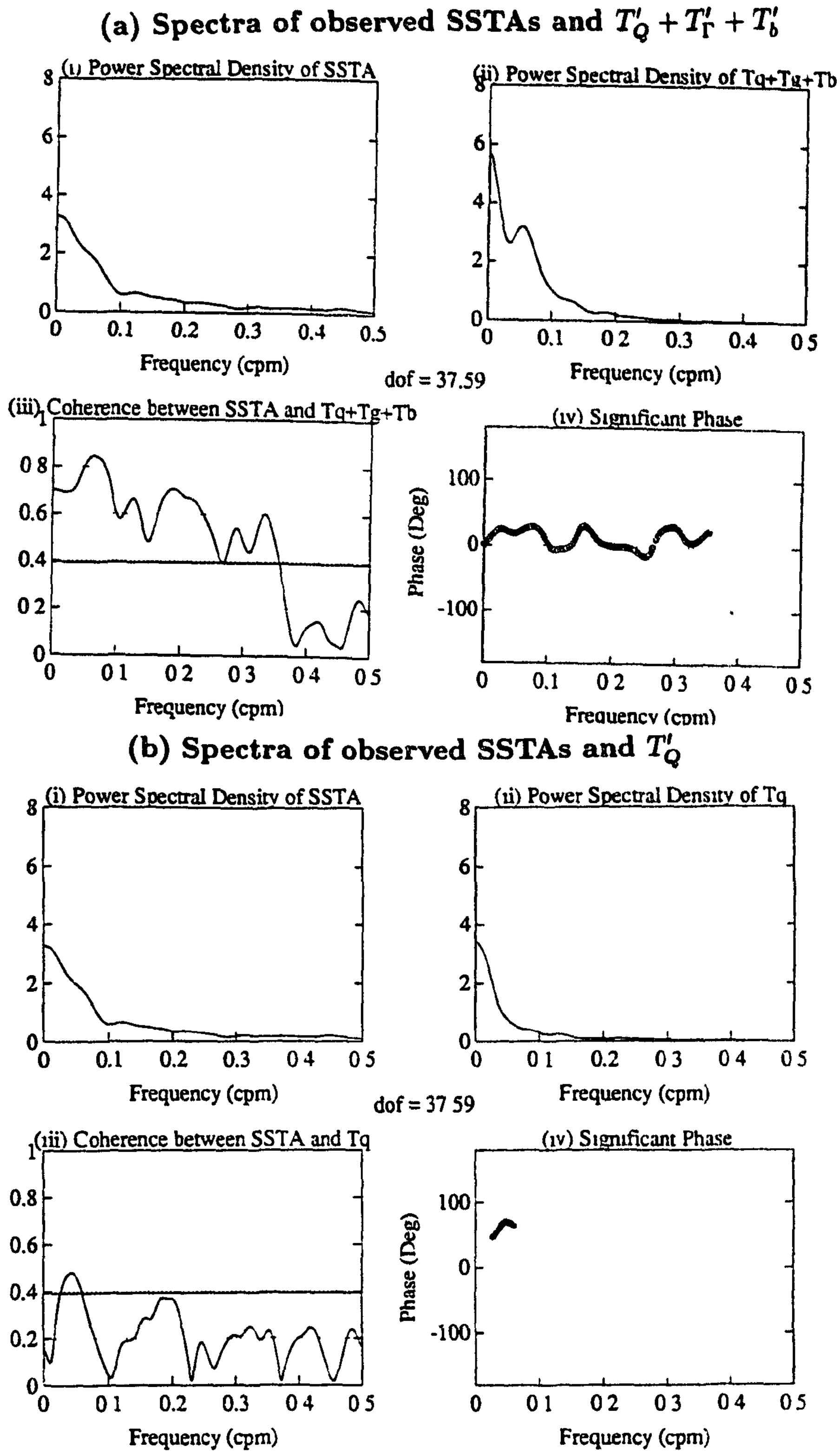

Figure 6.20: Power spectra of observed SSTAs, $T'_Q + T'_\Gamma + T'_b$, T'_Q and the coherence and phase between the SSTAs and the other quantities.

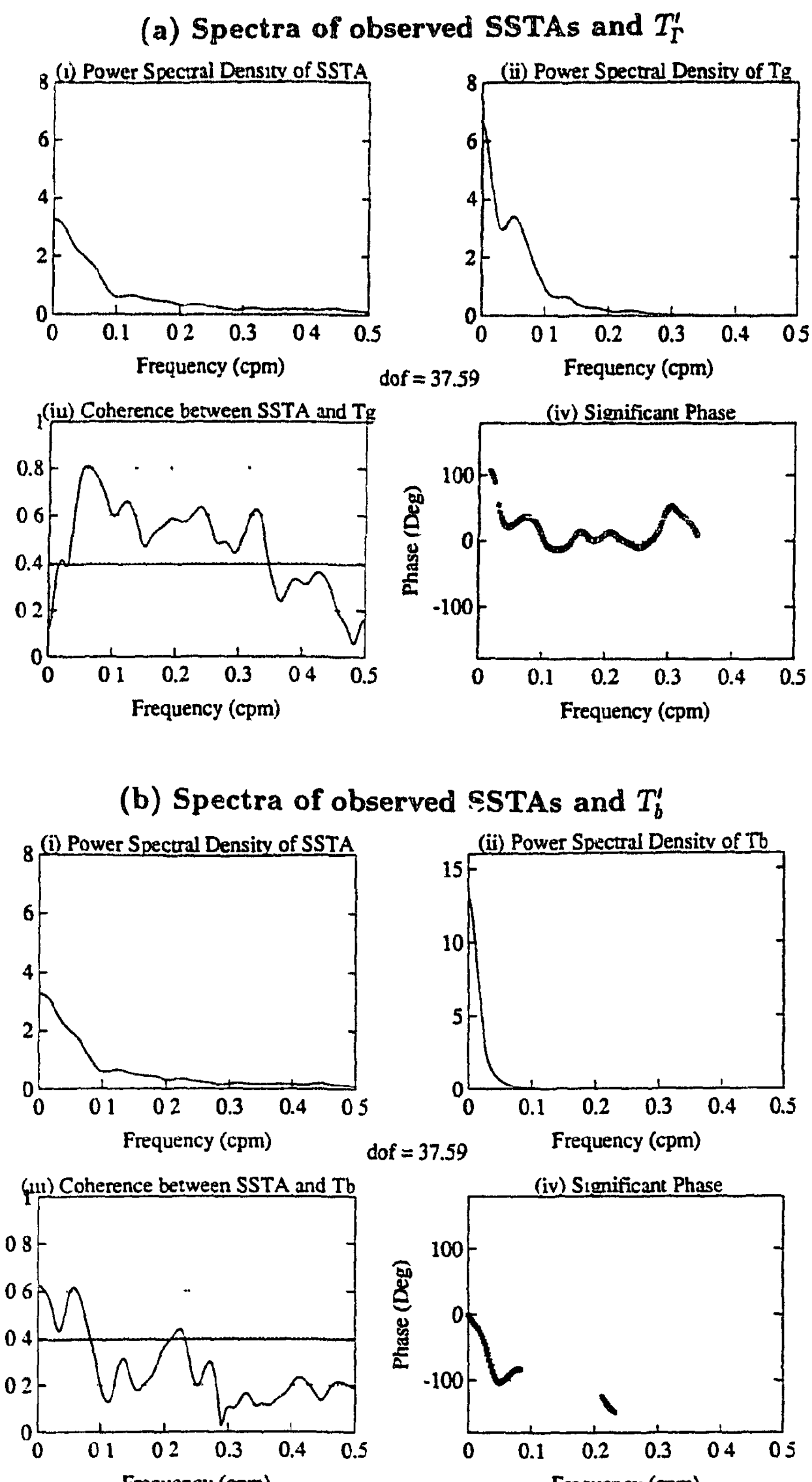

Figure 6.21: Power spectra of observed SSTAs, T_Γ', T_b' and the coherence and phase between the SSTAs and the other quantities.

Quantity	Maximum Squared Coherence* (%)	Period (month)	Phase* (Deg)
$T'_Q + T'_\Gamma + T'_b$	71	18.6	25
T'_Q	23	20.3	70
$T'_\Gamma + T'_b$	63	12.7	29
T'_Γ	66	13.1	37
T'_b	39	12.0	-83

* Significant at 5% significance level

Table 6.4: Spectral estimates between the observed and the predicted SSTAs.

the SSTAs, again, appears to come from Γ' - the ocean.

6.10 Oceanic Sources of the SSTAs

An important feature of the temperature record, as mentioned before, is the cooling trend from 1950-65, that is observed both at the surface and at depth. The goal of this section is to explore the possible oceanic sources of the cooling trend in particular, and of the whole temperature anomaly series in general. To tackle this problem, it is useful to consider the surface and the deep water temperature anomalies together. Figure 6.22a shows the plots of the raw temperature anomaly series, from 1948-87, for Emerald Basin. At depth the number of observations is lower than at the surface. Table 6.5 lists the number of observations that are used to compute the long-term monthly means, from which the monthly anomalies are determined. The total number of observations at each depth is shown in Table 6.5b, while Table 6.5c shows the number of gaps of various lengths (n in months) occurring in the raw anomaly record. For example, at 200 m depth, a 10-month (n) gap occurs 5 times in the raw anomalies series. To fill in the missing data, the series are linearly interpolated between two adjacent months with data. Figure 6.22b shows the time series plots of the interpolated series. The description of the data is presented to provide a background for the interpretation of the statistical analyses that follow.

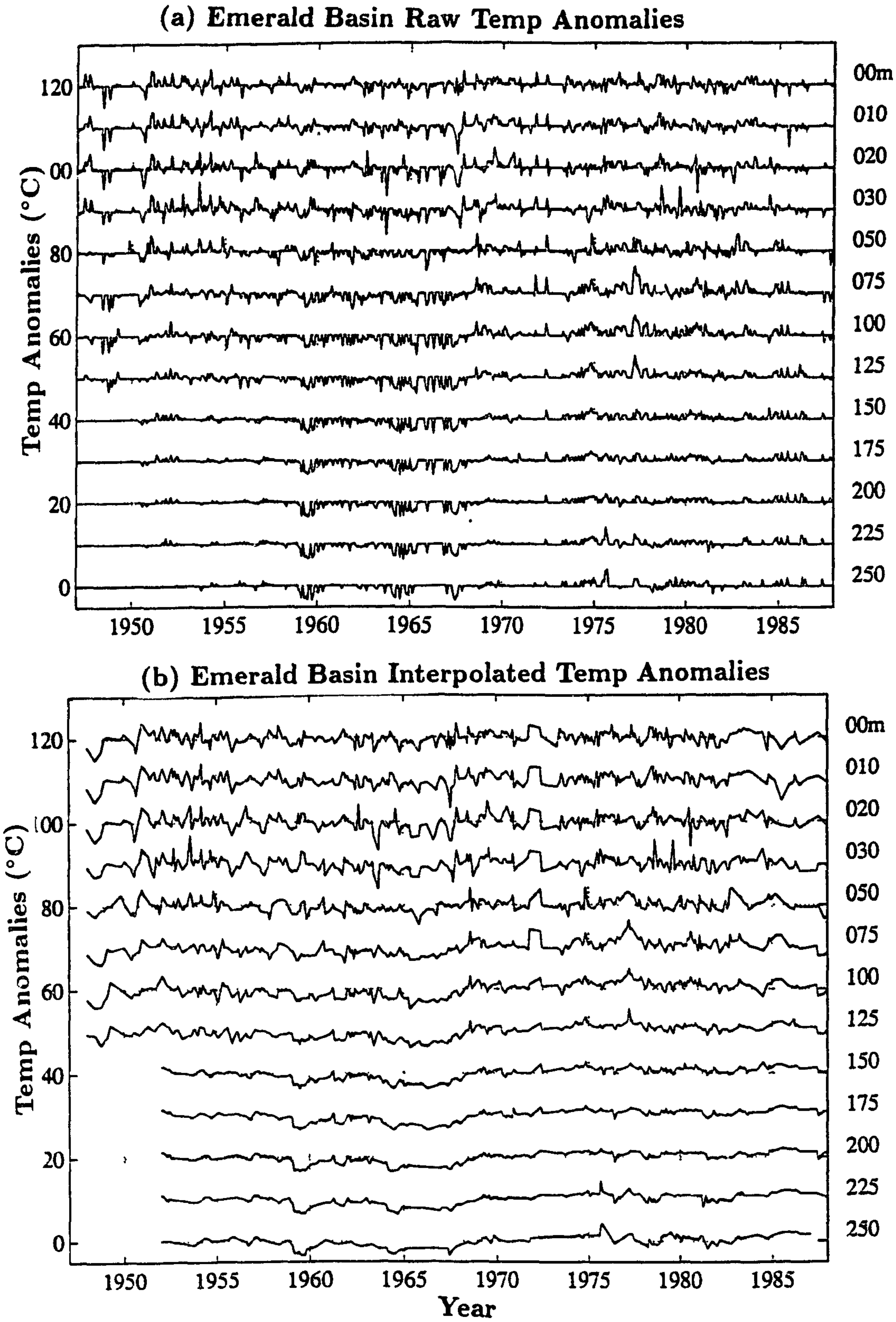

Figure 6 22: Time series plots of the (a) raw and (b) interpolated temperature anomalies for Emerald Basin.

(a) Number of observations of the raw data used to compute the long-term monthly means, from which the monthly anomalies are determined.

Depth (m)	Jan	Feb	Mar	Apr	May	Jun	Jul	Aug	Sep	Oct	Nov	Dec
0	16	22	25	23	28	23	27	27	22	28	32	19
10	16	21	25	22	28	22	27	25	22	28	32	20
20	16	21	25	22	28	22	27	25	21	28	32	19
30	16	21	25	22	28	23	27	25	21	28	32	19
50	16	21	25	22	27	23	27	25	22	28	32	19
75	16	21	25	22	27	21	27	23	21	28	32	19
100	16	20	24	22	27	21	27	23	21	27	29	18
125	16	19	22	22	26	20	27	22	20	25	29	18
150	12	18	20	20	26	18	25	19	17	21	29	15
175	12	18	20	19	25	18	25	18	15	20	26	13
200	12	18	20	16	24	16	24	17	14	19	22	12
225	11	16	17	17	19	15	20	15	10	18	19	9
250	8	10	15	10	15	11	18	10	7	15	9	6

(b) Total number of observations N of the raw data, for each depth.

Depth (m)	0	10	20	30	50	75	100	125	150	175	200	225	250
N	292	288	286	287	287	282	275	266	240	229	214	186	134

(c) Frequency of occurrence of gaps of various length, n, for each depth. For example, at 200 m depth, a gap of n=10 months occurs 5 times in the raw anomaly record.

	n (month)											
Depth (m)	1	2	3	4	5	6	7	8	9	10	11	12
0	62	26	10	5	0	3	0	0	1	1	1	0
10	62	27	11	6	0	4	0	0	1	1	0	0
20	63	27	11	5	0	3	0	0	1	1	1	0
30	63	27	11	5	0	3	0	0	1	2	0	0
50	63	27	11	5	0	3	0	0	1	2	0	0
75	62	29	10	5	1	3	0	0	1	2	0	0
100	61	28	12	4	1	3	0	1	1	2	0	0
125	65	28	12	4	2	3	0	1	1	2	0	0
150	56	33	11	3	1	2	0	0	1	3	0	0
175	55	33	12	5	0	3	0	0	1	3	0	0
200	50	35	12	6	0	2	1	0	0	5	0	0
225	39	31	11	7	2	4	3	1	0	5	0	0
250	25	22	7	7	5	6	3	2	4	2	0	0

Table 6.5: The list of the number of observations and missing data in the Emerald Basin temperature anomaly record.

The interpolated anomaly series, at each depth, is smoothed by passing the observed interpolated series through a 25-month running mean filter (and thus losing 12 months at both ends of the series). This low passed version is referred to as the low frequency anomaly. The plots of the low frequency anomaly series are shown in Figure 6.23a. The high frequency components (Figure 6.23b) are obtained by subtracting the low frequency from the observed series. I have divided the whole anomaly record into the cooling and the warming years. In the following subsections I present the cross correlation analyses of the cooling and the warming years, and of the whole record, followed by a brief summary.

6.10.1 The Cooling Period, 1950-65

The cross correlation between the low frequency SSTAs and the deep (> 100 m) water anomalies, with the SSTAs as the reference (Figure 6.24a(i)) indicates that the deep temperature anomalies lead the SSTAs. But when the low frequency anomalies are detrended (see Figure 6.24b), the cross correlation between the SSTAs and the deep temperature anomalies (Figure 6.24a(ii)) shows two distinct peaks: the one at the negative side of Figure 6.24a(ii) indicates that the SSTAs lead the $T'_{100\mathrm{m}}$, and the other at the positive side indicates that the deep (> 100 m anomalies lead the SSTAs. This result suggests that the cooling trend in the SSTAs might have originated from the deep ocean. The possible deep oceanic source of the SSTAs will be discussed below.

Relation with Sambro Light Vessel Temperature Anomalies

Sambro is a coastal station, about 50 km away from Emerald Basin. The Light Vessel measured the surface and bottom (about 90 m) water temperature, from about 1950-65; the time when the cooling occurred. The Sambro Light Vessel temperature data were kindly provided by Dr. B. Petrie of the Bedford Institute of Oceanography. The purpose here is to compare Sambro surface (bottom) temperature anomalies with Emerald Basin surface (100 m) temperature anomalies. Figure 6.25b shows the time series plots of the Sambro surface and bottom low frequency anomalies, for

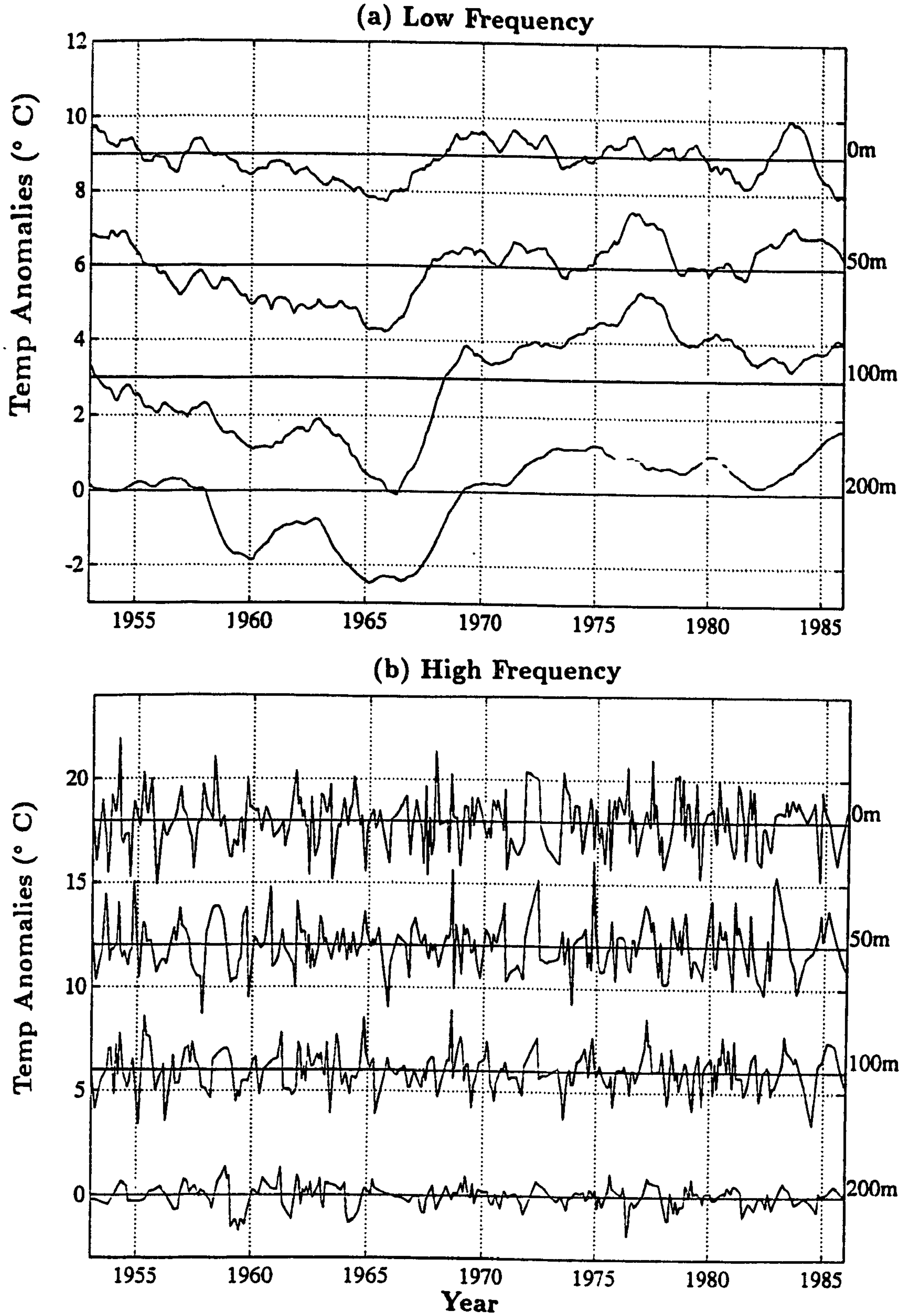

Figure 6.23: Time series plots of the (a) low and (b) high frequency components of the temperature anomalies for Emerald Basin.

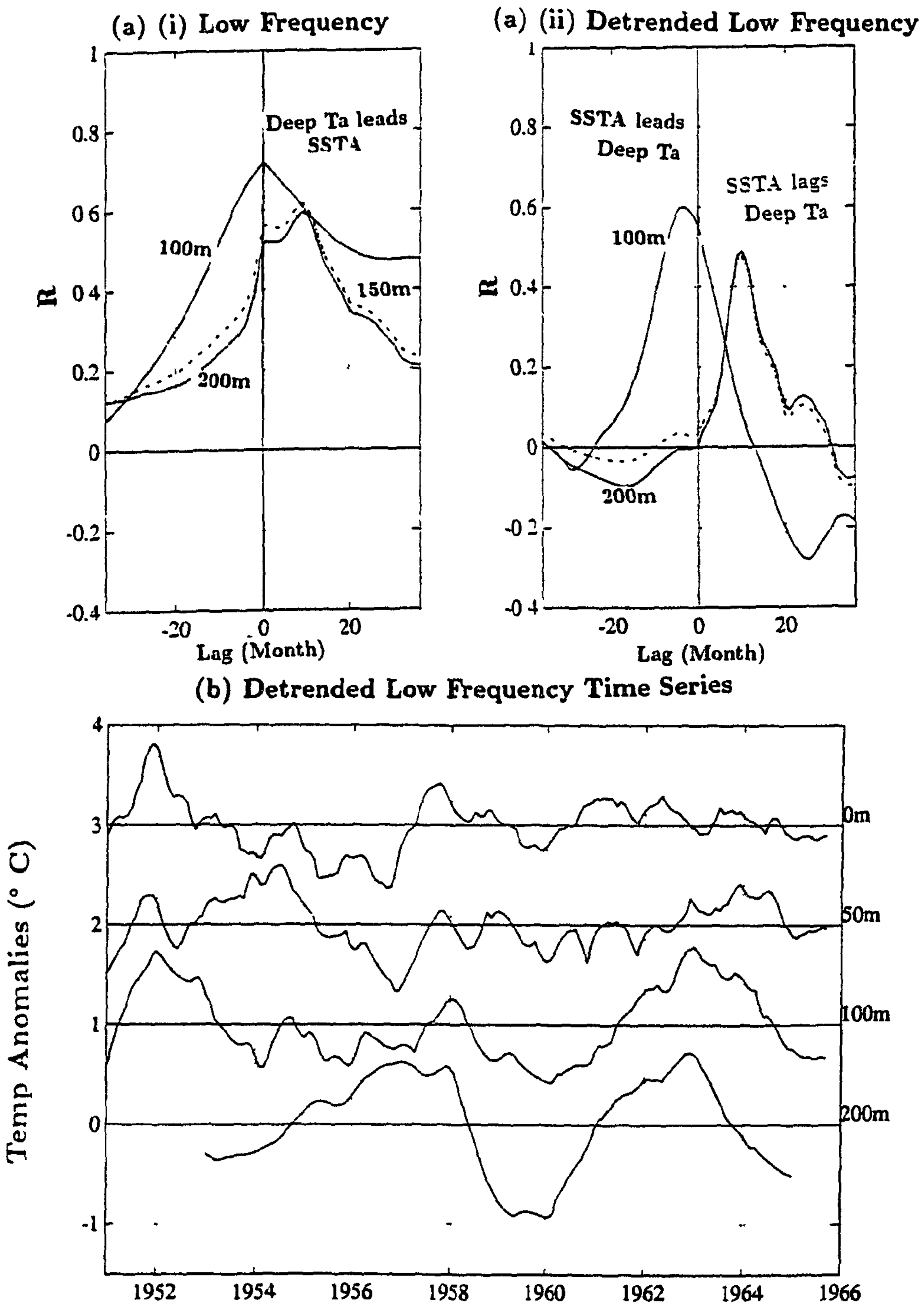

Figure 6.24: (a) The cross correlation function, R, between the Emerald Basin (i) low frequency and (ii) the detrended low frequency SSTAs and the deep temperature anomalies, with the SSTAs as the reference. (b) The time series plots of the detrended low frequency Emerald Basin temperature anomalies, for the cooling years, 1950-65.

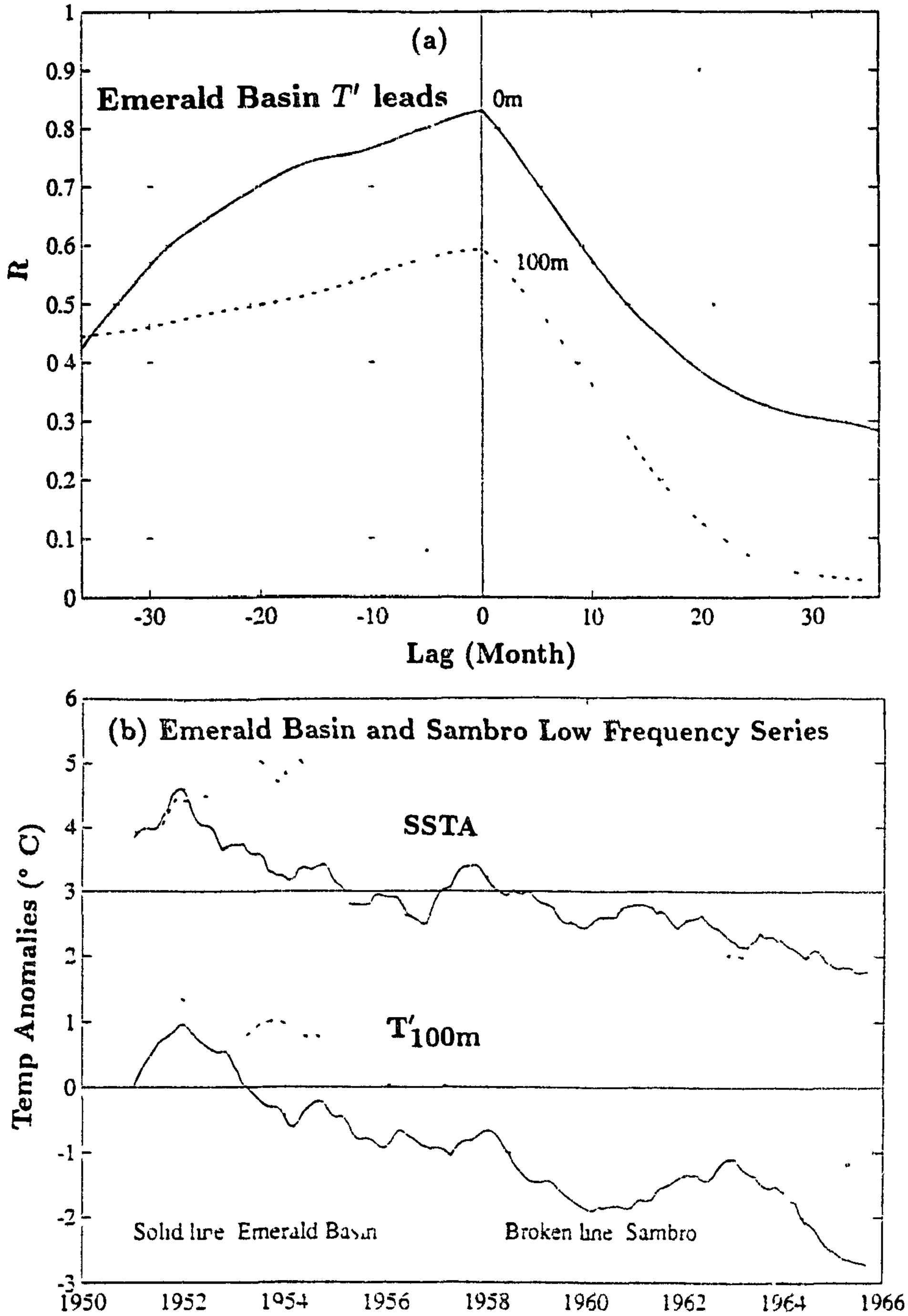

Figure 6.25: (a) The cross correlation function, R, between Emerald Basin and Sambro SSTAs, and Emerald Basin $T'_{100\text{ m}}$ and Sambro $T'_{90\text{ m}}$, with the Emerald Basin anomalies as the reference. (b) The comparison between the time series of the Emerald Basin and Sambro low frequency anomalies.

comparison with those of the Emerald Basin. The cross correlation function between the low frequency Sambro SSTAs and Emerald Basin SSTAs, and Sambro $T'_{90\ \mathrm{m}}$ and Emerald Basin $T'_{100\ \mathrm{m}}$ (Figure 6.25a) shows that the Emerald Basin temperature anomalies lead those of the Sambro, both at the surface and at about 100 m depth.

6.10.2 The Warming Period, 1970-87

The period, 1970-87 is called the warming years, to contrast it with the cooling period of the 50's. The cross correlation (Figure 6.26a) of the low frequency anomalies for the warming years, unlike the cooling period, indicate that the SSTAs lead the deep water anomalies. Even when the low frequency anomalies are detrended, the cross correlation of the detrended series (not shown) still show that the SSTAs lead the deep water anomalies. The cross correlation function of the high frequency components (Figure 6.26b) also show that the SSTAs lead the subsurface, but unlike the low frequency anomalies the high frequency decorrelates quickly with depth. At about 75 m depth, the correlation of the high frequency anomalies is about zero.

6.10.3 The Whole Period, 1950-87

Like the warming years, the cross correlation of the low frequency anomalies (Figure 6.27a) and that of the high frequency components (Figure 6.27b) of the whole period, 1951-87, show that the SSTAs lead the subsurface anomalies. This is consistent with the correlation of the unfiltered series, shown in Figure 6.15.

In summary, the cross correlation analyses show that on the whole, the SSTAs on the Scotian Shelf are in phase with the temperature anomalies of the top 50 m, but lead the deep water anomalies, suggesting that the SSTAs presumably originate from the upper 50 m of the water column. The cooling trend that was observed in the 50's appears to have been a special incident. The analysis indicates that the cooling trend might have originated from the deep sea. The above results could be influenced by the interpolated data, given the gappy nature of the anomaly record (see Table 6.5c). However, by filtering the series, the variance that might have been introduced

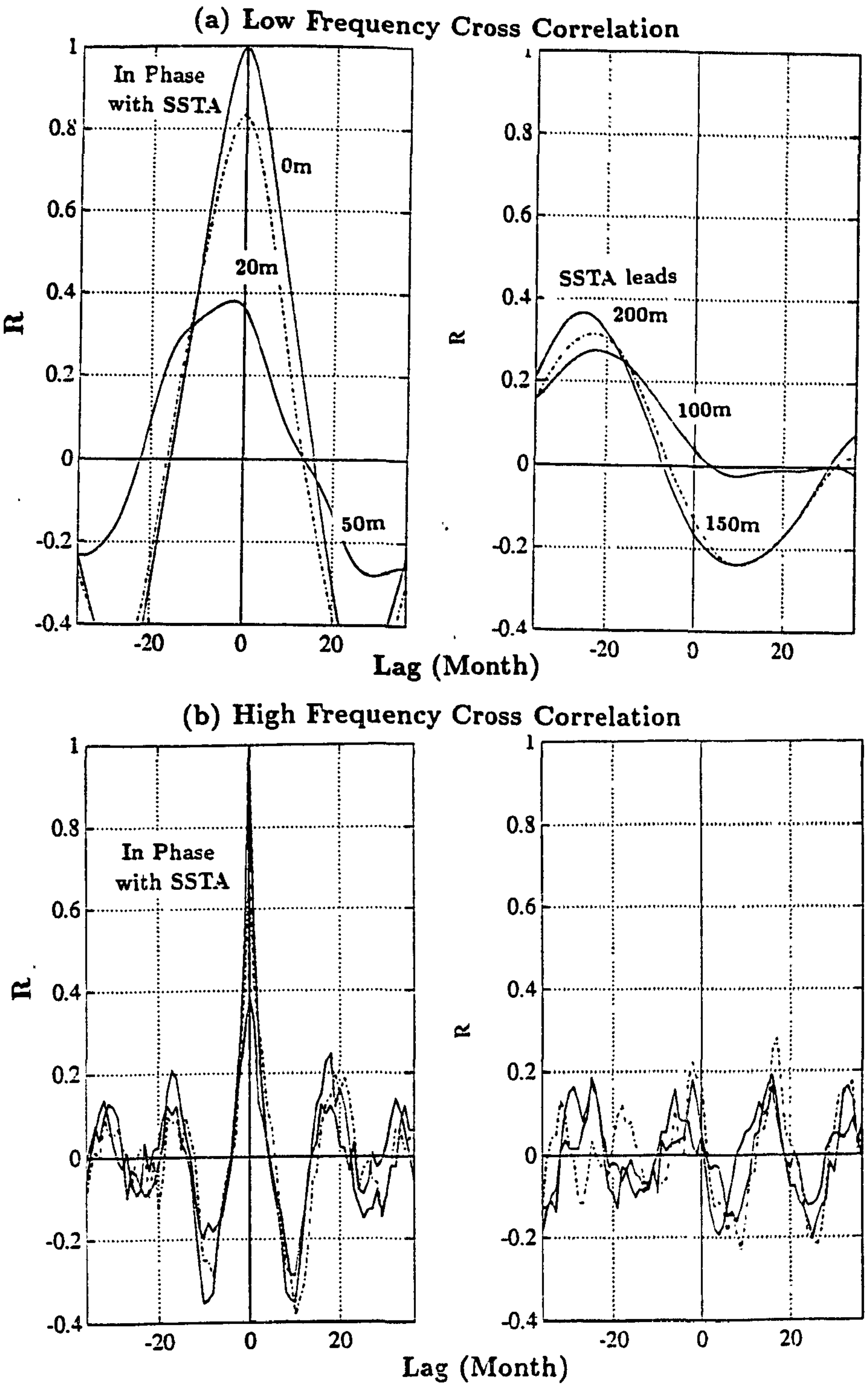

Figure 6.26: The cross correlation function, R, of (a) the low and (b) high frequency temperature anomalies for 1970-87, with the SSTAs as the reference.

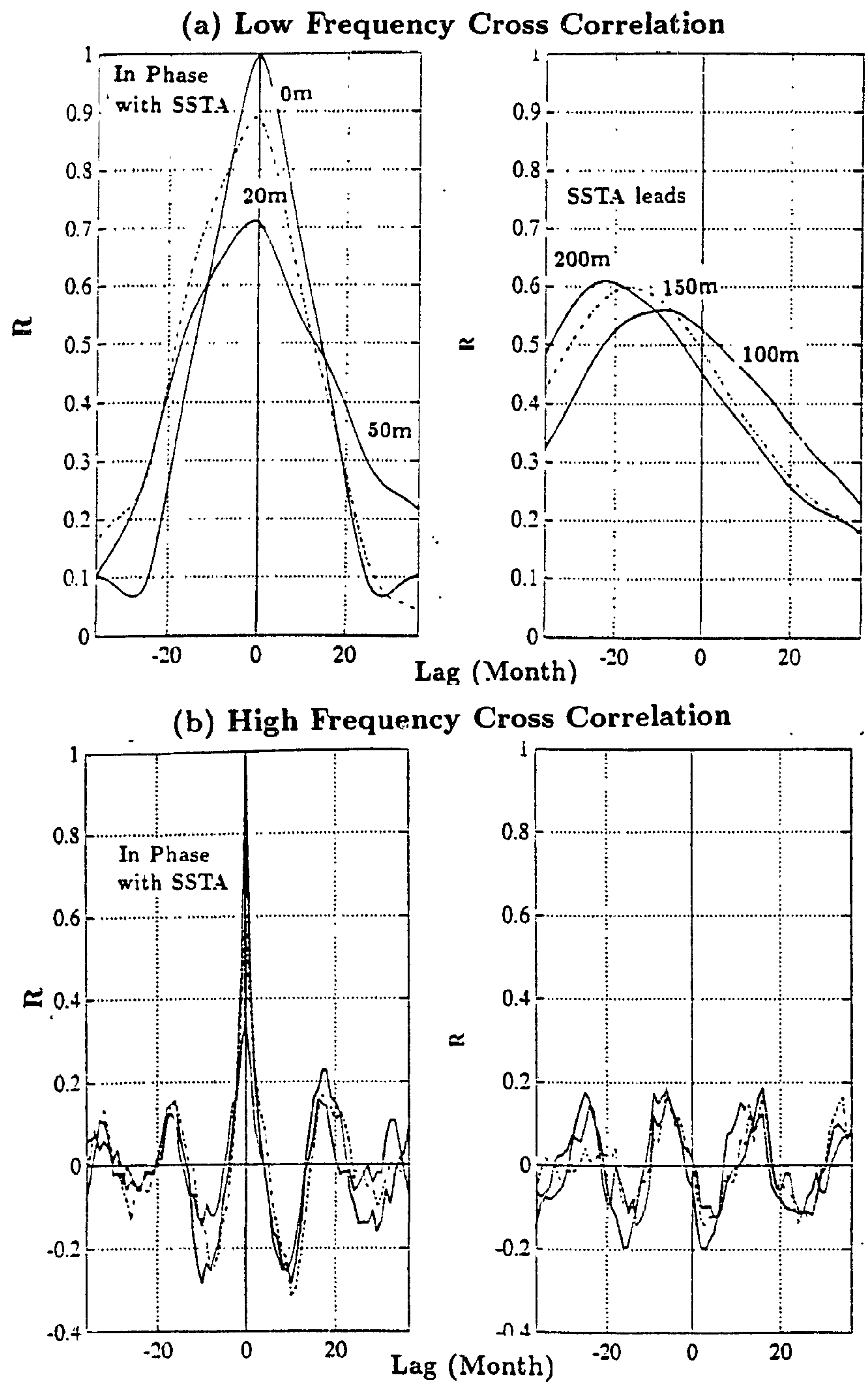

Figure 6.27: The cross correlation function, R, of (a) the low and (b) high frequency temperature anomalies for 1950-87, with the SSTAs as the reference.

by the interpolated data is reduced and is not expected to alter the results of the low frequency correlation presented above. To give an estimate of the energy in the raw anomaly record, I have plotted in Figure 6.28 the standard deviation of the raw (unfiltered, uninterpolated) anomalies, for each depth, using only available data. Also shown in the figure are the standard deviation of the anomalies stratified into seasons: winter (December, January and February) and summer (June, July and August). The important features are the two maxima (in the year-round and summer statistics) occurring at about 30 m and 75-100 m depth. The 30 m maximum is very likely to be due to the variability in the seasonal thermocline. Notice in Figure 6.28b that the depth of the seasonal thermocline for summer is about 30 m. Notice also the large drop in the summer temperature of the top 30 m and the layer below. It is clear that a small change in the depth of the seasonal thermocline (due to buoyancy flux or wind stirring effect) could produce a large change in temperature. The other maximum occurring at 75-100 m could be due to the effect of the horizontal advection (forced by the fluctuation in the river discharge from the Gulf of St. Lawrence/Labrador current) in the top 50 m of the water column. Recall that the correlation analysis show that the temperature anomalies of the top 50 m are in phase, but progressively lead those at 75 m and below. A possible reason why the two maxima do not occur at the surface is presumably due to the fact that the anomalies at the surface have equilibrated with the atmosphere. The variation of the standard deviations of the raw series with depth is thus consistent with the results of the cross correlation - that the temperature anomalies of the top 50 m lead the deep ones.

6.11 Sources of Error

For the COADS data set, a major source of error involves the changes in the methods of collecting data over the years. These particularly affect the wind and SST data. Prior to 1963 *[Fletcher, 1985]*, a large portion of the wind record was obtained by using the old Beaufort scale to convert the state of the sea surface to wind speed. Recently,

(a) Standard Deviation of Emerald Basin Raw Monthly Anomalies

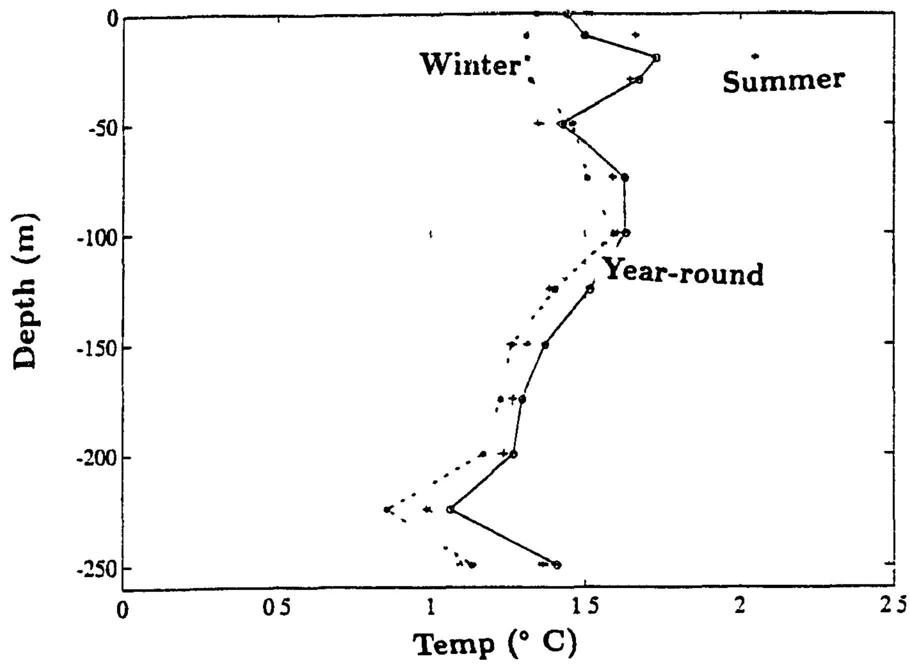

(b) Emerald Basin Mean Winter and Summer Temp Profile

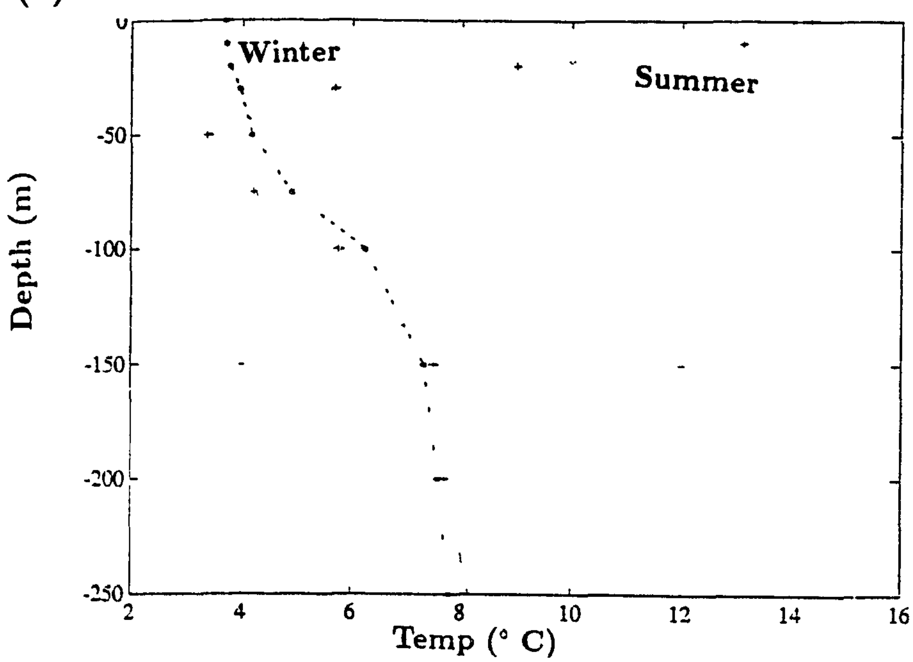

Figure 6.28: (a) Plots of the standard deviation of Emerald Basin raw monthly temperature, with depth, for (i) year-round, (ii) winter (December, January and February) and (iii) summer (June, July and August) (b) Plots of the mean winter and summer temperature profile

a revised Beaufort scale has been introduced, since some discrepancies between the actual measured wind at ocean weather stations and that estimated from the old Beaufort scale have been noticed [*Quayle, 1980*]. *Garrett et al.* [*1991*], in their estimates of the heat fluxes for the Mediterranean, recognized this problem and have allowed for the revised conversion from the Beaufort scale. *Isemer and Hasse's* [*1987*] map of the difference between the old and the revised Beaufort equivalent scale of *Kaufeld* [*1981*] for the North Atlantic shows that, in the study region, the difference is about 1 m s^{-1}. *Isemer and Hasse* note that an error in wind speed of about 2 m s^{-1} can have important consequences, especially in the tropics, as that could cause an error of about 25% in the estimates of the latent and sensible heat. For the study region, however, a typical wind speed is about 10 m s^{-1}, compared to about 1 m s^{-1} error in the conversion scale. Considering the small error in the study region, in the present study, the wind estimates of COADS are used without further correction.

As for the SST, COADS contains data that were sometimes measured through engine intake and sometimes by bucket. The difference between these two methods have been shown to be about 0.5° [*Ramage, 1984*]. The error associated with the measurement of air temperature is about 0.2°. If the difference, $T_s - T_a$, is small ($<$ 1°C), the error will be in the same order as the mean quantity (but in the study region, the monthly mean $T_s - T_a$ is typically 5°C). This will affect the estimates of the Q_I, Q_L and Q_H. Estimation of the error in Q is complicated due to the fact that Q is computed from many variables (both measured and derived), which themselves contain error. Therefore, to quote an exact error in Q is difficult [*Dr. Fred Dobson, personal communication*].

6.12 Discussion

Analysis of the heat fluxes shows that the variation in the net surface heat flux results primarily from latent and sensible heat flux anomalies, with a lesser contribution from the sensible heat flux, consistent with *Bunker* [*1976*]. Of all the components of the surface heat flux anomalies, the long wave radiation anomalies are the least variable. The sea surface temperature anomalies have a larger spatial and longer time scale than the net surface heat flux anomalies. Furthermore, the sea surface temperature anomalies persist longer in winter than in summer. Very importantly, the persistence of large scale sea surface temperature anomalies suggests an impact of the ocean on climate.

On the cause of the SSTAs on the Scotian Shelf, it has been suggested *[Thompson et al., 1988]* that the SSTAs in winter are primarily caused by the on-offshore wind. An offshore wind (blowing from land), because it is dry and cold, creates a large air-sea temperature and humidity difference which leads to a large heat loss from the ocean through latent and sensible heat fluxes. This explanation is expected to work in a region where the atmospheric forcing dominates the variability within the ocean and the ocean has a sufficient time to respond to the atmospheric circulation.

Based on the analyses carried out in this chapter, it is suggested that the primary cause of the SSTAs on the Scotian Shelf is from oceanic variabilities and not atmospheric fluctuations. This conclusion stems from the following reasons. First, if it is the on-offshore wind that creates the SSTAs, the SSTA will be more variable near the coast where the land-sea contrast is maximum. From the observations, this is not the case. Table 6.1b, column 8 shows that the standard deviation of the winter SSTAs is rather maximum (1.6°) offshore and submaximum (1.2°) near the coast. This observation confirms an independent estimate by *Cayan [1986]*, who also found that the maximum standard deviation of the SSTA occurs quite far away from land. Again, it can be seen (Table 6.1, column 2) that maximum fluctuation in the Q' also occurs offshore and not near the coast, which is to be expected in a situation where the SSTAs drive Q'. Second, and perhaps more importantly, the contribution of the atmospheric flux anomalies Q' in the model accounts for less than 1% of the observed SSTAs, whereas $\Gamma' + T_b'$ which represents contribution from oceanic factors accounts for about 32% of the observed SSTAs.

The next issue addressed is the performance of the model in simulating the SSTAs.

The model fit increases with depth, from R^2 = 39% at the surface to about R^2 = 69% at 50 m depth. When the model SSTAs are separated into different frequency components, it is shown that the model could account for about 71% of the observed SSTAs at a period of about 19 months. Q' alone explains about 23% of the observed SSTAs at a period of about 20 months.

On the issue of the oceanic sources of the SSTAs, both the coherence/phase spectra and the cross correlation function analyses confirm that, overall, the water anomalies of the top 50 m lead the deep water temperature anomalies. This fact suggests that the primary source of the SSTAs on the Scotian Shelf most likely originate from the upper 50 m of the water column. However, the cooling years (1950-65) appear to have been a special period. The phase spectra and cross correlation estimates for those years suggest that the deep water (> 100 m) temperature anomalies lead the SSTAs. A possible source of the deep water anomalies is the Slope Water, which is a mixture of the Labrador Slope Water and the warm Gulf Stream Water [*Gatien, 1976]*. Slope Water likely moved onto the Scotian Shelf and filled the deep basins allowing heat to diffuse to the surface *[Dr. B. Petrie, personal communication]*. It is important to note that the cooling trend in the 50's was a large scale phenomenon. It was observed in the sea and air temperature at St. Andrews (a coastal station on the Bay of Fundy) [*Lauzier, 1965]* and also in the SSTA off the Newfoundland Shelf. It was also noticed in the river discharge (Figure 6.29). It is possible that the remote cause of the cooling trend in the SSTAs was a shift in the large-scale atmospheric circulation, as suggested by *Thompson et al. [1988]*. But the shift in the atmospheric circulation, instead of changing the SSTAs via Q' as hypothesized by *Thompson et al [1988]*, perhaps changes the SSTAs through adjustments in the oceanic circulation and the river discharge. When one considers the fact that it is the atmospheric circulation that controls, to a large extent, the air temperature, precipitation (which in turn affects river discharge), and ocean circulation, it is easy to see how a shift in the atmospheric circulation might have been responsible for the large scale SSTAs in the cooling years Based on the statistical relationship, it is established that in the

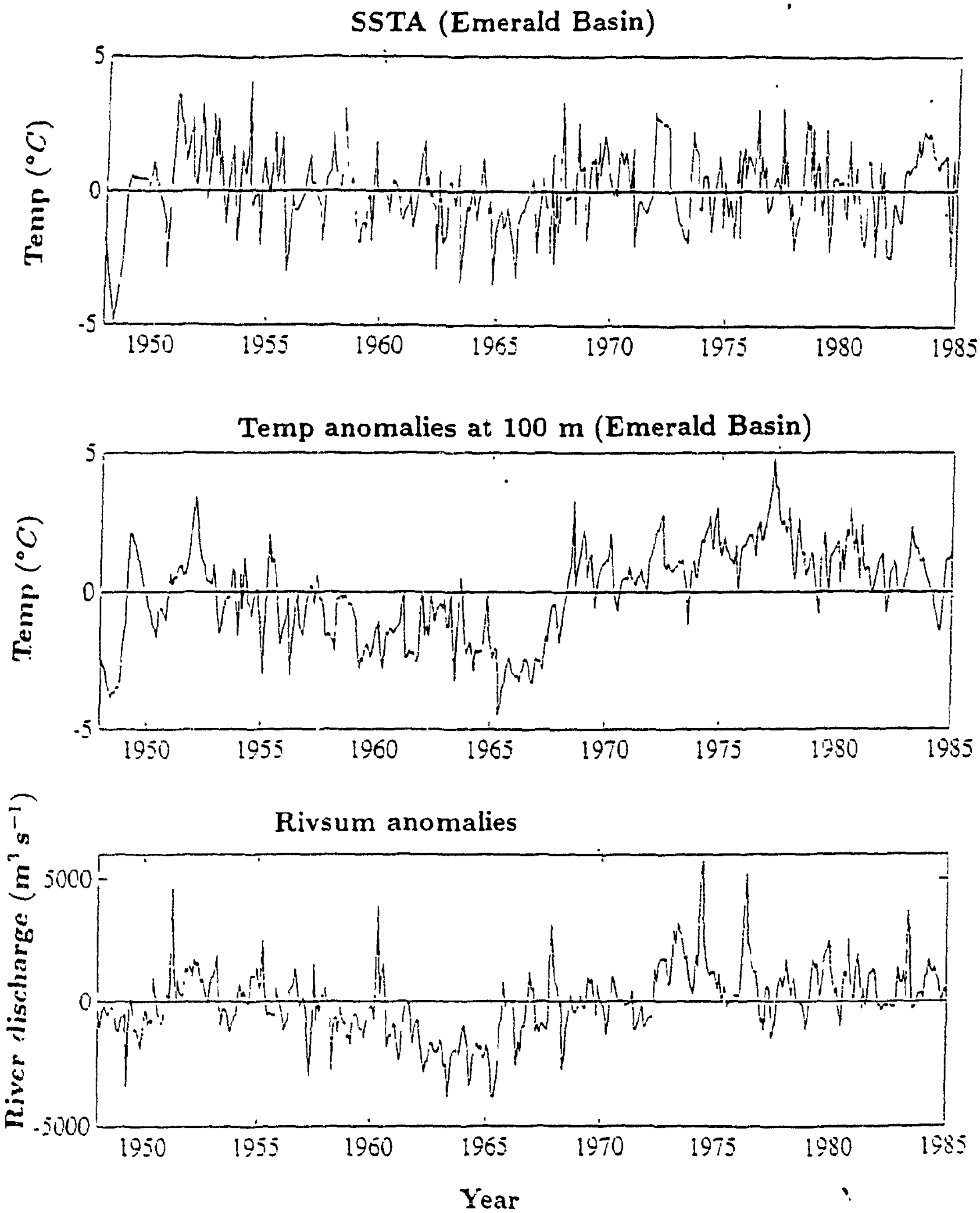

Figure 6.29: A time series of SSTAs (Emerald basin), subsurface temperature anomalies at 100 m depth, and Rivsum anomalies. The similarity between them suggests that the oceanic factors may be forcing the SSTAs.

normal years (in contrast with the unusual cooled years), the source of the SSTAs appears to originate in the surface waters. From the water masses [*Gatien, 1976*] and the circulation pattern in this region [*Sutcliffe et al, 1976*], the possible surface sources of the SSTAs include the cool water from the inshore Labrador current together with the flow from the Gulf of St. Lawrence.

Based on the empirical and model results, it hypothesized that the SSTAs on the Scotian Shelf develop predominantly from a combination of horizontal advection (perhaps forced by the flow from the Gulf of St. Lawrence and the Labrador current) and cross-shelf mixing from the Gulf Stream. These processes have been grouped and represented in the model as Γ'. Hence, to improve on the performance of the model for interannual changes, these processes must be explicitly represented in the model.

Clearly the results of the modelling of the seasonal cycle in this study are more conclusive than that of the interannual variability. More work is needed to substantiate the contribution of Q' to the development of the SSTAs. One approach is to estimate the interannual variability in the diffusivities, then use the Q' to force the model. On the contribution of the ocean to the creation of the SSTAs, it is suggested that the source should be sought around the Gulf of St. Lawrence, the Labrador current and the Gulf Stream. A comparison of the temporal changes in the temperature-salinity characteristics of these source waters, and that on the Scotian Shelf, may provide useful information on the primary cause of the SSTA on the Northwest Atlantic.

Chapter 7

DISCUSSION AND CONCLUSIONS

The Northwest Atlantic is a unique oceanographic region in the North Atlantic. It is the convergence zone of two important but contrasting current systems: the cold Labrador current from the north and the warm Gulf Stream from the south. The sea temperature of this region also has the largest variance in the North Atlantic. The large temperature variability affects climate and has, in fact, been shown to be useful in weather prediction in Europe *[Ratcliffe and Murray, 1970; Palmer and Sun, 1985]*. From a biological perspective, *Scott [1982]* pointed out that "temperature appears to be an important determinant of fish distribution ... on the Scotian Shelf". ***Rose*** *and Leggett [1989]* have shown that "sea surface temperature (directly and as a proxy for currents and salinities) and prey density interactively regulates cod distribution" in this region. Thus the success of commercial fisheries depends, in part, on the knowledge of the water temperature fluctuations.

The purpose of this study has been to explain seasonal and the interannual variability of the surface and subsurface temperature in the Northwest Atlantic. Before addressing the problem, I presented a description of the seasonal temperature and salinity variation on the Scotian Shelf. The observational study shows that a characteristic feature of the annual mean temperature structure is the existence of a subsurface temperature minimum, usually referred to as a cold intermediate layer, at about 50 m. The results of the temperature and salinity harmonic analyses indicate that the seasonal temperature signal penetrates to an average depth of about 75 m. This depth of the seasonal temperature penetration is consistent with that found in the central North Pacific, in a similar latitude range as the Scotian Shelf *[Barnett, 1981]*. Another feature of the harmonic analysis is the presence of a secondary maximum in the amplitude of the semi-annual temperature harmonic, at 30 m depth. For the salinity, a notable feature is the subsurface minimum of the amplitude of the salinity annual harmonic at about 30 m depth.

I have addressed the problem of explaining the seasonal and the interannual variability of the sea temperature in the study region through a combination of empirical and numerical modelling. As a first step toward the development of a model to explain the seasonal temperature cycle, the heat budget has been calculated. The salt budget was used as a control for the interpretation of the heat budget. This analysis focussed on the Shelf region because more complete data, in space and time, were available in this region than on the Slope region of the Northwest Atlantic. My analysis shows that the annual mean heat budget on the Scotian Shelf is dominated by horizontal advection, with a contribution of about -40 W m^{-2}. The contribution of the net surface heat flux, horizontal mixing, vertical diffusion of heat from the deep ocean, and upwelling are about 25, 11, 6 and 1 W m^{-2} respectively. On the seasonal time scale, about 85% of the local rate of heat storage on the Scotian Shelf can be explained by the net surface heat flux (Q). Horizontal advection is the next most important term in the seasonal heat budget: and together they explain about 99% of the amplitude of the local rate of heat storage. Thus, the seasonal sea temperature variability can be explained simply by only Q and horizontal advection.

Based on the heat budget, the seasonal temperature can be well represented (within $\pm 1°C$) by a model of the form

$$\frac{\partial T}{\partial t} = \frac{\partial}{\partial z}\left(K_v \frac{\partial T}{\partial z}\right) + \Gamma(z,t)$$

where Γ is dominated by horizontal advection. The model is clearly a modified one-dimensional heat diffusion equation. $\Gamma(z,t)$ is distributed with depth according to the observed vertical decorrelation scale of the sea temperature profile. The model uses estimates of the seasonal diffusivities that vary with density stratification, and hence with depth and time.

Considerable attention has been paid to the estimation of the monthly diffusivities: an extremely important parameter in the model. Besides needing K_V for the model, an accurate estimate is needed in other applications, such as estimating the effect of greenhouse warming due to carbon dioxide [see *Hansen et al., 1985; Yin and Fung, 1991*]. Three methods of estimating the $K_V(z,t)$ have been explored in this thesis. The methods differ in how $\Gamma(z,t)$ is represented in the model. In Method 1, $\Gamma(z,t)$ is separated into two components: one that varies through time and the other that varies with depth. The form of the depth-varying component is based on observations. This leads to an explicit expression for K_V that can be readily evaluated using observations. In Method 2, $\int_z^0 \Gamma(z,t)\,dz$ is minimized by least squares. In Method 3, the $K_V(z,t)'s$ are computed by minimizing the error between the observed and the predicted temperature. In Methods 2 and 3, the diffusivities are related to the buoyancy frequency, N, as

$$K_V(z,t) = K_O(1+\alpha N^p)^{-1}$$

where $2 \leq p \leq 4$. The parameterization (which is based on *Munk and Anderson [1948]*) depends only on three parameters: p, K_O and α which are determined empirically. In practice, since K_O and α covary, the effective number of independent parameters is 2: p and K_O/α. An important contribution of this thesis is providing an efficient approach of determining the parameters. The K_V in Methods 2 and 3 turn out to be almost identical. For $p=2$, in Method 2, the ratio $K_O/\alpha = 3.8\times10^{-8}\mathrm{m}^2\mathrm{s}^{-3}$ while in Method 3 $K_O/\alpha = 3.9\times10^{-8}\,\mathrm{m}^2\,\mathrm{s}^{-3}$. The attraction of Methods 2 and 3 is that they eliminate the problem of negative diffusivity, possible in Method 1. Method 3 is computationally more expensive than Method 2 but Method 3 pays off, in that, it has a sound physical basis and also has the added advantage of providing the uncertainty associated with the predicted temperatures. Method 3 was also further adapted to compute a constant diffusivity.

The predicted surface and subsurface $T(z,t)$ from the model with the seasonal varying $K_V(z,t)$ (from Method 3) for Emerald Basin compare much more favorably with the observations than the predicted $T(z,t)$ from the best *constant* K_V. This shows the importance of allowing $K_V(z,t)$ to vary with depth and time.

The model has been used to study the formation of the permanent cold intermediate layer (CIL), often observed at about 50 to 100 m depth on the Scotian Shelf. For the CIL to be formed it is established, through simple reasoning, that (i) there must be a net surface heat flux directed into the ocean from the surface and from below, and (ii) there must be advection of cold water into the region, otherwise the local heating will simply warm up the whole water column. Therefore, the CIL forms as result of the cold water being trapped between the heating from the surface and from below. The fact that the model with the seasonal varying diffusivities reproduces a more realistic CIL than the model with a constant diffusivity, again, emphasizes the importance of allowing diffusivities to vary with depth and time.

The problem of finding the primary causes of the interannual variability in the SST of the Northwest Atlantic has been addressed, as mentioned above, through statistical relationship and numerical modelling. The specific focus of the thesis has been to determine the contribution of Q' to the development of the SSTAs. The Q' is estimated using COADS. I have shown that over 90% of the interannual variability in Q' results from the sum of latent and sensible heat flux anomalies, with a lesser contribution from the sensible heat flux anomalies. The short wave radiative flux anomalies account for $< 1\%$ of Q'.

The spatial and temporal scales of both Q' and SSTAs have been estimated and compared, and I find that on the whole, Q' has a smaller spatial scale and shorter time scale than the SSTAs. The longer persistence of the winter SSTAs than those of summer, and the re-occurrence of the winter SSTAs in August, found in this study are consistent with the earlier finding of *Thompson et al. [1988]*. In the North Pacific, *Namias and Born [1970]* and *Namias et al. [1988]* also found that winter SSTAs last longer than that of summer, but the winter SSTAs reappeared about one year later. The longer persistence of the winter SSTAs might be explained, in part, by the deeper mixed layer depth (and hence the greater heat storage capacity) in winter.

The causes of the interannual variability in SST are generally thought to be through atmospheric forcing (such as Q' via wind and air temperature) and oceanic forcing (such as horizontal advection, upwelling and mixing). However, the correlations between the SSTAs and the atmospheric anomalies (particularly Q') are low and generally insignificant (except with T_a'), even when the data are stratified into seasons. A highly idealized coupled atmosphere-ocean model is used to interpret the empirical relationships and it shows that the zero correlation between the SSTAs and the Q' could mean, for example that (i) the SSTAs are driven by Q', (ii) the SSTAs are driven by the ocean and the atmosphere responds quickly to the oceanic forcing, or (iii) the data are dominated by noise. Some steps have been taken to eliminate some of the possibilities. The fact that the SSTAs (Q') in one COADS 2° square are correlated with the SSTAs (Q') in the neighbouring squares suggests that the SSTAs (Q') data are not entirely noise. To resolve the other two possibilities, a numerical model is used to determine the SSTAs caused by the Q'. Again the correlation between the observed and the model SSTAs due to Q' is low. This suggests that *the Q' is not the primary cause of the SSTAs in the Northwest Atlantic.*

To put this result into perspective, note that *Frankignoul and Hasselmann [1977]* used a stochastic forcing model to propose that SSTAs are generated as a response of the slowly varying upper ocean to the rapidly varying air-sea fluxes [see also *Hasselmann, 1976; Frankignoul, 1979, 1985; Frankignoul and Reynolds, 1983*]. This stochastic model presents the ocean as a passive follower of the atmosphere. *Reynolds [1978,1979]* tested the validity of the stochastic model in both North Pacific and North Atlantic Oceans. His results showed that the stochastic forcing model could explain the spectral shapes of the observed SSTAs in the open ocean, but failed in areas like the Gulf Stream and the Kuroshio Extension (North Pacific), where ocean currents are strong. The finding of this thesis further confirms that the stochastic forcing model can not explain the interannual SSTAs of the Scotian Shelf. Previous studies [e.g. *Bunker, 1976; Thompson et al., 1988]* have discussed qualitatively the relation between the SSTAs and Q', but this thesis is the first to attempt to quantify the contribution of Q' to the development of the SSTAs in the Northwest Atlantic through physical modelling.

The results of the cross correlation spectral analyses between sea surface temperature anomalies and subsurface temperature anomalies for Emerald Basin show that the temperature anomalies in the upper 50 m are in phase with the SSTAs and that the upper layer temperature generally leads the deep water (> 100m), suggesting that the primary cause of the SSTAs must be from the surface layers ($\sim$ 50m) and not from the deep water. However, in the 50's, when the great cooling occurred, the analysis suggests that the low frequency SSTAs may have originated from the deep ($\sim 100m$) water.

It is speculated that the SSTAs on the Scotian Shelf develop predominantly from a combination of cross-shelf horizontal mixing and horizontal advection from the Gulf of St. Lawrence and/or the inshore Labrador current. It is likely that the mixing of the warm slope water together with the fluctuations in the flux of cold fresh water from the Gulf of St. Lawrence/Labrador current may have an important influence on the SSTAs on the Scotian Shelf.

In summary the main conclusions of the thesis are:

- The average depth of the seasonal temperature signal penetration on the Scotian Shelf is about 75 m.

- The long term mean heat budget is dominated by horizontal advection.

- About 85% of the seasonal temperature variability may be explained by Q. The seasonal heat budget can be balanced, within error bars, simply by Q and horizontal advection.

- The seasonal temperature on the Scotian Shelf can be reproduced (within $\pm 1°C$ by a modified one-dimensional model of the form

$$\frac{\partial T}{\partial t} = \frac{\partial}{\partial z}\left(K_V \frac{\partial T}{\partial z}\right) + \Gamma(z,t)$$

where Γ is dominated by horizontal advection.

- Out of the three methods of estimating $K_V(z,t)$, the two methods in which K_V depends on N as

$$K_V(z,t) = K_0(1 + \alpha N^p)^{-1}$$

produce the most realistic vertical diffusivities.

- The fact that the model temperature with a seasonal varying $K_V(z,t)$ compares far more favourably with observations than the model with the best constant K_V emphasizes the importance of allowing $K_V(z,t)$ to vary with depth and time.

- The long-term annual mean cold intermediate layer on the Scotian Shelf results from cold water (advected into the region) being trapped between a local warm surface layer and a warm deeper layer.

- The major cause of the interannual variability in the net surface heat flux anomaly Q' is from latent and sensible heat flux anomalies.

- Q' has a shorter time scale and smaller spatial scale than the SSTAs.

- The primary cause of the interannual variability in the SSTAs is *not* Q', but the ocean.

- Overall, the oceanic source of the SSTA on the Scotian Shelf originates from the top 50 m of the water column.

Suggestions for Future Studies

As just mentioned, I have shown that Q' is not the primary cause of the interannual variability of the SSTAs and suggest that the primary cause lies in the ocean. The outstanding question now is: What oceanic mechanism is the primary cause of the SSTAs? I suggest that the answer may be found in the interannual variability of the temperature-salinity properties of the water on the Scotian Shelf. Given a time series of temperature and salinity for some locations on the Scotian Shelf, one can determine from the interannual T-S characteristics if cold years (1950's, for example) are associated with lower salinity. In which case, the probable cause might be increased cold water from the Gulf of St. Lawrence and/or the Labrador current. Warm-salty years might be the signatures of the Gulf Stream water. Again, comparison of the T-S characteristics of the source waters (from the Gulf of St. Lawrence, the Labrador current and the Gulf Stream) and that of the Scotian Shelf may reveal the primary cause of the SSTAs on the Scotian Shelf.

On modelling the interannual variability in the SSTAs, the outstanding problem is being able to balance the anomaly heat budget. More work should be done to quantify the contribution of Q' to the evolution of the SSTAs in the Northwest Atlantic. In the present study, seasonal diffusivities are used in the modelling of the interannual SSTAs. It is suggested that the diffusivities should be allowed to vary interannually. This could be done by using the interannual temperature and salinity to compute the interannual N, from which the diffusivities could be estimated. The model would then be forced with the Q'. This could also be done in other regions of the Northwest Atlantic for comparison. Even when this is done, the model still needs good quality data to reproduce (at least) the trend found in the temperature record. Let me illustrate this with the following example. Remember that an important feature of the temperature record on the Scotian Shelf is a decrease of about $5°C$ in 15 years, between 1950 and 1965. Let us assume that this $5°C$ temperature drop was caused by a heat loss from the upper 100 m of the water column. The heat flux that will produce this temperature drop is only -4W m^{-2}. This heat flux is small compared to the uncertainty in the estimate of Q. The implication of this small heat flux is that for a model to reproduce the downward trend in the temperature record, the uncertainty in the estimates of the Q must be less than 4W m^{-2}. On the other hand, if the $5°C$ temperature drop was caused by an increased flow of cold water on the Scotian Shelf, a similar accuracy in the estimate of the heat flux due to horizontal advection is required. This emphasizes the importance of empirical modelling.

Appendix A

DATA USED IN CHAPTER 2

1	Sydney bight	19	Roseway bank
2	N. Laurentian channel	20	Shelburne
3	S. Laurentian channel	21	Roseway basin
4	Banquereau	22	Browns bank
5	Misaine bank	23	Roseway channel
6	Canso	24	Lurcher shoal
7	Middle bank	25	E. Gulf of Main
8	The Gully	26	Georges basin
9	Sable Island	27	Georges shoals
10	Western bank	28	E. Georges bank
11	Emerald bank	29	N.E. channel
12	Emerald basin	30	Southern slope
13	Eastern shore	31	Southern offshore
14	South shore	32	Central offshore
15	Lahave basin	33	Central slope
16	Saddle	34	Northern slope
17	Lahave bank	35	Northern offshore
18	Baccaro bank		

Table A.1: Names of the subareas numbered in Figure 2.1.

(a) Annual mean temperature A_0

Subarea #	Depth (m) 0	10	20	30	50	75
1	6.23	5.95	5.15	3.88	1.70	1.02
2	5.54	5.23	3.86	2.49	1.16	0.73
3	6.54	6.47	5.43	4.23	2.34	1.46
4	7.20	7.27	6.14	4.61	2.71	2.38
5	6.66	6.60	5.51	3.70	1.73	1.40
6	6.50	5.88	4.91	3.57	2.09	1.41
7	7.47	7.14	5.35	3.94	2.12	1.96
8	7.78	7.47	6.72	4.93	3.83	3.14
9	8.44	8.31	7.59	6.77	4.45	4.47
10	9.31	8.99	8.02	6.86	5.40	5.62
11	9.41	9.05	7.91	6.49	4.83	5.67
12	8.74	8.35	7.11	5.48	3.80	4.45
13	7.71	6.84	5.57	4.49	2.76	2.40
14	7.36	6.83	5.28	4.03	2.93	2.51
15	8.12	7.48	6.09	4.76	3.29	3.37
16	9.39	8.58	7.40	6.27	4.88	5.21
17	8.57	8.11	6.76	5.32	3.82	3.76
18	8.23	7.53	6.61	5.49	4.32	4.37
19	8.18	7.94	6.28	4.97	3.56	3.04
20	7.12	6.20	5.11	4.31	3.68	3.42
21	7.27	6.49	5.77	4.83	3.62	3.68
22	8.47	7.69	7.09	6.47	5.77	5.92
23	6.69	6.38	5.95	5.52	5.15	5.22
24	6.43	6.21	6.07	6.00	5.86	5.63
25	7.34	7.30	6.99	6.70	6.33	6.32
26	9.45	9.09	8.34	7.47	6.31	5.75
27	9.26	9.13	8.83	8.62	8.13	6.82
28	9.03	8.66	8.04	7.60	7.09	6.58
29	9.13	9.05	8.68	8.12	7.30	7.30
30	10.76	10.46	10.06	9.52	8.81	8.80
32	13.96	13.55	13.44	14.01	12.91	12.25
33	10.11	9.73	8.98	8.19	6.91	7.32
34	9.70	9.41	8.65	7.68	6.37	6.31
35	13.66	13.18	12.91	12.08	10.54	10.27

(b) Annual mean salinity A_0

Subarea #	Depth (m) 0	10	20	30	50	75
1	30.23	30.39	30.58	30.87	31.39	32.03
2	31.22	31.32	31.50	31.69	32.03	32.33
3	31.86	31.82	31.94	32.10	32.32	32.65
4	31.58	31.64	31.78	31.92	32.31	32.83
5	30.99	31.03	31.19	31.42	31.92	32.31
6	30.48	30.59	30.84	31.10	31.56	32.05
7	31.14	31.23	31.40	31.57	31.94	32.33
8	31.66	31.64	31.76	31.89	32.24	32.69
9	31.59	31.59	31.68	31.79	32.30	33.20
10	32.03	32.06	32.18	32.34	32.74	33.43
11	31.92	31.97	32.16	32.37	32.79	33.55
12	31.51	31.55	31.75	31.99	32.45	33.19
13	30.78	30.94	31.17	31.38	31.73	32.24
14	31.04	31.10	31.32	31.49	31.83	32.24
15	31.24	31.38	31.61	31.81	32.16	32.73
16	31.62	31.70	31.96	32.22	32.84	33.38
17	31.32	31.33	31.47	31.71	32.16	32.68
18	31.58	31.69	31.81	32.00	32.47	32.92
19	31.25	31.26	31.39	31.59	31.96	32.42
20	31.42	31.49	31.61	31.72	31.88	32.35
21	31.45	31.54	31.63	31.77	32.04	32.44
22	31.87	31.92	32.04	32.22	32.60	33.02
23	31.89	31.98	32.12	32.24	32.44	32.60
24	31.82	31.91	31.97	32.02	32.24	32.47
25	32.25	32.29	32.34	32.42	32.62	32.93
26	32.43	32.46	32.52	32.60	32.79	33.14
27	32.55	32.65	32.68	32.69	32.77	32.94
28	32.48	32.50	32.57	32.64	32.76	32.94
29	32.20	32.39	32.50	32.63	32.97	33.47
30	32.76	32.96	33.09	33.25	33.61	34.04
32	33.98	34.00	34.15	34.54	34.77	34.97
33	32.44	32.50	32.72	32.92	33.30	33.90
34	32.51	32.56	32.70	32.92	33.31	33.78
35	33.66	33.67	33.94	34.14	34.40	34.69

(c) Annual mean density A_O $(kg\ m^{-3})$

Subarea #	Depth (m) 0	10	20	30	50	75
1	23.52	23.73	24.07	24.54	25.30	26.00
2	24.43	24.61	25.07	25.38	25.87	26.27
3	24.85	24.87	25.21	25.55	26.03	26.48
4	24.54	24.60	24.97	25.36	25.98	26.55
5	24.10	24.19	24.55	25.05	25.75	26.21
6	23.70	23.94	24.34	24.78	25.41	26.00
7	24.10	24.26	24.77	25.16	25.72	26.18
8	24.51	24.61	24.88	25.31	25.81	26.36
9	24.38	24.43	24.68	24.96	25.80	26.64
10	24.58	24.72	25.06	25.42	26.05	26.70
11	24.47	24.63	25.05	25.49	26.16	26.79
12	24.24	24.38	24.82	25.32	25.99	26.64
13	23.79	24.11	24.54	24.91	25.50	26.07
14	24.08	24.28	24.73	25.07	25.56	26.07
15	24.12	24.39	24.86	25.25	25.81	26.39
16	24.25	24.50	24.97	25.40	36.18	26.70
17	24.13	24.26	24.66	25.10	25.75	26.30
18	24.41	24.66	24.97	25.33	25.96	26.44
19	24.13	24.24	24.67	25.06	25.62	26.17
20	24.48	24.73	25.02	25.25	25.55	26.07
21	24.47	24.71	24.94	25.22	25.69	26.12
22	24.63	24.85	25.09	25.37	25.89	26.33
23	24.92	25.09	25.32	25.52	25.84	26.08
24	24.92	25.07	25.18	25.28	25.58	25.91
25	25.14	25.22	25.37	25.52	25.83	26.20
26	24.92	25.05	25.29	25.55	25.97	26.45
27	25.09	25.21	25.34	25.43	25.69	26.16
28	25.04	25.17	25.39	25.57	25.84	26.18
29	24.77	24.99	25.20	25.46	25.98	26.51
30	24.92	25.17	25.42	25.71	26.24	26.72
32	25.19	25.34	25.54	25.85	26.39	26.82
33	24.77	24.94	25.32	25.67	26.29	26.84
34	24.91	25.05	25.37	25.76	26.38	26.89
35	25.14	25.29	25.61	26.00	26.56	26.97

Table A.2: Spatial variation of the annual mean temperature, salinity and *in situ* density data.

(a) Amplitude A_1 ($^\circ C$), and phase t_1 (*days*), of the temperature annual cycle.

z (m)	0		10		20		30		50		75	
$S\,\#$	A_1	t_1	A_1	t_1	A_1	t_1	A_1	t_1	A_1	t_1	A_1	t_1
1	9.2	-142	9.0	-140	7.9	-136	6.0	-128	3.0	-112	1.6	-109
2	8.0	-142	7.5	-140	5.4	-133	3.4	-119	1.7	-103	0.8	-107
3	7.1	-142	7.0	-139	5.2	-132	3.5	-119	0.9	-87	0.5	105
4	7.5	-138	7.9	-135	6.2	-130	4.0	-118	1.6	-117	0.9	-151
5	8.3	-139	8.3	-136	6.7	-127	4.1	-113	1.5	-91	0.6	-67
6	8.8	-139	8.1	-136	6.7	-129	4.9	-117	2.9	-105	1.5	-98
7	8.8	-138	8.7	-134	6.0	-128	3.9	-119	2.0	-95	1.0	-51
8	7.8	-139	7.2	-135	6.4	-128	3.9	-111	2.9	-88	1.6	-93
9	7.5	-134	7.9	-131	7.0	-126	5.9	-119	2.3	-99	0.4	-174
10	7.9	-137	7.5	-134	5.9	-126	4.3	-112	2.2	-88	0.5	-28
11	7.9	-137	7.7	-134	6.2	-123	4.3	-107	2.2	-85	0.8	-58
12	8.4	-136	8.0	-133	6.2	-121	4.0	-104	1.9	-73	0.7	-56
13	8.6	-136	7.7	-133	6.1	-122	4.8	-110	2.4	-89	0.9	-68
14	7.9	-136	7.1	-130	5.3	-114	4.0	-97	2.8	-79	1.7	-79
15	8.1	-133	7.3	-130	5.5	-116	3.6	-101	2.1	-74	1.0	-79
16	7.7	-134	7.15	-135	5.6	-123	4.1	-108	2.5	-101	1.5	-83
17	7.8	-133	7.6	-129	5.7	-119	4.0	-99	2.3	-71	1.5	-60
18	7.1	-136	6.7	-135	5.3	-127	3.7	-112	1.9	-97	0.6	-80
19	7.7	-137	7.3	-133	5.1	-121	3.6	-105	2.1	-79	1.0	-98
20	5.8	-127	4.9	-122	3.7	-109	2.9	-94	2.4	-80	1.9	-77
21	6.3	-126	5.6	-125	4.8	-119	3.6	-109	2.0	-89	1.2	-69
22	6.3	-128	5.9	-128	5.1	-120	4.3	-112	3.0	-98	2.3	-88
23	5.4	-126	4.8	-124	4.2	-122	3.5	-125	2.6	-124	2.0	-129
24	4.8	-128	4.5	-125	4.3	-122	4.1	-120	3.7	-120	3.1	-115
25	4.9	-134	4.7	-133	4.3	-129	3.9	-124	3.2	-118	2.63	-112
26	6.6	-143	6.3	-139	5.4	-132	4.3	-121	2.9	-105	1.6	-91
27	5.9	-143	5.9	-132	5.5	-129	5.3	-126	4.3	-112	1.9	-106
28	6.0	-132	5.8	-127	4.9	-121	4.2	-116	3.4	-109	2.5	-97
29	7.0	-136	6.7	-131	5.8	-126	4.8	-120	3.1	-108	1.8	-101
30	7.5	-137	7.5	-132	6.7	-129	5.7	-123	3.8	-114	2.4	-113
32	8.9	-153	8.5	-151	8.0	-159	6.0	-136	3.3	-122	2.1	-121
33	8.0	-137	7.6	-134	6.4	-129	4.9	-121	2.6	-114	1.3	-131
34	7.5	-131	7.3	-129	6.1	-121	4.5	-110	2.3	-87	0.9	-95
35	5.3	-124	5.0	-116	4.6	-104	3.3	-82	2.4	-34	1.9	-8

(b) Amplitude A_1, and phase t_1 (*days*), of the salinity annual cycle.

z (m)	0		10		20		30		50		75	
S #	A_1	t_1	A_1	t_1	A_1	t_1	A_1	t_1	A_1	t_1	A_1	t_1
1	0.8	57	0.9	52	0.8	58	0.6	70	0.3	111	0.2	166
2	0.4	38	0.3	36	0.2	52	0.0	150	0.2	-134	0.2	-131
3	0.5	14	0.5	21	0.3	30	0.1	56	0.0	148	0.1	-147
4	0.7	63	0.6	63	0.5	74	0.4	96	0.2	165	0.3	-176
5	0.8	60	0.7	61	0.6	71	0.4	87	0.1	155	0.1	-135
6	0.8	59	0.7	60.	0.5	80	0.4	108	0.3	172	0.3	-177
7	0.6	68	0.5	72	0.4	94	0.3	122	0.3	168	0.1	-167
8	0.9	62	0.9	66	0.8	75	0.7	89	0.5	108	0.4	135
9	0.7	97	0.6	96	0.7	107	0.6	113	0.4	151	0.2	129
10	0.4	54	0.3	57	0.2	74	0.1	115	0.1	-170	0.1	155
11	0.5	33	0.5	36	0.2	48	0.0	122	0.3	-117	0.2	-33
12	0.4	41	0.4	40	0.2	82	0.1	158	0.2	-131	0.2	-77
13	0.9	95	0.4	95	0.4	130	0.5	156	0.5	-178	0.3	-161
14	0.2	74	0.3	89	0.3	143	0.4	169	0.4	-168	0.4	-143
15	0.1	74	0.1	44	0.2	-179	0.3	-169	0.4	-139	0.4	-118
16	0.2	-27	0.3	20	0.1	-28	0.2	-101	0.6	-93	0.5	-94
17	0.2	60	0.1	63	0.1	126	0.1	-121	0.3	-91	0.3	-79
18	0.1	101	0.1	-106	0.1	-158	0.2	-147	0.2	-102	0.2	-51
19	0.3	105	0.2	108	0.2	148	0.2	-160	0.4	-138	0.5	-104
20	0.1	152	0.2	173	0.3	-178	0.3	-165	0.3	-167	0.4	-81
21	0.3	149	0.3	166	0.3	181	0.4	-168	0.4	-151	0.3	-121
22	0.1	-82	0.1	-104	0.2	-99	0.2	-101	0.3	-89	0.3	-78
23	0.2	143	0.3	147	0.3	160	0.2	171	0.2	-157	0.2	-156
24	0.2	-164	0.3	-150	0.3	-144	0.3	-140	0.4	-139	0.5	-139
25	0.2	-112	0.2	-121	0.3	-124	0.3	-128	0.4	-130	0.4	-131
26	0.4	6	0.4	6	0.3	4	0.3	0.6	0.1	-5	0.1	-11
27	0.4	31	0.3	34	0.3	36	0.3	34	0.4	34	0.4	42
28	0.2	27	0.3	21	0.2	25	0.2	28	0.1	24	0.2	-0
29	0.1	-135	0.1	-93	0.1	-107	0.1	-131	0.2	-162	0.1	-167
30	0.3	-60	0.3	-102	0.3	-118	0.3	-127	0.3	-128	0.3	-132
32	0.2	123	0.2	141	0.4	162	0.1	-166	0.1	-146	0.1	-155
33	0.4	38	0.3	38	0.1	86	0.2	162	0.3	-165	0.3	-163
34	0.4	28	0.3	33	0.2	37	0.0	50	0.2	-138	0.2	-148
35	0.8	40	0.8	40	0.5	40	0.5	38	0.4	33	0.3	21

(c) Amplitude A_1 ($kg\,m^{-3}$), and phase t_1 ($days$), of in situ density annual cycle

z (m)	0		10		20		30		50		75	
$S\,\#$	A_1	t_1	A_1	t_1	A_1	t_1	A_1	t_1	A_1	t_1	A_1	t_1
1	1.8	46	1.8	46	1.5	52	1.0	62	0.4	93	0.2	135
2	1.3	39	1.1	40	0.7	51	0.3	76	0.1	178	0.2	-139
3	1.3	32	1.3	36	0.8	45	0.5	63	0.1	114	0.1	-121
4	1.5	50	1.6	52	1.2	61	0.7	80	0.2	125	0.2	181
5	1.7	48	1.7	51	1.2	62	0.7	80	0.1	116	0.1	-169
6	1.8	49	1.5	52	1.1	63	0.7	85	0.3	128	0.3	167
7	1.7	51	1.6	55	0.9	67	0.6	89	0.3	138	0.2	172
8	1.8	50	1.7	55	1.4	63	1.0	84	0.7	104	0.4	121
9	1.5	63	1.6	64	1.4	74	1.2	83	0.5	121	0.2	111
10	1.6	46	1.4	50	1.0	60	0.6	78	0.3	118	0.1	155
11	1.7	42	1.6	45	1.1	58	0.6	80	0.1	159	0.1	-9
12	1.6	45	1.5	48	1.0	65	0.5	94	0.2	166	0.1	-92
13	1.5	57	1.2	61	0.9	84	0.7	109	0.5	159	0.3	-175
14	1.2	51	1.1	60	0.7	88	0.6	120	0.4	157	0.3	-166
15	1.3	51	1.1	53	0.6	83	0.4	126	0.3	-179	0.2	-133
16	1.3	38	1.3	42	0.8	55	0.4	74	0.2	-84	0.3	-102
17	1.3	51	1.2	55	0.8	70	0.4	96	0.1	180	0.1	-106
18	1.1	51	0.9	46	0.6	61	0.3	87	0.1	106	0.1	-38
19	1.2	55	1.1	58	0.6	78	0.3	109	0.3	-177	0.3	-107
20	0.8	64	0.6	82	0.4	111	0.3	139	0.3	151	0.2	-85
21	0.9	72	0.7	76	0.5	93	0.4	120	0.3	178	0.2	-154
22	0.9	53	0.7	51	0.6	59	0.3	69	0.1	70	0.1	55
23	0.8	70	0.7	80	0.5	86	0.4	86	0.2	89	0.1	117
24	0.5	67	0.4	73	0.3	76	0.3	81	0.2	95	0.2	149
25	0.5	39	0.5	43	0.4	51	0.3	63	0.1	94	0.1	150
26	1.4	30	1.2	35	1.0	39	0.7	48	0.4	62	0.2	74
27	1.3	37	1.2	47	1.1	50	1.0	51	0.9	58	0.6	57
28	1.1	46	1.1	48	0.9	55	0.7	61	0.5	66	0.4	68
29	1.0	46	1.0	47	0.8	55	0.6	65	0.4	91	0.2	102
30	1.3	39	1.1	42	0.9	49	0.6	58	0.3	78	0.1	100
32	1.8	36	1.6	39	1.4	45	1.2	48	0.6	62	0.3	70
33	1.7	44	1.5	47	1.1	58	0.7	74	0.3	114	0.1	140
34	1.5	46	1.4	50	1.1	59	0.7	75	0.3	120	0.1	167
35	1.7	51	1.5	57	1.2	68	0.9	79	0.4	101	0.2	134

Table A.3: Spatial variation of the annual amplitude and phase of temperature, salinity and *in situ* density.

(a) Amplitude A_2 ($°C$) and phase t_2 ($days$), of the temperature semi-annual cycle.

z (m)	0		10		20		30		50		75	
S #	A_2	t_2	A_2	t_2	A_2	t_2	A_2	t_2	A_2	t_2	A_2	t_2
1	1.5	34	1.5	39	1.2	52	1.2	80	1.2	-75	0.9	-70
2	1.5	27	1.4	31	0.3	64	1.0	-72	0.7	-71	0.3	-72
3	1.9	29	2.0	38	0.9	59	1.1	-87	1.1	-66	0.4	-82
4	1.2	41	1.8	48	0.9	62	1.1	-82	0.6	-70	0.3	-24
5	1.9	40	1.9	43	1.5	64	1.3	-91	0.7	-70	0.1	-40
6	1.7	44	1.7	50	1.4	64	1.6	88	1.4	-76	0.9	-70
7	1.6	49	1.8	55	0.7	73	0.9	-70	1.3	-56	0.6	-68
8	0.8	26	0.9	37	0.8	59	1.1	-71	1.8	-67	0.7	-69
9	0.8	39	1.3	48	1.1	61	1.1	80	1.3	-60	0.2	86
10	1.3	33	1.1	40	0.4	73	1.2	-71	0.9	-67	0.1	9
11	1.2	29	1.1	34	0.6	72	1.2	-73	1.0	-43	1.1	-0
12	1.1	36	0.8	43	1.0	-87	1.4	-67	1.0	-48	0.2	-14
13	1.6	60	1.5	73	2.0	86	2.1	-89	1.3	-71	0.3	-62
14	0.4	51	0.5	80	1.3	-81	1.8	-71	1.6	-61	0.7	-57
15	0.2	42	0.6	-86	1.7	-71	2.1	-60	1.2	-51	0.2	-29
16	0.9	20	0.9	29	0.6	77	1.1	-88	0.9	77	0.5	37
17	0.8	43	0.5	44	0.7	-63	1.7	-60	1.2	-51	0.5	-37
18	0.4	-14	0.2	-41	0.7	-63	1.1	-64	1.0	-76	0.6	-75
19	0.5	58	0.3	68	1.2	-59	1.8	-58	1.4	-51	0.8	-43
20	1.0	-86	0.9	-80	1.2	-68	1.2	-61	1.3	-53	0.8	11
21	0.3	-80	0.5	-67	0.9	-66	1.2	-56	1.2	-42	0.8	-32
22	0.3	16	0.0	19	0.4	-74	0.7	-69	0.5	-58	0.4	-39
23	1.0	76	1.1	-84	1.2	-84	1.1	-80	0.7	-63	0.8	-43
24	0.5	75	0.5	89	0.5	90	0.5	-91	0.3	-84	0.3	-84
25	0.5	28	0.3	-10	0.2	-43	0.3	-66	0.3	-70	0.2	-62
26	1.0	12	0.8	15	0.3	26	0.2	88	0.3	-62	0.6	-23
27	0.5	12	0.3	34	0.2	75	0.3	90	0.2	-56	0.7	38
28	0.5	17	0.5	31	0.2	83	0.4	-71	0.7	-64	0.7	-54
29	0.6	42	1.0	51	0.9	64	0.9	78	0.9	86	0.6	80
30	1.2	23	1.3	22	0.9	18	0.6	12	0.6	-4	0.7	10
32	2.1	88	2.1	-89	2.6	91	2.0	-86	2.2	-77	1.4	-85
33	1.2	52	1.1	58	1.1	80	1.6	-85	1.5	-75	0.7	91
34	0.7	42	0.8	49	0.6	90	1.2	-69	1.3	-59	0.3	-51
35	1.4	4	1.0	7	0.6	-4	1.2	-25	1.4	-32	1.2	-15

(b) Amplitude A_2 and phase t_2 (*days*), of the salinity semi-annual cycle.

z (m)	0		10		20		30		50		75	
S #	A_2	t_2	A_2	t_2	A_2	t_2	A_2	t_2	A_2	t_2	A_2	t_2
1	0.1	-68	0.1	-56	0.0	-57	0.1	13	0.2	25	0.1	32
2	0.1	-64	0.1	-70	0.0	-54	0.0	33	0.0	-36	0.1	-64
3	0.0	-61	0.1	-35	0.2	-8	0.2	0	0.2	10	0.1	1
4	0.0	71	0.	-88	0.1	67	0.1	42	0.1	75	0.1	-86
5	0.1	62	0.0	68	0.1	32	0.2	38	0.1	71	0.1	84
6	0.0	-4	0.1	-20	0.1	18	0.2	25	0.2	43	0.1	78
7	0.1	77	0.2	83	0.2	73	0.2	67	0.2	82	0.0	0
8	0.1	-16	0.1	-23	0.1	-2	0.2	16	0.1	15	0.0	-91
9	0.1	75	0.1	66	0.1	54	0.1	47	0.3	84	0.3	73
10	0.1	-62	0.1	-64	0.0	-89	0.0	60	0.1	83	0.2	74
11	0.1	-46	0.0	-26	0.2	15	0.2	27	0.1	42	0.3	8
12	0.1	-65	0.0	-91	0.1	25	0.2	32	0.1	45	0.1	6
13	0.1	32	0.2	21	0.2	21	0.2	36	0.1	51	0.2	45
14	0.1	66	0.2	57	0.2	46	0.2	51	0.2	63	0.1	84
15	0.2	-70	0.2	-82	0.1	77	0.1	71	0.2	82	0.1	-91
16	0.2	73	0.2	53	0.2	49	0.3	55	0.2	82	0.2	51
17	0.0	-67	0.0	-87	0.1	54	0.1	68	0.1	-50	0.1	-46
18	0.1	-89	0.2	82	0.2	83	0.2	82	0.3	-83	0.3	-75
19	0.1	-1	0.1	1	0.1	41	0.1	72	0.1	-89	0.2	-47
20	0.1	-32	0.0	-74	0.1	-91	0.1	-85	0.1	83	0.1	25
21	0.1	9	0.1	16	0.1	19	0.0	20	0.1	83	0.1	-49
22	0.2	79	0.1	77	0.1	79	0.1	-88	0.1	-49	0.1	-34
23	0.1	23	0.1	31	0.1	-51	0.2	-60	0.2	-68	0.3	-60
24	0.0	-72	0.0	62	0.0	66	0.0	74	0.1	-84	0.1	89
25	0.1	-86	0.1	-73	0.1	-80	0.1	-71	0.1	-72	0.1	-85
26	0.0	11	0.1	-15	0.1	-12	0.1	-7	0.2	-9	0.2	-11
27	0.1	-91	0.1	42	0.1	28	0.1	26	0.1	0	0.1	79
28	0.1	-55	0.0	-64	0.0	-73	0.0	-37	0.0	-13	0.1	-23
29	0.3	79	0.3	69	0.3	68	0.3	64	0.3	66	0.3	67
30	0.2	86	0.2	30	0.2	19	0.2	17	0.2	16	0.2	24
32	0.6	-83	0.6	-79	0.5	-81	0.3	-60	0.3	-65	0.1	90
33	0.3	-71	0.3	-77	0.2	-85	0.2	-86	0.2	-91	0.2	88
34	0.3	-77	0.2	-76	0.1	-79	0.1	-79	0.1	-81	0.1	-79
35	0.2	-49	0.2	-47	0.2	-16	0.2	-5	0.2	-6	0.2	-9

(c) Amplitude A_2 ($kg\ m^{-3}$) and phase t_2 ($days$), of the density semi-annual cycle.

z (m)	0		10		20		30		50		75	
S #	A_2	t_2	A_2	t_2	A_2	t_2	A_2	t_2	A_2	t_2	A_2	t_2
1	0.5	-58	0.5	-53	0.3	-44	0.2	-13	0.3	20	0.1	26
2	0.5	-60	0.4	-59	0.1	-43	0.1	13	0.0	4	0.0	-57
3	0.4	-59	0.5	-50	0.2	-25	0.3	-2	0.2	17	0.1	6
4	0.3	-53	0.4	-47	0.1	-37	0.2	18	0.1	59	0.1	-91
5	0.4	-57	0.4	-51	0.2	-21	0.2	16	0.1	53	0.1	81
6	0.4	-48	0.4	-43	0.2	-23	0.3	7	0.3	30	0.1	62
7	0.4	-53	0.4	-49	0.1	-62	0.1	50	0.2	61	0.1	20
8	0.3	-51	0.3	-47	0.2	-29	0.3	15	0.3	21	0.1	24
9	0.2	-63	0.3	-50	0.2	-32	0.2	-2	0.2	63	0.3	71
10	0.5	-56	0.4	-51	0.1	-29	0.2	18	0.1	49	0.1	77
11	0.4	[illegible]	0.3	-48	0.3	-10	0.3	17	0.2	43	0.1	15
12	0.4	-52	0.3	-46	0.3	3	0.3	24	0.2	41	0.0	20
13	0.3	-32	0.4	-17	0.4	-4	0.3	8	0.2	34	0.2	42
14	0.2	-53	0.1	-25	0.2	18	0.3	31	0.2	43	0.1	62
15	0.3	-58	0.1	-53	0.2	22	0.3	39	0.2	61	0.1	80
16	0.3	-72	0.1	-68	0.1	17	0.2	27	[illegible]	84	0.1	54
17	0.3	-49	0.2	-46	0.1	22	0.2	33	0.1	40	0.0	-71
18	0.2	-68	0.1	-84	0.1	73	0.2	57	0.1	-87	0.2	-74
19	0.2	-38	0.2	-32	0.2	28	0.2	37	0.2	61	0.1	-49
20	0.2	-19	0.1	-6	0.1	28	0.1	56	0.2	50	0.0	51
21	0.1	-14	0.1	4	0.2	14	0.2	26	0.1	57	0.0	71
22	0.2	-81	0.1	-79	0.0	26	0.0	21	0.0	-6	0.0	-20
23	0.2	-16	0.2	-3	0.2	-13	0.1	-26	0.1	-62	0.2	-67
24	0.1	-35	0.1	-11	0.1	-8	0.1	-8	0.0	-51	0.0	91
25	0.2	-67	0.1	-68	0.1	-65	0.0	-38	0.0	-43	0.0	-82
26	0.2	-66	0.2	-54	0.2	-35	0.2	-13	0.2	-3	0.1	-3
27	0.2	-74	0.1	-46	0.1	-8	0.1	-2	0.2	3	0.1	-44
28	0.2	-57	0.2	-52	0.1	-25	0.1	4	0.1	15	0.1	18
29	0.2	-77	0.2	-68	0.1	-77	0.1	35	0.1	48	0.1	58
30	0.4	-69	0.2	-56	0.1	-36	0.1	-5	0.1	21	0.1	38
32	0.3	-59	0.3	-56	0.3	-40	0.4	-15	0.3	4	0.2	13
33	0.5	-56	0.4	-54	0.2	-39	0.1	-6	0.1	48	0.0	76
34	0.4	-60	0.4	-56	0.1	-39	0.1	17	0.1	46	0.1	-89
35	0.4	-68	0.3	-61	0.1	-41	0.1	36	0.2	37	0.1	77

Table A.4: Spatial variation of the semi-annual amplitude and phase of the temperature, salinity and *in situ* density.

S#	Jan	Feb	Mar	Apr	May	Jun	Jul	Aug	Sep	Oct	Nov	Dec	R
1	-197	-15	50	170	238	308	236	194	2	-241	-329	-415	723
2	-175	-65	44	160	145	178	207	124	-51	-125	-171	-272	479
3	-143	22	-3	152	134	74	198	155	-39	-164	-147	-240	438
4	-84	-4	-59	152	216	206	186	101	41	-135	-299	-319	535
5	-103	36	-70	81	176	224	226	126	52	-117	-281	-349	575
6	-211	67	53	52	167	267	264	172	47	-90	-319	-468	735
7	-249	-19	119	77	77	297	247	48	8	-6	-203	-398	695
8	-181	-36	-24	174	138	205	241	98	46	46	-221	-487	728
9	-181	27	-45	42	306	273	122	188	97	-140	-299	-391	697
10	-185	-27	-8	42	207	257	154	81	89	-34	-258	-318	575
11	-176	-160	-54	155	197	218	207	114	16	-49	-191	-278	496
12	-153	-80	-82	119	226	233	89	101	148	-18	-227	-356	589
13	-154	-50	87	120	48	227	157	250	151	-90	-289	-457	707
14	-312	-79	36	120	139	164	136	154	193	33	-192	-392	585
15	-256	-60	29	99	168	219	87	54	138	129	-166	-440	659
16	-52	-148	12	34	155	316	157	172	82	-84	-354	-290	670
17	-372	8	-75	99	218	163	175	109	100	1	-46	-380	598
18	-122	-96	-4	202	142	176	129	30	140	19	-286	-330	532
19	-276	-90	34	162	179	201	81	56	106	65	-123	-394	595
20	-270	-101	17	91	83	130	160	83	103	109	-93	-312	472
21	-256	-109	15	125	118	274	75	-19	162	58	-114	-329	604
22	-287	-45	-59	117	180	232	213	118	56	-53	-103	-370	602
23	-205	-138	104	267	69	100	162	168	65	-125	-195	-272	538
24	-130	-88	-15	139	172	240	196	116	70	-69	-293	-338	578
25	-154	-107	-26	150	232	223	138	108	35	-107	-226	-268	501
26	-188	-89	-91	206	245	160	267	120	-80	-115	-153	-282	549
27	-158	-71	-56	115	266	332	206	105	13	-114	-271	-367	699
28	-236	-78	-24	121	177	276	220	60	73	-22	-209	-356	632
29	-173	-10	-35	121	157	200	303	199	40	-178	-292	-331	633
30	-166	-257	-49	198	217	447	336	37	-91	-160	-246	-265	711
32	-230	35	208	585	-56	44	344	142	132	-273	-398	-534	1119
33	-105	24	2	206	149	192	240	116	99	-55	-384	-482	722
34	-154	-166	6	185	139	179	252	70	61	95	-304	-363	615
35	-15	-679	-54	299	7	59	245	-6	64	201	-248	128	978

Table A.5: Seasonal rates of local heat storage, $\partial H/\partial t$ ($W\,m^{-2}$). Annual minimum and maximum values, at each subarea, are underlined. R is the range.

$S\#$	Jan	Feb	Mar	Apr	May	Jun	Jul	Aug	Sep	Oct	Nov	Dec	Range
1	20.1	19.2	$\underline{16.8}$	18.2	21.9	22.2	26.1	28.0	$\underline{32.7}$	29.2	25.7	22.3	15.9
2	$\underline{16.3}$	17.2	16.8	16.6	17.2	18.1	20.3	21.3	$\underline{22.2}$	18.8	19.8	17.8	5.9
3	13.4	$\underline{13.4}$	15.8	15.0	16.1	16.7	19.3	19.1	$\underline{22.1}$	20.1	17.9	15.4	8.7
4	16.6	14.8	$\underline{13.2}$	14.4	14.4	17.0	20.6	21.0	22.7	$\underline{22.8}$	20.1	18.0	9.6
5	18.8	17.0	$\underline{14.1}$	17.9	17.6	19.3	22.7	24.1	25.7	$\underline{25.1}$	22.1	20.0	11.6
6	19.8	19.6	$\underline{17.8}$	18.2	20.7	20.0	23.0	26.1	27.0	$\underline{27.5}$	26.7	22.6	9.7
7	18.6	18.1	$\underline{15.3}$	16.0	16.9	18.5	22.1	23.4	23.5	23.5	$\underline{23.7}$	20.6	8.4
8	13.2	15.4	13.6	$\underline{12.0}$	14.3	16.5	20.6	23.4	24.3	25.5	$\underline{26.8}$	19.4	14.8
9	15.9	18.5	12.2	$\underline{12.2}$	15.3	18.1	19.7	23.6	$\underline{25.9}$	23.9	25.1	22.2	13.7
10	15.6	14.2	13.7	$\underline{12.6}$	14.5	16.8	20.2	20.0	21.4	$\underline{22.0}$	20.0	16.9	9.4
11	$\underline{13.4}$	13.4	14.0	13.7	14.8	17.6	19.7	19.2	20.9	$\underline{21.9}$	19.9	15.9	8.5
12	16.8	$\underline{14.5}$	15.4	15.9	16.6	18.2	20.1	19.7	21.9	$\underline{22.7}$	21.1	18.0	7.3
13	22.3	19.0	$\underline{18.2}$	19.1	19.0	18.8	20.3	21.1	26.7	26.1	$\underline{27.3}$	21.4	9.1
14	21.0	18.9	18.0	$\underline{17.6}$	18.5	19.8	20.2	19.5	22.3	24.6	$\underline{25.0}$	22.6	7.4
15	18.8	18.8	$\underline{16.5}$	16.7	17.1	19.3	19.4	19.2	19.2	$\underline{23.5}$	20.2	21.4	7.0
16	16.0	15.0	$\underline{14.0}$	16.1	17.8	18.8	19.6	18.7	$\underline{21.2}$	19.0	17.1	17.1	7.2
17	19.1	18.0	$\underline{16.4}$	18.7	17.1	20.7	21.4	20.6	22.9	$\underline{23.5}$	21.7	19.7	7.1
18	17.3	15.6	16.8	$\underline{15.4}$	15.6	19.0	$\underline{21.0}$	20.5	19.8	19.4	19.4	18.7	5.6
19	20.2	18.5	19.5	18.2	$\underline{18.0}$	20.5	21.5	20.8	21.6	22.4	$\underline{24.6}$	20.2	6.6
20	20.6	19.6	$\underline{17.4}$	17.7	18.0	18.8	18.4	18.8	20.0	22.3	$\underline{24.0}$	20.5	6.6
21	18.3	20.0	17.7	$\underline{17.1}$	17.9	17.5	20.2	17.3	19.9	22.3	$\underline{22.5}$	21.0	5.4
22	17.2	16.0	$\underline{15.4}$	16.1	16.3	18.4	20.0	19.4	20.3	$\underline{21.1}$	19.1	17.0	5.7
23	16.5	16.8	17.1	$\underline{13.9}$	14.5	18.0	17.3	17.8	$\underline{21.5}$	21.1	19.2	17.6	7.6
24	18.0	19.3	17.0	$\underline{16.8}$	17.0	19.0	18.8	18.9	21.3	$\underline{21.5}$	20.4	18.7	4.7
25	15.1	18.1	15.6	$\underline{14.5}$	15.9	18.1	18.3	17.7	$\underline{19.5}$	19.0	17.7	17.1	5.0
26	13.1	$\underline{11.7}$	13.5	14.2	15.7	17.2	19.4	$\underline{22.8}$	21.6	21.4	17.6	14.8	11.1
27	13.2	$\underline{10.5}$	12.0	13.0	14.5	18.3	23.4	23.3	$\underline{25.1}$	23.3	21.5	15.5	14.6
28	13.5	$\underline{12.4}$	13.3	13.6	14.3	17.1	20.8	21.0	21.7	$\underline{22.6}$	19.4	17.1	10.2
29	15.0	13.3	$\underline{13.0}$	13.7	14.5	16.8	20.3	20.1	20.5	$\underline{20.5}$	19.5	18.6	7.4
30	12.2	$\underline{11.4}$	12.6	11.7	13.5	15.9	18.2	19.1	$\underline{20.0}$	18.6	17.5	15.1	8.7
32	$\underline{7.0}$	9.3	9.0	8.3	13.4	14.9	18.1	21.4	$\underline{22.5}$	20.9	17.4	11.3	15.5
33	13.5	12.4	12.4	$\underline{10.6}$	12.1	15.9	17.9	19.4	$\underline{21.0}$	20.1	18.2	15.0	10.4
34	12.1	12.4	11.6	$\underline{10.8}$	11.9	14.3	17.8	19.5	18.0	$\underline{19.8}$	17.2	16.0	9.0
35	10.0	9.9	10.0	$\underline{7.1}$	9.3	12.9	16.3	18.2	18.0	18.3	$\underline{18.5}$	15.6	11.4

Table A.6: Spatial and temporal variation in steric height, η_S (cm). Annual minimum and maximum values, at each subarea, are underlined.

Appendix B

DATA USED IN CHAPTER 3

	$\partial H/\partial t$		Q	
$S\#$	A_1	t_1	A_1	t_1
1	320	143	181	158
2	217	146	180	160
3	182	143	174	156
4	235	145	179	154
5	233	151	179	154
6	282	151	186	154
7	240	151	187	153
8	251	156	188	154
9	270	151	196	156
10	228	155	200	156
11	235	157	202	155
12	227	159	199	155
13	251	157	200	156
14	239	166	206	155
15	218	162	206	155
16	242	156	209	157
17	230	166	210	157
18	208	152	213	159
19	216	158	207	155
20	186	173	207	155
21	198	163	210	158
22	244	161	214	161
23	211	149	214	161
24	245	153	231	163
25	230	150	223	162
26	241	150	217	162
27	280	150	214	160
28	251	157	218	161
29	264	152	217	161
30	312	150	225	162
32	325	134	238	164
33	270	147	220	160
34	242	159	198	158
35	164	-173	209	161

Table B.1: Comparison of the annual amplitude A_1 in $W\,m^{-2}$ and phase t_1 in days of $\partial H/\partial t$ and Q.

$S\#$	Jan	Feb	Mar	Apr	May	Jun	Jul	Aug	Sep	Oct	Nov	Dec	R
1	-19	128	61	73	86	$\underline{130}$	70	102	-6	-166	-211	$\underline{-249}$	379
2	3	$\underline{86}$	62	67	-3	1	38	30	-65	-54	-55	$\underline{-109}$	195
3	9	$\underline{135}$	14	69	-16	$\underline{-100}$	32	66	-33	-83	-20	-71	233
4	71	$\underline{102}$	-43	64	60	27	18	11	51	-51	$\underline{-167}$	-142	269
5	57	$\underline{152}$	-63	-14	20	46	63	37	57	-33	-151	$\underline{-172}$	324
6	-45	$\underline{185}$	53	-46	9	84	101	73	48	-1	-187	$\underline{-274}$	460
7	-90	90	$\underline{120}$	-20	-82	112	84	-52	15	88	-66	$\underline{-200}$	320
8	-21	75	-12	81	-24	17	70	-3	54	$\underline{137}$	-81	$\underline{-293}$	430
9	-20	$\underline{145}$	-21	-47	133	76	-61	78	103	-48	-151	$\underline{-192}$	337
10	-22	$\underline{94}$	10	-51	38	58	-27	-34	89	59	-105	$\underline{-110}$	203
11	-8	-39	-41	$\underline{57}$	27	20	29	-3	10	44	-35	$\underline{-61}$	118
12	16	38	-77	19	60	39	-82	-14	$\underline{140}$	75	-77	$\underline{-137}$	277
13	25	75	83	19	-112	35	-11	130	$\underline{136}$	2	-153	$\underline{-228}$	364
14	-135	40	39	12	-31	-30	-35	34	$\underline{174}$	124	-34	$\underline{-158}$	332
15	-79	59	32	-9	-2	25	-84	-66	119	$\underline{220}$	-7	$\underline{-207}$	426
16	$\underline{118}$	-17	35	-61	-19	111	-32	48	69	6	$\underline{-192}$	-68	310
17	$\underline{-198}$	$\underline{138}$	-55	-1	45	-39	-9	-15	79	89	117	-150	337
18	48	46	32	109	-33	-32	-65	-96	$\underline{115}$	100	$\underline{-121}$	-102	235
19	-95	29	34	51	9	8	-88	-65	81	$\underline{155}$	35	$\underline{-154}$	155
20	$\underline{-90}$	18	18	-20	-87	-63	-10	-38	79	$\underline{199}$	66	-72	289
21	-79	23	35	23	-53	76	-106	$\underline{-143}$	132	$\underline{140}$	45	-93	283
22	-108	$\underline{102}$	-20	24	9	29	19	-11	17	18	55	$\underline{-134}$	236
23	-26	9	143	$\underline{173}$	-102	$\underline{-104}$	-32	39	25	-53	-36	-36	278
24	$\underline{86}$	68	16	45	-5	32	-3	-33	5	-9	$\underline{-132}$	-70	218
25	47	46	9	56	$\underline{59}$	17	-59	-32	-20	-43	$\underline{-67}$	-14	126
26	4	59	-55	$\underline{109}$	75	-42	73	-14	$\underline{-128}$	-49	3	-36	237
27	27	68	-22	17	100	$\underline{130}$	9	-27	-20	-39	-113	$\underline{-130}$	260
28	-56	$\underline{71}$	20	30	8	67	14	-77	40	52	-46	$\underline{-122}$	193
29	5	$\underline{140}$	8	30	-15	-8	102	66	3	-106	$\underline{-129}$	-98	269
30	12	-98	5	114	41	$\underline{228}$	119	-108	$\underline{-124}$	-83	-73	-31	351
32	-44	209	276	$\underline{512}$	-242	-193	107	-17	103	-193	-221	$\underline{-298}$	809
33	69	$\underline{174}$	47	120	-31	-26	30	-21	78	28	-214	$\underline{-256}$	431
34	10	-43	41	102	-29	-20	60	-44	64	$\underline{182}$	-157	$\underline{-166}$	348
35	161	$\underline{-542}$	-1	223	-164	-151	34	-138	59	284	-101	$\underline{335}$	878

Table B.2: Seasonal variation in the residual, $(\partial H/\partial t - Q_{zm})$, in W m^{-2}. Q_{zm} is the net heat flux with zero annual mean. Minimum and maximum annual values at each subarea are underlined. R is the range.

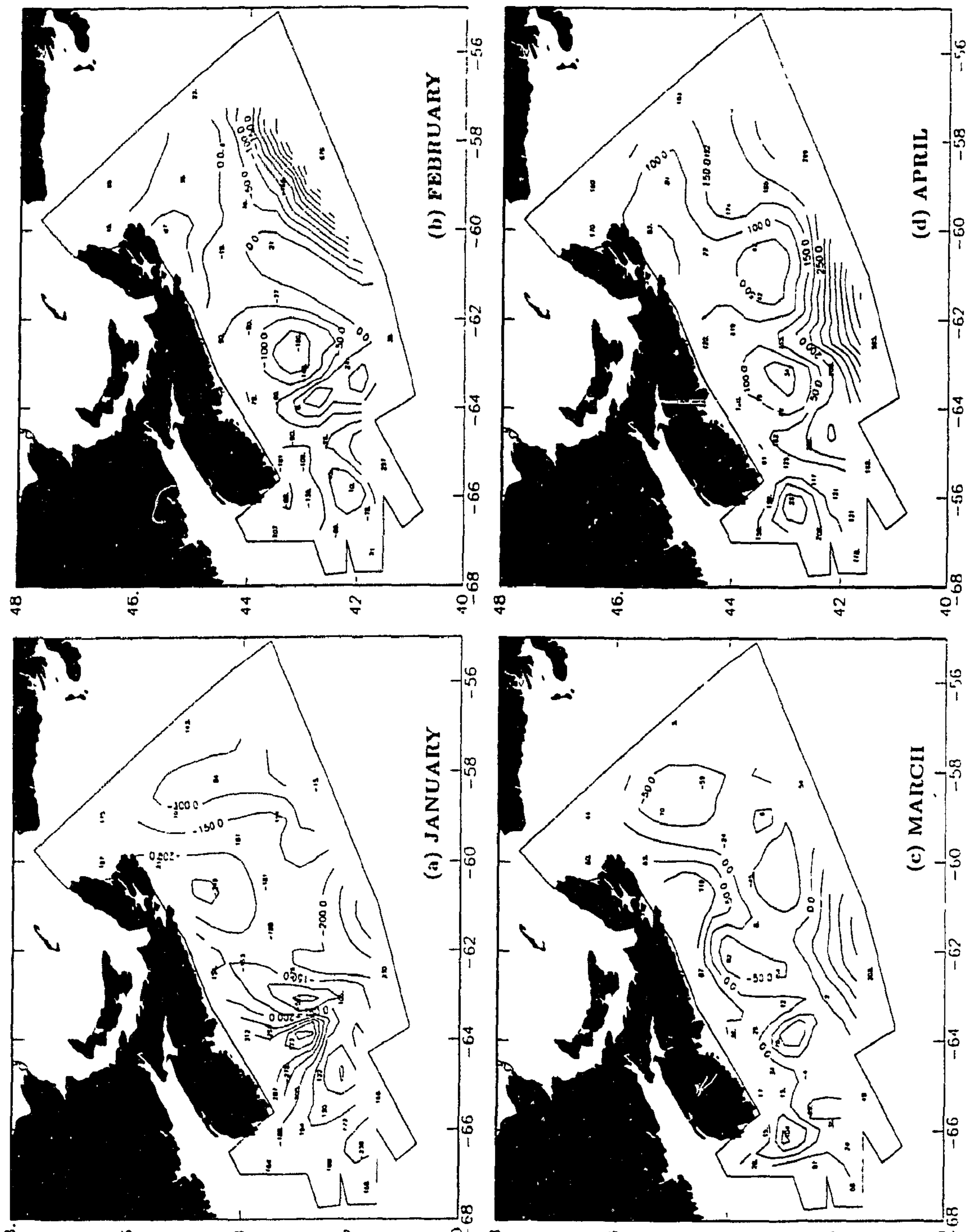

Figure B.1: January-April maps of the residual, $(\partial H/\partial t - Q_{zm})$, where Q_{zm} is the net surface heat flux with zero mean. Input data are plotted in small print. The contour interval is 50 W m^{-2}.

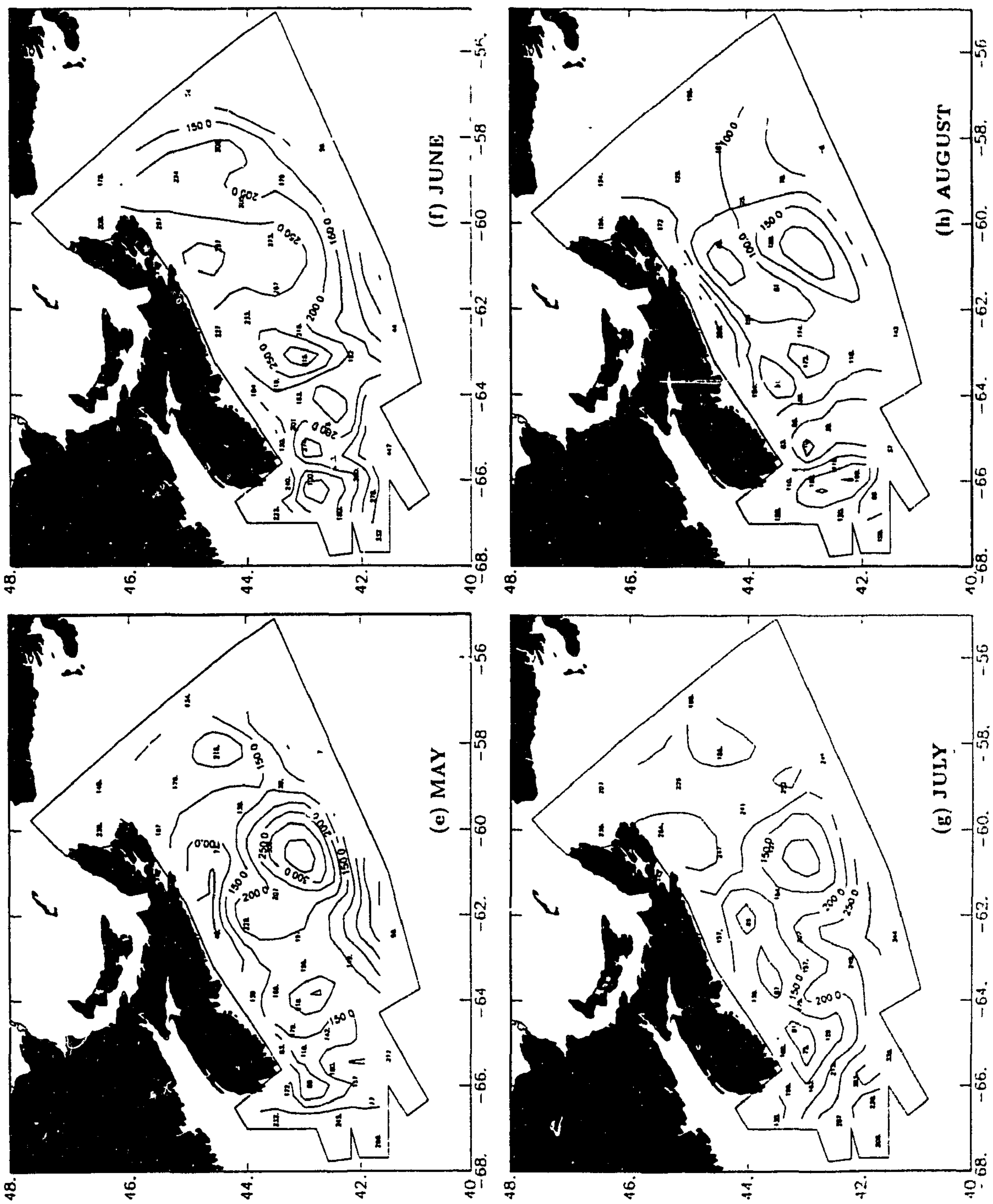

Figure B.2: May-August maps of the residual, $(\partial H/\partial t - Q_{zm})$. The contour interval is 50 W m^{-2}.

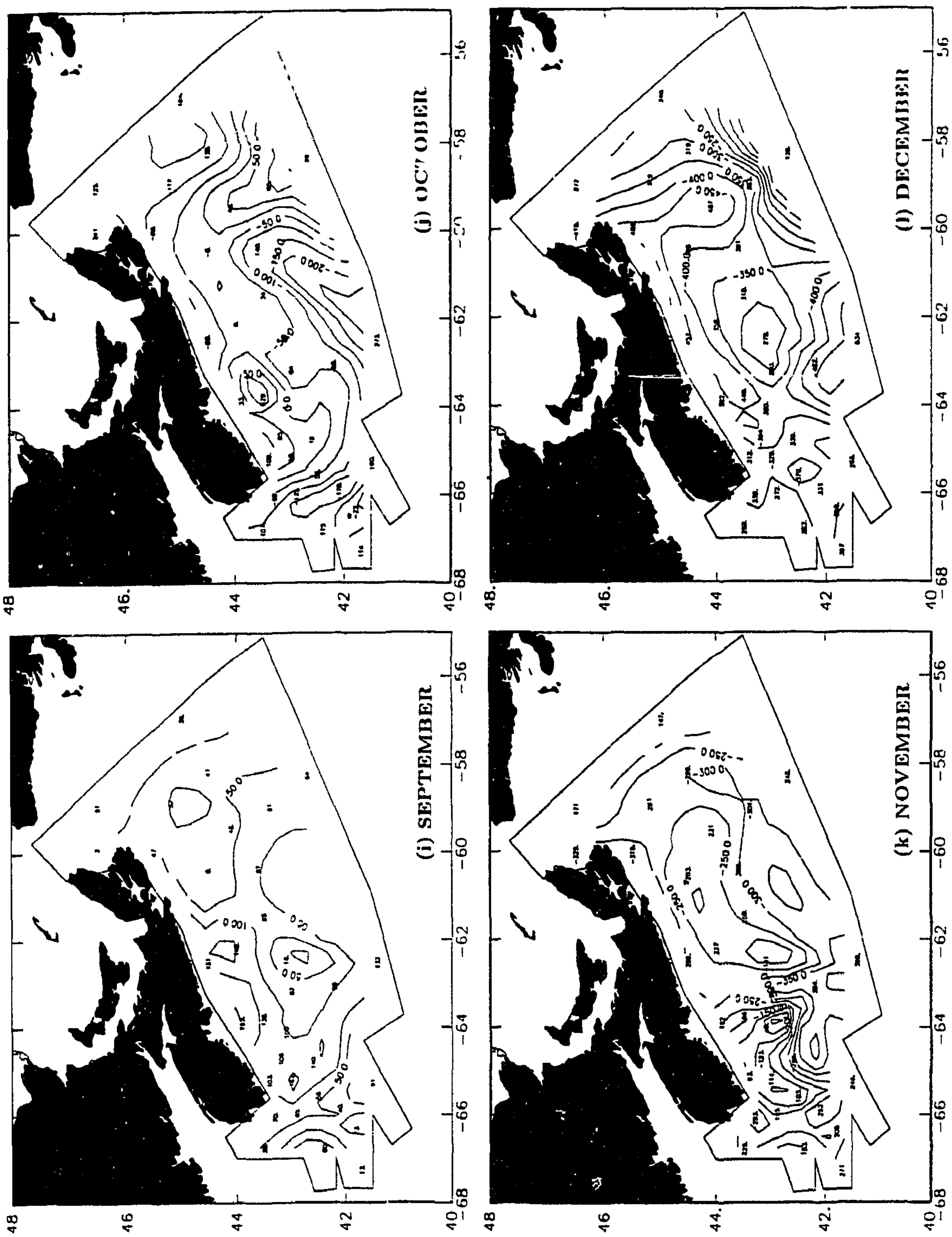

Figure B.3: September-Dec maps of the residual, $(\partial H/\partial t - Q_{zm})$. The contour interval is 50 W m^{-2}.

A1	Sydney Bight
A2	N. Laurentian Channel
A3	S. Laurentian Channel
A4	East Outer Shelf
A5	East Mid Shelf
A6	East Inner Shelf
A7	Central Outer Shelf
A8	Central Mid Shelf
A9	Central Inner Shelf
A10	West Outer Shelf
A11	West Inner Shelf
A12	E. Gulf of Main
A13	Western Slope
A14	Southern Slope
A15	Central Slope
A16	Northern Slope
A17	Central Offshore
A18	Northern Offshore

Table B.3: Names of the regrouped subareas numbered in Figure 3.5.

$$
\begin{aligned}
L &= \frac{\partial H}{\partial t} \\
Q &= Q \\
A &= -\rho c_p \int_{-h}^{0} \underline{u} \cdot \nabla T \, dz \\
U &= -\rho c_p \int_{-h}^{0} w \frac{\partial T}{\partial z} \, dz \\
M &= \rho c_p \int_{-h}^{0} K_H \cdot \nabla^2 T \, dz \\
D &= -\rho c_p K_v \left. \frac{\partial T}{\partial z} \right|_{-h} \\
R &= Q + A + U + M + D
\end{aligned}
$$

Subarea	Term	Mean ($\mathrm{W\ m^{-2}}$)	Amplitude ($\mathrm{W\ m^{-2}}$)	Phase (days)
A8 (shelf)	L	0	222	159
	Q	25	202	153
	A	−40	26	203
	U	1	6	64
	M	11	25	217
	D	6	20	95
	R	2	25	165
A15 (slope)	L	0	270	145
	Q	−53	220	158
	A	−80	38	326
	U	1	2	129
	M	144	22	162
	D	7	23	85
	R	19	55	3

Table B.4: Estimates of the terms in the mean heat budget for subareas A8 and A15.

(a) Central mid Shelf (A8)

	Jan	Feb	Mar	Apr	May	Jun	Jul	Aug	Sep	Oct	Nov	Dec
L	-204	-70	-27	109	197	226	88	78	143	55	-197	-398
Q	-147	-94	20	128	192	219	196	142	37	-68	-128	-200
A	-69	-65	-47	-37	-41	-41	-22	-21	7	-20	-48	-76
U	6	9	5	6	5	0	-2	-5	-2	-3	-7	-1
M	16	-15	-3	50	-15	-26	-10	72	96	34	-35	-38
D	22	24	26	20	13	12	14	9	-13	-8	-48	-23
R	-172	-140	1	168	154	163	177	197	150	-64	-265	-338

(b) Central Slope (A15)

	Jan	Feb	Mar	Apr	May	Jun	Jul	Aug	Sep	Oct	Nov	Dec
L	-105	24	2	206	148	192	240	116	99	-55	-384	-482
Q	-227	-203	-98	33	127	165	157	84	-32	-136	-223	-279
A	-23	-53	-54	-75	-257	-78	-74	-33	-131	-54	-93	-36
U	0	1	-1	2	5	0	1	-1	4	1	-5	-1
M	224	28	124	144	279	42	243	70	258	58	123	132
D	34	33	26	20	18	15	6	3	2	-15	-44	-13
R	9	-194	-2	125	171	145	331	124	101	-146	-242	-198

Table B.5: Estimates of the terms in the seasonal heat budget in W m^{-2}.for subareas A8 and A15

$$
\begin{aligned}
LS &= \frac{\partial S}{\partial t} \\
EP &= S_o(E-P) \\
AS &= -\int_{-h}^{0} \underline{u}\cdot\nabla S\,dz \\
US &= -\int_{-h}^{0} w\frac{\partial S}{\partial z}\,dz \\
MS &= \int_{-h}^{0} K_H\cdot\nabla^2 S\,dz \\
DS &= -K_v\,\frac{\partial S}{\partial z}\bigg|_{-h} \\
RS &= EP+AS+US+MS+DS
\end{aligned}
$$

Subarea	Term	Mean $\times 10^{-7}$(m s^{-1})	Amplitude $\times 10^{-7}$(m s^{-1})	Phase (days)
A8 (shelf)	LS	0	17	127
	EP	3	3	6
	AS	−28	10	115
	US	7	2	41
	MS	−8	15	112
	DS	26	7	341
	RS	−1	5	90
A15 (slope)	LS	0	15	78
	EP	9	6	354
	AS	−64	18	359
	US	1	1	56
	MS	82	16	318
	DS	24	1	353
	RS	52	23	345

Table B.6: Estimates of the terms in the mean salt budget in 10^{-7} m s^{-1} for subareas A8 and A15.

(a) Central mid Shelf (A8)

	Jan	Feb	Mar	Apr	May	Jun	Jul	Aug	Sep	Oct	Nov	Dec
LS	17	31	1	2	-6	12	33	22	-36	1	-10	-68
EP	5	5	3	2	1	0	0	1	2	3	5	5
AS	-23	-29	-14	-19	-29	-25	-17	-23	-30	-40	-49	-37
US	7	12	4	7	10	5	5	8	3	3	9	7
MS	-9	0	0	13	-14	8	-15	22	-34	8	-81	2
DS	30	35	22	21	20	23	26	19	21	25	31	39
RS	10	22	15	25	-12	12	0	27	-38	-1	-85	17

(b) Central Slope (A15)

	Jan	Feb	Mar	Apr	May	Jun	Jul	Aug	Sep	Oct	Nov	Dec
LS	27	32	45	77	-74	-54	41	-12	31	30	-70	-73
EP	15	14	11	9	6	4	3	5	7	10	13	14
AS	-26	-47	-38	-52	-161	-43	-73	-23	-129	-47	-88	-44
US	1	1	-1	2	6	0	-1	1	-4	-1	5	1
MS	165	37	80	54	107	14	131	23	164	29	83	102
DS	-32	-28	-20	-19	-23	-28	-22	-21	-29	-22	-18	-24
RS	187	32	73	33	-19	3	81	27	67	12	31	98

Table B.7: Estimates of the terms in the seasonal salt budget in 10^{-7} m s^{-1}. for subareas A8 and A15.

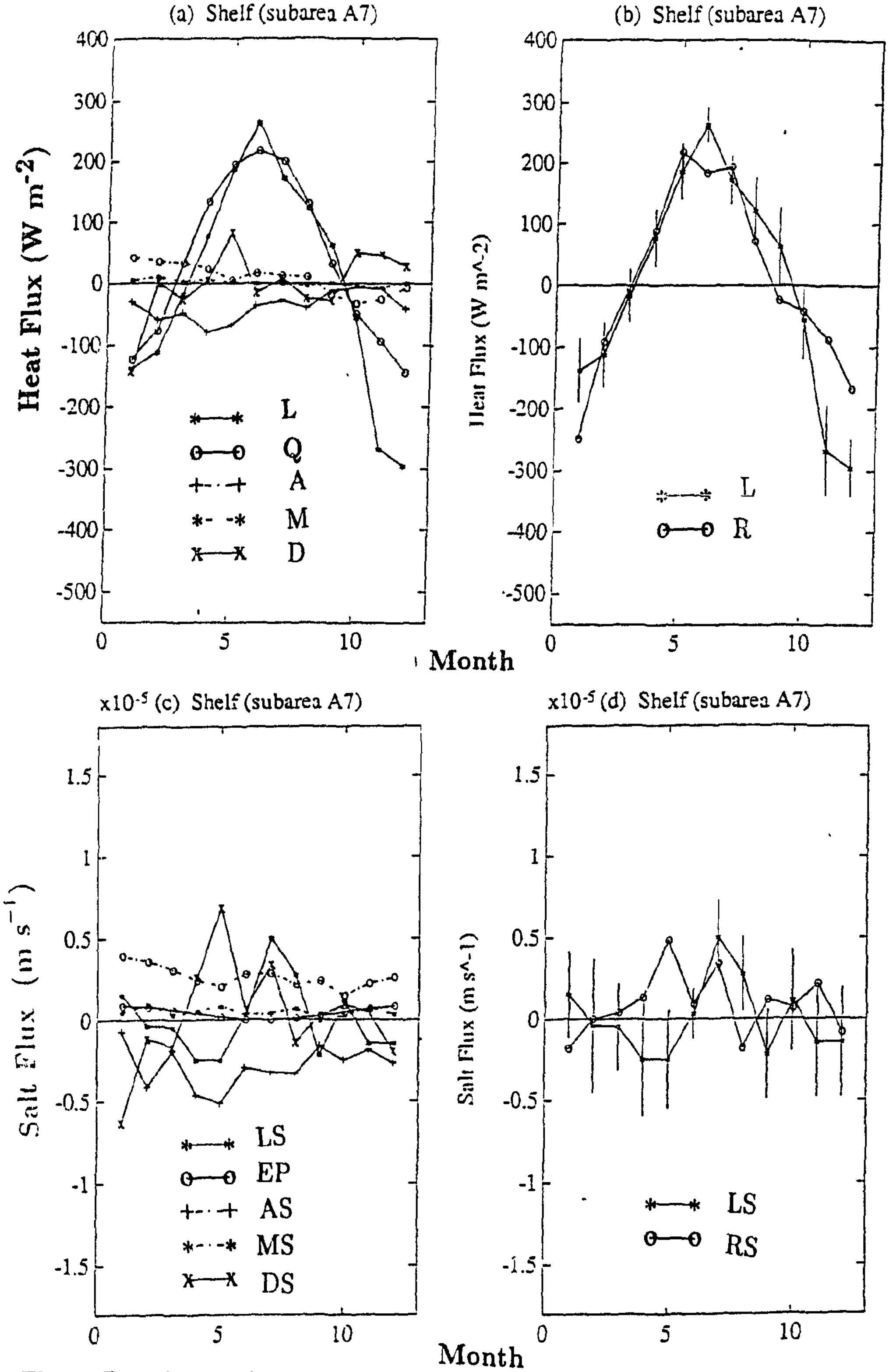

Figure B.4: Seasonal estimates of the terms in the heat and salt budget for subarea A7. (b) and (d) show the balance in the seasonal heat and salt budget respectively.

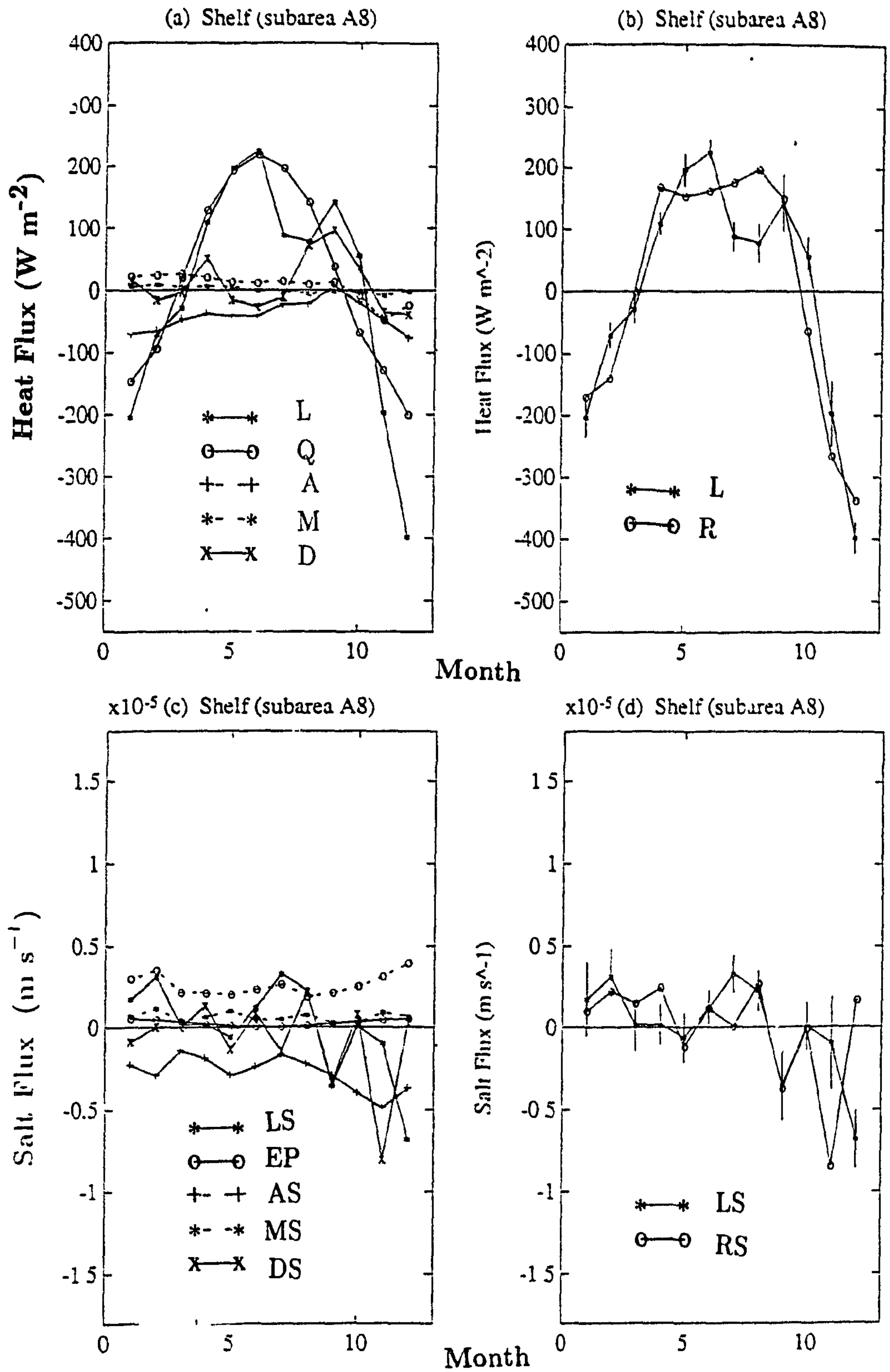

Figure B.5: Seasonal estimates of the terms in the heat and salt budget for subarea A8. (b) and (d) show the balance in the seasonal heat and salt budget respectively.

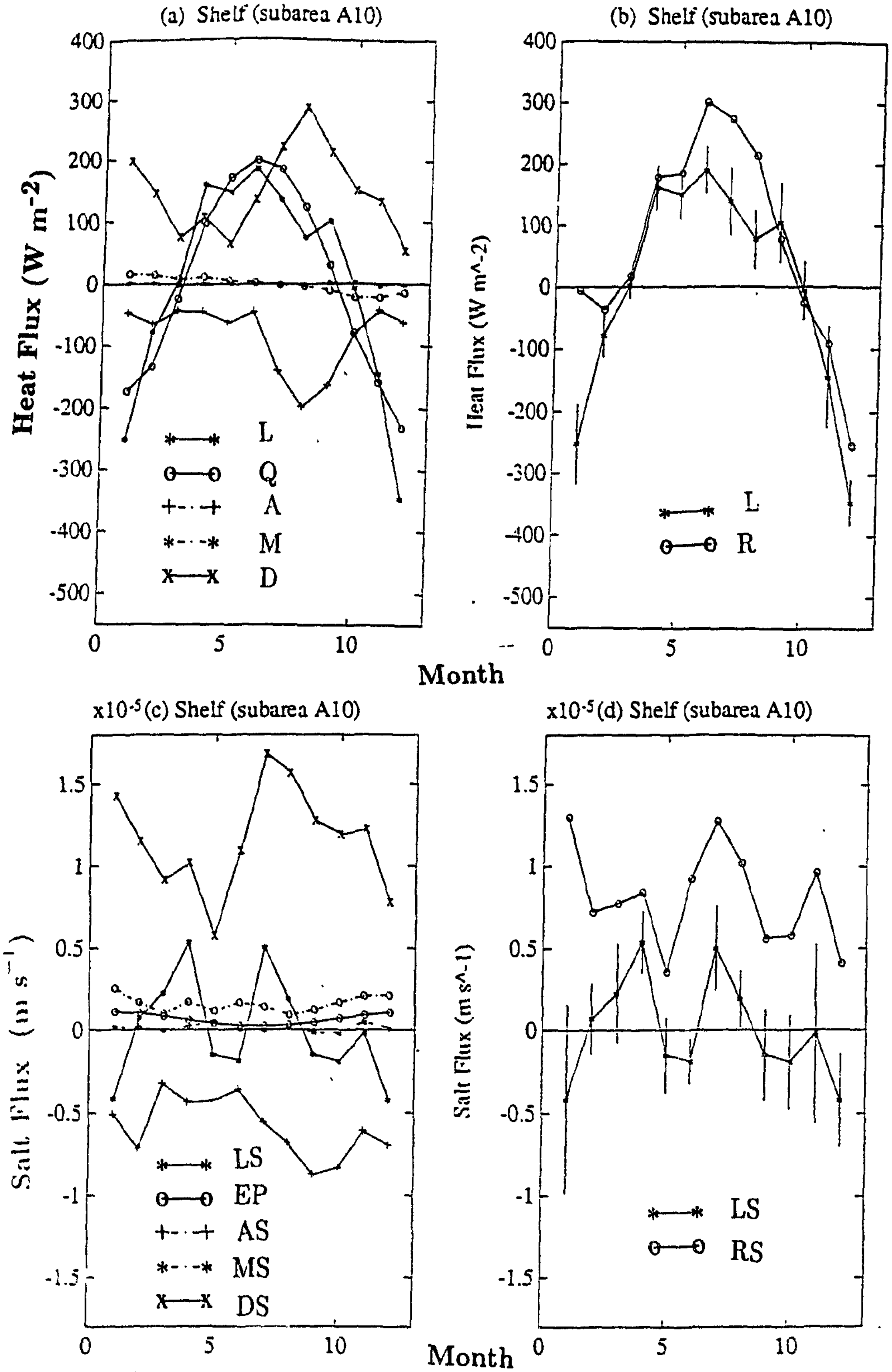

Figure B.6: Seasonal estimates of the terms in the heat and salt budget for subarea A10. (b) and (d) show the balance in the seasonal heat and salt budget respectively.

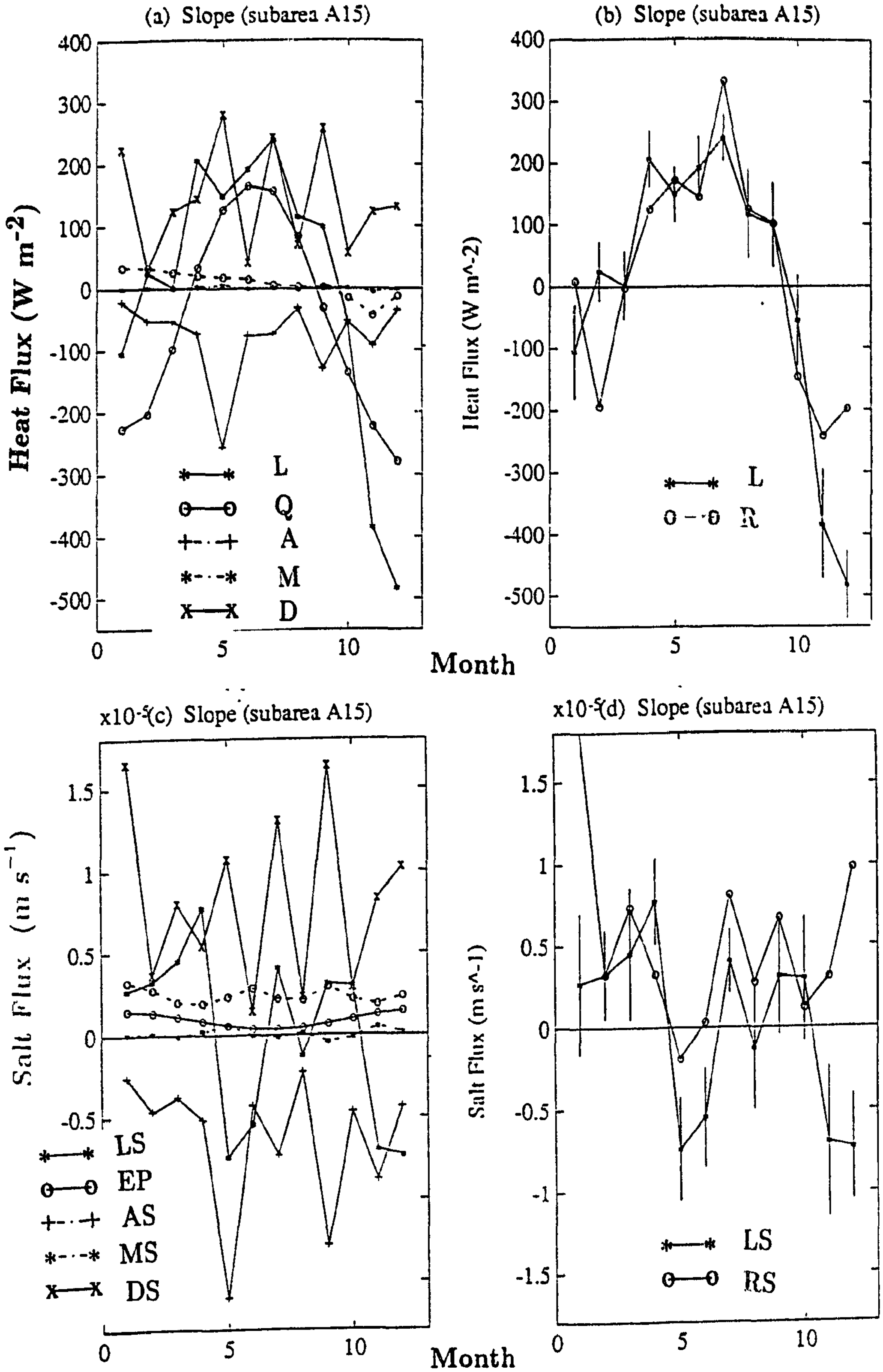

Figure B.7: Seasonal estimates of the terms in the heat and salt budget for subarea A15. (b) and (d) show the balance in the seasonal heat and salt budget respectively.

Appendix C

DEVELOPMENT OF THE MODIFIED 1-D HEAT DIFFUSION MODEL

C.1 The Model

In this section, the steps taken to develop the model are explained in detail. Basically, the development of the model involves three steps: (i) writing the heat diffusion equation using Crank-Nicholson finite difference scheme, (ii) expressing (i) in matrix form, and (iii) solving the matrix equation.

The model uses a one-dimensional vertical heat diffusion equation which may be expressed as

$$\frac{\partial T}{\partial t} = \frac{\partial}{\partial z}\left(K_V \frac{\partial T}{\partial z}\right) + \Gamma(z,t) \tag{C.1}$$

where

$$\int_{-h}^{0} \Gamma(z,t)\, dz = \frac{\partial}{\partial t}\int_{-h}^{0} T\, dz - \frac{Q}{\rho c_p} + K_V \left.\frac{\partial T}{\partial z}\right|_{-h} \tag{C.2}$$

K_V is the coefficient of eddy diffusivity. Q is the net surface heat flux, ρ the water density and c_p the specific heat capacity of sea water at constant pressure. Notice that the heat diffusion equation has been modified to include the imbalance $\Gamma(z,t)$.

The boundary condition at the surface is

$$K_v \frac{\partial T}{\partial z}\bigg|_{-h} = \frac{Q}{\rho c_p} \qquad z = 0 \tag{C.3}$$

At $z = -h$, the model is forced with the observed temperature. For simplicity, in the computation that follows in this Appendix, K_v and $\Gamma(z,t)$ will henceforth be written as K and Γ respectively. For the co-ordinate system, z is zero at the sea surface and increases upwards.

The first step is to write (C.1) in FTCS (forward time centered space) differencing scheme. If I form the average of the explicit and implicit FTCS schemes, I have the Crank-Nicholson scheme, which may be expressed generally as

$$\begin{aligned}\frac{T_j^{n+1} - T_j^n}{\Delta t} = \frac{1}{2dz_j} \qquad & \left[\left\{K_{j-1}^n \frac{(T_{j-1}^n - T_j^n)}{\Delta z_j} - K_j^n \frac{(T_j^n - T_{j+1}^n)}{\Delta z_{j+1}}\right\}\right. \\ & \left. + \left\{K_{j-1}^{n+1} \frac{(T_{j-1}^{n+1} - T_j^{n+1})}{\Delta z_j} - K_j^{n+1} \frac{(T_j^{n+1} - T_{j+1}^{n+1})}{\Delta z_{j+1}}\right\}\right] \\ & + \tfrac{1}{2}\left(\Gamma_j^n + \Gamma_j^{n+1}\right)\end{aligned} \tag{C.4}$$

The explicit method is second-order accurate in both space and time, but unstable for large time steps, whereas the implicit method is stable for arbitrarily large time steps, but only first-order accurate. Thus, the Crank-Nicholson scheme combines the second-order accuracy of the explicit method with the stability for large time steps of the implicit method *[Press et al., 1986]*. Equation (C.4) can be rearranged as

$$\begin{aligned} -\left(\frac{\Delta t K_{j-1}^{n+1}}{2dz_j \Delta z_j}\right) T_{j-1}^{n+1} + \left(1 + \frac{\Delta t K_{j-1}^{n+1}}{2dz_j \Delta z_j} + \frac{\Delta t K_j^{n+1}}{2dz_j \Delta z_{j+1}}\right) T_j^{n+1} - \left(\frac{\Delta t K_j^{n+1}}{2dz_j \Delta z_{j+1}}\right) T_{j+1}^{n+1} \\ = \left(\frac{\Delta t K_{j-1}^n}{2dz_j \Delta z_j}\right) T_{j-1}^n + \left(1 - \frac{\Delta t K_{j-1}^n}{2dz_j \Delta z_j} - \frac{\Delta t K_j^n}{2dz_j \Delta z_{j+1}}\right) T_j^n + \left(\frac{\Delta t K_j^n}{2dz_j \Delta z_{j+1}}\right) T_{j+1}^n \\ + \tfrac{\Delta t}{2}\left(\Gamma_j^n + \Gamma_j^{n+1}\right)\end{aligned} \tag{C.5}$$

where n and j refer to the time and depth index respectively. The model has a time step $\Delta t = 30 \times 24 \times 3600\,\mathrm{s}$. There are 6 levels (i.e., $j = 1,6$) in the vertical covering the $75\,m$ depth. Note that the diffusivity K_{j-1} (for example) is computed at the mid depth between levels $j-1$ and j. See Figure C.1 for the definition of other symbols

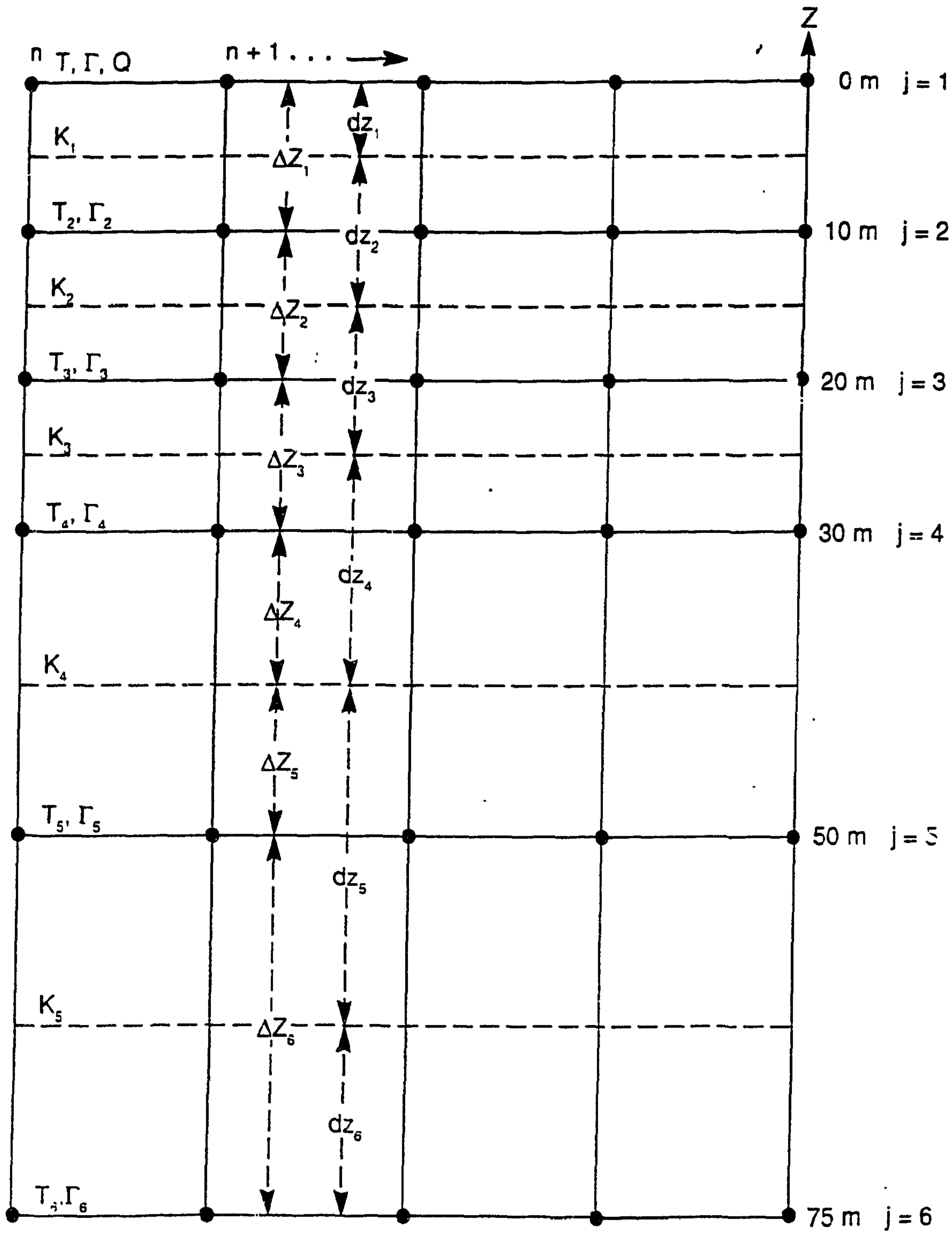

Figure C.1: Grid resolution and representation of parameters in the modified vertical one-dimensional heat diffusion model.

and the depths where T, Γ, Q and K are evaluated in the model. Δz_j is the depth interval between levels j and $j+1$, while dz_j is the depth increment between levels $j-1/2$ and $j+1/2$.

Equation (C.5) is written for $j = 1, 2 \ldots 6$, thereby giving 6 equations. At $j = 1$, when the surface boundary condition is applied, (C.5) becomes

$$\left(1 + \frac{\Delta t K_1^{n+1}}{2dz_1 \Delta z_1}\right) T_1^{n+1} - \left(\frac{\Delta t K_1^{n+1}}{2dz_1 \Delta z_1}\right) T_2^{n+1} =$$

$$\left(1 - \frac{\Delta t K_1^n}{2dz_1 \Delta z_1}\right) T_1^n + \left(\frac{\Delta t K_1^n}{2dz_1 \Delta z_1}\right) T_2^n + \frac{\Delta t \left(Q^n + Q^{n+1}\right)}{2\rho c_p dz_1} + \frac{\Delta t}{2}\left(\Gamma_1^n + \Gamma_1^{n+1}\right) \tag{C.6}$$

At j=6, the boundary condition is

$$T_6^n = T_{obs}^n \quad \text{and} \quad T_6^{n+1} = T_{obs}^{n+1} \tag{C.7}$$

where T_{obs}^n and T_{obs}^{n+1} are the observed temperature at $j = 6$ for time steps n and $n+1$ respectively.

The second step is to write the six equations (obtained from (C.5), (C.6) and (C.7)) as a matrix equation of the form

$$\mathbf{A}^{n+1}\underline{\mathrm{T}}^{n+1} = \mathbf{B}^n\underline{\mathrm{T}}^n + \underline{\mathrm{F}}^n \tag{C.8}$$

The elements of (C.8) may be written as

$$
\begin{bmatrix}
a_{11} & a_{12} & 0 & 0 & 0 & 0 \\
a_{21} & a_{22} & a_{23} & 0 & 0 & 0 \\
0 & a_{32} & a_{33} & a_{34} & 0 & 0 \\
0 & 0 & a_{43} & a_{44} & a_{45} & 0 \\
0 & 0 & 0 & a_{54} & a_{55} & a_{56} \\
0 & 0 & 0 & 0 & 0 & 1
\end{bmatrix}
\begin{bmatrix}
T_1^{n+1} \\ T_2^{n+1} \\ T_3^{n+1} \\ T_4^{n+1} \\ T_5^{n+1} \\ T_6^{n+1}
\end{bmatrix}
=
$$

$$
\begin{bmatrix}
b_{11} & b_{12} & 0 & 0 & 0 & 0 \\
b_{21} & b_{22} & b_{23} & 0 & 0 & 0 \\
0 & b_{32} & b_{33} & b_{34} & 0 & 0 \\
0 & 0 & b_{43} & b_{44} & b_{45} & 0 \\
0 & 0 & 0 & b_{54} & b_{55} & b_{56} \\
0 & 0 & 0 & 0 & 0 & 0
\end{bmatrix}
\begin{bmatrix}
T_1^{n} \\ T_2^{n} \\ T_3^{n} \\ T_4^{n} \\ T_5^{n} \\ T_6^{n}
\end{bmatrix}
+
\begin{bmatrix}
F_1 \\ F_2 \\ F_3 \\ F_4 \\ F_5 \\ F_6
\end{bmatrix}
\tag{C.9}
$$

where

$$a_{11} = 1 + \frac{\Delta t K_1^{n+1}}{2dz_1 \Delta z_1}, \quad a_{22} = 1 + \frac{\Delta t K_1^{n+1}}{2dz_2 \Delta z_1} + \frac{\Delta t K_2^{n+1}}{2dz_2 \Delta z_2},$$

$$a_{33} = 1 + \frac{\Delta t K_2^{n+1}}{2dz_3 \Delta z_2} + \frac{\Delta t K_3^{n+1}}{2dz_3 \Delta z_3}, \quad a_{44} = 1 + \frac{\Delta t K_3^{n+1}}{2dz_4 \Delta z_3} + \frac{\Delta t K_4^{n+1}}{2dz_4 \Delta z_4},$$

$$a_{55} = 1 + \frac{\Delta t K_4^{n+1}}{2dz_5 \Delta z_4} + \frac{\Delta t K_5^{n+1}}{2dz_5 \Delta z_5}, \quad a_{12} = -\frac{\Delta t K_1^{n+1}}{2dz_1 \Delta z_1}, \quad a_{21} = -\frac{\Delta t K_1^{n+1}}{2dz_2 \Delta z_1},$$

$$a_{23} = -\frac{\Delta t K_2^{n+1}}{2dz_2 \Delta z_2}, \quad a_{32} = -\frac{\Delta t K_2^{n+1}}{2dz_3 \Delta z_2}, \quad a_{34} = -\frac{\Delta t K_3^{n+1}}{2dz_3 \Delta z_3}, \quad a_{43} = -\frac{\Delta t K_3^{n+1}}{2dz_4 \Delta z_3},$$

$$a_{45} = -\frac{\Delta t K_4^{n+1}}{2dz_4 \Delta z_4}, \quad a_{54} = -\frac{\Delta t K_4^{n+1}}{2dz_5 \Delta z_4}, \quad a_{56} = -\frac{\Delta t K_5^{n+1}}{2dz_5 \Delta z_5},$$

and

$$b_{11} = 1 - \frac{\Delta t K_1^n}{2dz_1 \Delta z_1}, \quad b_{22} = 1 - \frac{\Delta t K_1^n}{2dz_2 \Delta z_1} - \frac{\Delta t K_2^n}{2dz_2 \Delta z_2},$$

$$b_{33} = 1 - \frac{\Delta t K_2^n}{2dz_3 \Delta z_2} - \frac{\Delta t K_3^n}{2dz_3 \Delta z_3}, \quad b_{44} = 1 - \frac{\Delta t K_3^n}{2dz_4 \Delta z_3} - \frac{\Delta t K_4^n}{2dz_4 \Delta z_4},$$

$$b_{55} = 1 - \frac{\Delta t K_4^n}{2dz_5 \Delta z_4} - \frac{\Delta t K_5^n}{2dz_5 \Delta z_5}, \quad b_{12} = \frac{\Delta t K_1^n}{2dz_1 \Delta z_1}, \quad b_{21} = \frac{\Delta t K_1^n}{2dz_2 \Delta z_1},$$

$$b_{23} = \frac{\Delta t K_2^n}{2dz_2 \Delta z_2}, \quad b_{32} = \frac{\Delta t K_2^n}{2dz_3 \Delta z_2}, \quad b_{34} = \frac{\Delta t K_3^n}{2dz_3 \Delta z_3}, \quad b_{43} = \frac{\Delta t K_3^n}{2dz_4 \Delta z_3},$$

$$b_{45} = \frac{\Delta t K_4^n}{2dz_4 \Delta z_4}, \quad b_{54} = \frac{\Delta t K_4^n}{2dz_5 \Delta z_4}, \quad b_{56} = \frac{\Delta t K_5^n}{2dz_5 \Delta z_5},$$

and

$$F_1 = \frac{\Delta t}{2\rho c_p dz_1}\left(Q^n + Q^{n+1}\right) + \frac{\Delta t}{2}\left(\Gamma_1^n + \Gamma_1^{n+1}\right)$$

$$F_2 = \frac{\Delta t}{2}\left(\Gamma_2^n + \Gamma_2^{n+1}\right), \quad F_3 = \frac{\Delta t}{2}\left(\Gamma_3^n + \Gamma_3^{n+1}\right),$$

$$F_4 = \frac{\Delta t}{2}\left(\Gamma_4^n + \Gamma_4^{n+1}\right), \quad F_5 = \frac{\Delta t}{2}\left(\Gamma_5^n + \Gamma_5^{n+1}\right), \quad F_6 = T_{obs}^{n+1}$$

The model is thus written to take care of the varing vertical space steps. The following depth resolutions are used:

$$\Delta z_1 = 10\,\text{m}, \quad \Delta z_2 = 10\,\text{m}, \quad \Delta z_3 = 10\,\text{m}, \quad \Delta z_4 = 20\,\text{m}, \quad \text{and} \quad \Delta z_5 = 20\,\text{m}$$

$$dz_1 = 5\,\text{m}, \quad dz_2 = 10\,\text{m}, \quad dz_3 = 10\,\text{m}, \quad dz_4 = 15\,\text{m}, \quad dz_5 = 22.5\,\text{m}, \quad \text{and}$$

$$dz_6 = 12.5\,\text{m}$$

The diffusivities are distributed as a function of water depth and time. The matrices $\mathbf{A}^{n+1}$ and $\mathbf{B}^{n}$ contain the diffusivities at time steps $n+1$ and n respectively. Notice that the two matrices are tridiagonal systems which one only has to store the non-zero elements and not the full 6×6 matrix. The vector $\underline{F}^{n}$ contains the forcing functions Q and Γ and the boundary condition at $z = -h$. The arrangement makes it easy to determine the contribution of each of the forcing functions in the creation of the water temperature structure.

The last step in the development of the model is to solve the matrix equation (C.8) simultaneously at each time step. This involves time-stepping the model forward .

With an initial zero temperature everywhere, the model is run until a periodic steady state is reached. The steady state surface and subsurface temperature for a given n (or month) becomes the model or predicted temperature for that month.

C.2 Estimation of the numerical diffusivity

The numerical computing scheme (described above) undoubtedly introduces some numerical (artificial) diffusivity into the analysis. To estimate the numerical diffusivity, I will compare the analytical and the numerical solutions for a constant K_V. The difference between the two solutions gives some idea of the numerical diffusivity in the computing scheme. The numerical diffusivity is created, in part, by the truncation error in the finite difference scheme. The estimate of this truncation error is presented below. It will be shown that the numerical diffusivity is very small and is not expected to alter significantly the results from the model.

(i) Analytical and numerical solutions

The analytical solution is obtained as follows. Consider a one-dimensional heat diffusion equation for a constant K_V written as

$$\frac{\partial T}{\partial t} = K_V \frac{\partial^2 T}{\partial z^2} \tag{C.10}$$

Let the temperature be expressed as

$$T = Re[A(z)e^{i\omega t}] \tag{C.11}$$

where $A(z)$ is the temperature amplitude, which varies with depth z, and $\omega = 2\pi/12\text{months}$ is the annual frequency. Substituting (C.11) into (C.10) gives

$$i\omega A = K_V \frac{\partial^2 A}{\partial z^2} \tag{C.12}$$

Assume that (C.12) has a solution of the form

$$A = C_1 \cosh\left[(1+i)\sqrt{\frac{\omega}{2K_V}}z\right] + C_2 \sinh\left[(1+i)\sqrt{\frac{\omega}{2K_V}}z\right] \tag{C.13}$$

For brevity, let

$$\delta = (1+i)\sqrt{\frac{\omega}{2K_V}} \tag{C.14}$$

Boundary conditions

(a) At the surface the model is forced with a periodic Q, i.e.,

$$\left.\frac{\partial T}{\partial z}\right|_{z=0} = \text{Re}\left[\frac{Qe^{iwt}}{K_V \rho c_p}\right] \tag{C.15}$$

Combining (C.11), (C.13) and (C.14) and differentiating one obtains

$$C_1\delta \sinh(\delta z) + C_2\delta \cosh(\delta z) = \frac{Q}{K_V \rho c_p}$$

from which, for $z = 0$,

$$C_2 = \frac{Q}{K_V \rho c_p \delta} \tag{C.16}$$

(b) At $z = -h$, I assume that $T = 0$. (C.11), (C.13) and (C.14) become

$$C_1 \cosh(\delta h) - C_2 \sinh(\delta h) = 0$$

therefore,

$$C_1 = \frac{Q}{K_V \rho c_p \delta} \frac{\sinh(\delta h)}{\cosh(\delta h)} \tag{C.17}$$

Substituting (C.13), (C.14), (C.16), (C.17) into (C.11) and rearranging, T becomes

$$T = \frac{Qe^{i(wt - \pi/4)}}{\rho c_p \sqrt{wK_v}} \left\{ \frac{\sinh\left[(1+i)\sqrt{\frac{w}{2K_v}}(h+z)\right]}{\cosh\left[(1+i)\sqrt{\frac{w}{K_v}}h\right]} \right\} \tag{C.18}$$

In both the analytical (C.18) and numerical (C.9) computations, I use Q = 200 W m^{-2} (which is a typical amplitude of Q on the Scotian Shelf), K_v = 1×10^{-4} m^2 s^{-1}. The temperature is computed at z = 0, 10, 20, 30, 50 and 75 m (the same depths used in the numerical scheme).

The analytical solutions (Figure C.2a) and the numerical solutions (Figure C.2b) are very similar. The magnitude of the difference between the two solutions has a maximum of about $0.3°C$. This is attributed to the effect of the numerical diffusivity. This is encouraging, for it shows that for the values of Q and the diffusivity used in this computation, the maximum effect on temperature of the numerical diffusivity is about $0.3°C$.

To have an idea of the effect of the numerical diffusivity on the estimated K_v, I kept the K_v in the analytical solution (C.18) constant at 1×10^{-4}m^2 s^{-1}. I then vary the K_v in the numerical scheme to determine the value of K_v that matches the analytical solution. I found that a K_v of about 0.9×10^{-4}m^2 s^{-1} closely matches the analytic solution. This means that for the values used, the numerical diffusivity is about 0.1×10^{-4}m^2 s^{-1}, which is about 10% of the real diffusivity.

(ii) Estimation of truncation error in the numerical scheme

Part of the numerical diffusivity in the numerical scheme may be due to truncation in the finite difference. The truncation error may be estimated using Taylor series expansion. The finite difference of (C.1), neglecting the $\Gamma(z,t)$ term, may be expressed as

$$\begin{aligned}\frac{T^{n+1} - T^n}{\Delta t} &= \frac{K^n_{j-1/2}\,\partial T^n/\partial z\big|_{j-1/2} - K^n_{j+1/2}\,\partial T^n/\partial z\big|_{j+1/2}}{1/2(\Delta z_j + \Delta z_{j+1})} \\ &= \frac{1}{1/2(\Delta z_j + \Delta z_{j+1})}\left[K^n_{j-1/2}\frac{(T^n_{j-1} - T^n_j)}{\Delta z_j} - K^n_{j+1/2}\frac{(T^n_j - T^n_{j+1})}{\Delta z_{j+1}}\right]\end{aligned} \tag{C.19}$$

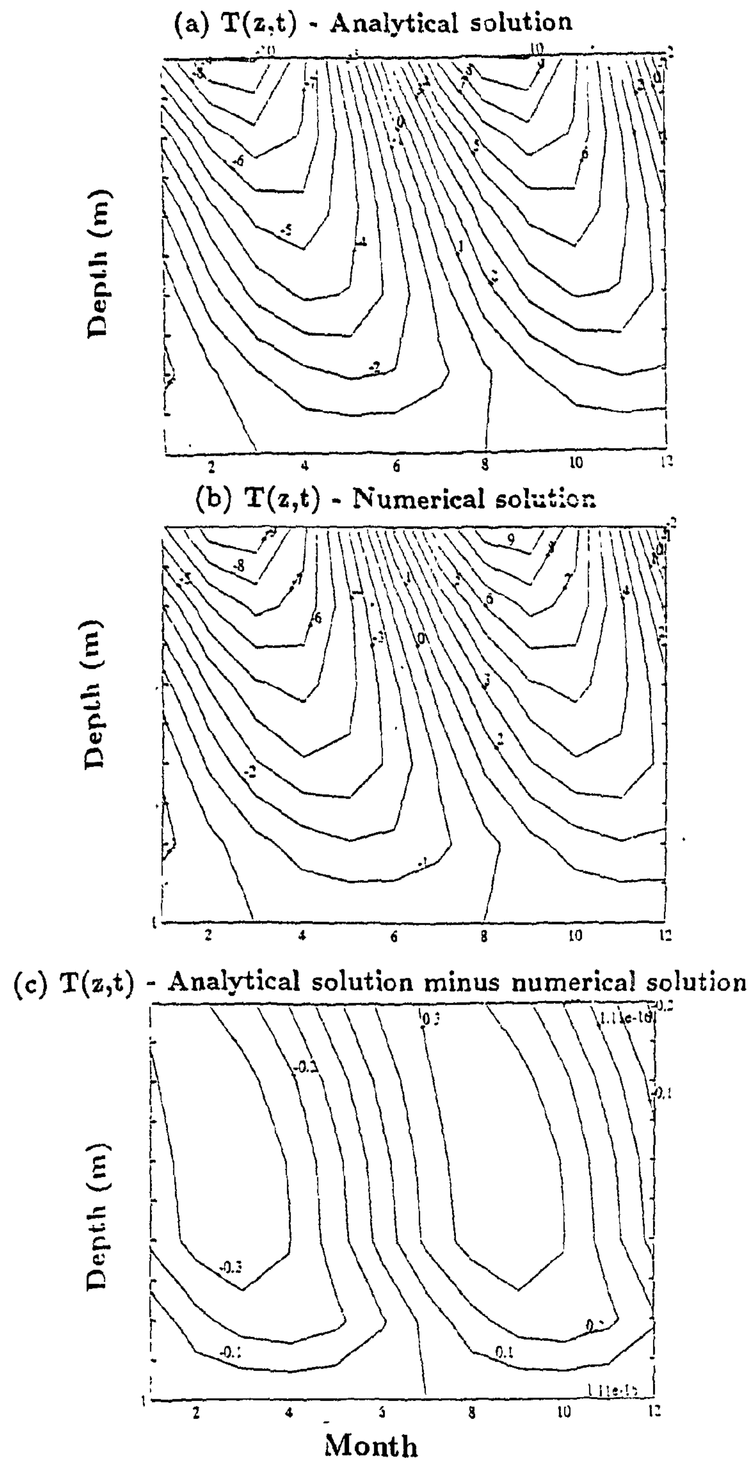

Figure C.2: The comparison of the analytical and numerical solutions, for a constant K_v.

(See Figure C.1 for the definition of the symbols) Applying Taylor series expansion, the temperatures in (C.19) may be written as

$$\begin{aligned} T^n_{j-1} &= T^n_{j-1/2} + \left.\frac{\partial T^n}{\partial z}\right|_{j-1/2} \frac{\Delta z_j}{2} + \frac{1}{2}\left.\frac{\partial^2 T^n}{\partial z^2}\right|_{j-1/2} \left(\frac{\Delta z_j}{2}\right)^2 \\ &+ \frac{1}{6}\left.\frac{\partial^3 T^n}{\partial z^3}\right|_{j-1/2} \left(\frac{\Delta z_j}{2}\right)^3 + O(\Delta z_j^4) \end{aligned} \tag{C.20}$$

$$\begin{aligned} T^n_j = \; & T^n_{j-1/2} - \left.\frac{\partial T^n}{\partial z}\right|_{j-1/2} \frac{\Delta z_j}{2} + \frac{1}{2}\left.\frac{\partial^2 T^n}{\partial z^2}\right|_{j-1/2} \left(\frac{\Delta z_j}{2}\right)^2 \\ & - \frac{1}{6}\left.\frac{\partial^3 T^n}{\partial z^3}\right|_{j-1/2} \left(\frac{\Delta z_j}{2}\right)^3 + O(\Delta z_j^4) \end{aligned} \tag{C.21}$$

$$\begin{aligned} T^n_j = \; & T^n_{j+1/2} + \left.\frac{\partial T^n}{\partial z}\right|_{j+1/2} \frac{\Delta z_{j+1}}{2} + \frac{1}{2}\left.\frac{\partial^2 T^n}{\partial z^2}\right|_{j+1/2} \left(\frac{\Delta z_{j+1}}{2}\right)^2 \\ & + \frac{1}{6}\left.\frac{\partial^3 T^n}{\partial z^3}\right|_{j+1/2} \left(\frac{\Delta z_{j+1}}{2}\right)^3 + O(\Delta z_{j+1}^4) \end{aligned} \tag{C.22}$$

$$\begin{aligned} T^n_{j+1} = \; & T^n_{j+1/2} - \left.\frac{\partial T^n}{\partial z}\right|_{j+1/2} \frac{\Delta z_{j+1}}{2} + \frac{1}{2}\left.\frac{\partial^2 T^n}{\partial z^2}\right|_{j+1/2} \left(\frac{\Delta z_{j+1}}{2}\right)^2 \\ & - \frac{1}{6}\left.\frac{\partial^3 T^n}{\partial z^3}\right|_{j+1/2} \left(\frac{\Delta z_{j+1}}{2}\right)^3 + O(\Delta z_{j+1}^4) \end{aligned} \tag{C.23}$$

Subtracting (C.21) from (C.20) one has

$$T^n_{j-1} - T^n_j = \left.\frac{\partial T^n}{\partial z}\right|_{j-1/2} \Delta z_j + \left.\frac{\partial^3 T^n}{\partial z^3}\right|_{j-1/2} \frac{\Delta z_j^3}{24} + O(\Delta z_j^4) \tag{C.24}$$

Again, subtracting (C.23) from (C.22) gives

$$T^n_j - T^n_{j+1} = \left.\frac{\partial T^n}{\partial z}\right|_{j+1/2} \Delta z_{j+1} + \left.\frac{\partial^3 T^n}{\partial z^3}\right|_{j+1/2} \frac{\Delta z_{j+1}^3}{24} + O(\Delta z_{j+1}^4) \tag{C.25}$$

Substituting (C.24) and (C.25) into (C.19) one obtains

$$\begin{aligned} \frac{T^{n+1} - T^n}{\Delta t} = \; & \frac{1}{1/2(\Delta z_j + \Delta z_{j+1})} \left[K^n_{j-1/2} \left(\left.\frac{\partial T^n}{\partial z}\right|_{j-1/2} + \frac{\Delta z_j^3}{24} \left.\frac{\partial^3 T^n}{\partial z^3}\right|_{j-1/2} \right) \right. \\ & \left. - K^n_{j+1/2} \left(\left.\frac{\partial T^n}{\partial z}\right|_{j+1/2} + \frac{\Delta z_{j+1}^3}{24} \left.\frac{\partial^3 T^n}{\partial z^3}\right|_{j+1/2} \right) \right] + O(\Delta z^2) \end{aligned} \tag{C.26}$$

Equation (C.26) shows what (C.19) should be to be second-order accurate in space, as quoted in the Crank-Nicholson scheme. But what the numerical scheme computes is (C.19). It is clear from (C.19) and (C.26) that the size of the truncation error is $(\Delta z^2/24)(\partial^3 T/\partial z^3)$ - which is proportional to the vertical grid spacing. The error affects the magnitude of the vertical temperature gradient and consequently the value of the vertical diffusivity.

To estimate the error, let us assume that $\partial^3 T/\partial z^3 = 10^{-3}\partial T/\partial z$. For Δz ranging from 10 m at the surface to 25 m at 75 m depth, the error accordingly ranges from 0 to 3% of the vertical temperature gradient. The error is small and is not expected to alter significantly the estimates of the diffusivities (in Chapter 4) and the predicted temperatures (in Chapters 5 and 6). The error could be further reduced by increasing the vertical resolution and maintaing a constant grid spacing.

Appendix D

DATA FOR THE COLD INTERMEDIATE LAYER

S#	Jan	Feb	Mar	Apr	May	Jun	Jul	Aug	Sep	Oct	Nov	Dec
1	50	-	-	50	50	75	75	100	100	100	100	100
2	20	-	10	-	75	75	75	100	100	75	100	100
3	30	30	-	50	100	75	75	100	75	100	100	100
4	30	10	30	50	50	50	75	50	75	100	100	-
5	-	-	10	50	75	75	75	100	-	75	150	-
6	10	-	50	50	75	75	75	100	100	100	-	-
7	-	50	50	50	75	75	75	100	-	-	-	-
8	-	-	30	50	75	75	50	75	-	-	-	-
9	-	30	10	30	75	50	100	50	-	-	-	-
10	-	10		30	50	50	75	50	75	-	-	-
11	10	-	30	30	50	50	50	50	50	75	75	-
12	10	-	10	20	50	50	50	50	50	75	75	75
13	10	10	10	30	50	50	50	75	75	-	-	-
14	-	10	20	50	50	75	50	50	75	-	-	-
15	-	-	20	50	50	50	50	50	50	75	75	75
16	10	10	-	20	75	50	50	50	75	75	50	50
17	-	10	10	50	50	75	50	50	75	75	75	-
18	10	10	10	10	50	50	75	75	75	75	75	75
19	20	10	30	50	50	75	50	50	75	75	100	75
20	20	20	20	-	-	-	50	50	50	-	10	10
21	20	10	30	30	50	50	75	100	100	75	75	
22	10	10	10	30	50	50	75	75		100	100	10
23	-	20	20	-	-	50	-	-	-	75	50	30
24	-	10	20	50	-	30	-	30	50	-	20	-
25	-	-	-30	75	75	100	-	-	-	-	-	
26	-	-	20	50	50	75	75	100	100	100	100	50
27	20	-	10	50	-	-	-	-	-	-	20	75
28	-	-	10	10	50	100	100	100	-	-	-	20
29	-	-	-	-	50	50	75	-	- 75	75	100	-
30	-	10	10	10	50	50	75	75	100	100	75	75
32	10	10	10	-	- 200	75	-	50	-	10	-	-
33	10	10	10	10	20	50	50	50	50	75	100	100
34	10	10	10	10	30	50	50	50	75	75	75	100
35	-	-	10	10	50	50	75	75	50	-	75	75

Table D.1: Distribution of the cold intermediate layer (CIL) in space and time. The first column is the number of the subarea grouped by *Drinkwater and Trites [1987]* (see Figure 2.1). The value below a particular month shows the depth in metres where the CIL is found in that month. A month without any value beneath it, for a given subarea means there is no CIL for that month. For example, at subarea 12, in September, the CIL is found at 50 m depth.

Table D.2: Variation in temperature of the observed CIL and the temperature difference between the CIL and the next level above and below the CIL. The value below a given month shows the temperature in $°C$ of the CIL for that month. The superscript and the subscript (both written in small print) indicate the temperature difference between the CIL and that of the water level above and below the CIL respectively. For example at subarea 12, the value under September is $3.47^{5.35}_{0.89}$. This means that the temperature of the CIL in September is $3.47°C$, the temperature of the next level above the CIL is $3.47 + 5.35°C$, and the temperature of the next level below the CIL is $3.47 + 0.89°C$. Note that the temperature are measured at 0, 10, 20, 30, 50, 75, 100 m, etc. levels. The larger the temperature difference, the better defined the CIL.

$S\#$	Jan	Feb	Mar	Apr	May	Jun	Jul	Aug	Sep	Oct	Nov	Dec
1	$-1.16^{0.02}_{0.34}$	-	-	$-0.42^{0.16}_{0.74}$	$0.50^{1.15}_{0.06}$	$0.78^{0.88}_{0.17}$	$1.07^{1.16}_{0.42}$	$1.15^{0.03}_{1.46}$	$1.80^{1.23}_{1.16}$	$0.86^{1.14}_{1.56}$	$1.65^{2.26}_{1.18}$	$0.82^{0.73}_{1.48}$
2	$-0.27^{0.02}_{0.06}$	-	$-1.16^{0.03}_{0.02}$	-	$0.80^{0.17}_{0.17}$	$0.23^{0.17}_{0.41}$	$0.64^{0.26}_{0.47}$	$0.84^{0.17}_{1.55}$	$1.48^{0.56}_{1.03}$	$1.42^{1.38}_{0.32}$	$1.11^{0.36}_{1.28}$	$0.92^{0.07}_{1.13}$
3	$1.33^{0.01}_{0.03}$	$0.91^{0.01}_{0.15}$	-	$0.76^{0.26}_{0.02}$	$3.50^{0.27}_{0.62}$	$0.81^{0.24}_{0.95}$	$1.42^{0.58}_{0.41}$	$0.50^{0.18}_{2.88}$	$1.15^{1.42}_{0.36}$	$2.16^{0.20}_{0.93}$	$-0.30^{0.76}_{4.18}$	$0.57^{0.36}_{2.13}$
4	$0.57^{0.03}_{0.21}$	$2.01^{0.91}_{0.02}$	$0.75^{0.02}_{0.10}$	$0.90^{0.25}_{0.13}$	$2.55^{0.78}_{0.57}$	$3.09^{1.23}_{0.61}$	$2.28^{0.79}_{1.41}$	$3.22^{3.72}_{0.27}$	$2.66^{1.07}_{1.20}$	$3.21^{0.08}_{2.32}$	$1.21^{0.79}_{1.33}$	-
5	-	-	$0.46^{0.20}_{0.08}$	$-0.20^{0.26}_{0.32}$	$1.43^{0.18}_{0.08}$	$0.76^{0.22}_{0.33}$	$1.46^{0.09}_{0.27}$	$1.03^{0.01}_{1.03}$	-	$2.25^{1.69}_{0.02}$	$2.13^{0.10}_{0.62}$	-
6	$-1.12^{0.09}_{0.08}$	-	$0.13^{0.09}_{0.16}$	$0.03^{0.19}_{0.86}$	$0.35^{0.24}_{0.28}$	$0.72^{0.72}_{0.29}$	$1.87^{0.58}_{0.09}$	$0.97^{0.36}_{2.10}$	$1.45^{0.74}_{1.87}$	$2.68^{0.26}_{0.78}$	-	-
7	-	$-0.58^{0.21}_{2.40}$	$0.28^{0.05}_{0.69}$	$1.22^{0.58}_{1.74}$	$0.78^{0.12}_{0.16}$	$0.29^{0.78}_{0.62}$	$2.31^{1.15}_{0.28}$	$1.12^{0.13}_{0.09}$	-	-	-	-
8	-	-	$0.68^{0.06}_{0.02}$	$1.78^{0.15}_{0.16}$	$2.74^{0.12}_{0.16}$	$2.03^{0.78}_{0.62}$	$3.29^{1.15}_{0.28}$	$3.62^{0.13}_{0.09}$	-	-	-	-
9	-	$2.44^{0.02}_{0.19}$	$2.23^{0.61}_{0.01}$	$1.61^{0.16}_{0.10}$	$2.60^{0.44}_{2.30}$	$5.79^{0.55}_{1.66}$	$4.35^{0.36}_{1.97}$	$2.16^{9.93}_{1.1}$	-	-	-	-
10	-	$3.37^{0.02}_{0.17}$	-	$3.38^{0.06}_{0.19}$	$3.39^{0.99}_{0.73}$	$5.27^{2.02}_{0.98}$	$4.72^{0.18}_{3.29}$	$5.57^{3.60}_{0.20}$	$5.28^{0.58}_{2.75}$	-	-	-
11	$3.78^{0.90}_{0.01}$	-	$1.51^{0.02}_{0.19}$	$3.00^{0.18}_{0.02}$	$3.31^{1.40}_{0.74}$	$4.55^{1.43}_{1.35}$	$4.22^{2.37}_{1.37}$	$6.02^{2.12}_{0.76}$	$4.70^{5.67}_{0.46}$	$5.35^{1.62}_{0.87}$	$6.19^{1.91}_{0.24}$	-
12	$2.24^{0.06}_{0.05}$	-	$1.12^{0.33}_{0.09}$	$1.79^{0.03}_{0.06}$	$2.60^{0.80}_{1.38}$	$3.04^{2.27}_{1.17}$	$3.85^{2.66}_{0.67}$	$3.20^{2.09}_{0.71}$	$3.47^{5.35}_{0.89}$	$5.24^{0.58}_{0.88}$	$5.58^{1.96}_{1.17}$	$4.38^{1.24}_{1.11}$
13	$0.14^{0.13}_{0.17}$	$0.69^{0.09}_{0.19}$	$-0.41^{0.71}_{0.04}$	$2.63^{0.25}_{0.01}$	$1.03^{0.49}_{0.24}$	$1.12^{2.25}_{0.07}$	$2.49^{2.25}_{0.04}$	$3.13^{0.13}_{0.42}$	$1.32^{2.30}_{0.68}$	-	-	-

14	-	$0.46^{0.09}_{0.01}$	$0.33^{0.02}_{0.08}$	$1.09^{0.03}_{0.24}$	$1.42^{0.62}_{0.18}$	$1.40^{0.33}_{0.87}$	$1.78^{2.18}_{0.37}$	$2.66^{1.41}_{0.13}$	$2.80^{0.75}_{0.94}$	-	-	-
15	-	-	$0.50^{0.01}_{0.19}$	$1.91^{0.22}_{1.10}$	$1.91^{0.81}_{0.12}$	$2.34^{2.79}_{0.17}$	$2.99^{2.31}_{0.99}$	$3.14^{1.74}_{0.32}$	$3.24^{2.17}_{0.59}$	$3.93^{0.30}_{0.84}$	$4.60^{3.56}_{1.47}$	$4.67^{1.40}_{0.47}$
16	$4.21^{0.74}_{0.05}$	$2.86^{0.06}_{0.16}$	-	$3.57^{0.29}_{0.19}$	$1.63^{0.50}_{1.81}$	$4.08^{1.88}_{0.61}$	$4.84^{1.87}_{1.86}$	$5.51^{1.37}_{0.82}$	$5.09^{2.97}_{0.58}$	$6.93^{1.23}_{0.78}$	$8.26^{1.93}_{0.51}$	$2.60^{3.20}_{0.10}$
17	-	$2.26^{0.20}_{0.03}$	$1.42^{0.57}_{0.10}$	$1.14^{0.12}_{0.35}$	$2.88^{0.37}_{0.75}$	$2.47^{0.47}_{0.70}$	$2.33^{3.37}_{0.34}$	$3.96^{2.55}_{1.68}$	$4.01^{0.22}_{1.69}$	$4.84^{0.85}_{0.70}$	$5.10^{1.77}_{0.88}$	-
18	$1.95^{0.07}_{0.11}$	$2.16^{0.15}_{0.36}$	$0.55^{0.32}_{0.12}$	$2.73^{0.33}_{0.04}$	$3.62^{0.57}_{0.57}$	$3.42^{1.61}_{0.71}$	$3.94^{0.01}_{1.72}$	$3.99^{0.96}_{0.15}$	$3.87^{0.64}_{0.38}$	$6.46^{1.99}_{0.43}$	$5.78^{1.03}_{0.31}$	$3.69^{0.69}_{0.66}$
19	$1.49^{0.01}_{0.12}$	$1.96^{0.07}_{0.05}$	$0.50^{0.06}_{0.03}$	$2.26^{0.30}_{0.55}$	$2.49^{0.34}_{0.40}$	$2.68^{0.45}_{0.37}$	$3.18^{2.47}_{0.36}$	$3.16^{2.61}_{0.30}$	$2.52^{1.10}_{1.16}$	$4.53^{0.82}_{0.08}$	$4.11^{0.07}_{1.56}$	$4.22^{2.32}_{0.43}$
20	$2.40^{0.05}_{0.23}$	$1.62^{0.02}_{0.01}$	$1.10^{0.03}_{0.04}$	-	-	-	$3.09^{0.61}_{1.69}$	$4.19^{2.03}_{0.16}$	$3.11^{1.84}_{1.36}$	-	$9.08^{0.27}_{0.22}$	$6.49^{0.56}_{0.01}$
21	$2.18^{0.10}_{0.13}$	$1.66^{0.27}_{0.06}$	$0.57^{0.06}_{0.31}$	$2.04^{0.28}_{0.17}$	$2.26^{0.46}_{0.06}$	$3.01^{1.27}_{0.04}$	$4.18^{0.56}_{0.25}$	$3.10^{0.24}_{0.84}$	$3.69^{0.13}_{2.25}$	$3.77^{0.73}_{0.11}$	$5.87^{1.66}_{0.11}$	-
22	$2.52^{0.24}_{0.03}$	$3.03^{0.48}_{0.27}$	$2.00^{0.28}_{0.03}$	$2.81^{0.02}_{0.20}$	$3.85^{0.41}_{0.35}$	$4.68^{1.04}_{0.23}$	$5.88^{0.23}_{0.99}$	$7.10^{0.07}_{1.21}$	-	$7.86^{0.10}_{3.40}$	$7.77^{0.39}_{0.67}$	$8.03^{2.34}_{0.39}$
23	-	$1.96^{0.01}_{0.03}$	$0.91^{0.03}_{0.06}$	-	-	$4.54^{0.40}_{1.21}$	-	-	-	$5.77^{2.22}_{0.47}$	$6.94^{0.31}_{0.42}$	$5.14^{0.56}_{0.14}$
24	-	$2.88^{0.01}_{0.22}$	$1.56^{0.01}_{0.05}$	$2.83^{0.07}_{0.53}$	-	$5.65^{0.20}_{0.15}$	-	$8.81^{0.11}_{0.36}$	-	-	$8.80^{0.03}_{0.05}$	-
25	-	-	-	$3.19^{0.03}_{0.16}$	$4.88^{0.11}_{0.42}$	$6.17^{0.18}_{0.22}$	$6.96^{0.32}_{0.16}$	-	-	-	-	-
26	-	-	$2.74^{0.02}_{0.07}$	$3.34^{0.02}_{0.07}$	$5.13^{1.32}_{0.01}$	$5.16^{0.34}_{0.35}$	$5.98^{0.32}_{0.20}$	$6.50^{0.13}_{1.20}$	$5.82^{0.88}_{0.40}$	$6.38^{0.41}_{0.59}$	$6.50^{0.61}_{0.79}$	$7.85^{0.10}_{0.01}$
27	$4.17^{0.06}_{0.05}$	-	$3.48^{1.00}_{0.01}$	$3.77^{0.36}_{1.14}$	-	-	-	-	-	-	$11.61^{0.06}_{0.10}$	$6.81^{0.98}_{0.29}$
28	-	-	$3.17^{0.89}_{0.03}$	$4.12^{0.14}_{0.01}$	$5.24^{0.03}_{0.05}$	$4.95^{0.66}_{0.73}$	$6.53^{0.67}_{0.85}$	$7.19^{0.48}_{0.23}$	-	-	-	$8.31^{0.01}_{0.01}$
29	-	-	-	-	$6.16^{0.12}_{0.54}$	$5.74^{0.97}_{0.31}$	$6.61^{0.65}_{0.24}$	-	$9.52^{1.15}_{0.05}$	$9.73^{1.45}_{0.80}$	$7.77^{0.41}_{0.87}$	-
30	-	$5.66^{0.15}_{0.16}$	$2.27^{1.23}_{0.06}$	$4.57^{0.01}_{0.29}$	$5.96^{0.16}_{0.21}$	$8.04^{1.04}_{0.19}$	$10.73^{0.59}_{0.01}$	$11.44^{1.00}_{0.06}$	$10.08^{0.48}_{0.07}$	$10.63^{0.04}_{0.11}$	$9.78^{1.21}_{0.37}$	$8.81^{0.58}_{0.01}$
32	$1.60^{0.01}_{0.03}$	$7.10^{0.08}_{0.02}$	$5.41^{1.50}_{1.01}$	-	-	$7.69^{0.38}_{1.70}$	-	$12.06^{4.20}_{0.26}$	-	$18.53^{0.03}_{0.37}$	-	-
33	$2.47^{0.04}_{0.01}$	$4.72^{0.09}_{0.10}$	$2.70^{0.28}_{0.07}$	$4.88^{0.13}_{0.12}$	$6.27^{0.34}_{0.38}$	$6.22^{1.52}_{0.86}$	$7.01^{2.81}_{0.32}$	$8.47^{2.25}_{0.19}$	$7.71^{5.19}_{0.13}$	$10.13^{0.89}_{0.62}$	$8.29^{0.07}_{0.81}$	$5.69^{0.36}_{1.39}$
34	$4.44^{0.19}_{0.08}$	$3.99^{0.02}_{0.19}$	$2.13^{0.20}_{0.06}$	$4.27^{0.16}_{0.11}$	$5.42^{0.11}_{0.03}$	$5.86^{1.18}_{0.15}$	$5.01^{3.70}_{0.59}$	$7.73^{2.78}_{0.16}$	$5.49^{0.04}_{0.62}$	$7.71^{2.30}_{0.26}$	$8.04^{2.67}_{0.36}$	$4.57^{0.50}_{0.76}$
35	-	-	$4.79^{0.19}_{0.06}$	$9.43^{0.87}_{0.28}$	$9.87^{0.03}_{0.07}$	$8.50^{2.20}_{0.35}$	$8.42^{0.50}_{0.76}$	$10.49^{0.30}_{0.32}$	$5.46^{6.20}_{1.24}$	-	$10.66^{2.44}_{0.13}$	$10.61^{0.10}_{1.49}$

Appendix E

ESTIMATION OF Q AND THE DERIVATION OF THE SSTA EQUATION

E.1 Method of Estimating the Surface Heat Fluxes

Following *Isemer et al. [1989]*, the net surface heat flux into the ocean is computed as

$$Q = Q_S - Q_I - Q_L - Q_H \tag{E.1}$$

where Q_S is the net shortwave radiation, Q_I the net longwave radiation, Q_L the latent heat flux, and Q_H the sensible heat flux. The short wave radiative flux is computed using the formula *[Reed, 1977]*

$$Q_S = Q_O(1 - \alpha)(1 - 0.636n + 0.0019h) \tag{E.2}$$

where Q_O is the solar radiation at the top of the atmosphere, for an atmospheric transmission of 0.7, which is kept constant for all months. α is the albedo of the sea surface, which varies with latitude and time. The monthly average values were taken from the tables of *Payne [1972]*. For latitude $40°N$, the monthly mean albedos from January to December are: 0.10, 0.09, 0.07, 0.07, 0.06, 0.06, 0.06, 0.06, 0.07, 0.08, 0.10, 0.11. n is the fractional cloud cover; the monthly averages were obtained from COADS. The noon solar altitude h (in degrees) is calculated as *[Duffie and Beckman, 1974]*

$$h = 90° - \phi + \delta \tag{E.3}$$

where ϕ is the latitude (positive north). The declination δ is given *[Cooper, 1969]* by

$$\delta = 23.45 \sin\left[2\pi\frac{284 + d}{365}\right] \tag{E.4}$$

where d is the day of the year. The clear sky insolation was computed from the Smithsonian formula given by *Reed [1977]* as

$$Q_o = A_o + A_1 \cos\gamma + B_1 \sin\gamma + A_2 \cos 2\gamma + B_2 \sin 2\gamma \tag{E.5}$$

where

$$\gamma = \frac{2\pi}{365}(d - 21) \tag{E.6}$$

The coefficients in (E.5) are functions of latitudes. For latitude $40°N$ to $60°N$,

$$\begin{aligned} A_o &= 342.61 - 1.97\phi - 0.018\phi^2 \\ A_1 &= 52.08 - 5.86\phi + 0.043\phi^2 \\ B_1 &= -4.80 + 2.46\phi - 0.017\phi^2 \\ A_2 &= 1.08 - 0.47\phi + 0.011\phi^2 \\ B_2 &= -38.79 + 2.43\phi - 0.034\phi^2 \end{aligned} \tag{E.7}$$

The values of h and Q_O were computed for each day of the month, then the monthly mean taken.

The net longwave radiation is given by

$$Q_I = \epsilon\sigma T_a^4(0.254 - 0.00495e_a)(1 - cn^d) + 4\epsilon\sigma T_a^3\overline{(T_s - T_a)} \tag{E.8}$$

where $\epsilon = 0.96$ is the emissivity of the ocean surface. $\sigma = 5.67 \times 10^{-8}$W m^{-2}K^{-4} is the Stefan-Boltzmann constant. In the computations that follow, the subscripts a

and s refer to air and sea respectively. T is temperature in degrees Kelvin. c is the cloud cover coefficient which depends on latitude *[Budyko, 1974]*. For latitude 45°, $c = 0.70$. For the cloud cover exponent d, the revised value $d = 1.1$ of *Isemer et al. [1989]* was used. n is the total cloud cover; its monthly averages were obtained from COADS. e_a is the water vapour pressure in hPa (1hPa = 10^2 Pa), which is estimated from

$$e_a = r\, e_s(T_a) \tag{E.9}$$

where r is the relative humidity (monthly means were obtained from COADS), and e_s the saturation vapour pressure at air temperature. Following *Pruppacher and Klett [1980]*, e_s was parameterized as

$$e_s = a_0 + T_a(a_1 + T_a(a_2 + T_a(a_3 + T_a(a_4 + T_a(a_5 + a_6 T_a))))) \tag{E.10}$$

where

$a_0 = 6.107799961$ $\quad a_1 = 4.436518521 \times 10^{-1}$

$a_2 = 1.428945805 \times 10^{-2}$ $\quad a_3 = 2.650648471 \times 10^{-4}$

$a_4 = 3.031240396 \times 10^{-6}$ $\quad a_5 = 2.034080948 \times 10^{-8}$

$a_6 = 6.136820929 \times 10^{-11}$

The monthly mean air temperature T_a was also obtained from COADS. Here T_a is in degrees Celsius and e_a in millibars.

The latent and sensible heat fluxes are computed from the following bulk formula:

$$Q_L = \rho_a L C_E \overline{(q_s - q_a)U} \tag{E.11}$$

$$Q_H = \rho_a c_p C_H \overline{(T_s - T_a)U} \tag{E.12}$$

where

$$\rho_a = \frac{p}{RT_a} \tag{E.13}$$

is the air density in kg m^{-3}. p is the sea level pressure in millibars and R = 287J kg^{-1}K^{-1} is the gas constant for dry air. The latent heat of vaporization L

which is a function of T_s is given *[Pruppacher and Klett, 1980]* as

$$L = 597.3 \left(\frac{273.15}{T_s}\right)^{\beta} \tag{E.14}$$

where

$$\beta = 0.167 + 3.67 \times 10^{-4}\, T_s$$

T_s is in degrees Kelvin and L in J kg^{-1}. C_E and C_H are the bulk exchange coefficients. The values of the exchange coefficients used are the revised and adjusted estimates of *Isemer et al. [1989]*, in which C_E varies with wind speed U and stability, and $C_H = 0.94C_E$. The stability dependence of C_E is expressed by the virtual temperature difference $(\overline{T}_{sv} - \overline{T}_{av})$, where the overbar denotes a monthly mean. The virtual temperatures (in degrees Kelvin) are given by *[Gill, 1982]*

$$\overline{T}_{sv} = \overline{T}_s[1 + 0.6078\, q_s(\overline{T}_s)] \tag{E.15}$$

$$\overline{T}_{av} = \overline{T}_a[1 + 0.6078\, q_a(\overline{T}_a)] \tag{E.16}$$

q_s and q_a are the saturation specific humidity at the sea surface and the specific humidity of the surface air layer respectively. $c_p = 1005$J $\mathrm{kg}^{-1}\mathrm{K}^{-1}$ is the specific heat of air at constant pressure. The monthly average product $\overline{(q_s - q_a)U}$, $\overline{(T_s - T_a)U}$, $\overline{T}_s$, $\overline{T}_a$ and $\overline{U}$ were obtained from COADS. (Please note that all quantities obtained from COADS data set were trimmed.)

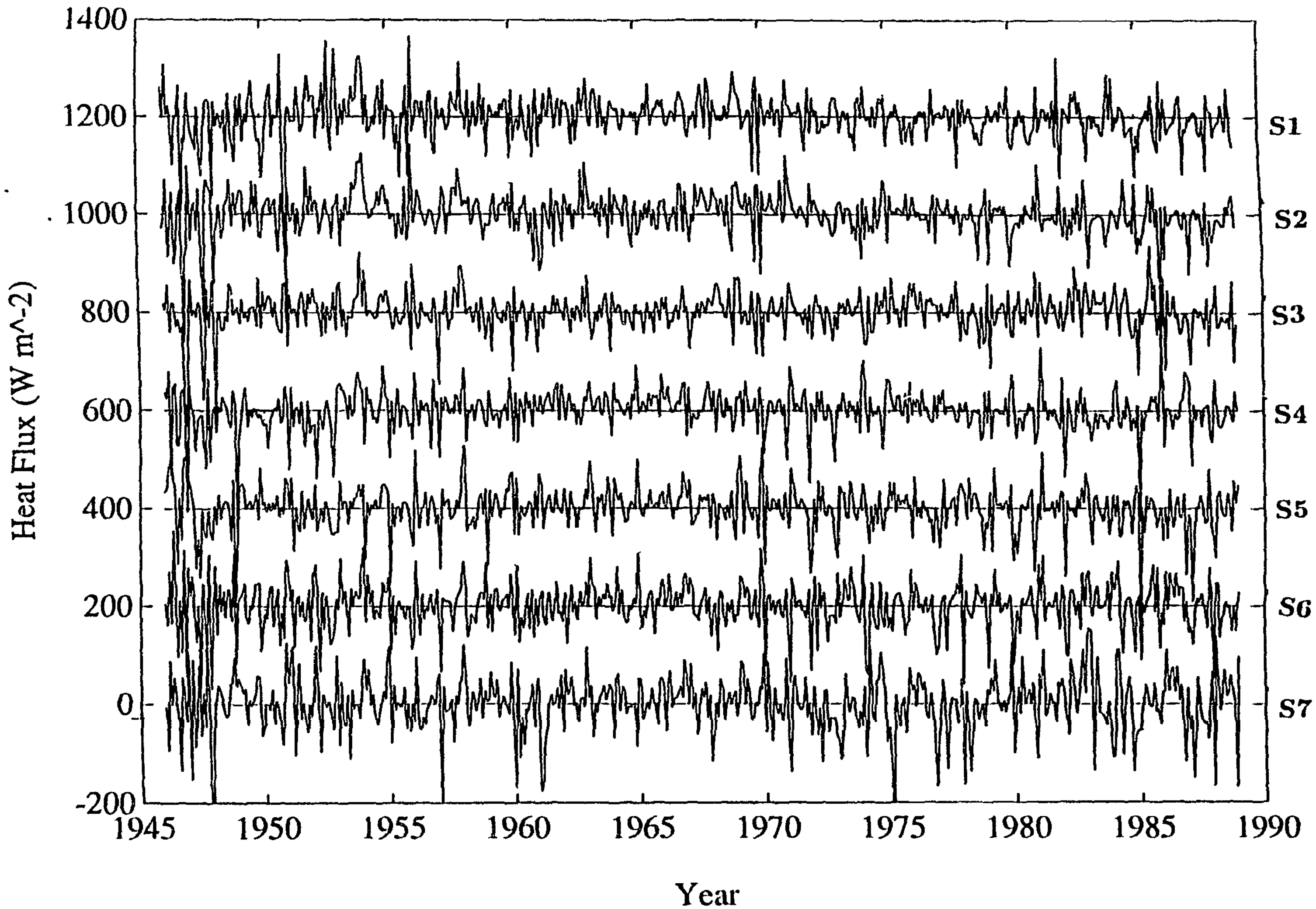

Figure E.1: Interannual variability of Q' on the Scotian Shelf and Slope region.

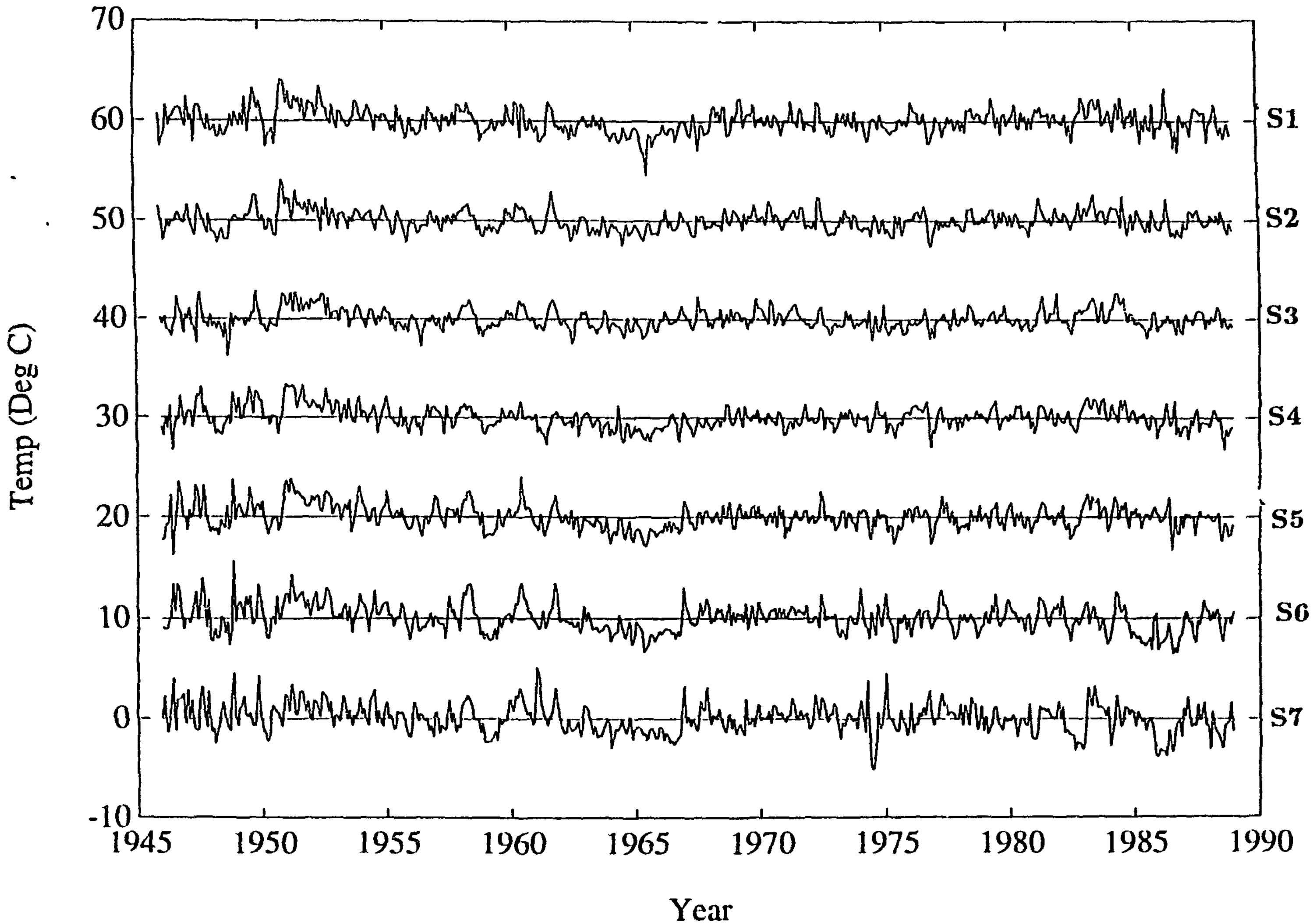

Figure E.2: Interannual variability of SSTAs on the Scotian Shelf and Slope region.

E.2 Derivation of the Water Temperature Anomaly Equation

The temperature equation is given as

$$\frac{\partial T}{\partial t} = \frac{\partial}{\partial z}\left(K_V \frac{\partial T}{\partial z}\right) - \underline{u} \cdot \nabla T - w\frac{\partial T}{\partial z} + K_H \nabla^2 T \tag{E.17}$$

The variables are written as the sum of the long term (climatological) monthly mean (denoted by tilde ˜) and a deviation from the long term mean (symbolised by prime ′), i.e.,

$$T = \tilde{T} + T', \quad K_V = \widetilde{K}_V + K_V', \quad \underline{u} = \tilde{\underline{u}} + \underline{u}', \quad w = \tilde{w} + w' \quad \text{and} \quad K_H = \widetilde{K}_H + K_H' \tag{E.18}$$

where the primed quantities are the anomalies. If we substitute (E.18) into (E.17) we have

$$\begin{aligned}\frac{\partial(\tilde{T}+T')}{\partial t} = {} & \tfrac{\partial}{\partial z}\left[\left(\widetilde{K}_V + K_V'\right)\tfrac{\partial}{\partial z}\left(\tilde{T}+T'\right)\right] - (\tilde{\underline{u}} + \underline{u}')\cdot\nabla(\tilde{T}+T') \\ & -(\tilde{w}+w')\tfrac{\partial}{\partial z}\left(\tilde{T}+T'\right) + (\widetilde{K}_H + K_H')\nabla^2(\tilde{T}+T')\end{aligned} \tag{E.19}$$

By taking the long term mean of (E.19) and assuming that the tilded and primed quantities are uncorrelated we have

$$\begin{aligned}\frac{\partial\tilde{T}}{\partial t} = {} & \tfrac{\partial}{\partial z}\left(\widetilde{K}_V \tfrac{\partial\tilde{T}}{\partial t}\right) - \tilde{\underline{u}}\cdot\nabla\tilde{T} - \tilde{w}\tfrac{\partial\tilde{T}}{\partial z} + \widetilde{K}_H\nabla^2\tilde{T} \\ & +\tfrac{\partial}{\partial z}\left(\widetilde{K_V'\tfrac{\partial T'}{\partial t}}\right) - \widetilde{\underline{u}'\cdot\nabla T'} - \widetilde{w'\tfrac{\partial T'}{\partial z}} + \widetilde{K_H'\nabla^2 T'}\end{aligned} \tag{E.20}$$

The temperature anomaly equation is obtained by subtracting (E.20) from (E.19). The result is

$$\begin{aligned}\frac{\partial T'}{\partial t} = {} & \tfrac{\partial}{\partial z}\left(\widetilde{K}_V\tfrac{\partial T'}{\partial z}\right) - \tilde{\underline{u}}\cdot\nabla T' - \tilde{w}\tfrac{\partial T'}{\partial z} + \widetilde{K}_H\nabla^2 T' \\ & +\tfrac{\partial}{\partial z}\left(K_V'\tfrac{\partial\tilde{T}}{\partial z}\right) - \underline{u}'\cdot\nabla\tilde{T} - w'\tfrac{\partial\tilde{T}}{\partial z} + K_H'\nabla^2\tilde{T} \\ & -\tfrac{\partial}{\partial z}\left(\widetilde{K_V'\tfrac{\partial T'}{\partial z}}\right) + \widetilde{\underline{u}'\cdot\nabla T'} + \widetilde{w'\tfrac{\partial T'}{\partial z}} - \widetilde{K_H'\nabla^2 T'} \\ & +\tfrac{\partial}{\partial z}\left(K_V'\tfrac{\partial T'}{\partial z}\right) - \underline{u}'\cdot\nabla T' - w'\tfrac{\partial T'}{\partial z} + K_H'\nabla^2 T'\end{aligned} \tag{E.21}$$

At the surface

$$K_v \frac{\partial T}{\partial z} = \frac{Q}{\rho c_p} \tag{E.22}$$

Expressing the quantities in (E.22) as the sum of their means and anomalies, as before, we have

$$\left(\widetilde{K}_v + K_v'\right) \frac{\partial}{\partial z} \left(\tilde{T} + T'\right) = \frac{\tilde{Q}}{\rho c_p} + \frac{Q'}{\rho c_p} \tag{E.23}$$

The long term mean of (E.23) gives

$$\widetilde{K}_v \frac{\partial \tilde{T}}{\partial z} + \widetilde{K_v' \frac{\partial T'}{\partial t}} = \frac{\tilde{Q}}{\rho c_p} \tag{E.24}$$

The anomaly equation for the surface boundary condition is found by subtracting (E.24) from (E.23), i.e.,

$$\widetilde{K}_v \frac{\partial T'}{\partial z} + K_v' \frac{\partial \tilde{T}}{\partial z} + K_v' \frac{\partial T'}{\partial z} - \widetilde{K_v' \frac{\partial T'}{\partial z}} = \frac{Q'}{\rho c_p} \tag{E.25}$$

References

Barnett, T. P., 1981. On the nature and causes of large-scale thermal variability in the Central North Pacific ocean. *J. Phys. Oceanogr.*, **11**, 887-904.

Bjerknes, J., 1964. Atlantic Air-Sea Interaction. *Adv. Geophys.*, **10**, 1-82.

Brown, W. S. and R. C. Beardsley, 1978. Winter circulation in the western Gulf of Maine: Part 1. Cooling and water mass formation. *J. Phys. Oceanogr.*, **8**, 265-277.

Brown, W. S. and J. D. Irish, 1992. The annual evolution of geostrophic flow in the Gulf of Maine: 1986-1987. *J. Phys. Oceanogr.*, **22**, 445-473.

Bryan, K. and E. Schroeder, 1960. Seasonal heat storage in the North Atlantic Ocean. *J. Meteorol.*, **17**, 670-674.

Bunker, A. F., 1976. Computation of surface energy flux and annual air-sea interaction cycles of the North Atlantic Ocean. *Mon. Weather Rev.*, **104**, 1122-1140.

Cayan, D. R., 1985. North Atlantic seasonal sea surface temperature anomalies and associated statistics, 1949-85. *SIO 85-19, Scripps Institution of Oceanography*, 89 pp.

Clark, N. E., 1972. Specification of Sea Surface Temperature Anomaly Patterns in the Eastern North Pacific. *J. Phys. Oceanogr.*, **2**, 391-404.

Cooper, P. I., 1969. The absorption of solar radiation in solar stills. *Solar Energy*, **12**.

Csanady, G. T., 1979. The pressure field along the western margin of the North Atlantic. *J. Geophys. Res.*, **84**, 4905-4915.

Daly, A. W., 1978. The response of North Atlantic sea surface temperature to atmospheric forcing processes. *Quart. J. R. Met. Soc.*, **104**, 363–382.

Davis, R. E., 1976. Predictability of Sea Surface Temperature and Sea Level Pressure Anomalies over the North Pacific Ocean. *J. Phys. Oceanogr.*, **6**, 249–266.

Davis, R. E., 1978. Predictability of Sea Level Pressure Over the North Pacific Ocean. *J. Phys. Oceanogr.*, **8**, 233-246.

Draper, N. and H. Smith, 1981. **Applied regression analysis.** John Wiley and

Sons, New York.

Duffie, J. A. and Beckman, W. A., 1974. Solar energy thermal processes, John Wiley and Sons, New York.

de Young, B. and S. Pond, 1988. The deepwater exchange cycle in Indian Arm, British Columbia. *Estuarine, Coastal and Shelf Science*, **26**, 285-308.

Drinkwater, K., B. Petrie and W. H. Jr. Sutcliffe, 1979. Seasonal geostrophic volume transports along the Scotian Shelf. *Estuarine, Coastal and Shelf Science*, **9**, 17-27.

Drinkwater, K. and G. Taylor, 1982. Monthly means of the temperature, salinity and density along the Halifax section. *Can. Tech. Rep. of Fish. and Aquatic Sci.*, **No.1093**, 67 pp.

Drinkwater, K. F. and R. W. Trites, 1987. Monthly means of temperature and salinity in the Scotian Shelf region. *Can. Tech. Rep. of Fish. and Aquatic Sci.*, **No.1539**, 101 pp.

Fleagle, R. G. and J. A. Businger, 1980. **An Introduction to Atmospheric Physics**, Academic Press, New York. 432pp.

Fletcher, J., 1985. Comprehensive Ocean-Atmosphere Data Set. Release 1.

Frankignoul, C. and K. Hasselmann, 1977. Stochastic climate models II, Application to sea surface-temperature temperature variability and the thermocline variability, *Tellus*, **29**, 287-384.

Frankignoul, C., 1979a. Stochastic Forcing Models of climate variability. *Dyn. Atm. Oceans*, **3**, 465-479.

Frankignoul, C., 1979b. Large scale air-sea interactions and climate predictability. In **Marine Forecasting**, edited by Nihoul, J. C. J. Elsevier, New York, 199-209.

Frankignoul, C. and R. W. Reynolds, 1983. Testing a Dynamical Model for Mid-latitude Sea Surface Temperature Anomalies. *J. Phys. Oceanogr.*, **13**, 1131-1145.

Frankignoul, C., 1985. Sea Surface Temperature Anomalies, Planetary Waves, and

Air-Sea Feedback in the Middle Latitudes. *Rev. Geophys.*, **23**, 357-390.

Gargett, A. E., 1984. Vertical eddy diffusivity in the ocean interior. *J. Mar. Res.*, **42**, 359-393.

Garrett, C., R. Outerbridge and K. Thompson, 1991. Interannual variability in Mediterranean Heat and Water Fluxes. *Submitted to Nature*

Gaspar, P., 1987. Modeling the Seasonal cycle of the upper ocean. *J. Phys. Oceanogr.*, **18**, 161-180.

Gill, A. E., 1982. **Atmosphere-Ocean Dynamics**, Academic Press, Toronto, 662pp.

Gill, A. E, 1983. Patterns of interannual variability associated with the ocean and atmosphere, *WCRP Publ. Series No. 1*, **2**, 57-75.

Gill, A. E. and P. P. Niiler, 1973. The theory of the seasonal variability in the ocean. *Deep Sea Res.*, **20**, 141-177.

Hachey, H. B., 1938. The origin of the cold water layer of the Scotian Shelf. *Trans. Roy. Soc. Can.*, **3**, 29-42.

Haney, R. L., 1971. Surface Thermal Boundary Condition for Ocean Circulation Models. *J. Phys. Oceanogr.*, **1**, 241-248.

Hansen, J., G. Russell, A. Lacis, I. Fung, D. Rind and P. Stone, 1985. Climate response times: Dependence on climate sensivity and ocean mixing. *Science*, **229**, 857-859.

Hasselmann, K., 1976. Stochastic climate models. Part I. Theory. *Tellus*, **28**, 473-484.

Henderson-Sellers, B., 1982. A simple formula for vertical eddy diffusion coefficients under conditions of nonneutral stability. *J. Geophys. Res.*, **87**, 5860-5864.

Holton, J. R., 1979. **An Introduction to Dynamical Meteorology**, Academic Press, New York. 391 pp.

Isemer, H. and L. Hasse, 1987. **The Bunker Climate Atlas of the North Atlantic Ocean**. *Volume 2: Air-Sea Interaction*, Spinger-Verlag Heidelberg, New York.

Isemer, H., J. Willerbrand and L. Hasse, 1989. Fine adjustment of large scale air-sea energy flux parameterizations by direct estimates of ocean heat transport. *J. of Climate*, **2**, 1173-1184.

Jassby, A. and T. Powell, 1975. Vertical patterns of eddy diffusion during stratification in Castle Lake, California. *Limnol. Oceanogr.*, **20**, 530-543.

Kaufeld, L., 1981. The development of a new Beaufort equivalent scale. *Meteorol Rundsch*, **34**, 17-23.

Kraus, E. B. and J. S. Turner, 1967. A one-dimensional model of the seasonal thermocline, II. *Tellus*, bf 19, 98-106.

Lacy, B. J., 1988. The Couple Atmosphere-Ocean System: An Analysis of North Atlantic Air Pressure and Sea Surface Temperature. *M.Sc. Thesis*, 101 pp.

Large, W. G. and S. Pond, 1981. Open ocean momentum flux measurement in moderate to strong winds. *J. Phys. Oceanogr.*, **11**, 324-336.

Lau, N.-C. and Nath M. J., 1989. A General Circulation Model Study of the Atmospheric Response to Extratropical SST Anomalies Observed in 1950-79. *Submitted for publication in the J. of Climate*

Lauzier, L. M., 1967b. Bottom residual drift on the continental shelf area of the Canadian Atlantic Coast. *J. Fish. Res. Board Can.*, **24**, 1845-1858.

Lisitzin, E. and J. Pattullo, 1961. The principal factors influencing the seasonal oscillation of sea level. *J. Geophys. Res.*, **66**, 845-852.

Loder, J. W., 1990. Summertime bottom temperature on the southeast shoal of the Grank Bank, and implication for exchange rates. *Submitted for publication.*

Lowe, P. R. and Ficke, J. M., 1974. Techn. Paper, No.4-74, Environmental Prediction Res. Facility, Naval Post Grad. School, Monterey, Calif.

Malkus, J. S., 1962. Large-Scale Interactions. In *The Sea*, Hill, M. N. (ed.), **1**, 88-294.

Mckenzie, R. A., 1934. The relation of the cod to water temperatures. *Can. Fisherman.*, **21**, 11-14.

McLellan, H. F., 1954. Temperature-salinity relations and mixing on the Scotian

Shelf. *J. Fish. Res. Board Can.*, **11**, 419-430.

Merle, J., 1980. Seasonal variation of heat storage in the tropical Atlantic Ocean. *Oceanol. Acta*, **3**. 455-463.

Miller, J. R., 1976. The salinity effect in a mixed layer ocean model. *J. Phys. Oceanogr.*, **6**, 29-35.

Monin, A. S., V. M. Kamenkovich and V. G. Kort, 1977. **Variability in the Ocean**. (Ed. Lumley, J. J.) John Wiley and Sons, New York.

Munk, W. H. and E. R. Anderson, 1948. Notes on a theory of the thermocline. *J. Mar. Res.*, **7**, 276-295.

Namias, J. and R. M. Born, 1970. Temporal coherence in North Pacific sea-surface temperature patterns. *J. Geophys. Res.*, **75**, 5952-5955.

Namias, J, X. Yuan and D. R. Cayan, 1988. Pereistence of North Pacific seas surface temperature and atmopsheric flow patterns. *J. Climate*, **1**, 682-703.

Palmer, T. N. and Z. Sun, 1985. A modelling and observational study of the relationship between sea surface temperature in the north-west Atlantic and the atmospheric general circulation. *Quart. J. Roy. Meteor. Soc.*, **111**, 947-975.

Pattullo, J., W. Munk, R. Revelle, and E. Strong, 1955. The seasonal oscillation in sea level *J. Mar. Res.*, **14**, 89-156.

Paxton, P., 1986. **The Statesman's year-book world gazetteer**. St. Martin's Press, New York, p.15.

Petrie, B., B. J. Topliss and D. G. Wright, 1987. Coastal upwelling and eddy development off Nova Scotia. *J. Phys. Oceanogr.*, **29**, 12979-12991.

Petrie, B., S. Akenhead, J. Lazier and J. Loder, 1988. The cold intermediate layer on the Labrador and Northeast Newfoundland Shelves, 1978-86. *NAFO Sci. Coun. Studies*, **12**, 57-69.

Petrie, B., J. W. Loder, S. Akenhead and J. Lazier, 1991. Temperature and salinity variability on the Eastern Newfoundland. *Atmos-Ocean.*, **29**, 14-36.

Press, W. H., B. P. Flannery, S. A. Teukolsky, and W. T. Vetterling, 1986. **Nu-**

merical Recipes. Cambridge University Press, New York, 818 pp.

Price, J. F., E. A. Terray and R. A. Weller, 1987. Upper Ocean dynamics. *Rev. Geophys.*, **25**, 193-203.

Price, J. F., R. A. Weller and R. Pinkel, 1986. Diurnal cycling: observation and models of the upper ocean response to diurnal heating, cooling, and wind mixing. *J. Geophys. Res.*, **91**, 8411-8427.

Pruppacher, H. R. and Klett, J. D., 1980. Microphysics of clouds and precipitation, D. Reidel Publishing Company, Boston, USA.

Quayle, R. G., 1980. Climatic comparisons of estimated and measured wind from ships. *J. Appl Meteor.*, **19**, 142-156.

Ramage, C. S., 1984. Can shipboard measurements reveal secular changes in tropical air-sea heat flux? *J. Climate Appl. Meteor.*, **23**, 187-193.

Ratcliffe, R. A. S. and R. Murray, 1970. New lag associations between North Atlantic sea temperature and European pressure applied to long-range weather forecasting. *Quart. J. Met. Soc.*, **96**, 226-246.

Reynolds, R. W., 1978. Sea surface temperature in the North Pacific Ocean. *Tellus*, **30**, 97-103.

Reynolds, R. W., 1979. A stochastic forcing model of sea surface temperature anomalies in the North Pacific and North Atlantic. **Rep 8**, Clim. Res. Inst., Oregon State Univ., Corvallis.

Rose, G. A. and W. C. Leggett, 1989. Interactive effects of geophysically-forced sea temperature and prey abundance on mesoscale coastal distributions of marine predator, Atlantic codd (Gadus morhua). *Can. J. Fish. Aquat. Sci.*, **46**, 1904-1913.

Ruiz De Elvira, A. and P. Lemke, 1982. A Langevin equation for stochastic models with periodic feedback and forcing variance. *Tellus*, **34**, 313-320.

Schmitt, R. W., P. S. Bogden and C. E. Dorman, 1989. Evaporation minus precipitation and density fluxes for the North Atlantic. *J. Phys. Oceanogr.*, **19**, 1208-1221.

Schwing, F. B., 1989. Subinertial circulation on the Scotian Shelf: observations and models. **Ph. D. Thesis**, 207 pp.

Scott, J. S., 1982. Depth, temperature and salinity preferences of common fishes of the Scotian Shelf. *J. Northw. Atl. Fish. Sci.* **3**, 29-39.

Smith, P. C., 1978. Low frequency fluxes of momentum, heat, salt, and nutrients at the edge of the Scotian shelf. *J. Geophys. Res.*, **83**, 4079-4096.

Smith, P. C., 1983. The mean and seasonal circulation off southwest Nova Scotia. *J. Phys. Oceanogr.*, **13**, 1034-1054.

Smith, P. C, B. Petrie, and C. R. Mann, 1978. Circulation, variability, and dynamics of the Scotian Shelf and slope. *J. Fish. Res. Board Can.*, **35**, 1067-1083.

Sutcliffe, W. H. Jr., R. H. Loucks and K. F. Drinkwater, 1976. Coastal circulation and physical oceanography of the Scotian Shelf and the Gulf of Main. *J. Fish. Res. Board Can.*, **33**, 98-115.

Thompson K. R., 1986. North Atlantic sea level and circulation. *Geophys. J. Roy. Astron. Soc.*, **87**, 15-32.

Thompson K. R., 1990. North Atlantic sea level and circulation. In **Sea-level change. National Academy Press, Washington**, USA, 52-62.

Thompson, K. R. and M. G. Hazen, 1983. Interseasonal changes of wind stress and Ekman upwelling: North Atlantic, 1950-1980. *Can. Tech. Rep. of Fish. and Aquatic Sci.*, **No.1214**, 175 pp.

Thompson, K. R., R. F. Marsden and D. G. Wright, 1983. Estimation of low-frequency wind stress fluctuation over the open ocean. *J. Phys. Oceanogr.*, **13**, 1003-1011.

Thompson, K. R., R. H. Loucks, and R. W. Trites, 1988. Sea Surface Temperature Variability in the Shelf-Slope Region of the Northwest Atlantic. *Atmosphere-Ocean*, **26**, 282–299.

Trites, R. W. and R. E. Banks, 1958. Circulation on the Scotian Shelf as indicated by drift bottles. *J. Fish. Res. Board Can.*, **15**, 79-89.

Umoh, J. U. and K. R. Thompson, 1990. Air-sea fluxes and heat storage in the

Northwest Atlantic. *Eos*, **71 (43)**. A paper presented at the American Geophysical Union, 1990 Fall Meeting, San Francisco, California, U.S.A.

Unesco, 1981. The practical salinity scale 1978 and the international equation of state of seawater 1980. *Unesco technical papers in marine science*, **36**, 25pp.

Weare, B. C., 1977. Empirical orthogonal function analysis of Atlantic Ocean surface temperatures. *Q. J. R. Meteorol. Soc.*, **103**, 467-478.

Weare, B. C., A. R. Navato and R. E. Newell, 1976. Empirical orthogonal function analysis of Pacific sea surface temperature . *J. Phys. Oceanogr.*, **6**, 671-678.

Weaver, A. J. and E. S. Sarachik, 1990. On the importance of vertical resolution in certain ocean general circulation models. *J. Phys. Oceanogr.*, **20**, 600-609.

Yin, F. L. and I. Y. Fung, 1991. Net diffusivity in ocean general circulation models with nonuniform grids. *J. Geophys. Res.*, **96**, 10773-10776.